Title

The synthesis and characterization of isolated Ga3+ cations in Ga/H-MFI and the kinetics of light alkane dehydrogenation and cracking over [GaH]2+ and [GaH2]+ cations

Author

Phadke, Neelay M

Publication Date

2019

Peer reviewed|Thesis/dissertation

The synthesis and characterization of isolated Ga^{3+} cations in Ga/H-MFI and the kinetics of light alkane dehydrogenation and cracking over $[GaH]^{2+}$ and $[GaH_2]^{+}$ cations

By

Neelay Makarand Phadke

A dissertation submitted in partial satisfaction of the

requirements for the degree of

Doctor of Philosophy

in

Chemical Engineering

in the

Graduate Division

of the

University of California-Berkeley

Committee in charge:

Professor Alexis T. Bell, Chair
Professor Alex Katz
Professor T. Don Tilley

Spring 2019

The synthesis and characterization of isolated Ga^{3+} cations in Ga/H-MFI and the kinetics of light alkane dehydrogenation and cracking over $[GaH]^{2+}$ and $[GaH_2]^{+}$ cations

Abstract

The synthesis and characterization of isolated Ga^{3+} cations in Ga/H-MFI and the kinetics of light alkane dehydrogenation over $[GaH]^{2+}$ and $[GaH_2]^{+}$ cations

by

Neelay Makarand Phadke

Doctor of Philosophy in Chemical Engineering

University of California, Berkeley

Professor Alexis T. Bell, Chair

Ga-exchanged H-MFI (Ga/H-MFI) is known to be a highly reactive and selective heterogeneous catalyst for the conversion of light alkanes (ethane, propane and n-butane) into alkenes and aromatics and H_2 via dehydrogenation and dehydrocylization reactions. However, the chemical structure of ion-exchanged Ga complexes, their state under reaction conditions and their catalytic role during light alkane conversion, are not well understood. The aim of this dissertation is to study the synthesis of isolated and well-defined Ga species that are ion-exchanged in Ga/H-MFI, to characterize Ga structures formed as a function of the Ga/Al ratio and to examine the site requirements, kinetics and mechanisms of light alkane dehydrogenation and cracking over these catalysts. These findings enable the rational design of zeolite-based dehydrogenation catalysts that contain Ga species that are specifically tailored to be catalytically active for a given alkane reactant.

The synthesis of isolated and well-defined Ga species ion-exchanged in Ga/H-MFI remains a formidable challenge. In addition, there has been considerable debate with regard to the structure of the Ga species that is kinetically relevant during alkane dehydrogenation and dehydrocyclization. In Chapter 2, we examine synthetic protocols for the preparation of Ga/H-MFI via the vapor phase exchange of dehydrated H-MFI with $GaCl_3$. Catalysts with a range of Ga/Al ratios (0.1-0.7) are prepared using this protocol and Ga species in these materials are characterized under oxidizing and reducing conditions using a number of chemical and spectroscopic probes. We find that gas-phase $GaCl_3$ monomers or dimers react with Brønsted acid O-H groups in H-MFI to form monovalent $[GaCl_2]^{+}$ cations and HCl. The treatment of $GaCl_2$-MFI materials with 10^5 Pa H_2 at 823 K leads to the stoichiometric removal of Ga-bound Cl ligands as HCl and the formation of $[GaH_2]^{+}$ cations. These structures upon oxidation in O_2 form isolated $[Ga(OH)]^{2+}$ cations at low Ga/Al ratios (~ 0.1) and isolated $[Ga(OH)_2]^{+}$-H^{+} cation pairs at Ga/Al ratios higher than 0.1 but less than 0.3, as evidenced by infrared spectroscopy, NH_3-TPD, Ga K-edge XANES and EXAFS. Both structures require the presence of proximate cation-exchange sites (either present as next-nearest neighbors (NNN) or next, next-nearest

neighbors (NNNN)). At a Ga/Al ratio of 0.3, the available proximate cation-exchanges sites become saturated by Ga^{3+} species and further addition of Ga to these materials leads to the formation of neutral, condensed GaO_x oligomers. Upon exposure of isolated, oxidized Ga^{3+} structures to H_2 at elevated temperatures, H_2-TPR, NH_3-TPD, infrared spectroscopy, Ga K-edge XANES and EXAFS suggest that $[GaH]^{2+}$ cations, $[Ga(OH)H]^+$-H^+ cation pairs and $[GaH_2]^+$ cations form. Theoretically generated thermodynamic phase diagrams suggest that the nature of Ga^{3+} species formed under oxidizing or reducing conditions is highly sensitive to the framework Al-Al distance between cation-exchange sites, H_2 and H_2O partial pressures. Under sufficiently anhydrous reducing conditions ($< 10^{-1}$ Pa H_2O), these calculations together with experimental data suggest that $[GaH]^{2+}$ cations and $[GaH_2]^+$-H^+ cation pairs are the only structures that form in Ga/H-MFI with Ga/Al ratios ≤ 0.3.

The synthesis of isolated Ga^{3+} species that are well-characterized under oxidizing and reducing conditions allows the identification of catalytically relevant Ga species and the mechanisms by which these species catalyze light alkane dehydrogenation. In Chapter 3, we examine the site requirements, the kinetics and the mechanisms for propane (C_3H_8) dehydrogenation and cracking over Ga/H-MFI catalysts prepared in the manner described in Chapter 2. It is observed that dehydrogenation and cracking rates over Ga/H-MFI are 2 orders and 1 order of magnitude higher than the corresponding reaction rates over H-MFI. Both reactions are catalyzed by $[GaH]^{2+}$ cations; $[GaH_2]^+$ cations are inactive for these reactions. It is also observed that both reactions exhibit a Langmuir-Hinshelwood dependence on C_3H_8 partial pressure and are inhibited H_2 in a manner such that ratios of dehydrogenation to cracking are independent of C_3H_8 and H_2 partial pressures. Experimentally measured activation enthalpies together with theoretical analysis of reaction pathways suggest that both reactions proceed over $[GaH]^{2+}$ via the heterolytic dissociation of C_3H_8 by $[GaH]^{2+}$ to form $[C_3H_7\text{-}GaH]^+$-H^+ cation pairs. Dehydrogenation rates are limited by β-hydride elimination within the alkyl fragment to form C_3H_6 and H_2. Cracking rates are limited by the H^+ attack of the C-C bond in the alkyl fragment. Both reactions are inhibited in the presence of H_2 due to the formation of $[GaH_2]^+$-H^+ cation pairs.

In Chapter 4, we extend our study of light alkane dehydrogenation over Ga/H-MFI to ethane (C_2H_6) and n-butane (n-C_4H_{10}) reactants. We find that C_2H_6 dehydrogenation rates are catalyzed by both $[GaH]^{2+}$ and $[GaH_2]^+$ cations, consistent with the similar free energy barriers for this reaction over both structures predicted by theoretical calculations. Over $[GaH_2]^+$ cations, C_2H_6 dehydrogenation rates are weakly inhibited by H_2 and bear a Langmuirian dependence on C_2H_6 partial pressure. Measured activation enthalpies together with theoretical calculations are consistent with a mechanism involving the heterolytic C-H activation of C_2H_6 by $[GaH_2]^+$ cations to form $[C_2H_5\text{-}GaH]^+$ cations and H_2. A subsequent β-hydride elimination from the C_2H_5 fragment results in the formation of C_2H_4. At low C_2H_6 pressures, dehydrogenation rates are first-order in C_2H_6 and are limited by initial C-H cleavage. At high C_2H_6 partial pressures, dehydrogenation rates are zero-order in C_2H_6 partial pressure and are limited by the β-hydride elimination step. On the other hand, C_4H_{10} dehydrogenation, terminal and central cracking reactions are catalyzed only by $[GaH]^{2+}$ rates (and not $[GaH_2]^+$ cations) with turnover frequencies that are 3 orders, 2 orders and 1 order of magnitude higher than the turnover frequencies of the corresponding reactions over H-MFI. Kinetic rate measurements together with theoretical results suggest the mechanism for C_4H_{10} dehydrogenation and cracking over Ga/H-MFI is analogous to the mechanism for C_3H_8 dehydrogenation. In this case, $[GaH]^{2+}$ cations activate secondary C-H bonds in n-C_4H_{10} to form $[sec\text{-}C_4H_9\text{-}GaH]^+$-$H^+$ cation pairs. These

intermediates then either undergo dehydrogenation via β-hydride elimination to form 1-butene, 2-butene and H_2 or undergo terminal or central cracking via C-C bond attack by the proximal Brønsted acid O-H group. The transition state for central cracking is more constrained than that for terminal cracking resulting in terminal cracking rates over Ga/H-MFI that are a factor of 3 higher than central cracking rates. $[GaH_2]^+$ cations are inactive for the conversion of alkane reactants with carbon chain length greater than 2 due to entropic losses associated with the rate-limiting transition state over these species.

Dedication

To my wife, my brother and my parents, who have stood by me through this journey. And to my grandparents, who have taught me through their struggle, to find strength and courage to carry on, even in the face of adversity.

Table of Contents

List of Figures

List of Schemes

List of Tables

Acknowledgements

I can look back at my almost 6.5 years of graduate school at Berkeley, as one of the most rewarding, exciting yet challenging and at times, even agonizing experiences I have ever had. It has been rewarding and exciting not only because of the science, but also because of the relationships that I have been bestowed with along the way. A wise person once told me that your greatest strength in life is the group of people you surround yourself with. I couldn't agree more with this statement. As I stand at the end of this chapter in life, I consider it pertinent to thank those who have helped me get to this point. Their contribution to this journey has been immense and varied. Some have supported and encouraged me when times were tough and have celebrated my success like it was their own while others spent hours of their time to teach me about everything from physical chemistry to car insurance. There are also those individuals who in spite of being hundreds of miles away, made it a point to make me laugh whenever I got too gloomy about life. Without their gracious support, I would likely not be writing this document.

Firstly, I would like to thank my mentor, Professor Alexis T. Bell for the immense contribution he has made to my development as a researcher and to this research project. At a particularly low point in my graduate school career during my 3rd year, I was seeking a new research home. Alex welcomed me into his group and immediately made me feel at ease and emphasized that I would be working with him rather than for him. This latter point is particularly significant and embodies the collaborative work spirit of the Bell group. Alex has spent countless hours over the last 3.5 years working with me, teaching me how to do research and how to present my work to an audience. While our regular weekly meetings ensured that we stayed on course, Alex encouraged me to push the boundaries and seek out new and innovative techniques to answer challenging research questions. His friendly nature, systematic work approach and his quest to uncover fundamental details about catalytic chemistry have proved greatly inspirational to me. I will forever carry the lessons he has taught me.

I would like to thank my parents-Makarand and Yogeshree Phadke, who have stood by me all of these years. Their boundless love, support for every endeavor of mine and the sound advice they have always given me, are all factors that helped shape me into the person that I am. Not enough can be said to thank my brother Ameya Phadke. He has not only been a best friend to me, but also a role model who has taught me much about navigating through the sometimes choppy waters in life. I would also like to thank my mother-in-law Medha Joshi, my sister-in-law Mugdha Joshi and Nakul Valsangkar, all of whom have given me so much love and a wonderful new perspective on life, these past three years. I am grateful to my grandparents for their profound wisdom and support. Their struggle has taught me the importance of hard work and perseverence.

I have many close friends to thank, for making these past 6.5 years so enjoyable and meaningful. Ashutosh Dharap and Jayada Karandikar, friends of mine since my days at Wisconsin, are like family to me. I will forever cherish our dinners, bar crawls, road trips and long, long conversations. Nigel Becknell, who is almost like a brother to me, has not only stood by my side through rough patches during grad school but also stood by my side when I got married. I got to know Stef Dulak through Nigel (they are married) and she has since become a very close friend of mine. I would like to thank Salil Deosthale and Abhinav Gaikwad, two of my best friends in Berkeley, for all of the fun times we have had together. This city would not be the same to me, without you two. In particular, I would always enjoy and look forward to

grabbing lunch with Salil during the work week. A dear friend of mine since our days in Barnard Hall at UW-Madison, Alison Dirr and I have stayed in touch even 6.5 years after moving on from Madison. We still have frequent and lengthy phone conversations and her bright-as-the-sun demeanor has never failed to bring a smile to my face. Melanie Drake and Brandon Curtis are among my closest friends at Berkeley. From my early days in Berkeley, when I was homeless and had to crash on Brandon's sofa for a few nights, to our cooking adventures and engaging conversations-I thank you for all of these wonderful memories. Our weekend picnics-in-the park with Aman and Prerna took me out of lab and helped me put my graduate school life in perspetive. I must thank Ashok Katdare, a dear friend of mine, for the many evenings of delightful conversation we had together over the delicious meals he would prepare for us. Abe and Patricia at Abe's café and the folks at Caffe Stradda have provided me with nourishment and countless cups of coffee, all of which have kept me going through graduate school.

There are several friends in at UC-Berkeley who I owe an immense amount of gratitude to. During my 3rd year of graduate school, when I decided to change course and essentially re-start my PhD, I had lost all self-confidence. At this time, James Dombrowski, graciously helped me set up my new PhD research project. Through his passion for chemistry, his generosity and remarkably kind demeanor, he has not only been a mentor to me but also a great friend. I will always cherish our coffee breaks to Stradda, during which we chatted endlessely about inorganic chemistry and catalysis. I owe a tremendous amount to Chris Ho. When I was new to the Bell lab, Chris immediately made me feel like I was part of the crew and this greatly assisted my transition into the group. He also showed me how to use every characterization tool in the lab and was always available to answer questions about experiments or bounce off ideas. His friendship has meant so much to me these past 3.5 years. I would also like to thank my dear friend Julie Rorrer. Her cheerful demeanor and passion for science made working in lab a pleasure. Jeroen was fantastic to work with, during our collaborative project. His commitment to detail was a constant source of inspiration to me. The Bell lab is a fantastic group of people to work with. It has been a pleasure knowing and working with Bell lab members present and past-Christianna, Danna, Paul, Darinka, Philomena, Oyin, Julie (F), Ezra, Lin, Alex Wang, Joaquin, Rachel, Greg, Deepak and Shylesh. You guys rock! Sam Wood and Matthieu Bondil were Masters' students that I worked with whose efforts greatly aided the progress of my research project. I would like to make special mention of Andrew 'Bean' Getsoian. When I was completely new to X-ray Absorption Spectroscopy (XAS), Bean wrote me lengthy emails describing the workings of this technique in painful detail. These notes were a godsend to me and made possible, all of the XAS results presented in this dissertation. Anton Mlinar, a former Bell group student was my email buddy when I got accepted into Berkeley. His positive outlook and cheerful demeanor convinced me to come to Berkeley. Later, it was through his words of support, that I decided to join Prof. Bell's research group. I am indebted to him for his thoughtful words of advice. I also thank Amber Janda for her help and advice for how to navigate through graduate school.

There a few more UC-Berkeley friends who I would like to thank- Alex and Sarah Wang for being great friends through the ups and downs, Sukanya Sasmal and Katerina Georgiou for all of the fun dinners and homework sessions during our first year and beyond, Lisa and Mike for their enthusiasm and energy. Will Knaeble, Andrew Jones, Michele Sarazen, Stan Herrmann, Allie Landry, David Hibbitts, Sarika Goel, Edwin Yik, Fabio Toniolo, Monica Garcia, Kim Strasbourg and Prashant Deshlahra for their assitance in helping me with my qualifying exam and for supporting me through the first 3 years of grad school. During the last 3 years, I have

also had the pleasure of knowing and hanging out with Haefa Mansour, Ari Fischer, Sam Leung, Marianne Sleiman. They are not only bright scientists but also wonderful human beings. Professors Jeff Reimer, Brian Mccloskey and Susan Muller were always willing to hear me out and provided me with much needed advice at a very crucial moment in my graduate school career. That advice has made this dissertation possible. I would also like to thank Professor Enrique Iglesia for the work we did during my first two years of graduate school. A special thanks must be given to Carlet Altamirano for her helping take care of department-related matters. I would also like to thank Joel, Sigrid, Katie and Jeff for their hard work in ensuring the smooth functioning of the Bell research group.

My professors and mentors at UW-Madison-my undergraduate alma mater-played a signficant role in my decision to pursue a graduate degree at UC-Berkeley. It was because of Professor Jamie Schauer (Civil and Environmental Engineering, UW-Madison) that I got my start in academic research, as an undergraduate research assistant. During my time at the water chemistry lab, I had the honor and pleasure of working with Mike Olson, Chris Worley and Betsy Stone. Later, my work with Prof. James Dumesic (CBE department, UW-Madison) and my graduate mentor Mark Tucker made me consider pursuing a graduate degree in catalysis. And then it was through Professor Dan Klingeberg's (CBE department, UW-Madison) persuasion that I finally decided to apply to graduate schools as opposed to taking up a job in industry. I am indebted to all of these individuals for believing in me.

Finally, not enough can be said about the immense contribution that my wife Radha has made to this work. In the early days of our relationship, she was in India while I was in Berkeley. In spite of this long distance relationship, she stood firmly by me through some of the toughest days of graduate school. Later, we got married, she moved to Berkeley and since then, she has enriched my life in more ways than I can describe. Through the long nights of working in lab or on writing at home, she has patiently supported all of my efforts. She has also endured the hardships of a daily 3 hour long commute to work, for 2 years simply so we could live in Berkeley where I could be in close proximity to lab. I am forever in debt to her for these and many other sacrifices that she makes for me on a daily basis. Her kind-hearted nature, ability to not take life too seriously and her sincere commitment to our relationship are just some of her attributes that have had a profound impact on me during these past 3 years. I thank her from the bottom of my heart for making the work presented in this dissertation, a reality.

Chapter 1

1 Introduction

1.1 Relevance of zeolite based catalysts for the conversion of light alkane feedstocks to alkenes and aromatics.

Recent years have witnessed a sharp increase in the availability of natural gas in the U.S as a result of the discovery of new shale gas reserves and improvements in gas extraction technologies.[1] These developments have resulted in a cheap and abundant supply of shale gas condensates-ethane, propane, butane- which may constitute up to 20% of the shale gas yield obtained from some reserves.[1] This abundant availability of light alkanes has spurred a renewed interest in their utilization as chemical feedstocks for catalytic conversion to industrially relevant chemical precursors, such as alkenes and aromatics.[2–4] As an example, significant efforts have been made to develop effective strategies to enable the catalytic conversion of propane to propylene.[2] For several petrochemical conversion processes, zeolite based catalysts offer a wide range of compositional diversity and reactivity towards hydrocarbons and therefore form an important class of catalytic materials that are used industrially.[5]

Zeolite-based catalysts are among the most structurally diverse and catalytically reactive materials used industrially for hydrocarbon conversions.[6,7] Zeolites are crystalline aluminosilicates consisting of TO_4 (T= Si or Al) tetrahedra that are arranged periodically to form well-defined three dimensional structures typically consisting of channels and voids that are of molecular dimesions.[8] The isomorphous substitution of a Si^{4+} atom with a Al^{3+} atom in the zeolite framework results in a charge imbalance and a net negative charge in the framework at the isomorphous cation substitution site.[7] Extra-framework cations must therefore balance the net negative charge in the framework. When the extra-framework cation is a proton (H^+), a Brønsted acidic O-H group is generated at the cation-exchange site.[6] Brønsted acid O-H groups formed in this fashion are catalytically active for a number of acid-catalyzed hydrocarbon transformations.[5,6] It has been shown by a number of researchers that the reactivity of these Brønsted acid O-H groups is significantly influenced by their location within difference pore topologies.[9–11] Theoretical studies indicate that these variations in reactivity arise from the confinement of adsorbed reactants and reaction transition states within zeolite channels and voids and the interactions of these hydrocarbon fragments with zeolite framework atoms.[12,13]

An additional factor that plays an important role in zeolite catalyzed chemistry is the proximity of Brønsted acid O-H groups in the zeolite channels and voids. This proximity is influenced by the relative distance between framework Al atoms in the zeolite. Framework Al atoms that are proximal to one another and are separated by one framework –O-Si-O- linkage are termed as Next-Nearest Neighboring (NNN) cation exchange sites, while those framework Al atoms that are separated by a framework –O-Si-O-Si-O- linkage are termed as Next, Next-Neighboring (NNNN) cation exchange sites.[14] Those framework Al atoms that are separated by –O-Si-O- linkages that are longer than the two cases discussed above are considered to be isolated cation exchange sites. The fraction of isolated cation-exchange sites and proximate cation-exchange sites (both NNN and NNNN) can be measured by means of Co^{2+} titration and information regarding the location of these cation-exchange sites may be derived from the d-d transitions of Co^{2+} cations observed via UV-visible spectroscopy.[11,14,15] As described before, in

the H-form of the zeolite, cation-exchange sites are associated with Brønsted acid O-H groups. The proximity of cation-exchange sites in zeolites may alter the catalytic reactivity of Brønsted acid O-H groups. As shown by Bernauer et al. in the case of C_3H_6 oligomerization over H-MFI, oligomerization turnover rates over proximate Brønsted acid sites are several fold higher than those over isolated Brønsted acid O-H groups.[16] The location of Brønsted acid O-H groups within different voids and channels in the zeolite crystal can also have a significant effect on the selectivity towards different reaction pathways. For n-butane conversion over H-MFI for example, Janda et al. have shown that the dehydrogenation of n-butane is more favorable than the cracking of n-butane over Brønsted acid O-H groups located in the MFI intersection voids.[11] When charge-balancing species in zeolites consist of metal cations, the presence of isolated or proximate framework Al atoms has consequences for the structure of metal complexes that are formed at cation-exchange sites.[17] These metal complexes may adopt a large variation of structural motifs, and can serve as highly active and selective active sites for a number of catalytic reactions, as shown previously for Cu, Fe and V-exchanged zeolites.[18–21] As we will discuss in section 1.3, metal exchanged zeolites, particularly Ga, Zn and Co-exchanged MFI are effective catalysts for light alkane conversion to alkenes and aromatics. Metal cations in these materials display higher reactivity towards alkane reactants than the corresponding bulk metal oxide.[22] There remain however, several challenges in the preparation of well-defined isolated metal cationic species in zeolites. This is in turn has led to difficulties in understanding the structure and role of catalytically relevant ion-exchanged metal species during light alkane conversion. Chapters 2, 3 and 4 of this thesis will delve into a deeper understanding of how to tackle some of these challenges.

1.2 Light alkane conversion catalyzed by Brønsted acid O-H groups in zeolites.

Brønsted acid O-H groups in the H-form of zeolites catalyze the conversion of light alkane reactants via either monomolecular or bimolecular dehydrogenation and cracking pathways.[23] Monomolecular pathways are prevalent at high temperatures, low alkane partial pressures and low alkane conversions while biomolecular pathways prevail at lower temperatures and higher alkane conversions.[11,23–25] In the monomolecular mechanism, alkane reactants are protonated at cation-exchange sites. The resulting carbonium ions may crack to yield smaller hydrocarbons or undergo dehydrogenation to form an alkene with the same carbon chain length as the reactant and molecular H_2.[23] On the other hand, bimolecular mechanisms proceed via a chain-transfer type process wherein hydride transfer occurs between alkane reactants and intrazeolitic carbenium ion species resulting in the formation of an alkane and another carbenium ion.[23] At low alkane conversions, monomolecular cracking and dehydrogenation are prevalent over the H-form of zeolites. For C_3H_8 and n-C_4H_{10} reactants, relative yields of dehydrogenation and cracking products over H-MFI at low alkane partial pressures and temperatures > 750 K are similar.

1.3 Light alkane conversion catalyzed by Ga species ion exchanged in Ga/H-MFI.

While H-forms of zeolites are able to catalyze the conversion of light alkanes to alkenes and aromatics via Brønsted acid catalyzed monomolecular and bimolecular reactions as discussed above, the yields of these products are limited by concurrent cracking and hydride

transfer, which lead to the formation of undesirable alkanes.[26,27]On the other hand, reactions of light alkanes over metal modified zeolites (M= Ga, Zn, Co) lead to alkane conversion rates and selectivities to alkenes and aromatics that are higher than those over the H-form of the zeolites.[26–29] Among these metal-modified zeolite systems, the most catalytically active and widely studied system is gallium-exchanged H-MFI (henceforth referred to as Ga/H-MFI).[29] The conversion of light alkanes to aromatics over Ga/H-MFI involves a complex interplay between concurrent dehydrogenation, cracking, oligomerization and cyclization reactions.[29] It is known that the first step of this sequence – the dehydrogenation of the alkane reactant to its corresponding alkene and H_2 – limits overall conversion of light alkanes to aromatics and in general, is the most energetically demanding reaction of the sequence.[27] As a consequence, this dissertation focuses on understanding the catalytic role of Ga species during the dehydrogenation of light alkanes to alkenes and H_2. There is also debate in the literature with regard to the role of cationic Ga species in catalyzing the cracking of light alkane reactants. In addition to the significant enhancement in the rate of propane dehydrogenation over Ga/H-MFI, it has been shown that the rate of propane cracking is also higher over Ga/H-MFI than over H-MFI.[22] This enhancement has been attributed to a hydrogenolysis pathway by which alkanes are cracked by Ga species with the assistance of H_2.[30]Conclusive evidence for the existence of such a pathway has however not been provided.

1.3.1 Ga Structures in Ga/H-MFI that have been proposed to be catalytically relevant for light alkane conversion

It is generally accepted that extra-framework Ga cations, rather than isomorphously substituted framework Ga atoms, are responsible for the enhanced alkane conversion rates observed over Ga/H-MFI.[31] However, several aspects regarding the structure, coordination and molecularity of the catalytically relevant extra-framework Ga species have been a subject of intense debate in the literature.[29] Many cationic complexes of Ga have been proposed in the literature to be catalytically relevant for alkane dehydrogenation over Ga/H-MFI; these proposed structures are shown here in Figure 1.3.1-1. Among these proposed structures, $[Ga_2O_2]^{2+}$ and $[GaH]^{2+}$ require the presence of proximate cation-exchange sites in order to balance the overall +2 charge in these complexes, while the remaining Ga complexes, which have an overall charge of +1, can form at isolated cation-exchange sites. In earlier studies, monovalent, reduced Ga^+ cations were proposed to be the predominant species present during propane conversion over Ga/H-MFI on the basis of red shifts observed in the Ga K-edge X-ray Near Edge Absorption spectrum (XANES) upon exposure of Ga/H-MFI samples to H_2 /propane at elevated temperatures (> 700K).[32] However, recent work by Getsoian et al. has shown that red shifts in the absorption edge spectrum of Ga/H-MFI may also be attributed to the formation of formally trivalent Ga complexes coordinated to –H or –R (alkyl) ligands.[33] Indeed, evidence for GaH_x or GaR_x (R=alkyl) species in Ga/H-MFI has been reported via infrared spectroscopy studies.[34–36] However, definitive evidence regarding the exact structure and coordination of these species as well as the mechanism by which they catalyze alkane conversion has not been provided. Later studies have also reported that O ligated structures $[GaO]^+$ and $[Ga_2O_2]^{2+}$ are more reactive for alkane activation but that these structures decompose into GaH_x or Ga^+ under the reducing conditions prevalent during alkane dehydrocyclization.[37–40] Consequently, such oxidized structures may not be relevant to steady-state alkane conversion.

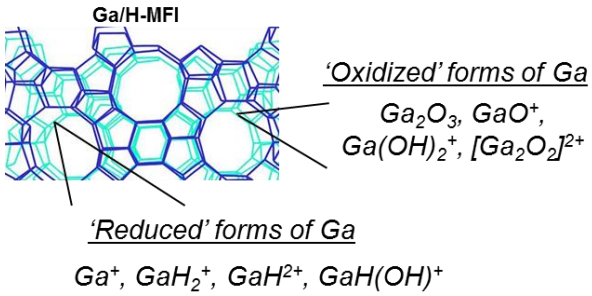

Figure 1.3.1-1. Structures of cationic Ga species proposed in the literature to be catalytically relevant during light alkane conversion.

1.3.2 Synthesis of Ga/H-MFI via conventional incipient wetness impregnation

The lack of consensus regarding the nature of the active site is partially a result of the manner by which Ga/H-MFI is synthesized (Figure 1.3.2-1). Ga/H-MFI is typically synthesized via incipient wetness impregnation of H-MFI with an aqueous solution of $Ga(NO_3)_3$.[41] Due to steric and electronic constraints, large hydrated aqueous Ga^{3+} complexes in these solutions diffuse slowly into the MFI channels during ion-exchange procedures, resulting in low levels of ion-exchange and the formation of agglomerates of GaO_x at the outer surfaces of the zeolite crystal surface.[42] Upon exposure of impregnated materials to H_2 or alkane reactants at temperatures > 700 K, ion-exchange has been reported to occur, presumably via transformation of GaO_x agglomerates into volatile gas-phase Ga species that can ion-exchange with intrazeolitic Brønsted acid O-H groups.[32,43] These materials have however been reported to contain detectable concentrations of GaO_x even after H_2/alkane exposure.[42] Consequently, synthesis via wetness impregnation followed by H_2 reduction results in materials that may contain both GaO_x and exchanged Ga cations. The application of spectroscopic tools (which often probe the average environment around Ga atoms) to conventionally prepared Ga/H-MFI containing non-uniform Ga structures may lead to equivocal conclusions regarding the structure of Ga species that is catalytically relevant. Attempts to synthesize well-defined and isolated Ga^{3+} structures using highly reactive and volatile precursors (such as $Ga(CH_3)_3$) have also been reported.[44] However, the reactivity and volatility of such precursors preclude controlled grafting of Ga centers at cation-exchange sites.[44,45] Therefore, an approach that combines the controlled grafting of well-defined Ga species at cation-exchange sites in H-MFI, together with spectroscopic and chemical probes, kinetic measurements and DFT calculations is required to identify catalytically relevant Ga species and their role in alkane dehydrogenation reactions. In Chapter 2, the synthesis of isolated Ga^{3+} species via vapor phase exchange of H-MFI with $GaCl_3$ is described, together with a detailed chemical, spectroscopic and theoretical analysis of the Ga structures formed as a function of the Ga/Al ratio.

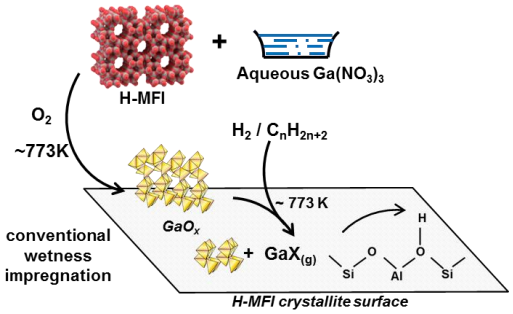

Figure 1.3.2-1. Synthesis of Ga/H-MFI via incipient wetness impregnation of H-MFI with aq. $Ga(NO_3)_3$ and subsequent dispersion and gas-phase ion-exchange of Ga upon exposure of impregnated zeolitic materials to H_2 or alkane reactants at temperatures > 700 K.

1.3.3 Effects of Ga/Al ratio on the structure and reactivity of Ga/H-MFI

Another factor essential to identifying the structure of the catalytically relevant Ga species is the effect of Ga loading or Ga/Al ratio on the catalytic reactivity. If the introduction of Ga at different loadings into H-MFI produces uniform and well-defined structures with similar reactivity towards alkanes, alkane conversion rates should scale linearly with Ga content or the Ga/Al ratio. Thus, alkane conversion turnover frequencies (normalized per Ga atom) should be independent of the Ga/Al ratio. There has, however, been a lack of clarity in the literature with regard to the effects of Ga content in Ga/H-MFI on the rate of alkane dehydrogenation/dehydrocylization. Krishnamurthy et al. have reported an optimal Ga/Al ratio of 0.5 for propane conversion to aromatics[46] while Schreiber et al. have recently reported an optimal Ga/Al ratio of 0.5 for propane dehydrogenation and cracking.[22] This non-monotonic dependence of alkane dehydrogenation rates on the Ga/Al ratio suggests that uniform, well-defined and structurally similar Ga structures do not form in Ga/H-MFI as the Ga loading is increased. It should be noted that samples used in both studies were synthesized via incipient wetness impregnation with $Ga(NO_3)_3$, a protocol which does not guarantee site isolated and uniform Ga species, as described above. As also noted previously, the cation-exchange sites in MFI, which are the anchoring locations for cationic Ga species, are not uniformly isolated from one another. Bernauer et al. have recently reported that in commercial MFI samples, the fraction of proximate framework Al atoms (NNN or NNNN) is between 30-50% of the total Al content, independent of the Si/Al ratio.[16] Moreover, the interatomic Al-Al distance between proximate cation-exchange sites is expected to vary significantly for cation-exchange sites located in different channels and voids of the zeolite crystal. The reactivity and stability of divalent Ga^{3+} structures such as $[GaH]^{2+}$ that could anchor at such sites is expected to depend sensitively on the interatomic Al-Al distance between cation-exchange sites, as theoretical studies have shown.[47–49] By varying the Ga loading, it is conceivable that a variety of Ga structures could form, as proximate and isolated cation-exchange sites are populated to differing extents. Such structures are also expected to exhibit a wide range of reactivity[40,47–49] towards alkanes and therefore some of the structures may be more catalytically relevant than others. The effects of Ga loading or Ga/Al ratio on the structure of isolated Ga^{3+} species are examined in detail in Chapter 2 and the activity of these structures is probed using a variety of light alkane reactants in Chapters 3 and 4.

1.3.4 Mechanism of alkane dehydrogenation and effects of alkane chain length on reactivity of Ga/H-MFI catalysts

A large number of studies have been devoted to understanding the mechanism of propane dehydrogenation over Ga/H-MFI.[29] On the basis of H/D scrambling experiments, Biscardi et al. proposed that propane undergoes C-H activation over residual Brønsted acid O-H groups in Ga/H-MFI and that univalent Ga^+ cations in Ga/H-MFI catalyze the rate determining recombinative desorption of H atoms as molecular H_2.[27] The presence of Ga^+ cations in Ga/H-MFI has been disputed experimentally[33] and theoretically.[49,50] Theoretical studies have also shown that alkane dehydrogenation is kinetically unfavorable over Ga^+ cations.[49] Subsequent studies have suggested instead that GaH_x species ($[GaH_2]^+$ or $[GaH]^{2+}$) catalyze propane dehydrogenation via alkyl-Ga intermediates.[33,47–49,51,52] In a recent report, Schreiber et al. proposed that Ga^+-H^+ cation pairs catalyze propane dehydrogenation via the formation of highly Lewis acidic $[GaH]^{2+}$ intermediates.[22] In summary, there is a lack of consensus in the literature with regard to the operative mechanism for alkane dehydrogenation and cracking over Ga/H-MFI. While most studies have focused on the dehydrogenation of propane catalyzed by Ga species, an enhancement of propane cracking rates over Ga/H-MFI has also been reported, but has not been satisfactorily explained.[22] In Chapter 3, we will examine the mechanism and kinetics of propane dehydrogenation and cracking over Ga/H-MFI using experimental kinetic studies supported by theoretical calculations.

The effect of alkane chain length on the reactivity of Ga/H-MFI has been studied to only a limited degree. Theoretical studies have used ethane as probe reactant to examine the mechanism of alkane dehydrogenation over Ga/H-MFI, but no comparisons to propane or butane reactants were presented.[47,48,51] Pereira et al. have conducted a theoretical study of the effect of carbon chain length (using ethane, propane and butane as reactants) on the reactivity of $[GaH_2]^+$ cations for alkane dehydrogenation.[52,53] It was a reported that an increase in the carbon chain length of the reactant alkane leads to the concerted mechanism for alkene formation becoming more favorable than the 3-step mechanism involving the formation of chemisorbed alkyl-Ga intermediates.[52] By contrast, Mansoor et al. have recently reported that an increase in carbon chain length of alkane reactants leads to an increase in Gibbs free energy barriers for the 3-step alkyl mechanism over $[GaH_2]^+$ cations due to increased entropic losses at the transition state.[49] By comparison, the concerted mechanism for alkane dehydrogenation over $[GaH_2]^+$ cations was found to be unfavorable for all alkane reactants examined. A comparison of $[GaH_2]^+$ cations and $[GaH]^{2+}$ cations for different mechanisms and alkane reactants led to the conclusion that with an increase in alkane chain length, the alkyl mediated mechanism for alkane dehydrogenation over $[GaH]^{2+}$ becomes more favorable than the 3-step alkyl mechanism over $[GaH_2]^+$.[49] Few experimental studies have attempted to compare the reactivity of different alkane reactants over Ga/H-MFI. In a recent study, Schreiber et al. have reported butane dehydrogenation rates measured over Ga/H-MFI that were a factor of 5 lower than propane dehydrogenation rates measured over the same samples under similar conditions, even though measured activation energies for the two alkane reactants were similar.[54] The discrepancy between the measured rates and activation energies was not explained. In conclusion, while theoretical studies have predicted trends with regard to the reactivity of Ga species towards alkane reactants of different carbon chain length, few experimental studies exist to corroborate these findings. In Chapter 4, the kinetics and mechanisms for ethane and butane dehydrogenation and cracking over Ga/H-MFI catalysts will be examined in detail.

Chapter 2

2 Characterization of isolated Ga^{3+} cations in Ga/H-MFI prepared by vapor-phase exchange of H-MFI with $GaCl_3$

Adapted from ACS. Catal. ***2018****, 8, 6106-6126. This work was originally coauthored with Jeroen Van der Mynsbrugge, Erum Mansoor, Andrew "Bean" Getsoian, Martin Head-Gordon and Alexis T. Bell. These individuals have approved the inclusion of this work in this dissertation.*

2.1 Abstract

Ga/H-MFI was prepared by vapor-phase reaction of $GaCl_3$ with Brønsted acid O-H groups in dehydrated H-MFI. The resulting $[GaCl_2]^+$ cations in the as-exchanged zeolite are treated in H_2 at 823 K to stoichiometrically remove Cl ligands and form $[GaH_2]^+$ cations. Subsequent oxidation in O_2 and characterization by IR spectroscopy and NH_3-TPD suggests that for Ga/Al ratios ≤ 0.3, Ga^{3+} exists predominantly as $[Ga(OH)_2]^+$-H^+ cation pairs and to a lesser degree as $[Ga(OH)]^{2+}$ cations at low Ga/Al ratios (~0.1); while both species are associated with proximate cation-exchange sites, calculated free energies of formation suggest that $[Ga(OH)]^{2+}$ cations are more stable on cation-exchange sites associated with NNN (next-nearest neighbor) framework Al atoms, than on those associated with NNNN (next, next-nearest neighbor) framework Al atoms. XANES measurements indicate that under oxidizing conditions and for all Ga/Al ratios, all Ga species are in the +3 oxidation state and tetrahedrally coordinated to 4 O atoms. Fourier analysis of Ga K-edge EXAFS data supports the conclusion that Ga^{3+} is present predominantly as $[Ga(OH)_2]^+$ cations (or $[Ga(OH)_2]^+$-H^+ cation pairs). For Ga/Al ratios ≤ 0.3, wavelet analysis of EXAFS data evidences backscattering from nearest neighboring O atoms and next-nearest-neighboring framework Al atoms. For Ga/Al > 0.3, backscattering from next-nearest-neighboring Ga atoms is also evident, characteristic of GaO_x species. Upon reduction in H_2, the oxidized Ga^{3+} species produce $[Ga(OH)H]^+$-H^+ cation pairs, $[GaH_2]^+$-H^+ cation pairs, and $[GaH]^{2+}$cations. Computed phase diagrams indicate that the thermodynamic stability of the reduced Ga^{3+} species depends sensitively on temperature, Al-Al interatomic distance, and H_2 and H_2O partial pressures. For Ga/Al ratios ≤ 0.2, it is concluded that $[GaH_2]^+$-H^+ cation pairs and $[GaH]^{2+}$cations are the predominant species present in Ga/HMFI reduced above 673 K in 10^5 Pa H_2 and the absence of water vapor.

2.2 Introduction

The U.S. has large reserves of shale gas, much of which contains significant fractions of ethane and propane.[1] The availability of this relatively inexpensive source of light alkanes has stimulated the chemical industry to seek ways to use this resource for the production of olefins and aromatics via dehydrogenation and dehydrocylization.[2] While Brønsted acid O-H groups in zeolites are capable of catalyzing both reactions, they also catalyze alkane and alkene cracking,

thereby limiting the yields of alkenes and particularly aromatics.[55] By contrast, Ga, Zn, and Co-exchanged H-MFI have been found to be active and selective catalysts for the dehydrogenation and dehydrocylization of light alkanes.[27,56,57] To date, the most effective catalyst for the conversion of C_2-C_4 alkanes into olefins and aromatics has proven to be Ga/H-MFI, which is currently used in the Cyclar process.[58–60] For this reason, there has been considerable interest in understanding the nature of the Ga species present in Ga/H-MFI and understanding the role of these species in the dehydrogenation and dehydrocyclization of light alkanes.

A number of studies have focused on elucidating the structure of Ga cations ion exchanged into H-MFI and their role in promoting C_3H_8 dehydrocylization.[9–18] Nevertheless, the exchange stoichiometry, chemical structure and molecularity of Ga species in Ga/H-MFI is not fully defined, in large part because of the way in which Ga/H-MFI is typically prepared. A conventional approach to introducing Ga cations into the MFI zeolite proceeds via incipient-wetness impregnation of H-MFI or NH_4-MFI with an aqueous solution of a Ga^{3+} salt, most commonly $Ga(NO_3)_3$, followed by calcination in O_2 at elevated temperatures in order to decompose the NO_3 ligands.[22,41] Ga/H-MFI prepared in this manner contains relatively little ion-exchanged Ga^{3+}, and a large fraction of the Ga deposits on the external surfaces of the zeolite crystal as crystalline GaO_x.[42] The reason for this is that hydrated Ga^{3+} cations undergo slow diffusion into the MFI channels due to steric and electronic repulsion, resulting in low levels of Ga^{3+} ion exchange.[42,64] Ion-exchange between Brønsted acid O-H groups and Ga species has been observed to occur when Ga/H-MFI prepared by this means is reduced in H_2 or treated with gas-phase alkanes at temperatures > 700 K.[32,43] It has been proposed that cation-exchange occurs via reduction of GaO_x agglomerates to form volatile Ga_2O monomers, which migrate into the MFI channels and react with Brønsted acid O-H groups to form Ga^+ or GaH_x cations.[41,42,64,65] It is notable that even after H_2 reduction, Ga/H-MFI is found to contain detectable amounts of crystalline GaO_x.[42] As a result of the non-uniform state of Ga species (either as exchanged cations or neutral GaO_x) in conventionally prepared Ga/H-MFI, elucidation of the structure of the active form of exchanged Ga cations has proven to be challenging.[29]

Attempts have been made to prepare isolated Ga cations in H-MFI by means other than wet impregnation with $Ga(NO_3)_3$. Kwak and Sachtler have synthesized Ga/H-MFI by vapor-phase reaction of Brønsted acid O-H groups with $GaCl_3$.[63] However, these authors did not provide conclusive evidence for $GaCl_3$ grafting, removal of residual Cl ligands, and the chemical structure of the Ga^{3+} cations existing in the as-prepared materials. Garcia-Sanchez et al. and Rane et al. have synthesized Ga/H-MFI by grafting Ga^{3+} at cation-exchange positions in the zeolite via reaction of $Ga(CH_3)_3$ with Brønsted acid O-H groups.[37,45] This volatile precursor was found to react unselectively with both Brønsted acid O-H as well as Si-OH groups. While complete titration of Brønsted acid OH groups in the zeolite with Ga^{3+} cations could be achieved (i.e., Ga/Al = 1), no attempts were made to systematically examine the effects of Ga/Al ratio on the structure of the grafted Ga^{3+} cations.[37]

The aim of the present work was to produce isolated Ga^{3+} species in Ga/H-MFI with Ga/Al ratios of 0.1 to 0.7. This objective was achieved via the reaction of Brønsted acid O-H groups in H-MFI with $GaCl_3$ vapor. By carefully controlling synthesis parameters and employing detailed chemical and spectroscopic probes in combination with theoretical calculations, we were able to demonstrate that in the oxidized state and for Ga/Al ratios ≤ 0.3, Ga/H-MFI contains predominantly isolated $[Ga(OH)_2]^+$ cations, present as $[Ga(OH)_2]^+$-H^+ cation pairs, and a small fraction of divalent $[Ga(OH)]^{2+}$ cations. Both cationic species are associated with proximate cation-exchange sites associated with pairs of framework Al atoms. Experimental determination

of the Ga^{3+} exchange stoichiometry in concert with theoretical calculations suggest that at low Ga/Al ratios (~ 0.1), $[Ga(OH)]^{2+}$ cations form at proximate cation-exchange sites for which the Al-Al distances is ≤ 5 Å, whereas $[Ga(OH)_2]^{+}$-H^{+} cation pairs form at proximate cation-exchange sites for which the framework Al atoms are farther apart. The concentration of the latter structure increases with increasing Ga content until all available proximate cation-exchange sites are saturated at a Ga/Al ratio of ~0.3. For higher Ga/Al ratios, introduction of additional Ga results in the formation of GaO_x oligomers. Upon H_2 reduction of as-prepared Ga/H-MFI, both $[Ga(OH)]^{2+}$ cations and $[Ga(OH)_2]^{+}$ -H^{+} cation pairs convert into $[Ga(OH)H]^{+}$-H^{+} cation pairs. For proximate cation-exchange sites with sufficiently short interatomic framework Al-Al distances (≤ 5 Å) at low Ga/Al ratios, $[Ga(OH)H]^{+}$ cations may undergo condensation with proximate Brønsted acid O-H groups to form $[GaH]^{2+}$ cations. Theoretically determined phase diagrams of Ga^{3+} hydride structures suggest that the nature of Ga^{3+} species formed upon H_2 reduction is highly sensitive to the framework Al-Al interatomic distance in proximate cation-exchange sites and to the relative partial pressures of H_2O and H_2. Under sufficiently anhydrous reducing conditions (≤ 10^{-1} Pa H_2O, > 10^{3} Pa H_2), $[Ga(OH)H]^{+}$-H^{+} cation pairs may further reduce to $[GaH_2]^{+}$-H^{+} cation pairs. At temperatures above 713 K, $[GaH_2]^{+}$ cations undergo a change in coordination from 4 to 3, with a reduction in the number of framework Ga-O_f bonds from 2 to 1.

2.3 Experimental and theoretical methods

2.3.1 Synthesis of Ga/H-MFI catalysts

The parent H-MFI sample was prepared by heating 1-2 g batches of NH_4-MFI (Zeolyst, CBV 3024E) in quartz boats placed in a tubular quartz tube, at 2 K min^{-1} from ambient temperature to 773 K in flowing synthetic dry air (Praxair, ultra zero, 100 ml min^{-1}). Samples were held at 773 K for 4 h to convert the NH_4-form of the zeolite into the H-form. The bulk Si/Al ratio of the zeolite was determined to be 16.5 ± 1.0 by ICP-OES carried out by Galbraith Laboratories (Knoxville, TN). Previous work (using Co^{2+} cation titration) in our group has shown that the fraction of proximate cation-exchange site pairs associated with pairs of framework Al atoms present as either next-nearest-neighbors (NNN) or next-next-nearest-neighbors (NNNN) is approximately 45% of the framework Al.[11]

Prior to carrying out the vapor-phase exchange with $GaCl_3$, H-MFI was dehydrated by placing 2 g of the zeolite in a 20 ml glass ampule and heating it to 573 K in a sand bath for 3 h under dynamic vacuum using a Schlenk line. The dehydrated H-MFI was sealed and then transferred into a N_2-purged glovebox. This material was intimately mixed with anhydrous $GaCl_3$ (99.999% Strem chemicals) in a porcelain crucible inside the glovebox, to achieve Ga/Al ratios of 0.1 to 0.7. Each physical mixture was then loaded into a fresh glass ampule and taken out the glovebox, sealed under N_2. Samples were cooled by immersing in a liquid N_2 bath, to prevent loss of Ga content due to evaporation of $GaCl_3$. The ampule was then evacuated and flame sealed under dynamic vacuum and heated in a furnace at 5 K min^{-1} to 478 K and held at this temperature for 2 h before being cooled to ambient temperature. This procedure led to sublimation of $GaCl_3$ and reaction of gas-phase $GaCl_3$ with Brønsted acid O-H groups in the zeolite. Following the sublimation step, the contents of the ampule were transferred to quartz boats (1-2 g) and heated in a tubular quartz tube under flowing dry synthetic air (Praxair, ultra zero, 100 ml min^{-1}) at 2 K min^{-1} to 773 K, held for 1 h, and then cooled to 363 K. The system

was flushed with He for 5 min and the flow was then switched to 10^5 Pa H_2 (Praxair, 100 ml min^{-1}). Samples were heated under H_2 flow at 5 K min^{-1} to 823 K, held at this temperature for 2 h, and then cooled to 623 K. At this temperature, the system was flushed with pure He for 10 min after which flow was switched back to dry synthetic air (Praxair, ultra zero, 100 ml min^{-1}). Samples were heated under flowing air at 5 K min^{-1} to 773 K, held for 1 h and then cooled to ambient temperature. This procedure was required to convert grafted $[GaCl_2]^+$ to $[GaH_2]^+$ cations and to oxidize the latter species to $[Ga(OH)_2]^+$ cations. The effluent from these reduction/oxidation treatments was passed through an $H_2O/NaHCO_3$ trap in order to trap any HCl released. Ga/H-MFI samples were stored in a glovebox until further use. Chloride titration was performed on the contents of the $H_2O/NaHCO_3$ trap (attached to the outlet line from the synthesis reactor) in order to quantify the HCl released during reduction/oxidation treatments of grafted samples. These titrations were performed using Mohr's method – $NaHCO_3$ was added to the solution until it reached a neutral pH. The resulting solution was then titrated against $Ag(NO_3)_3$ using K_2CrO_4 as an indicator in order to directly estimate Cl concentrations.[66] Ga/Al ratios and Cl/Ga ratios of Ga/H-MFI samples (post reduction/oxidation treatments) were determined by ICP-OES at Galbraith Laboratories.

2.3.2 Chemical and spectroscopic characterization of Ga/H-MFI samples

Raman spectra of Ga/H-MFI samples were acquired using a LabRam HR Horiba Jobin Yvon Raman spectrometer with a 532 nm C.W. 50 mW laser. Samples of Ga/H-MFI (~100 mg) were loaded into an in-situ Raman cell equipped with a quartz window (Linkam stage, CCR1000) and heated under flowing dry air (Praxair, extra dry, 100 ml min^{-1}) from ambient temperatures at 5 K min^{-1} to 1023 K, held at this temperature for 0.5 h and then cooled to ambient temperature. Raman spectra of β-Ga_2O_3 (Sigma Aldrich) were acquired at ambient temperature. An average of three Raman scans was recorded per measurement. Raman spectra were normalized to the band at 800 cm^{-1} characteristic of T-O-T vibrations of the zeolite framework.[67]

Infrared spectra of H-MFI and Ga/H-MFI samples were acquired in transmission mode using a Nicolet 670 FTIR spectrometer. Samples (~30 mg) were pressed into thin wafers and transferred into a cylindrical stainless steel sample holder. The sample and sample holder were sealed in a low dead-volume, in-situ infrared cell equipped with CaF_2 windows. Prior to the acquisition of spectra, all samples were heated under flowing dry synthetic air (Praxair, ultra zero, 100 ml min^{-1}) at 2 K min^{-1} to 773 K, held for 0.5 h and then cooled to 723 K. Spectra were collected at 723 K by averaging 64 scans with a resolution of 2 cm^{-1}. In order to examine the effects of H_2 treatment, calcined samples were exposed to 3% H_2/He (Praxair, 75 ml min^{-1}) at 773 K, treated for 1 h at this temperature. Samples were then cooled to 473 K for measurement. All infrared spectra were baseline corrected (using a Spline function) and normalized to the intensity of Si-O-Si framework overtone bands occurring between 1700 cm^{-1} and 2000 cm^{-1}. The fraction of Brønsted acid O-H groups exchanged by Ga^{3+} at each Ga/Al ratio was determined by integrating the area of the infrared band of Brønsted acid O-H stretching vibrations at 3593 cm^{-1} for each Ga/Al ratio and then normalizing this area by the area of this band in the parent H-MFI sample, as shown in equation (2.3.2-1) below:

$$\text{Fraction of Brønsted } H^+ \text{ exchanged per total } H^+ = 1 - \frac{\text{Integrated area of } 3593 cm^{-1} \text{ band, Ga/H-MFI}}{\text{Integrated area of } 3593 cm^{-1} \text{ band, H-MFI}} \quad (2.3.2\text{-}1)$$

NH_3- temperature programmed desorption (TPD) profiles of H-MFI and Ga/H-MFI samples were measured using a home-built apparatus. Samples (~ 0.2 g) were placed on a quartz wool plug inside a tubular quartz reactor (~ 0.6 cm sample bed height) with a thermocouple placed directly above the catalyst bed. Samples were treated under flowing dry synthetic air (Praxair, ultra zero) at a flow rate of 100 ml min^{-1} and heated at 5 K min^{-1} from ambient temperature to 773 K and held at this temperature for 0.3 h. The reactor was then cooled to 433 K upon which the flow to the samples was switched to a gas mixture consisting of 1.7 % NH_3 (Praxair, 99.9%) diluted in He (Praxair, UHP) at a flow rate of 305 ml min^{-1}. The samples were exposed to this gas mixture for 1h in order to saturate Brønsted acid O-H groups with NH_3. The specific saturation temperature was chosen to minimize NH_3 adsorption at Lewis acid centers since the maximum rate of NH_3 desorption from Lewis acid sites in H-MFI was found to occur at 433 K. After completion of the saturation step, samples (at 433 K) were flushed in 300 ml min^{-1} He (Praxair, UHP) for 0.2 h. This step was followed by a treatment of the sample (held at 433 K) in 1 % H_2O diluted in He (Praxair, UHP) at a flow rate of 300 ml min^{-1} for a period of 8 h. H_2O was introduced into the system via a syringe pump (Cole-Parmer) at a flow rate of 0.13 ml/h. This treatment was found to be necessary to remove NH_3 bound to Lewis acid centers in samples. Samples (held at 433 K) were then purged in dry He (Praxair, He) at a flow rate of 300 ml min^{-1} for 4 h before being cooled to 323 K. NH_3-TPD profiles were measured by heating samples at 5 K min^{-1} from 323 K to 673 K under a gas mixture consisting of 1 % Ar (Praxair, CSG) diluted in He (Praxair, UHP) at a flow rate of 300 ml min^{-1}. A capillary connected directly below the sample carried the reactor effluent into a mass spectrometer (MKS, Cirrus) and was used to quantify the desorbed NH_3. The NH_3 response factor was calibrated using mixtures of NH_3 and He. Ar was used as an internal standard to correct for drift in the NH_3 response factor. NH_3-TPD measurements on H_2-treated Ga/H-MFI samples were conducted after NH_3-TPD measurements on the same oxidized Ga/H-MFI samples. After an initial NH_3-TPD measurement, samples at 823 K were exposed to 5 % H_2/He at a total flow rate of 300 ml min^{-1}, for a duration of 1 h. For both oxidized and reduced Ga/H-MFI samples, the remaining steps in the experimental protocol were identical. The fraction of Brønsted acid O-H groups exchanged by Ga^{3+} species was estimated from equation (2.3.2-2) and measured values of NH_3/Al_{tot} for H-MFI and Ga/H-MFI assuming a 1:1 stoichiometry between desorbed NH_3 and Brønsted acid O-H groups

$$\text{Fraction of } H^+ \text{ sites exchanged per total } H^+ = 1 - \frac{NH_3/Al_{tot,\ Ga/H\text{-}MFI}}{NH_3/Al_{tot,\ H\text{-}MFI}} \qquad (2.3.2\text{-}2)$$

^{29}Si MAS and ^{27}Al MAS NMR spectra were acquired at the NMR facility at the University of California, Davis on a 500 MHz NMR spectrometer. Samples (~300 mg) were hydrated in a desiccator containing H_2O for 24 h prior to measurement. Samples were then loaded into ZrO_2 rotors. All ^{29}Si MAS NMR spectra were collecting using 7 mm probe at a spinning frequency of 6 kHz with a pulse length of 1.9 μs (corresponding to a 45° tip angle) and a relaxation delay time of 30 s. Spectra were referenced to tetramethylsilane (TMS) for which the isotropic chemical shift was set to 0 ppm. Framework Si/Al_f ratios were determined from ^{29}Si MAS NMR spectra by integrating the areas of bands obtained by spectral deconvolution.[68] All ^{27}Al MAS NMR spectra were collected using a 2.5 mm probe spinning at a frequency of 25 kHz with a pulse length of 0.23 μs (corresponding to a 30° tip angle) and a relaxation delay time of 0.2 s. The final spectra were obtained by averaging 8192 scans. Spectra were referenced with

respect to aqueous $Al(NO_3)_3$ for which the isotropic chemical shift was set to 0 ppm. Tetrahedral framework Al centers in zeolites show a chemical shift of roughly 56 ppm relative to aq. $Al(NO_3)_3$ while octahedral Al centers in zeolites show no shift relative to aq. Al $(NO_3)_3$ i.e a chemical shift of 0 ppm.[69] The relative fraction of tetrahedral and octahedral Al centers was determined by integrating the areas under spectral bands.

Ga K-edge X-ray absorption spectroscopy (XAS) data were acquired at beamline 5BMD at the Argonne Photon Source (APS). The monochromator energy was calibrated using β-Ga_2O_3 and all measurements were conducted in transmission mode. All edge energies were referenced to β-Ga_2O_3 for which the edge energy was set to 10375.1 eV. Ga^{3+} standards- β-Ga_2O_3 (Sigma Aldrich) and $Ga(acac)_3$ (Strem chemicals) were sealed inside Kapton tape for measurements. Ga/H-MFI samples (~10 mg) were pressed into self-supporting pellets and placed inside a stainless steel 6-shooter sample holder. The sample holder was placed inside a quartz tube with a gas inlet and outlet and sealed at two ends with Kapton windows. The quartz tube was fitted inside a clam-shell furnace connected to a heater and temperature controller. Gases were metered to the in-situ cell via mass flow controllers. XAS measurements were acquired on samples in their hydrated state at ambient conditions, upon calcination in 20% O_2/He (Airgas, 100 ml min^{-1}) to 773 K and upon treatment in 3% H_2/He (Airgas, 100 ml min^{-1}) at 713 K. Measurements were made at both the near-edge region of the XAS spectrum (XANES) and in the extended post-edge region of the XAS spectrum (EXAFS). X-ray absorption spectra were background-corrected and normalized using the Athena software.[70] Ga-K edge energies were defined by the lowest energy inflection point in the edge region of the first derivative of the XAS spectrum. EXAFS spectra were Fourier transformed and fitted to the first coordination shell using the Artemis software,[70] amplitude and phase shift scattering functions were calculated using the crystal structure of $CaGa_2O_4$[71] in Artemis via FEFF6, while values for the amplitude reduction factor S_0^2 were obtained by fitting the first coordination shell of the EXAFS spectra of β-Ga_2O_3. Wavelet transforms of EXAFS spectra were obtained by using the k^2 -weighted EXAFS signal ($k^2\chi(k)$) as an input to the HAMA software [72] and wavelet contour plots were prepared using OriginPro 2017.

H_2-Temperature programmed reduction (TPR) profiles were measured using a home-built apparatus. Samples (~0.18 g) were supported on a quartz wool plug placed inside a tubular quartz reactor with a thermocouple placed above the catalyst bed. Under 100 ml min^{-1} dry synthetic air (Praxair, ultra zero), samples were heated at 5 K min^{-1} to 773 K and held at this temperature for 1 h, before being cooled to 323 K. H_2-TPR profiles were measured by heating samples at 10 K min^{-1} from 323 K to 1023 K under a flowing gas mixture of 1 % H_2, 1 % Ar diluted in He (Praxair, CSG) at a flow rate of 30 ml min^{-1}. A capillary placed directly below the sample carried the reactor effluent to a mass spectrometer (MKS, Cirrus). The response factor for H_2O, was determined by flowing mixtures of H_2O (introduced into the system via syringe pump) diluted in He (UHP). The Ar in the gas mixture was used as internal standard to correct for drift in the H_2O mass spectrometer response factor.

2.3.3 Theoretical calculations

All structures proposed for the isolated Ga^{3+} species were modeled using a hybrid quantum mechanics/molecular mechanics method[73,74] applied to a large cluster model of MFI containing 437 tetrahedral atoms (T437), shown in Figure 2.3.3-1. A T14 cluster containing a distorted 6-ring at the intersection of the straight and sinusoidal channel and two adjacent 5-rings was treated quantum mechanically with the dispersion-corrected ωB97X-D[75,76] functional, while

the remainder of the framework was described with molecular mechanics parameters taken from previous work (P2 parameter set)[74].

Both univalent and divalent site structures were investigated. The univalent site structures (e.g., $[Ga(OH)_2]^+$and $[GaH_2]^+$) compensate the charge associated with an isolated Al atom in the MFI framework. The Al atom associated with these sites was placed in a T12 crystallographic position, which is located at the intersection of the straight and sinusoidal channels. This location is commonly selected for Al substitution in theoretical studies on H-MFI.[13,77–82] On the other hand, oxidized divalent cations- $[Ga(OH)]^{2+}$ and $[Ga(OH)_2]^+$-H^+ cation pairs and reduced divalent cations – $[GaH]^{2+}$, $[Ga(OH)H]^+$-H^+ and $[GaH_2]^+$-H^+ cation pairs are compensated by proximate cation-exchange sites associated with pairs of framework Al atoms. Two cases with different Al-Al distances were examined: a next-nearest neighbor (NNN) pair, in which the two framework Al atoms are separated by one framework Si atom and a next-next nearest neighbor (NNNN) pair, in which the two framework Al atoms are separated by two framework Si atoms. To create the pair sites, an additional Al atom was inserted in an NNN or NNNN T7 position relative to the T12 position (see Figure 2.3.3-1). This particular NNNN configuration was found to be relevant in earlier theoretical work[47,83] for ethane dehydrogenation catalyzed on $[GaH]^{2+}$ structures in Ga/H-MFI.

Initial geometries were constructed with ZEOBUILDER.[84] Geometry optimizations and frequency calculations were performed using the ωB97X-D/6-31G(d,p) level of theory for the QM region. Subsequent energy refinements on the stationary points were calculated at the ωB97X-D/6-311++G(3df,3pd) level. All QM/MM calculations were performed with a developmental version of Q-Chem.[85] Gibbs free energies at reaction temperatures (773 K for oxidized structures and 673 K for reduced structures) were derived from a normal mode analysis using the quasi-rigid rotor/harmonic oscillator approximation[74,86] on the various stationary points obtained from QM/MM. Phase diagrams for oxidized and H_2-treated Ga^{3+} structures located at proximate cation-exchange sites associated with NNN and NNNN pairs of framework Al atoms were constructed by comparing the free energy of formation for various candidate structures starting from $[Ga(OH)_2]^+$-H^+ cation pairs, and plotting the regions in which specific structures exhibit the lowest free energy of formation as a function of temperature, and H_2 partial pressure at a given H_2O partial pressure. The following equations were used to determine the free energy of formation of specific Ga^{3+} structures from $[Ga(OH)_2]^+$-H^+ cation pairs:

$$[Ga(OH)_2]^+ - H^+ + (x-2)H_2O + \left(2 - x + \frac{y-3}{2}\right)H_2 \rightarrow \left[GaO_xH_y\right]^{2+} \quad (2.3.3\text{-}1)$$

$$\Delta G_{form} = \Delta G_{\left[GaO_xH_y\right]^{2+}} - \Delta G_{[Ga(OH)_2]^+ - H^+} - (x-2)\left(\Delta G_{H_2O} - \Delta G_{H_2}\right) - \left(\frac{y-3}{2}\right)\Delta G_{H_2} \quad (2.3.3\text{-}2)$$

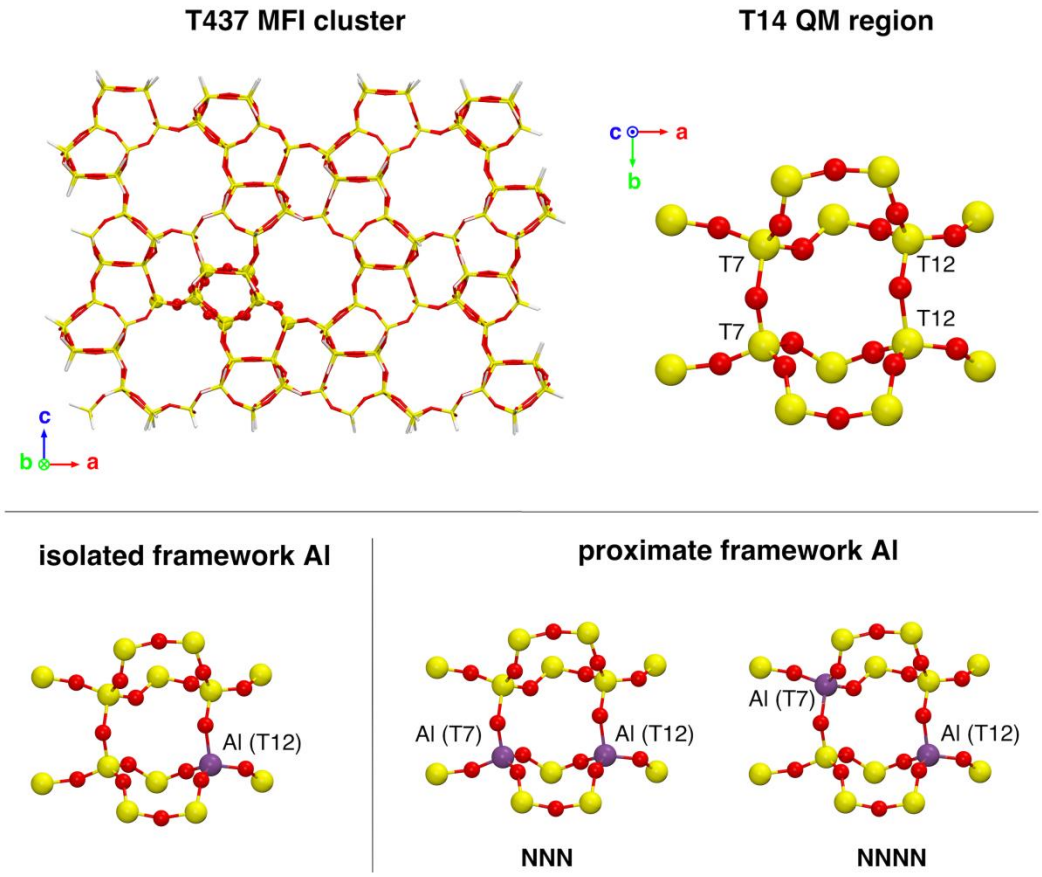

Figure 2.3.3-1. (Top left) T437 MFI cluster model used for QM/MM calculations, with T14 QM region shown in ball-and-stick representation; (Top right) Close-up of T14 QM region, with indication of T sites considered for Al substitution (T7 and T12); (Bottom left) Location of isolated framework Al in T14 QM region; (Bottom right) Location of proximate framework Al atoms in next-nearest neighboring (NNN) or next-next nearest neighboring (NNNN) configuration in T14 QM region.

2.4 Results and Discussion

2.4.1 Characterization of Ga/H-MFI prepared by treatment of H-MFI with $GaCl_3$ vapor and subsequent removal of Ga-bound Cl by H_2 reduction

When physical mixtures of anhydrous H-MFI and $GaCl_3$ are heated to 478 K under vacuum, vapor-phase ion exchange occurs via the reaction of gas-phase $GaCl_3$ monomers or Ga_2Cl_6 dimers [87] with Brønsted acid O-H groups associated with framework Al sites located inside the channels of H-MFI. This reaction, shown in Scheme 2.4.1-1, is assumed to result in the grafting of $GaCl_3$ at cation-exchange sites associated with isolated framework Al atoms to

form monovalent $[GaCl_2]^+$ cations or at proximate cation-exchange sites associated with pairs of framework Al atoms-either NNN (next-nearest neighbor) or NNNN (next, next-nearest neighbor) to form either divalent $[GaCl]^{2+}$ cations or monovalent $[GaCl_2]^+$ cations. Reduction of the grafted samples in flowing 10^5 Pa H_2 at 823 K resulted in near complete removal (> 95% of Cl initially present, see Table 2.7-1 in section 2.7.1) of the Cl associated with Ga^{3+} species. Table 2.4.1-1 lists the composition of Ga/H-MFI samples prepared with Ga/Al ratios of 0.1 to 0.7. Attempts to synthesize samples with Ga/Al > 0.7 were unsuccessful; loss of Ga from such samples was observed during H_2 reduction, presumably due to removal of Ga^{3+} as gas-phase $GaHCl_x$[88] (see section 2.7.1). HCl generated as a result of H_2 treatment was collected in an H_2O trap and quantified via chloride titration. HCl/Ga ratios determined by this means, shown in Table 2.4.1-1, ranged from 1.5 - 2.2 (with an average HCl/Ga = 1.7 ± 0.5). This stoichiometry suggests the grafting of $GaCl_3$ predominantly produces $[GaCl_2]^+$ cations, as suggested in Scheme 2.4.1-1. Since most of the Cl in these cations is removed during H_2 reduction, we propose that the $[GaH_2]^+$ cations form as a result of this treatment. Evidence for $[GaH_2]^+$ cations was obtained from in-situ infrared spectra of reduced $GaCl_x$/H-MFI, which showed the presence of an infrared band at 2051 cm^{-1} which was absent in the infrared spectra of H-MFI upon H_2 treatment (see section 2.7.1, Figure 2.7-1). This band is assigned to Ga-H stretching vibrations, consistent with previous experimental and theoretical studies.[34,89,90]

Table 2.4.1-1. Elemental composition of Ga/H-MFI (Ga/Al ratios)[b] and HCl/Ga[c] ratios derived by quantifying HCl desorbed during H_2 treatment of $GaCl_x$/H-MFI at 10^5 Pa H_2 and 823 K.

Sample	HCl/Ga[c]
H-MFI[a]	--
Ga/Al[b]	
0.1	1.5
0.2	1.6
0.3	1.8
0.4	2.2
0.5	1.6
0.7	1.7

[a] H-MFI, Zeolyst Batch CBV3024E, Si/Al_{tot} = 16.5 ± 1.0 (ICP-OES, Galbraith Laboratories)
[b] Elemental compositions determined by ICP-OES (Galbraith Laboratories)
[c] HCl/Ga ratios determined via Mohr's Cl titration protocol[66] on effluent collected in H_2O/ $NaHCO_3$ trap during H_2 treatment of $GaCl_x$ –MFI samples at 823 K

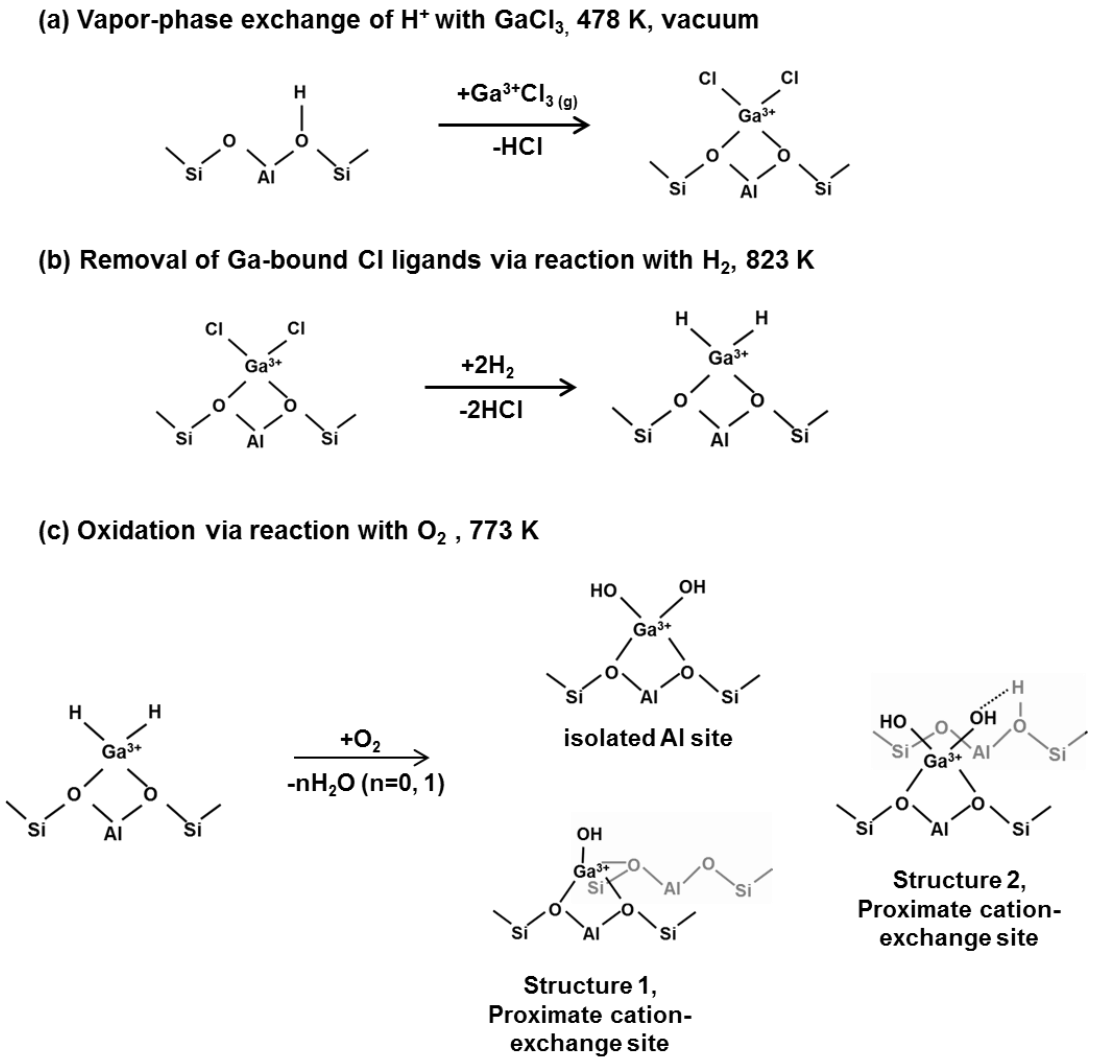

Scheme 2.4.1-1. Grafting of $[Ga(OH)_x]^{(3-x)+}$ (x=1, 2) cations at isolated and proximate cation-exchange sites in Ga/H-MFI via $GaCl_3$ vapor phase exchange. (a) Grafting of $GaCl_3$ at cation-exchange sites at 478 K under vacuum, (b) removal of Cl ligands via reaction by reaction with H_2, at 823 K and 10^5 Pa H_2 (100 ml min^{-1}) (c) Oxidation of GaH_x cations to $[Ga(OH)_x]^{(3-x)+}$ (x=1,2) cations.

2.4.2 Characterization of as-prepared Ga/H-MFI following oxidation

Following H_2 reduction of as-exchanged Ga/H-MFI, samples were oxidized in 2 x 10^4 Pa of O_2 at 773 K for 1 h in order to form air-stable Ga^{3+} hydroxide species, as shown in Scheme 2.4.1-1. The resulting materials showed no evidence for the formation of crystalline β-Ga_2O_3 in Raman spectra of even the highest Ga/Al ratios synthesized (Ga/Al =0.5, 0.7) (see section 2.7.2 and Figure 2.7-2). Oxidized Ga/H-MFI samples were characterized in order to determine the fraction of Brønsted acid O-H groups that were ion-exchanged and the exchange stoichiometry of the resulting Ga^{3+} cations. The local chemical environment around Ga^{3+} centers was then

characterized by Ga K-edge X-ray absorption spectroscopy (XANES and EXAFS). Theoretical calculations were performed in order to evaluate the stability of candidate Ga^{3+} structures on isolated cation-exchange sites and on proximate cation-exchange sites associated with NNN and NNNN pairs of framework Al atoms. Infrared spectroscopy and temperature-programmed desorption of NH_3 (NH_3-TPD) were used to probe the fraction of Brønsted acid O-H groups in oxidized Ga/H-MFI exchanged by Ga^{3+} and the exchange stoichiometry of the resulting Ga^{3+} cations.

Figure 2.4.2-1a shows the infrared spectra of H-MFI and Ga/H-MFI samples measured under oxidizing conditions at 723 K. All spectra show a band at ~ 3593 cm^{-1} attributable to ν(O-H) of Brønsted acid O-H groups [91] and a band at ~3740 cm^{-1} attributable to ν(O-H) of Si-OH groups, located at defect sites inside the zeolite pores or at the external surfaces of the zeolite crystals.[92] As the Ga content in the samples increases, the area of the band at 3593 cm^{-1} decreases monotonically up to a Ga/Al ratio of ~ 0.3, suggesting that Ga^{3+} species replace Brønsted acid O-H groups in these samples. For samples with Ga/Al ratios > 0.3, the band at 3740 cm^{-1} decreases slightly in area (< 30%), suggesting that $GaCl_3$ may also have reacted with less acidic Si-OH groups.The infrared spectra of all Ga/H-MFI samples also show a weak band at 3660 cm^{-1}, absent in the infrared spectra of H-MFI. This band has been attributed previously to Al-OH groups in extra-framework Al (EFAl) species[93] or to OH groups coordinated to extra-framework cations (for example, $[Cu(OH)]^+$ cations in Cu-exchanged zeolites).[35,17] Contact with $GaCl_{3(g)}$ during vapor-phase exchange and with $HCl_{(g)}$ during Cl removal treatments, could in principle, lead to the extraction of framework Al and the concomitant formation of EFAl, in a manner similar to that reported for zeolites treated with $SiCl_4$ vapor at elevated temperatures.[94] Na-exchange [11] and NH_3-TPD (discussed below) reveal that our parent H-MFI sample contains approximately 13-15% EFAl. Framework Si/Al_f ratios, estimated via deconvolution of ^{29}Si MAS NMR spectra (see Figure 2.7-4) for H-MFI (Si/Al_f =16.8) were similar within (10-15%) uncertainty to Si/Al_f values for Ga/H-MFI (14.4-17.7) and to Si/Al_{tot} values from elemental analysis (16.5 ± 1.0) (see Table 2.7-2). In addition, no discernable trend was observed in Si/Al_f values as a function of Ga content. As discussed in section 2.7.3, these data suggest that the fraction of EFAl is similar in H-MFI and in Ga/H-MFI samples. As a consequence, we infer that the band at 3660 cm^{-1} in the infrared spectra of Ga/H-MFI is most likely attributable to OH groups coordinated to Ga^{3+} centers in either $[Ga(OH)]^{2+}$ or $[Ga(OH)_2]^+$ cations and $[Ga(OH)_2]^+$-H^+ cation pairs.

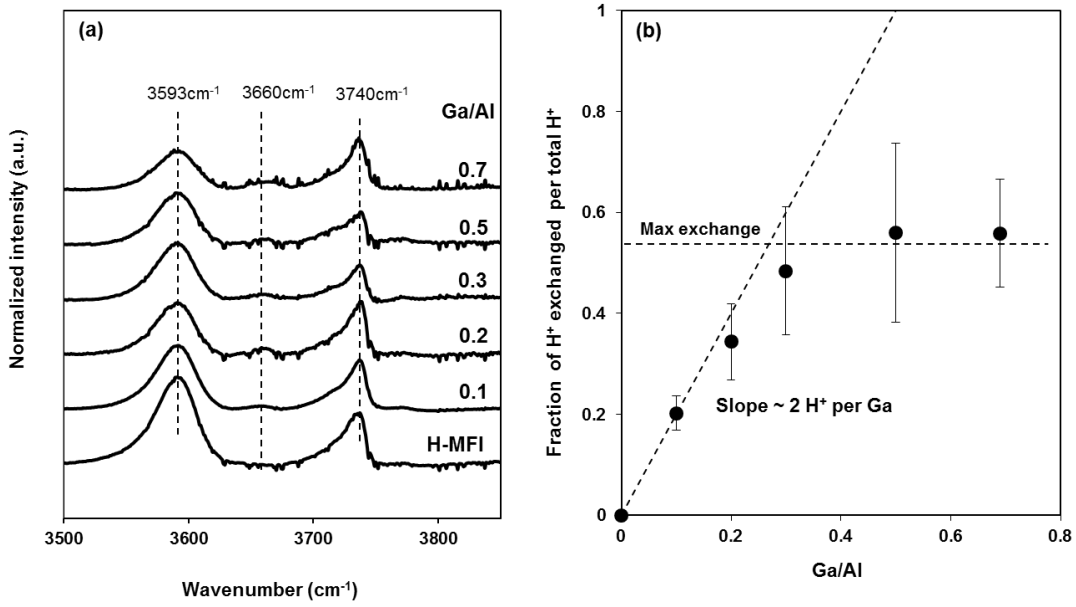

Figure 2.4.2-1.(a) Infrared spectra of H-MFI and Ga-MFI samples with Ga/Al ranging from 0.1 to 0.7. Infrared spectra were collected at 723 K under flowing dry air (b) Fraction of H^+ (Brønsted O-H) exchanged per H^+_{total} determined from infrared spectra, as a function of Ga/Al ratio. Dotted lines indicate slope of plot and maximum extent of H^+ exchange. Reported uncertainties are for 95% confidence intervals.

The fraction of Brønsted acid O-H groups replaced by Ga^{3+} cations can be determined for each Ga/Al ratio on the basis of Eq (2.3.2-1) (experimental section) and the integrated area of the ν(O-H) band at 3593 cm^{-1} observed in the infrared spectra of Ga/H-MFI and H-MFI. This fraction is plotted as a function of the Ga/Al ratio in Figure 2.4.2-1b. It is apparent from the slope of this plot (dotted line in Figure 2.4.2-1b) that for Ga/Al ratios ≤ 0.3, each Ga^{3+} replaces approximately two Brønsted acid O-H groups. This exchange stoichiometry is consistent with the presence of divalent $[Ga(OH)]^{2+}$ cations, that involve the titration of two Brønsted acid O-H groups at proximate cation-exchange sites associated with pairs of framework Al atoms, by one Ga^{3+} atom. Consistent with this interpretation, the fraction of Brønsted acid O-H groups replaced by Ga^{3+}cations reaches a maximum value of approximately 50% at a Ga/Al ratio of ~ 0.3. This maximum extent of Brønsted acid O-H exchange is similar to the total fraction of proximate cation-exchange sites associated with pairs of framework Al atoms in our sample of H-MFI (~45% of Al_f by Co^{2+} titration[11]). This finding suggests that under oxidizing conditions, Ga^{3+} cations exchange predominantly with Brønsted acid O-H groups at proximate cation-exchange sites, rather than isolated cation-exchange sites. For samples with Ga/Al ratios > 0.3, no further exchange of Brønsted acid O-H groups by Ga^{3+} cations is observed in Figure 2.4.2-1a and 2.4.2-1b. Raman spectroscopy showed no evidence for crystalline β-Ga_2O_3 in any of the samples of Ga/H-MFI (see section 2.7.2). Consequently, we hypothesize that an increase in Ga content beyond a ratio Ga/Al of 0.3 leads to the formation of GaO_x oligomers that do not occupy cation-exchange sites. Evidence for the presence of such species will be presented below.

The extent of exchange of Brønsted acid O-H groups by Ga^{3+}cations was also estimated by titrating the residual Brønsted acid O-H groups in Ga/H-MFI with gas-phase NH_3. The protocol used here was that developed by Di Iorio et al. to selectively titrate residual Brønsted acid O-H groups in Cu- and Co-exchanged zeolites, without concomitant titration of Lewis acid sites by NH_3.[19] NH_3 -TPD profiles for H-MFI and Ga/H-MFI, shown in Figure 2.4.2-2a, exhibit a single NH_3 desorption feature at 660 K associated with desorption of NH_3 from Brønsted acid O-H groups.[19] This feature decreases in area with increasing Ga content, consistent with the titration of fewer residual Brønsted acid O-H groups in Ga/H-MFI after Ga^{3+} exchange. The NH_3/Al_{tot} value for H-MFI (Table 2.4.2-1) is less than unity: 0.87 ± 0.11, suggesting that approximately 13% of Al_{tot} is not associated with Brønsted acid O-H groups, likely present as EFAL. This estimated Brønsted acid O-H density of 0.87 ± 0.11 H^+/Al_{tot} is also consistent with the value measured using Na^+ exchange protocols (0.84 H^+/Al_{tot}).[11] As observed in Table 2.4.2-1, the value of NH_3/Al_{tot} decreases with increasing Ga content up to Ga/Al ratios of 0.3. For Ga/Al ratios higher than this value, the value of NH_3/Al_{tot} becomes nearly constant, suggesting that exchange of Brønsted acid O-H groups by Ga^{3+} occurs predominantly at proximate cation-exchange sites associated with pairs of framework Al atoms. This finding is consistent with the infrared spectroscopy measurements discussed above.

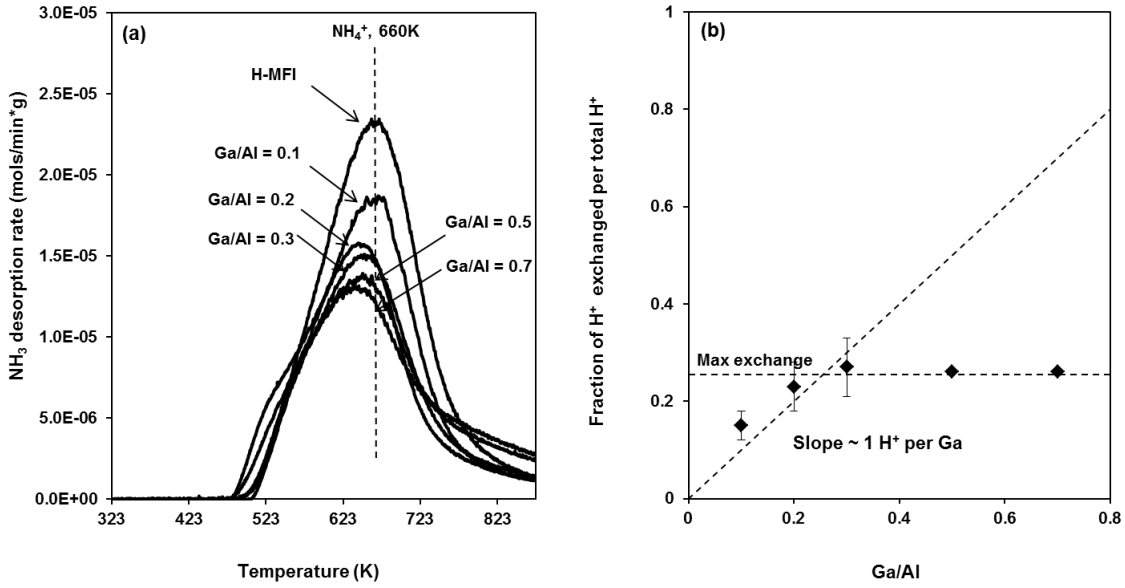

Figure 2.4.2-2. (a) NH_3-TPD profiles (5 K min^{-1}) of H-MFI and Ga-MFI samples with Ga/Al ranging from 0.1 to 0.7. (b) Fraction of H^+ (Brønsted O-H) exchanged per H^+_{total} determined from NH_3-TPD profiles, as a function of Ga/Al ratio. Dotted lines indicate slope of plot and maximum extent of Brønsted acid O-H exchange. Reported uncertainties are for 95% confidence intervals.

Table 2.4.2-1. NH_3/Al_{tot} ratios for H-MFI and oxidized Ga/H-MFI samples, derived from NH_3-TPD profiles. Ratios were obtained by integrating area of feature at 660 K and normalized to Al_{tot} content

Sample	NH_3/Al_{tot} [c]
H-MFI[a]	0.87 ± 0.13
Ga/Al[b]	
0.1	0.74 ± 0.13
0.2	0.67 ± 0.09
0.3	0.64 ± 0.11
0.5	0.64
0.7	0.64

[a] H-MFI, Zeolyst Batch CBV3024E, Si/Al_{tot} = 16.5 ± 1.0 (ICP-OES, Galbraith Laboratories)
[b] Elemental compositions determined by ICP-OES (Galbraith Laboratories)
[c] Samples were calcined at 773 K for 0.3 h prior to NH_3 saturation at 433 K. After NH_3 saturation, samples at 433K were purged in 1% H_2O/He for 8 h. Reported uncertainties reflect 95% confidence intervals.

The fraction of Brønsted acid O-H groups exchanged by Ga^{3+} cations at each Ga/Al ratio can be estimated using the measured values of NH_3/Al_{tot} in conjunction with Eq (2.3.2-2) (experimental section). The results, plotted as a function of the Ga/Al ratio are show in Figure 2.4.2-2b, and suggest that for Ga/Al ratios ≤ 0.3, each Ga^{3+} center titrates approximately one Brønsted acid O-H group. This exchange stoichiometry is only consistent with Structure 2 in Scheme 2.4.1-1, i.e $[Ga(OH)_2]^+$-H^+ cation pairs, in contrast to the result obtained from infrared spectroscopy, which suggested that for Ga/Al ratios ≤ 0.3, each Ga^{3+} exchanged with two Brønsted acid O-H groups. It should be noted that the exchange stoichiometry of the Ga/Al = 0.1 sample was higher than one Brønsted acid O-H group replaced per Ga^{3+} (1.3 ± 0.3), consistent with the presence of $[Ga(OH)]^{2+}$ cations in addition to $[Ga(OH)_2]^+$-H^+ cation pairs at low Ga/Al ratios. In addition, the maximum extent of exchange of Brønsted acid O-H groups, measured by NH_3-TPD is approximately 25%. This value is approximately a factor of 2 lower than the maximum extent of Brønsted acid O-H exchange measured via infrared spectroscopy (~50%). The contradiction in exchange stoichiometries estimated by infrared spectroscopy and NH_3-TPD can be resolved by examining the thermodynamics for forming Structures 1 and 2 from their reactants on proximate cation-exchange sites associated with pairs of framework Al atoms.

The Gibbs free energy of formation (ΔG_f) at 773 K and 10^5 Pa for both $[Ga(OH)]^{2+}$ cations (Structure 1) and $[Ga(OH)_2]^+$-H^+ cation pairs (Structure 2) was estimated starting from $GaCl_3$, H_2 , O_2, and two proximate Brønsted acid O-H groups associated with NNN and NNNN pairs of framework Al atoms. Given the distribution of framework Al atoms among different crystallographic positions in the zeolite framework, the Al-Al interatomic distance between proximate cation-exchange sites, is likely to vary considerably. While current experimental and theoretical methods do not allow estimation of the distribution of Al site pairs in terms of interatomic framework Al-Al distances in our zeolite samples, the two types of proximate cation-exchange sites used here provide benchmarks for two representative classes of Al-Al site pairs. For optimized structures involving NNN pairs of Al framework atoms, the interatomic Al-Al distances are ≤ 5 Å while for optimized structures involving NNNN pairs of framework Al atoms, the interatomic Al-Al distances are > 5 Å. The formation of isolated $[Ga(OH)_2]^+$ cations

from the same set of reactants and a Brønsted-acid O-H group associated with an isolated framework Al atom in the T12 position was also considered.

The Gibbs free energies of formation (ΔG_f) obtained for $[Ga(OH)]^{2+}$ cations, $[Ga(OH)_2]^+$-H^+ cation pairs and isolated $[Ga(OH)_2]^+$ cations are shown in Table 2.4.2-2. It is apparent that the formation of $[Ga(OH)_2]^+$-H^+ cation pairs at proximate cation-exchange sites associated with pairs of framework Al atoms is more favorable (ΔG_f = -379 kJ/mol and ΔG_f = -384 kJ/mol on NNN and NNNN pairs of framework Al, respectively) than the formation of $[Ga(OH)_2]^+$ cations at cation-exchange sites associated with isolated framework Al atoms (ΔG_f = -338 kJ/mol). In addition to electrostatic stabilization by the anionic zeolite framework, the $[Ga(OH)_2]^+$ cation in a $[Ga(OH)_2]^+$-H^+ cation pair is additionally stabilized via H-bonding between the Ga-bound OH group and the proximate Brønsted acid O-H group. The data in Table 2.4.2-2 also suggest that the formation of $[Ga(OH)_2]^+$-H^+ cation pairs at proximate cation-exchange sites associated with NNNN pairs of framework Al atoms, is significantly more favorable than the formation of divalent $[Ga(OH)]^{2+}$ cations at such cation-exchange sites (ΔG_f = -296 kJ/mol). The Ga^{3+} center in a divalent $[Ga(OH)]^{2+}$ cation is under considerable conformational strain resulting from the need to form a tetrahedron with 3 framework O atoms and 1 OH group. This conformational strain likely destabilizes the $[Ga(OH)]^{2+}$ structure relative to the $[Ga(OH)_2]^+$-H^+ cation pair structure, for which the Ga^{3+} center can form a less strained tetrahedron with 2 framework O atoms and 2 OH groups. As noted above, H-bonding between the Ga-bound OH group and the proximate Brønsted acid O-H group may further stabilize this structure. On the other hand, at proximate cation-exchange sites associated with NNN pairs of framework Al atoms, the formation of $[Ga(OH)]^{2+}$ cations is only slightly less favorable (ΔG_f = -352 kJ/mol) than the formation of $[Ga(OH)_2]^+$-H^+ cation pairs (ΔG_f = -379 kJ/mol). This suggests that at lower H_2O partial pressures ($\leq$ 10 Pa H_2O for dehydrated zeolites), $[Ga(OH)]^{2+}$ cations will be increasingly thermodynamically favored over $[Ga(OH)_2]^+$-H^+ cation pairs at proximate cation-exchange sites with shorter Al-Al interatomic distances, such as those associated with NNN pairs of framework Al atoms (also see thermodynamic phase diagrams presented in section 2.4.3). These findings highlight the sensitivity of Ga^{3+} structures to the interatomic distance between Al atoms in proximate cation-exchange sites: shorter interatomic Al-Al distances allow the Ga^{3+} center to bridge both cation-exchange sites with a lower conformational strain to form divalent $[Ga(OH)]^{2+}$ cations, while longer interatomic Al-Al distances inhibit the formation of such structures, resulting instead in the formation of $[Ga(OH)_2]^+$-H^+ cation pairs.

Table 2.4.2-2. QM/MM derived Gibbs free energies of formation of $[Ga(OH)]^{2+}$ cations and $[Ga(OH)_2]^{+}$-H^{+} pairs from $GaCl_3$, H_2, O_2 and H^{+} pairs at isolated Al sites (denoted as $H^{+}Z^{-}$) and Al site pairs (NNN and NNNN; denoted as $2H^{+}Z^{-}$, and shown in Figure 2.3.3-1) at 773 K (10^5 Pa pressure)

Reactions	Al site type	ΔG_f (at 773 K)[a] (kJ/mol)
$GaCl_3 + 2H_2 + O_2 + H^{+}Z^{-} \longrightarrow [Ga(OH)_2]^{+}Z^{-} + 3HCl$	Isolated	-338
$GaCl_3 + 2H_2 + O_2 + 2H^{+}Z^{-} \longrightarrow [Ga(OH)]^{2+}2Z^{-} + 3HCl + H_2O$	NNN	-352
	NNNN	-296
$GaCl_3 + 2H_2 + O_2 + 2H^{+}Z^{-} \longrightarrow [Ga(OH)_2]^{+}$-$H^{+}$ $2Z^{-} + 3HCl$	NNN	-379
	NNNN	-384

[a] Energies calculated at 10^5 Pa total pressure

Our theoretical calculations also suggest that for $[Ga(OH)_2]^{+}$-H^{+} cation pairs, H-bonding between the Ga-bound OH group and the proximate Brønsted acid O-H group shifts the O-H stretching frequency of the proximate Brønsted acid O-H group to 2436 cm^{-1}, a value significantly lower than that for an isolated Brønsted acid O-H group, 3610 cm^{-1}. This suggests that the proximate Brønsted acid O-H group in $[Ga(OH)_2]^{+}$-H^{+} pairs would be masked by the strong infrared absorption of the zeolite framework. The presence of a single infrared band reflecting this Brønsted acid O-H group is also unlikely, since the red-shift in the O-H stretching frequency may also depend on the proximity between Ga-bound OH groups and their corresponding proximate Brønsted acid O-H groups. This proximity is in turn expected to depend on the interatomic Al-Al distance in proximate cation-exchange sites. Therefore, the presence of either $[Ga(OH)]^{2+}$ cations or $[Ga(OH)_2]^{+}$-H^{+} cation pairs would result in an apparent exchange stoichiometry of two Brønsted acid O-H groups replaced per Ga^{3+} atom as measured via infrared spectroscopy monitored at 3593 cm^{-1}. The proximate Brønsted acid O-H group in $[Ga(OH)_2]^{+}$-H^{+} cation pairs, should in principle, be detectable by titration with NH_3. This structure should therefore result in an exchange stoichiometry of one Brønsted acid O-H group replaced per Ga^{3+} atom, as measured via NH_3-TPD. Furthermore, for low Ga/Al ratios (~ 0.1), NH_3-TPD indicates that between one and two Brønsted O-H groups are replaced per Ga^{3+} atom, suggesting that $[Ga(OH)]^{2+}$ cations may also form in addition to $[Ga(OH)_2]^{+}$-H^{+} cation pairs at low Ga/Al ratios. If Ga^{3+} siting is assumed to be thermodynamically controlled, it is plausible that at low Ga/Al ratios, the most stable $[Ga(OH)_2]^{+}$ -H^{+} cation pairs form at proximate cation-exchange sites associated with pairs of framework Al atoms with Al-Al interatomic distances ≤ 5 Å. For low H_2O partial pressures (≤ 10 Pa), such structures may readily undergo condensation to form $[Ga(OH)]^{2+}$ cations, a conclusion supported by the phase diagrams presented in Figure 2.4.3-2. We therefore conclude on the basis of infrared spectroscopy, NH_3-TPD and theoretical calculations, that for Ga/Al ratios ~ 0.1, $[Ga(OH)]^{2+}$ cations form at proximate cation-exchange sites associated with pairs of framework Al atoms with Al-Al interatomic distances ≤ 5 Å. On the other hand, $[Ga(OH)_2]^{+}$-H^{+} cation pairs form in greater proportion at proximate cation-exchange sites associated with pairs of framework Al atoms for which the Al-Al distances are > 5 Å for Ga/Al ratios between 0.1 and 0.3. The concentration of $[Ga(OH)_2]^{+}$-H^{+} cation pairs increases with increasing Ga/Al ratio until all proximate cation-exchange sites associated with

pairs of framework Al atoms are saturated. For Ga/Al ratios higher than ~ 0.3 the formation of neutral GaO_x species occurs. Such species may be formed via hydrolysis of $[Ga(OH)_2]^+$ cations associated with isolated cation-exchange sites during the oxidation of the H_2-reduced Ga/H-MFI at 773 K in O_2.

Further evidence supporting the formation of $[Ga(OH)_2]^+$-H^+ cation pairs was obtained from Ga K-edge X-ray absorption spectroscopy (XAS). XANES spectra of Ga/H-MFI and of two Ga^{3+} standards - β-Ga_2O_3 and $Ga(acac)_3$, are shown in Figure 2.4.2-3. The Ga K-edge energy, defined as the lowest energy inflection in the first derivative of the absorption edge region of the XAS spectrum, was measured for both Ga^{3+} standards and for Ga/H-MFI samples (at 773 K under O_2); these values are shown in Table 2.4.2-3. The Ga K-edge energies for Ga/H-MFI samples (~10374.0 - 10375.1 eV) are similar to those of the Ga^{3+} standards (10375.1 eV for β-Ga_2O_3 and 10376.6 eV for $Ga(acac)_3$), confirming that Ga^{3+} cations in Ga/H-MFI samples have an oxidation state of +3 and are coordinated to O atoms. The maximum of the absorption intensity in the edge region for all Ga/H-MFI samples occurs at approximately 10376 eV (Figure 2.4.2-3). The XANES spectra of β-Ga_2O_3 (Figure 2.4.2-3) shows two maxima in the edge region, one at 10376 eV and the other at 10379 eV, whereas the XANES spectrum of $Ga(acac)_3$ shows a single maximum in the edge region at 10379 eV. The XANES spectra of aqueous Ga-O complexes exhibit absorption intensity maxima at 10378 eV for tetrahedral Ga-O complexes and at 10379 eV for octahedral Ga-O complexes.[95] These findings are consistent with the observation of two maxima in the XANES spectrum of β-Ga_2O_3- which contains Ga^{3+} in both tetrahedral and octahedral coordination with O atoms,[96] and the observation of only the higher energy maximum (~10379 eV) in Ga(acac), which contains Ga^{3+} only in octahedral coordination with O atoms.[97] The observation in Figure 2.4.2-3 of a single absorption maximum at 10376 eV for XANES spectra of all Ga/H-MFI suggests that exchanged Ga^{3+} cations are tetrahedrally coordinated with O atoms at all Ga/Al ratios.

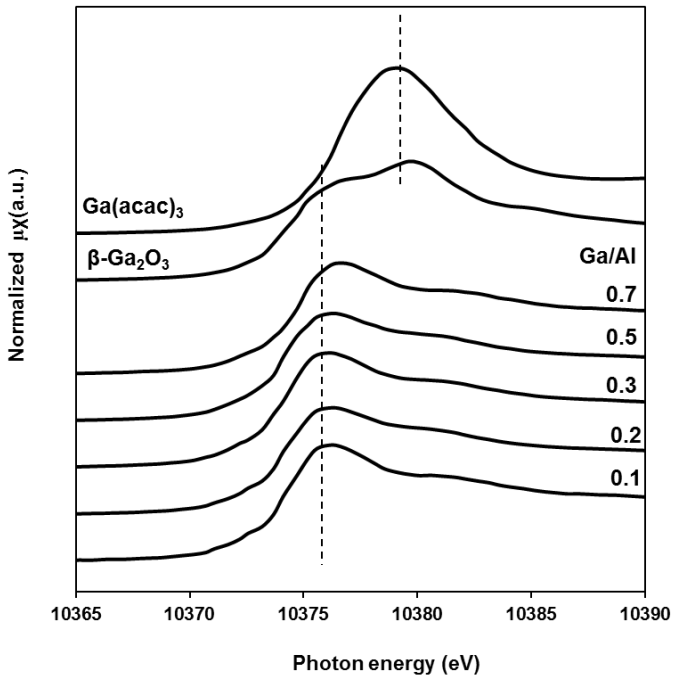

Figure 2.4.2-3. Normalized Ga K-edge X-ray Absorption Near Edge Spectra (XANES) for Ga/H-MFI samples, collected at 773 K under flowing 20% O_2/He. Also shown are XANES spectra for β-Ga_2O_3 and $Ga(acac)_3$, collected at ambient temperatures. Dotted lines indicate positions of absorption maxima.

Table 2.4.2-3. Ga K-edge XANES edge energies of Ga^{3+} standards (at ambient conditions) and Ga/H-MFI samples, measured at 773 K under flowing 20% O_2/He

Sample	XANES edge energy (eV)[a]
β-Ga_2O_3 [b]	10375.1
$Ga(acac)_3$ [b]	10376.6
Ga/Al (measured)[c]	
0.1	10374.3
0.2	10374.0
0.3	10375.0
0.5	10375.1
0.7	10375.0

[a] Edge energies are defined as inflection point of the absorption edge in the μ(E) spectrum. A β-Ga_2O_3 reference was used to calibrate all edge energies.
[b] Powdered standards (acquired from Sigma-Aldrich) were spread on Kapton tape, folded to yield an approximate absorption length of 2
[c] Ga/H-MFI samples (~0.01 g) were pressed into self-supporting pellets and installed in a six-shooter sample holder inside the in-situ XAS cell

EXAFS spectra (k^2-weighted) of Ga/H-MFI samples (shown in Figure 2.7-8) were Fourier-transformed (FT) and analyzed in order to determine the structure of Ga^{3+} cations around the first coordination shell. The magnitudes of the (k^2-weighted) FT Ga K-edge EXAFS spectra of Ga/H-MFI samples, collected at 773 K under flowing 20% O_2/He, are shown in Figure 2.4.2-4. For Ga/H-MFI samples with Ga/Al ratios < 0.2, sufficient X-ray absorption could not be achieved due to the low Ga content of these samples (< 1wt% Ga). As a result, our EXAFS analysis is limited to Ga/H-MFI with Ga/Al ratios ≥ 0.2. Also shown in Figure 2.4.2-4 is the magnitude of the FT- EXAFS spectrum of β-Ga_2O_3. The peak positions in these spectra do not correspond to exact interatomic distances, due to the phase shifts incurred by photoelectrons from absorbing and scattering atoms and therefore, peak maxima appear 0.3 - 0.5 Å lower than true interatomic distances.[98] Fourier-transformed EXAFS spectra of all Ga/H-MFI samples and β-Ga_2O_3 (Figure 2.4.2-4) show dominant features between 1 Å and 2 Å in R-space corresponding to backscattering from O atoms coordinated to Ga^{3+} centers. The FT-spectra of β-Ga_2O_3 in Figure 2.4.2-4 exhibits a large peak between 2 Å and 3 Å, corresponding to backscattering from next-neighbor Ga atoms in Ga-O-Ga linkages. The second coordination shell in the EXAFS spectra of all Ga/H-MFI samples also show features between 2 Å and 3 Å that are less intense than the feature in the EXAFS of β-Ga_2O_3. These features correspond to backscattering from framework Al, Si or extra-framework Ga atoms (for example, in condensed GaO_x species).

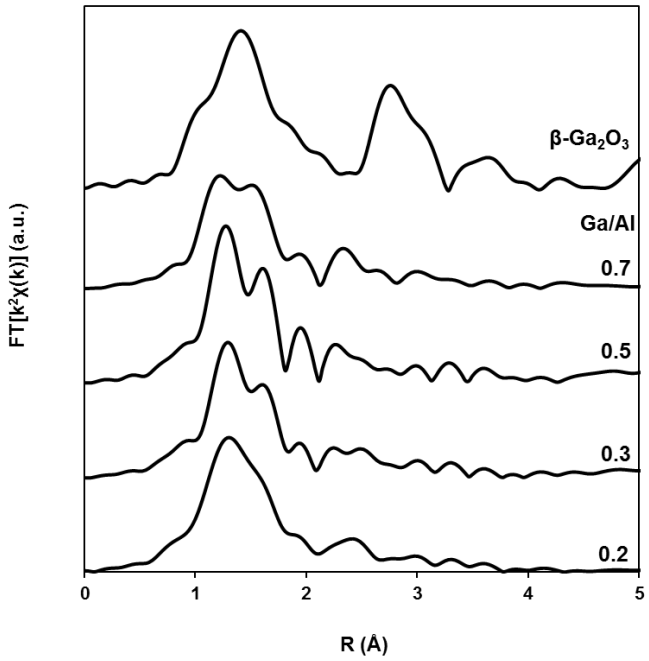

Figure 2.4.2-4. Magnitudes of k^2-weighted Fourier-transformed Ga-K edge EXAFS spectra of β-Ga_2O_3 measured at ambient temperature and of Ga/H-MFI samples (Ga/Al =0.2 - 0.7), measured at 773 K under 20% O_2/He.

EXAFS fitting of the first coordination shell was undertaken for spectra of Ga/H-MFI samples in order to determine the average number of neighboring O atoms and their interatomic distances from Ga^{3+} centers. The procedure used for EXAFS fits is outlined in detail in section 2.7.5. Satisfactory fits of the spectra were obtained for all Ga/H-MFI samples, as evidenced by the close agreement between dotted lines and the solid lines shown in Figure 2.7-9 for the first-coordination shell . Fitted parameters for Ga/H-MFI spectra are presented in Table 2.4.2-4. These results suggest that on average, each Ga^{3+} center is coordinated to 2 O atoms at an interatomic distance of approximately 1.77 Å and to 2 O atoms at an interatomic distance of approximately 1.92 Å. This interatomic bonding is consistent with the structure of tetrahedral $[Ga(OH)_2]^+$ cations, for which theoretical simulations (see section 2.7.4 for theoretically generated structures) indicate that the Ga^{3+} cation is coordinated to 2 OH groups with a Ga-O interatomic distance of 1.79 Å and to 2 framework O atoms at a Ga-O interatomic distance of 1.99 Å. The fitted interatomic distance assigned to bonding between Ga^{3+} and Ga-bound OH groups (~1.77 Å) agrees well with measured values for aqueous tetrahedral $Ga(OH)_4^-$ complexes for which the Ga-O interatomic distance is ~1.80 Å.[95] The fitted interatomic distance between Ga^{3+} and framework O atoms (~ 1.92 Å) is approximately 0.07 Å lower than the distance for these bonds determined from our DFT calculations (~1.99 Å). It should be noted that exact agreement between theoretical predictions of interatomic distances and values obtained from EXAFS fits is not expected. This discrepancy is well-documented and is ascribed to the effects of structural and thermal disorder on the absorber-scatterer interatomic pair distribution, which is assumed to have a Gaussian form in the conventional EXAFS equation.[99,100,101] A high degree of thermal and structural disorder (typical for measurements on highly dispersed metal sites in solids at high temperatures) may skew this pair-distribution, leading to slightly lower fitted interatomic distances when conventional EXAFS analysis is used.[102]

Table 2.4.2-4. Fitted coordination numbers, interatomic distances, Debye-Waller factors, energy shift parameters and R-factor values for fits to Fourier-transformed Ga K-edge EXAFS of Ga/H-MFI samples at 773 K under flowing 20% O2/He. Fits were performed using CaGa2O4 as a model structure.

Ga/Al[a]	Ga-O shell[b]	$N^c_{(i)}$	Total N	$R^d_{(i)}$ (Å)	$\sigma^{2\,e}$ (10^{-3} Å^2)	$\Delta E_0{}^f$ (eV)	R-factor (10^{-2})
0.2	$Ga\text{-}O_1$	2.0	3.9	1.77	4.0	3.1	0.7
	$Ga\text{-}O_2$	1.9		1.92			
0.3	$Ga\text{-}O_1$	1.7	3.5	1.77	1.0	2.6	2.2
	$Ga\text{-}O_2$	1.8		1.93			
0.5	$Ga\text{-}O_1$	1.7	3.8	1.75	0.1	1.7	2.1
	$Ga\text{-}O_2$	2.1		1.92			
0.7	$Ga\text{-}O_1$	1.5	3.8	1.73	3.2	1.3	1.4
	$Ga\text{-}O_2$	2.3		1.90			

[a] Samples were pressed into self-supporting pellets into sample holder in in-situ cell. Measurements were conducted at 773 K under flowing 20% O_2/He. EXAFS spectra, obtained after normalization and background subtraction, were k^2-weighted, a Hanning window function was applied between k = 2-14 Å^{-1} and first shell fits were performed from R = 1 - 2.1 Å. $S_0{}^2$ values were determined to be 0.94, by fitting experimental EXAFS spectra of β-Ga_2O_3 to Ga-O shells generated using the crystal structure of β-Ga_2O_3 [103] in FEFF.

[b] Two Ga-O shells were generated in FEFF using the crystal structure of $CaGa_2O_4$, which was obtained from [71].

[c] Coordination numbers (N_i where i =1-2) for each shell were determined with a ± 0.60 uncertainty.
[d] Ga-O interatomic distances (R_i where i = 1-2) for each shell were determined with a ± 0.04 Å uncertainty.
[e] Debye-Waller factors (σ^2) were held same for each shell.
[f] Energy shift parameters (E_0) were determined with a ±2 eV uncertainty.

From the preceding discussion, it is clear that under oxidizing conditions, exchange of Brønsted acid O-H groups by Ga^{3+} results in a saturation of proximate cation-exchange sites associated with pairs (NNN or NNNN) of framework Al atoms at a Ga/Al ratio of ~ 0.3. EXAFS analysis of the first coordination shell around Ga^{3+} centers (Table 2.4.2-4), however, suggests that exchanged Ga^{3+} cations and neutral GaO_x species (present at Ga/Al ratios > 0.3) are both predominantly tetrahedrally ligated to O atoms. In the second-coordination sphere, however, isolated Ga^{3+} cations are expected to be proximate to framework Al or Si atoms only. On the other hand, Ga^{3+} centers in multinuclear cationic Ga^{3+} species such as the $[Ga_2O_2]^{2+}$ structures proposed by Hensen et al,[39] or in neutral GaO_x species, are expected to be proximate to extra-framework Ga^{3+} atoms, via Ga-O-Ga linkages. Evidence for $[Ga(OH)_2]^+$-H^+ cation pairs at Ga/Al ratios ≤ 0.3 and for the formation of GaO_x species at Ga/Al ratios > 0.3 was obtained by wavelet analyses of the EXAFS spectra. This method of EXAFS data analysis allows the construction of a two-dimensional picture that enables the wavenumber space (k-space) and radial space (R-space) dependence of the EXAFS signal to be examined simultaneously.[72,104–108] A maximum in the wavelet transform occurs when the frequency and amplitude components in the transformed signal coincide with those in the wavelet.[72] A detailed description of the methods used to compute wavelet transforms of simulated Ga^{3+} structures and of experimentally measured EXAFS data, is included in section 2.7.6.

The wavelet transform of the k^2 -weighted EXAFS spectrum of the simulated $[Ga(OH)_2]^+$ cation (Figure 2.4.2-5a) shows a single intense feature in the second coordination shell at R = 2.5 Å in R-space and between 3 $Å^{-1}$ and 8 $Å^{-1}$ in k-space, due to backscattering from the framework Al atom associated with the cation-exchange site. On the other hand, the wavelet transform of the experimentally measured EXAFS spectrum of β-Ga_2O_3 (Figure 2.4.2-5b) shows a single intense feature in the second coordination shell at R = 2.7 Å in R-space and between 7 $Å^{-1}$ and 13 $Å^{-1}$ in k-space, due to backscattering from next nearest neighboring Ga atoms. It is apparent that while framework Al atoms associated with $[Ga(OH)_2]^+$ cations and Ga atoms associated in β-Ga_2O_3, are at similar interatomic distances from Ga^{3+} centers, they exhibit very different k-space dependences. It has been shown that, in general, atoms with higher atomic numbers exhibit maxima in their backscattering amplitudes at higher wavenumbers (values of k) than atoms with lower atomic numbers.[98] Ga atoms, with their higher atomic number (Z = 31) exhibit a wavelet maximum at higher k values than that observed for the wavelet maximum of Al atoms (Z = 13). The wavelet transforms of k^2-weighted EXAFS spectra of Ga/H-MFI with Ga/Al ratios ≤ 0.3 (i.e., Ga/Al = 0.2, 0.3; Figure 2.4.2-6a, b) show a single dominant feature in the second coordination shell at 2.5 Å in R-space and 3-8 $Å^{-1}$ in k-space, consistent with backscattering from framework Al atoms. This finding confirms that Ga^{3+} cations in samples with Ga/Al ≤ 0.3 do not possess other extra-framework Ga^{3+} atoms in their vicinity and are therefore site isolated. Wavelet transforms of k^2-weighted EXAFS spectra of Ga/H-MFI with Ga/Al ratios > 0.3 (i.e., Ga/Al = 0.5, 0.7; Figure 2.4.2-6c, d) also show the feature associated with Al backscattering in the second coordination shell. However, a second, overlapping feature is also observed in these spectra with wavelet coordinates (R = 2.2-3.0 Å and k = 7-13 $Å^{-1}$) consistent with backscattering from Ga atoms. This finding suggests that at Ga contents higher than Ga/Al ~ 0.3, Ga^{3+} species

containing condensed Ga-O-Ga linkages co-exist with exchanged $[Ga(OH)]^{2+}$ cations and $[Ga(OH)_2]^{+}$-H^{+} cation pairs.

The data presented and discussed above suggest that for Ga/Al ratios ≤ 0.3, isolated $[Ga(OH)]^{2+}$ cations and $[Ga(OH)_2]^{+}$-H^{+} pairs form at proximate cation exchange sites associated with pairs of framework Al atoms. The population of the latter structure increases with increasing Ga loading, until the available proximate cation-exchange sites are saturated at a Ga/Al ratio of ~ 0.3. The addition of Ga in excess of this saturation stoichiometry leads to Ga^{3+} structures in oxidized Ga/H-MFI with condensed Ga-O-Ga linkages that do not appear to be ion-exchanged at cation-exchange sites. Our data are therefore not consistent with the presence of binuclear $[Ga_2O_2]^{2+}$ cations at Ga/Al ratios > 0.3, as proposed by Hensen et al.[39] We suggest instead that the addition of Ga at levels higher than Ga/Al ratios of 0.3 leads to the formation of weakly bound $[Ga(OH)_2]^{+}$ cations at residual cation-exchange sites associated with isolated framework Al atoms. In the presence of trace levels of H_2O during calcination, these structures may de-anchor via reaction of $[Ga(OH)_2]^{+}$ with H_2O to form a Brønsted acid O-H group and mobile $Ga(OH)_3$ species, which may undergo subsequent condensation to form neutral, GaO_x oligomers with structures that may resemble the Ga_4O_4 complexes proposed by Faro et al.[109] As noted above, Ga-O-Ga linkages in these structures are detectable by wavelet analysis of the EXAFS spectra. Our data, however, do not let us discern whether the GaO_x species are located inside the zeolite micropores or on the surface of the zeolite crystals.

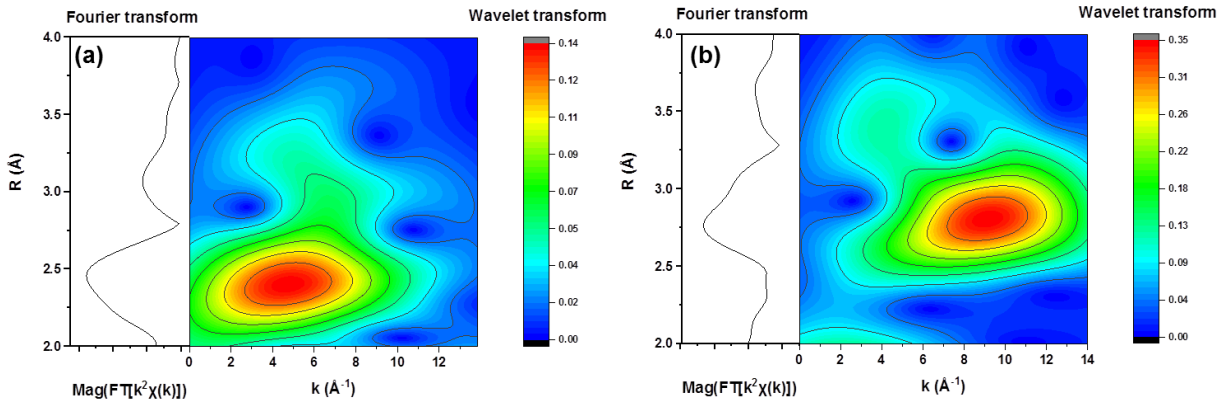

Figure 2.4.2-5. Wavelet transforms of the second coordination shell (2< R< 4 Å) of k^2-weighted Ga K-edge EXAFS spectra for (a) DFT-simulated isolated $[Ga(OH)_2]^{+}$ cation (b) β-Ga_2O_3 measured at ambient temperature. Wavelet transforms were computed in the HAMA software[72] using a Morlet wavelet function with κσ values set to 15. See section 2.7.6 for details on the methods used to compute Figure 2.4.2-5.

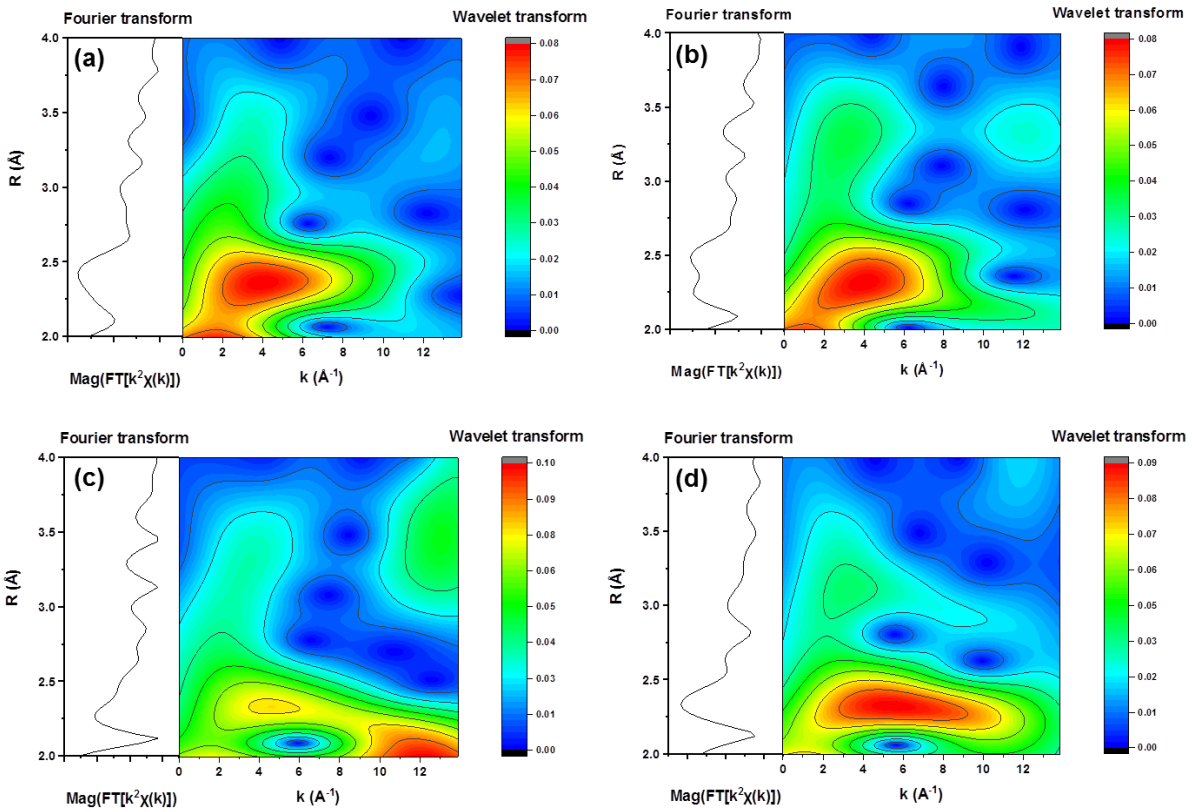

Figure 2.4.2-6. Wavelet transforms of the second coordination shell of k^2-weighted Ga K-edge EXAFS spectra of Ga/H-MFI samples, measured at 773 K under flowing 20% O_2/He (a) Ga/Al = 0.2 (b) Ga/Al = 0.3 (c) Ga/Al = 0.5 (d) Ga/Al = 0.7. Wavelet transforms were computed using the HAMA software[72] using a Morlet wavelet function with κσ values set to 15. See section 2.7.6 for details on the methods used to compute Figure 2.4.2-6

2.4.3 The state of Ga^{3+} cations in H_2-treated Ga/H-MFI

We next report our findings on the structure of Ga^{3+} species produced by H_2 reduction of oxidized Ga/H-MFI. Scheme 2.4.3-1 illustrates several pathways by which $[Ga(OH)]^{2+}$ cations and $[Ga(OH)_2]^{+}$-H^{+} cation pairs at proximate cation-exchange sites associated with pairs of framework Al atoms, might undergo reduction. According to this scheme, the reaction between divalent $[Ga(OH)]^{2+}$ cations (Structure 1) and one equivalent of H_2 could result in the re-protonation of one cation-exchange site and the formation of $[Ga(OH)H]^{+}$-H^{+} cation pairs (Structure 3). $[Ga(OH)_2]^{+}$-H^{+} cation pairs (Structure 2) may also react with one equivalent of H_2 to form $[Ga(OH)H]^{+}$-H^{+} cation pairs (Structure 3) and 1 equivalent of H_2O. $[Ga(OH)H]^{+}$ cations may undergo condensation with the proximate Brønsted acid O-H group to form $[GaH]^{2+}$ cations (Structure 4) and form one equivalent of H_2O. Alternatively, $[Ga(OH)H]^{+}$-H^{+} cation pairs could further react with one equivalent of H_2 to form $[GaH_2]^{+}$-H^{+} cation pairs (Structure 5) and one equivalent of H_2O.

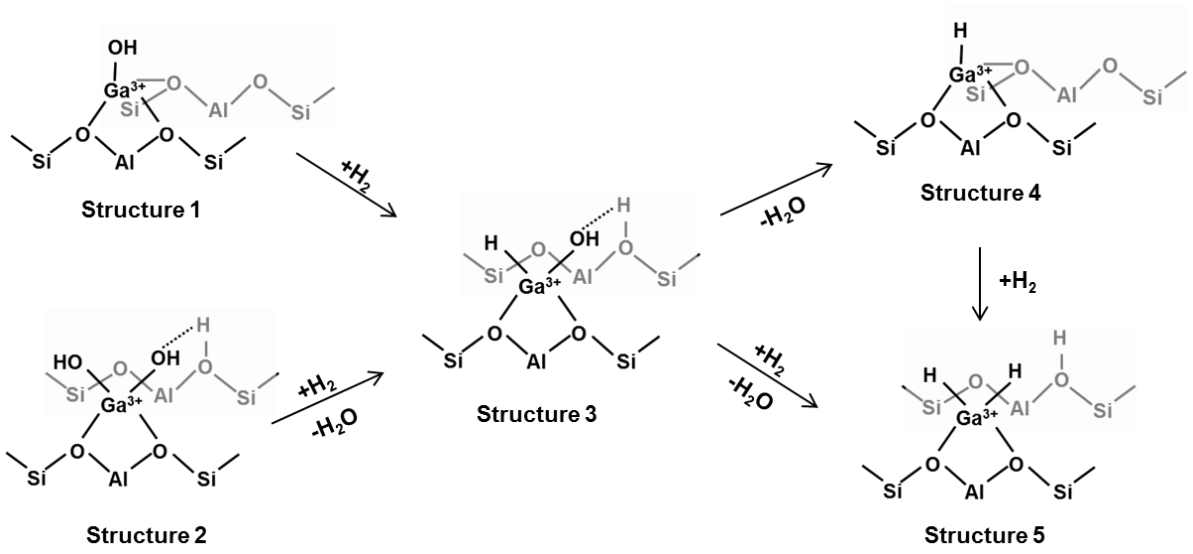

Scheme 2.4.3-1. Pathways for reactions between $[Ga(OH)]^{2+}$ cations and $[Ga(OH)_2]^{+}$-H^{+} cation pairs and H_2 to generate Structure 3- $[Ga(OH)H]^{+}$-H^{+} cation pairs, Structure 4- $[GaH]^{2+}$ cation , Structure 5-$[GaH_2]^{+}$-H^{+} cation pairs.

H_2- Temperature programmed reduction (H_2-TPR) profiles of Ga/H-MFI with Ga/Al ratios of 0.1- 0.3 are shown in Figure 2.4.3-1, as the molar consumption rate of H_2 per gram of catalyst (Figure 2.4.3-1a) and as the molar formation rate of H_2O per gram of catalyst (Figure 2.4.3-1b). A single H_2 consumption and H_2O formation peak is observed at 723 K for all three Ga/H-MFI samples; the intensities of these features increase with increasing Ga content. The H_2O formation profiles for Ga/H-MFI (Figure 2.4.3-1b) exhibit an additional feature for H_2O formation at temperatures > 823 K. This feature was also observed in the H_2-TPR profile of H-MFI and is likely due to dehydroxylation of proximate Si-OH groups and of framework Al atoms that undergo dealumination at temperatures > 1000 K.[18,110] The area under the H_2 consumption and H_2O generation peaks can be integrated to assess the molar consumption of H_2 and the molar formation of H_2O per Ga atom. Integrated H_2O molar yields for Ga/H-MFI samples were corrected for H_2O desorption from the zeolite by subtracting the integrated H_2O molar yield for H-MFI from that of Ga/H-MFI. These data, presented in Table 2.4.3-1, suggest that for Ga/Al ratios of 0.1 to 0.3, approximately 1 equivalent of H_2 is consumed per Ga atom. For Ga/Al ratios ≤ 0.1, these data are consistent with the reduction of $[Ga(OH)]^{2+}$ cations (~30% of the Ga^{3+} in oxidized Ga/Al = 0.1 sample, by NH_3-TPD) to either $[Ga(OH)H]^{+}$-H^{+} cation pairs or to divalent $[GaH]^{2+}$ cations. H_2/Ga ratios of 1 are also consistent with the reduction of $[Ga(OH)_2]^{+}$-H^{+} cation pairs to either $[Ga(OH)H]^{+}$-H^{+} cation pairs (Structure 3) or into divalent $[GaH]^{2+}$ cations (Structure 4). However, the observed H_2 consumption yields are not consistent with the reduction of $[Ga(OH)]^{2+}$ or $[Ga(OH)_2]^{+}$-H^{+} cation pairs to $[GaH_2]^{+}$-H^{+} cation pairs (Structure 5), since both reactions require the consumption of two equivalents of H_2 per Ga atom. The formation of $[Ga(OH)H]^{+}$-H^{+} cation pairs and $[GaH]^{2+}$ cations from $[Ga(OH)]^{2+}$ cations requires the formation of zero and one equivalents of H_2O, respectively, while the formation of these two structures from $[Ga(OH)_2]^{+}$-H^{+} cation pairs would require the formation of one and two equivalents of H_2O, respectively. Measured H_2O/Ga and H_2O/H_2 ratios determined from H_2-TPR profiles for all three Ga/H-MFI samples (Table 2.4.3-1) are greater than 1, but less than 2, with values

decreasing closer to unity with increasing Ga/Al ratio. These data suggest that under the conditions prevailing during H_2-TPR, $[Ga(OH)]^{2+}$ cations and $[Ga(OH)_2]^{+}$-H^{+} cation pairs convert to both $[GaH]^{2+}$ cations and $[Ga(OH)H]^{+}$-H^{+} cation pairs –$[GaH]^{2+}$ cations appear to be present at all Ga/Al ratios but in a higher proportion at lower Ga/Al ratios.

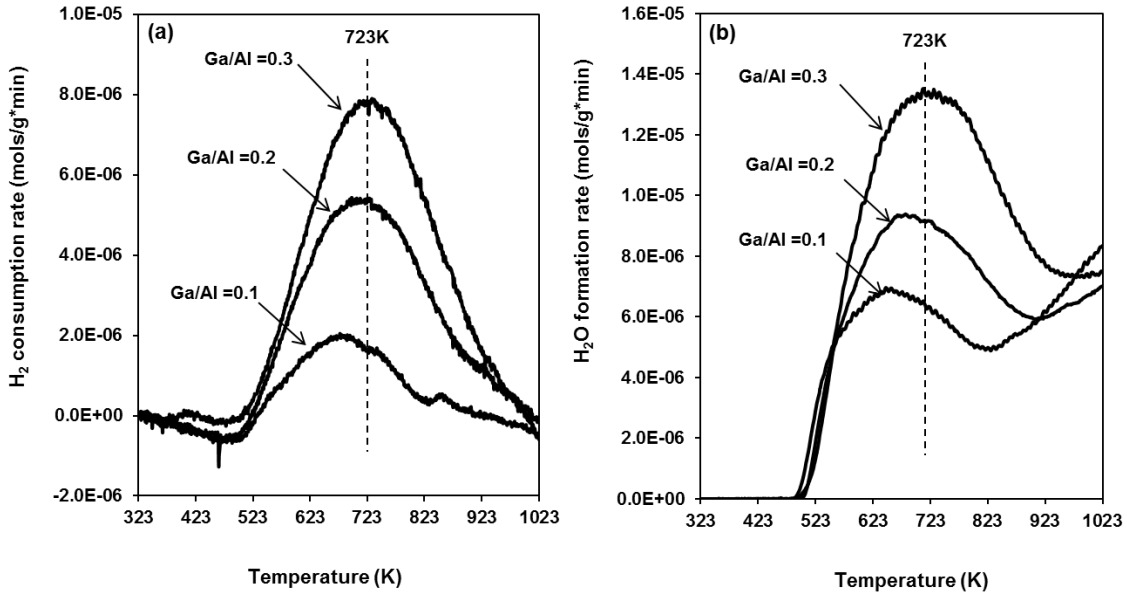

Figure 2.4.3-1. H_2-Temperature Programmed Reduction (H_2-TPR) profiles ($10Kmin^{-1}$) for Ga/H-MFI samples (Ga/Al = 0.1 – 0.3). (a) H_2 consumption rates per g (b) H_2O formation rates per g. Integrated H_2/Ga and H_2O/Ga ratios are tabulated in Table 2.4.3-1.

Also shown in Table 2.4.3-1, is the fraction of Brønsted acid O-H groups replaced by Ga^{3+} for H_2-treated Ga/H-MFI samples, determined from NH_3-TPD. Exchange stoichiometries determined from these data suggest that for the Ga/Al = 0.1 sample, two Brønsted acid O-H groups are replaced per Ga^{3+} atom, consistent with the presence of $[GaH]^{2+}$ cations in this sample after H_2 treatment. With an increase in Ga content (up to a Ga/Al ratio of 0.3), the exchange stoichiometry of H_2-treated Ga/H-MFI decreases to between one and two Brønsted acid O-H groups replaced per Ga^{3+} atom, consistent with a higher concentration of $[Ga(OH)H]^{+}$-H^{+} cation pairs as the Ga/Al ratio increases. In conclusion, NH_3-TPD and H_2-TPR data provide evidence for the formation of $[GaH]^{2+}$ cations at low Ga/Al ratios (Ga/Al = 0.1) and the formation of $[Ga(OH)H]^{+}$-H^{+} cation pairs in increasing concentration for Ga/Al ratios between 0.1 and 0.3.

Table 2.4.3-1. Integrated H_2/Ga, H_2O/Ga and H_2O/H_2 ratios for H_2-TPR profiles of Ga/H-MFI samples (Ga/Al = 0.1 to 0.3) and H^+_{exch}/H^+_{total} and H^+_{exch}/Ga values measured via NH_3-TPD after H_2 treatment of Ga/H-MFI samples at 823 K.

Ga/Al	H_2/Ga[a]	H_2O/Ga[a]	H_2O/H_2	H^+_{exch}/H^+_{tot}	H^+_{exch}/Ga[b]
0.1	0.8	1.3	1.7	0.25	2.2
0.2	0.8	1.1	1.3	0.34	1.5
0.3	0.8	1.1	1.4	0.41	1.2

[a] Ratios were obtained by integrating the area of H_2 molar consumption and H_2O molar formation feature at 723 K and normalizing these areas by the molar Ga content. Integrated H_2O formation was corrected for H_2O desorption from H-MFI using the H_2-TPR profile of H-MFI.

[b] Obtained from NH_3-TPD profiles of H_2-treated Ga/H-MFI samples. NH_3/Al_{tot} values from these experiments were used together with Eq (2.3.2-2) in order to estimate H^+_{exch}/H^+_{tot}. These values were then normalized by the Ga/Al_f ratio (obtained by dividing Ga/Al_{tot} values by the Al_f/Al_{tot} value for H-MFI, to reflect framework Al_f in order to obtain values of H^+_{exch}/Ga.

We have shown above that under oxidizing conditions, the formation of $[Ga(OH)]^{2+}$ cations at proximate cation-exchange sites depends sensitively on the framework Al-Al interatomic distance and H_2O partial pressure. In an analogous manner, we propose that the stability of $[GaH]^{2+}$ cations and their tendency to decompose into $[Ga(OH)H]^+$-H^+ or $[GaH_2]^+$-H^+ cation pairs depends on both the framework Al-Al interatomic distance between proximate cation-exchange sites and also upon the partial pressures of H_2 and H_2O. To assess the validity of this hypothesis, we generated theoretical phase diagrams in order to illustrate the regions of stability for various Ga^{3+} structures as a function of temperature and H_2 partial pressure for a given H_2O partial pressure. Each region of stability in these phase diagrams is representative of a Ga^{3+} structure that exhibits the lowest free energy of formation from $[Ga(OH)_2]^+$-H^+ cation pairs. Equations (2.3.3-1) and (2.3.3-2) (theoretical methods, section 2.3.3) were used to calculate these free energies of formation. Phase diagrams were generated for Ga^{3+} structures at proximate cation-exchange sites associated with both NNN and NNNN pairs of framework Al atoms in order to assess the effect of framework Al-Al interatomic distance on the stability of Ga^{3+} species. Figure 2.4.3-2 shows the phase diagrams for stability of Ga^{3+} species at temperatures between 473 K and 823 K, H_2 partial pressures ranging between 10^{-1} Pa and 10^6 Pa and for a fixed H_2O partial pressure of 10 Pa. Phase diagrams for additional H_2O partial pressures are included in section 2.7.7 (see Figures 2.7-10 and 2.7-11). As seen in Figure 2.4.3-2, at an H_2O partial pressure of 10 Pa and for all temperatures, $[Ga(OH)_2]^+$-H^+ cation pairs are the most favorable structure on proximate cation-exchange sites associated with NNNN pairs of framework Al atoms when Ga/H-MFI is in the oxidized state (H_2 partial pressure < 10^2 Pa). When the interatomic Al-Al distance is lowered to ≤ 5 Å for NNN pairs of framework Al atoms in Figure 2.4.3-2, $[Ga(OH)_2]^+$-H^+ cation pairs are stable only for temperatures < 623 K under oxidizing conditions. Above this temperature, the phase diagram predicts that $[Ga(OH)_2]^+$-H^+ cation pairs would undergo intra-pair condensation to form $[Ga(OH)]^{2+}$ cations. These findings are in agreement with experimental observations discussed earlier.

Upon reaction between $[Ga(OH)_2]^+$-H^+ cation pairs and H_2 (> 10^2 Pa) and in the presence of 10 Pa H_2O, the phase diagram in Figure 2.4.3-2 indicates that the conversion of $[Ga(OH)_2]^+$-H^+ cation pairs at NNNN cation-exchange sites into $[Ga(OH)H]^+$-H^+ pairs is highly favorable thermodynamically. $[Ga(OH)H]^+$-H^+ pairs are the most stable structure throughout the

temperature range examined (473-823 K) and at H_2 partial pressures as high as 10^5 Pa. At H_2 pressures > 10^5 Pa and temperatures > 673 K (and a fixed H_2O partial pressure of 10 Pa), Figure 2.4.3-2 shows that $[Ga(OH)H]^+$-H^+ cation pairs on NNNN cation-exchange sites may further reduce to $[GaH_2]^+$-H^+ pairs. These stability trends also appear to be a strong function of H_2O partial pressure. Under conditions with lower H_2O partial pressure (10^{-1} Pa), the phase diagram for NNNN cation-exchange sites (see Figure 2.7-11) predicts that the $[Ga(OH)H]^+$-H^+ cation pairs would form $[GaH_2]^+$-H^+ cation pairs at H_2 partial pressures as low as 3 x 10^3 Pa and temperatures > 700 K. On the other hand, for H_2 pressures lower than 3 x 10^3 Pa and at temperatures higher than 700 K, $[Ga(OH)H]^+$-H^+ cation pairs would undergo intra-pair condensation to form $[GaH]^{2+}$ cations. For Ga^{3+} structures at NNN cation-exchange sites, the phase diagram in Figure 2.4.3-2 predicts that at temperatures < 623 K and H_2 partial pressures > 10^2 Pa (and fixed H_2O partial pressure 10 Pa), $[Ga(OH)_2]^+$-H^+ cation pairs at NNN cation-exchange sites would also form $[Ga(OH)H]^+$-H^+ cation pairs. At temperatures > 623K, these structures would convert into $[GaH]^{2+}$ cations. $[GaH]^{2+}$ cations at NNN proximate cation-exchange sites appear to be stable and resistant to the formation of $[GaH_2]^+$-H^+ cation pairs at all H_2 partial pressures tested. Even at very low H_2O partial pressures (10^{-1} Pa), $[GaH]^{2+}$ cations are still the most thermodynamically stable structure in the presence of H_2 (see Figure 2.7-10)

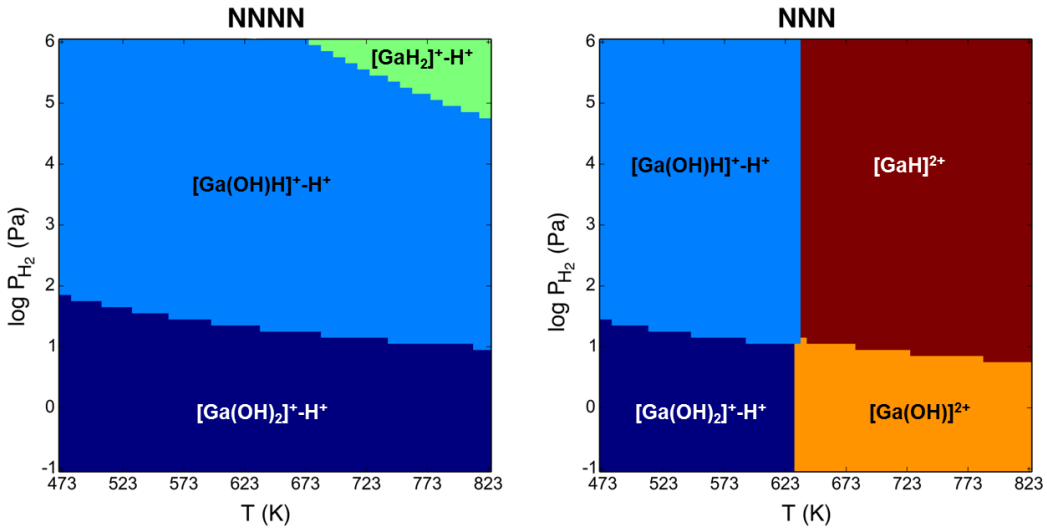

Figure 2.4.3-2. Theoretical thermodynamic phase diagrams for Ga^{3+} structures at cation-exchange sites associated with NNNN and NNN proximate framework Al atoms. Colored regions reflect a Ga^{3+} structure that has the lowest free energy of formation from $[Ga(OH)_2]^+$-H^+ cation pairs at a given temperature (T) and hydrogen partial pressure (P_{H2}), and water partial pressure (P_{H2O}) of 10 Pa. The H_2O partial pressure used for this diagram is representative of conditions prevalent during H_2-TPR and NH_3-TPD.

Further evidence for the presence of GaH_x cations was obtained from in-situ infrared spectra of Ga/H-MFI samples, taken at 473 K, after treating Ga/H-MFI samples in 2.5% H_2/He for 1 h at 823 K. Spectra of all three Ga/H-MFI samples (Ga/Al = 0.2, 0.3, 0.5) are shown in Figure 2.4.3-3. Two bands are observed at approximately 2040 cm^{-1} and 2060 cm^{-1}, that are

absent in the infrared spectra of oxidized Ga/H-MFI samples. In order to assign these vibrational modes to specific GaH_x structures, we examined Ga-H vibrational frequencies computed from QM/MM calculations, for $[GaH]^{2+}$ cations, $[Ga(OH)H]^{+}$-H^{+} cation pairs, and $[GaH_2]^{+}$-H^{+} cation pairs. The predicted frequency for Ga-H stretches in $[GaH]^{2+}$ cations is 2059 cm^{-1} while for $[Ga(OH)H]^{+}$-H^{+} cation pairs, the predicted Ga-H stretching frequency is 2109 cm^{-1}. For $[GaH_2]^{+}$ cations (likely present as $[GaH_2]^{+}$-H^{+} cation pairs), the symmetric and asymmetric Ga-H stretching frequencies are predicted to be 2003 cm^{-1} and 2043 cm^{-1}, respectively. We, therefore, assign the band at 2060 cm^{-1} in the infrared spectra of Ga/H-MFI to Ga-H stretching vibrations in $[GaH]^{2+}$ cations. We also assign the experimentally observed band at 2040 cm^{-1} to asymmetric to Ga-H stretching vibrations in $[GaH_2]^{+}$ cations. These assignments are consistent with previous observations of GaH_x species in the infrared spectra of H_2 treated Ga/H-MFI.[34] We were unable to observe the Ga-H stretching frequency predicted for $[Ga(OH)H]^{+}$-H^{+} cation pairs in our spectra, likely because of low H_2O partial pressures prevalent in our transmission infrared pellets (~30 mg sample). Low H_2O concentrations (~10^{-1} Pa) may enable $[Ga(OH)H]^{+}$-H^{+} cation pairs to reduce to $[GaH_2]^{+}$-H^{+} cation pairs, as predicted by our theoretical calculations. It should also be noted that the relative intensity of the 2040 cm^{-1} band in Figure 2.4.3-3 increases as a function of Ga/Al, consistent with the presence of a higher concentration of $[Ga(OH)H]^{+}$-H^{+} cation pairs or $[GaH_2]^{+}$-H^{+} cation pairs with increasing Ga content.

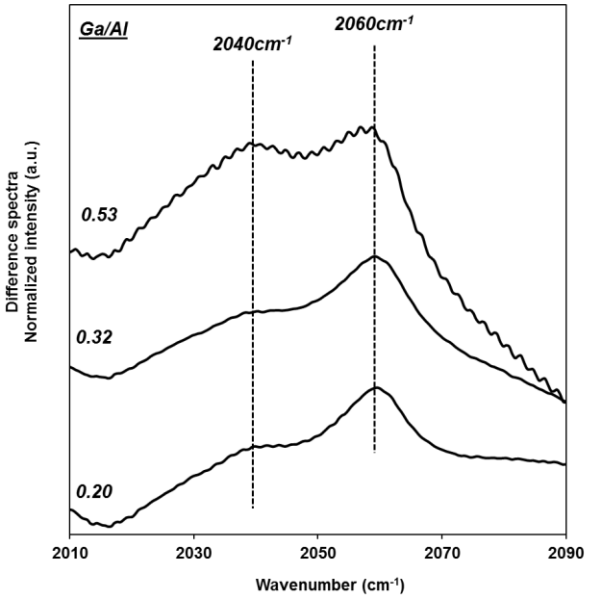

Figure 2.4.3-3. In-situ infrared 'difference' spectra of Ga/H-MFI samples at 473 K, after treatment in 2.5% H_2/He at 823 K for 1 h. 'Difference' spectra were obtained by subtracting the infrared spectra of H-MFI at 473 K from normalized infrared spectra of Ga/H-MFI at 473 K. All spectra were normalized to framework Si-O-Si overtone bands between 1900 cm^{-1}- 2100 cm^{-1}. Dotted lines show Ga-H vibrational modes

Additional information about the structures of Ga^{3+} cations in H_2-treated Ga/H-MFI was obtained from the XANES portion of X-ray absorption spectroscopy measurements conducted on H_2-treated Ga/H-MFI samples. As reported in prior studies,[32,33,45,109] we observe that upon heating Ga/H-MFI in H_2, the XANES absorption maximum shifts from 10376.6 eV for oxidized Ga/H-MFI to approximately 10372 eV for Ga/H-MFI, H_2-treated at 823 K, as seen in Figure 2.4.3-4a for the Ga/Al = 0.3 sample. An increase in temperature from 603 K to 823 K during treatment in H_2 results in an increase in the intensity of the lower energy absorption edge (~10372 eV). Previous XANES studies of reduced Ga/H-MFI have attributed the feature at 10372 eV to the presence of Ga^+.[22,32,45] This interpretation has been brought into question by the recent work of Getsoian et al., who examined the effects of Ga coordination and ligation on Ga K-edge XANES spectra.[33] XANES spectra of Ga^{3+} organometallic compounds in which the coordination and identity of Ga-bound ligands was varied systematically revealed that for every O ligand in a 4-coordinate Ga^{3+} compound, replaced by a less electronegative, more strongly σ-donating H (hydride) or R (alkyl) ligand, the XANES absorption maximum (and edge energy) decreased by approximately 1.5 eV. In addition, when the coordination number around Ga^{3+} decreased from a 4 to 3, an additional 1.5 eV decrease in the XANES absorption maximum occurred.[33] On the basis of these data, it was proposed that 3-coordinate $[GaH_2]^+$ cations form upon H_2 treatment of Ga/H-BEA .[33]

We can predict the XANES absorption maximum (or edge energy) for different GaH_x species in H_2-treated Ga/H-MFI, using the guidelines developed by Getsoian et al.[33] For $[Ga(OH)]^{2+}$ and $[Ga(OH)_2]^+$-H^+ cation pairs, which have a XANES absorption maximum at 10376.6 eV, H_2 reduction of these species to 4-coordinate $[Ga(OH)H]^+$ cations is expected to decrease the position of the absorption maximum by ~1.5 eV to 10375.1 eV. The conversion of $[Ga(OH)H]^+$-H^+ cation pairs to form 4- coordinate $[GaH]^{2+}$ cations is not expected to affect the XANES absorption maximum since both structures have 3 O ligands and 1 H ligand. Further reduction of both species ($[Ga(OH)H]^+$ and $[GaH]^{2+}$ cations) to 4-coordinate $[GaH_2]^+$ cations is expected to decrease the position of the XANES absorption maximum by another 1.5 eV to about 10373.6 eV. As proposed by Getsoian et al., the weakened Lewis acidity of Ga^{3+} in 4-coordinate $[GaH_2]^+$ cations may result in the loss of the dative Ga-O_f bond at high temperatures, to form 3-coordinate $[GaH_2]^+$ cations, bound to only one framework Ga-O_f bond.[33] Such a conversion would further lower the XANES absorption maximum by 1.5 eV to about 10372.1 eV. Our XANES measurements presented in Figure 2.4.3-4a for the Ga/Al = 0.3 sample (XANES spectra for other Ga/Al ratios are given in Figure 2.4.3-5a, b, c) show a decrease in the energy of the absorption maximum from 10376.6 eV for oxidized Ga/H-MFI to about 10372 eV upon reduction in H_2 at 823 K (a ~4.6 eV decrease), consistent with the presence of 3-coordinate $[GaH_2]^+$ cations in H_2-treated samples.

Figure 2.4.3-4b shows the difference XANES spectra for the Ga/Al = 0.3 sample, at various temperatures during treatment in H_2 from ambient temperatures to 823 K (Difference XANES spectra were obtained by subtracting the spectrum of the oxidized Ga/H-MFI spectrum taken at 773 K from the spectrum of H_2-treated Ga/H-MFI). Upon heating oxidized Ga/H-MFI in H_2 to 603K, the difference XANES spectra show the emergence of three features at 10375.1 eV, 10373.5 eV, and 10372 eV that are lower in energy than the absorption maximum for oxidized Ga/H-MFI (10376.6 eV). On the basis of the preceding discussion, the feature at 10375.1 eV may reflect either 4-coordinate $[Ga(OH)H]^+$-H^+ cation pairs or 4-coordinate $[GaH]^{2+}$ cations. On this basis, we assign the feature at 10373.5 eV to 4-coordinate $[GaH_2]^+$-H^+ cation pairs and the lowest energy feature to 3-coordinate $[GaH_2]^+$-H^+ cation pairs. As seen in Figure 2.4.3-4b, we

observed that upon heating samples in H_2 from 603 K to 713 K and finally to 823 K, the feature at 10372 eV increases in intensity and becomes the dominant feature in the difference XANES spectrum at 823 K. The spectrum continues to evolve even as samples are heated past the peak temperature in the H_2-TPR response (~723 K), suggesting that the feature at 10372 eV is not likely to be due to a Ga^{3+} species that is further reduced than 4-coordinate $[GaH_2]^+$ cations but rather due to a Ga^{3+} species with a lower coordination to framework O atoms. The spectrum in Figure 2.4.3-4b suggests that 3-coordinate $[GaH_2]^+$ cations form in increasing concentration with increasing temperature. As seen in Figures 2.4.3-5a, b and c, a similar increase in the intensity of the absorption maximum at 10372 eV with an increase in temperature was observed in XANES spectra of other H_2-treated samples of Ga/H-MFI (Ga/Al = 0.1, 0.2, 0.5 and 0.7) suggesting that 3-coordinate $[GaH_2]^+$ cations may be present at all Ga/Al ratios. On the basis of our previous characterization, which showed that $[GaH]^{2+}$ cations form in greater concentration at low Ga/Al ratios, we propose that the observed similarity in the absorption maxima (10372 eV) regardless of Ga/Al ratio, is a likely a result of a higher absorption intensity of 3-coordinate $[GaH_2]^+$ cations in comparison to 4-coordinate $[GaH]^{2+}$ or $[GaH_2]^+$ cations.

A decrease in Ga^{3+} coordination from 4 to 3 corresponds to a change in hybridization around the metal center from sp^3 to sp^2. Consequently, the Ga $4p_z$ orbital becomes non-bonding in 3-coordinate Ga^{3+} structures. In a similar manner to what has been shown for XANES of low-coordinated Zn^{2+} compounds,[111] the allowed photoelectron excitation of a Ga 1s electron into the non-bonding Ga $4p_z$ orbital would result in a stronger absorption at the Ga K-edge than for a similar 1s electron excitation into bonding 4p orbitals. Therefore, even if 3-coordinate $[GaH_2]^+$ cations were present at a lower concentration relative to 4-coordinate $[GaH]^{2+}$ cations at low Ga/Al ratios, these species would be expected to dominate the XANES absorption edge. We also note that the absorption maximum at 823 K for the Ga/Al = 0.1 sample (~10373 eV) seen in Figure 2.4.3-5c is about 1 eV higher than the absorption maxima for the samples with Ga/Al = 0.2 and Ga/Al = 0.3 (~10372 eV). The presence of $[GaH]^{2+}$ cations (with an absorption maximum of ~10375 eV), in co-existence with some 3-coordinate $[GaH_2]^+$ cations (with an absorption maximum of ~10372eV) at low Ga/Al ratios may be responsible for this observation. The EXAFS spectra of H_2-treated Ga/H-MFI, when fit to a 2 shell Ga-O model, showed a total decrease in Ga-O coordination from 4 in oxidized Ga/H-MFI to between 2 and 3 in Ga/H-MFI treated in H_2 at 723 K (see Table 2.7-4 in section 2.7.8). Due to the weak photoelectron scattering from H atoms,[112] the observed decrease in Ga-O coordination is consistent with the replacement of Ga-bound OH ligands with H ligands. We could not perform a more detailed analysis of the EXAFS spectra of H_2-treated Ga/H-MFI due to the co-existence of multiple Ga species.

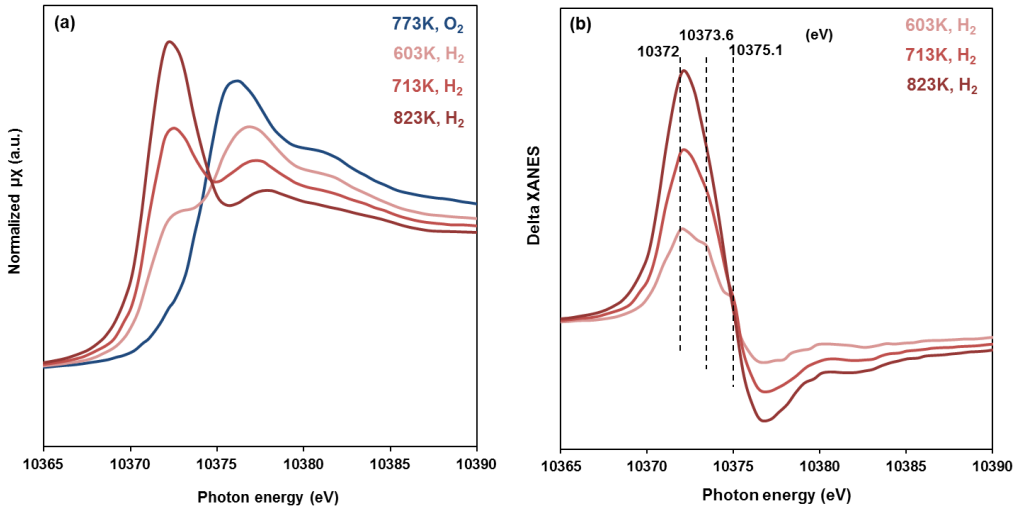

Figure 2.4.3-4. (a) Ga K-edge XANES spectra of H_2-treated Ga/H-MFI (Ga/Al = 0.3) at various temperatures during heating of oxidized Ga/H-MFI in 3% H_2/He (b) Difference (or Delta) XANES spectra of H_2-treated Ga/H-MFI (Ga/Al =0.3) obtained by subtracting the XANES spectrum for oxidized Ga/H-MFI from the XANES spectrum of H_2-treated Ga/H-MFI at 603 K, 713 K and 823 K. Dotted lines in delta XANES plot indicate positions of features at 10375.1 eV, 10373.6 eV and 10372 eV.

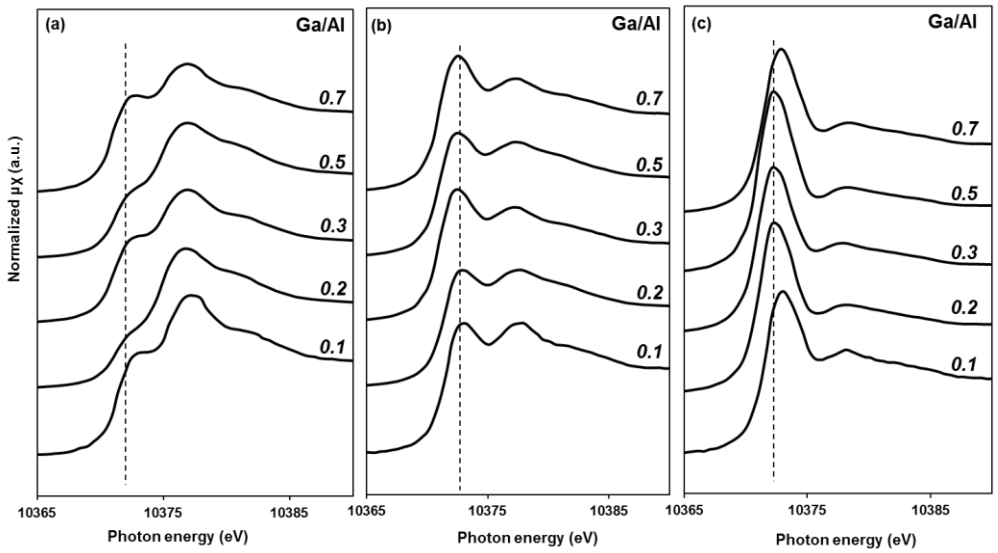

Figure 2.4.3-5. Ga K-edge XANES spectra of H_2-treated Ga/H-MFI (Ga/Al = 0.1 to 0.7) after heating oxidized Ga/H-MFI in 3% H_2/He at (a) 603 K (b) 713 K (c) 823 K. Spectra were collected after 1 h of H_2 treatment at each temperature. Dotted lines show positions of absorption maxima.

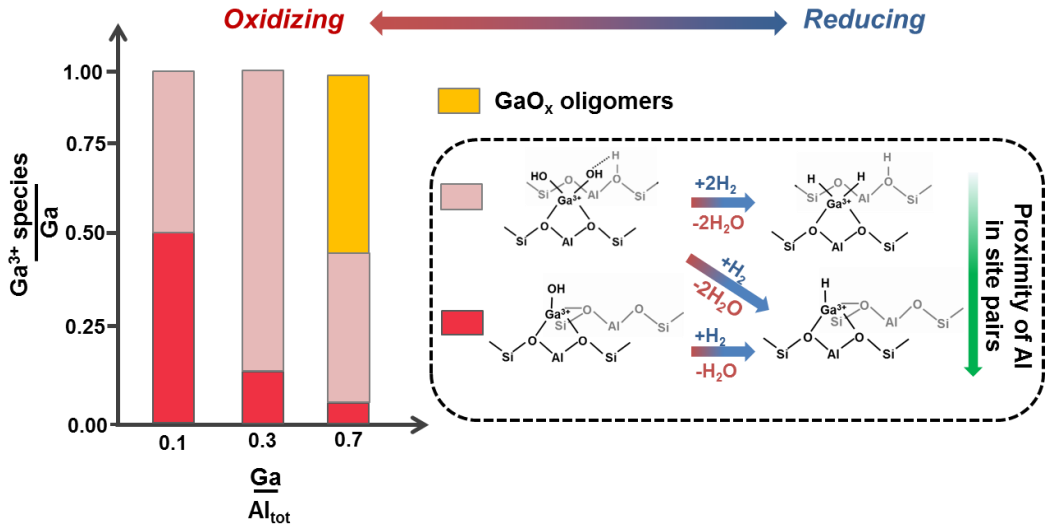

Figure 2.4.3-6. Ga^{3+} speciation in Ga/H-MFI under oxidizing conditions (red) and reducing conditions (blue)

2.5 Conclusions

Ga/H-MFI with Ga/Al ratios ranging from 0.1 to 0.7 was synthesized via the vapor-phase reaction of dehydrated H-MFI with $GaCl_3$. This process results in the exchange of Brønsted acid O-H groups by monovalent $[GaCl_2]^+$ cations. The maximum level of cation exchange achievable by this means is ~ $[GaCl_2]^+/Al_{tot}$ = 0.7. H_2 reduction at 823 K of the as-exchanged zeolites results in the stoichiometric removal of Ga-bound Cl as HCl and the formation of $[GaH_2]^+$ cations. Upon O_2 oxidation at 773 K, these structures form oxidized Ga^{3+} species; however, crystalline β-Ga_2O_3 is not detectable by Raman spectroscopy. For Ga/Al = 0.1 about half of the $[GaH_2]^+$ cations are oxidized to divalent $[Ga(OH)]^{2+}$ cations, bound to proximate cation-exchange sites associated with pairs of framework Al atoms located ≤ 5 Å apart, whereas the remainder $[GaH_2]^+$ cations are oxidized to $[Ga(OH)_2]^+$-H^+ cation pairs bound to proximate cation-exchange sites associated with pairs of framework Al atoms located > 5 Å apart. For Ga/Al ratios above 0.1 but below 0.3, an increasing fraction of the cation-exchanged Ga^{3+} is present as $[Ga(OH)_2]^+$-H^+ cation pairs bound to proximate cation-exchange sites. For Ga/Al ratios higher than 0.3, wavelet analysis of EXAFS data shows that neutral GaO_x species, not associated with cation-exchange sites are formed. Upon H_2 reduction of oxidized Ga/H-MFI, $[Ga(OH)]^{2+}$ cations and $[Ga(OH)_2]^+$-H^+ cation pairs form $[GaH]^{2+}$ cations at low Ga/Al ratios (~0.1), and $[Ga(OH)H]^+$-H^+ cation pairs for Ga/Al ≤ 0.3. Phase diagrams calculated to assess the thermodynamic stability of species formed upon H_2 reduction of $[Ga(OH)_2]^+$-H^+ cation pairs indicate that $[GaH]^{2+}$ cations are more stable at proximate cation-exchange sites with (NNN) framework Al-Al interatomic distances ≤ 5Å, while for proximate cation-exchange sites with (NNNN) framework Al-Al interatomic distances > 5 Å, $[Ga(OH)H]^+$-H^+ cation pairs are more likely to form when H_2 reduction is carried with a background partial pressure of H_2O of 10 Pa. For lower partial pressures of H_2O (10^{-1} Pa) , the calculated phase diagrams predict that $[Ga(OH)H]^+$-H^+ cation pairs associated with NNNN framework Al atoms further reduce to $[GaH_2]^+$-H^+ cation pairs. Evidence for $[GaH]^{2+}$

cations and $[GaH_2]^+$-H^+ cation pairs was obtained via infrared spectroscopy under reducing conditions. For temperatures above 713 K, XANES data suggests that, 4-coordinate $[GaH_2]^+$ cations transform to 3-coordinate $[GaH_2]^+$ cations. The preferential formation of $[GaH]^{2+}$ cations at low Ga/Al ratios (~ 0.1) is a consequence of the thermodynamic preference for these cations to locate at cation-exchange sites associated with (NNN) framework Al atoms that are ≤ 5 Å apart. A summary of how Ga^{3+} speciation changes with Ga/Al ratio in both the oxidized and reduced forms of Ga/H-MFI is shown in Figure 2.4.3-6. The present study provides essential information for understanding the structure of reduced Ga^{3+} species as active centers for the dehydrogenation and dehydrocylization of light alkanes to alkenes and aromatics.

2.6 Acknowledgements

This work was supported by Chevron Energy Technology Company. Computational resources were provided by UC Berkeley's Molecular Graphics and Computation Facility (supported by NIH S10OD023532). We would like to thank James Dombrowski and Sam Wood for assistance with development of synthetic protocols, Christopher Ho for helpful technical discussions We also thank Dr. Ping Yu (UC-Davis) for assistance with NMR measurements. This research used resources of the Advanced Photon Source, a U.S. Department of Energy (DOE) Office of Science User Facility operated for the DOE Office of Science by Argonne National Laboratory under Contract No. DE-AC02-06CH11357. XAS measurements were conducted at Beamline 5BMD at the Advanced Photon Source (APS), Argonne National laboratory. We thank Dr. Qing Ma (Advanced Photon source, ANL) and Prof. Jeffrey Miller (Purdue University) for assistance with XAS measurements.

2.7 Supporting Information

2.7.1 Removal of Ga-bound Cl ligands via H_2 treatment at 823 K

Previous reports of the synthesis of Ga/H-MFI via gas phase ion exchange with $GaCl_3$ employed a thermal treatment in He at 773 K to remove Cl ligands after the $GaCl_3$ grafting reaction[113]. During the course of our studies, we found this thermal treatment to be inefficient at completely removing Cl ligands from grafted Ga species. Treatment of $[GaCl_2]^+$ /H-MFI samples in H_2 at 823 K on the other hand, led to > 95% removal of elemental Cl initially present in samples. The Cl content in Ga/H-MFI samples, after H_2/O_2 thermal treatments, is shown in Table 2.7-1. H_2 reduction of $[GaCl_2]^+$/H-MFI also led to the appearance of a new band at 2051 cm^{-1} in the infrared spectra of $[GaCl_2]^+$/H-MFI materials, as shown in Figure 2.7-1. This band is consistent with Ga-H vibrations in GaH_x species,[34,36] thereby indicating the formation of $[GaH_2]^+$ cations in theses samples.

Table 2.7-1. Elemental Cl/Ga ratios of Ga/H-MFI after $GaCl_3$ grafting, followed by H_2 treatment at 823 K and O_2 treatment at 773 K. Atomic ratios were determined via ICP-OES (Galbraith Laboratories)

Ga/Al	Cl/Ga
0.1	0.12
0.2	0.07
0.3	0.11
0.5	0.08
0.7	0.01

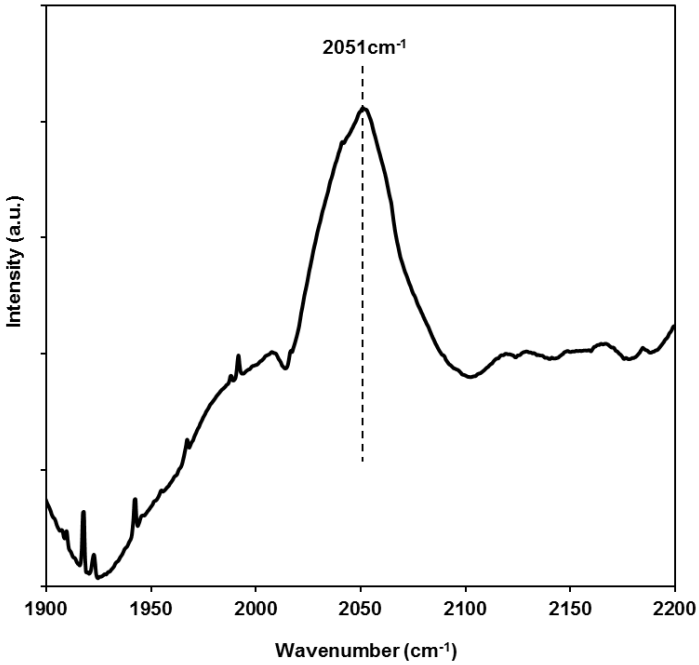

Figure 2.7-1. Difference infrared spectra of GaClx/H-MFI (Ga/Al =0.7), relative to spectra of H-MFI, measured under 2.5%H2/He at 373 K. Spectra were collected after treating GaClx/H-MFI in 2.5%H2/He at 823 K for 0.5 h. Dotted line indicates position of Ga-H vibrations in GaHx cations.

The atomic Ga/Al ratio for each of the Ga/H-MFI samples is listed in Table 2.4.1-1. For Ga/Al ratios ≤ 0.7, measured Ga/Al ratios are similar to Ga/Al ratios of physical mixtures of $GaCl_3$/H-MFI used to prepared to prepare samples. Although attempts were made to prepare samples with Ga/Al ratios > 0.7, the Ga/Al ratios of these samples after H_2 reduction and calcination in O_2 were lower than that expected. Also, during H_2 treatment of $GaCl_x$/H-MFI samples (with Ga/Al ratios > 0.7) at 823 K, a colorless white residue was observed to form at the cooler end of the quartz synthesis reactor. The exact origin of this residue is uncertain, but we

believe that the formation of the residue, together with the observed losses of Ga may be attributed to a reaction between H_2 and weakly bound $GaCl_3$ to form chlorogallane-like species- $H_{(3-x)}GaCl_x$ (x= 0 to 3). Chlorogallanes have been synthetically isolated by previous researchers and are known to decompose upon mild heating, into H_2 and colorless white crystals of $GaCl_3$.[88] Consequently, the maximum Ga/Al ratio achievable using our synthetic protocol was 0.7.

2.7.2 Raman spectra of H-MFI and Ga/H-MFI samples.

Raman spectra of H-MFI and Ga/H-MFI (Ga/Al = 0.5, 0.7) are shown in Figure 2.7-2. The Raman spectra of H-MFI exhibit strong bands at 300 cm^{-1}, 380 cm^{-1} and 450 cm^{-1}, which have been ascribed to T-O vibrations in 5, 6 and 10 member rings in the MFI framework.[67] The Raman band at 800 cm^{-1} is attributable to symmetric Si-O-Si vibrations while the band at around 1100 cm^{-1} is attributable to asymmetric Si-O-Si vibration.[67] For comparison, Raman spectra of Ga/H-MFI samples with the two highest Ga/Al ratios (Ga/Al = 0.5 and Ga/Al = 0.7) are shown alongside the Raman spectrum of H-MFI. The spectra of the Ga/H-MFI samples are nearly identical to that of H-MFI and, in all cases, only bands characteristic of the zeolite framework are observed. The inset in Figure 2.7-2 shows the Raman spectrum of β-Ga_2O_3. The bands appearing at 630 cm^{-1}, 656 cm^{-1} and 767 cm^{-1} are due to bending and stretching modes of tetrahedral GaO_4 moieties in β-Ga_2O_3, whereas the bands at 319 cm^{-1}, 347 cm^{-1}, 417 cm^{-1} and 475 cm^{-1} are due to bending and stretching modes of octahedral GaO_2 moieties in β-Ga_2O_3.[114] It is clear that the Raman spectra of Ga/H-MFI do not show any evidence for crystalline β-Ga_2O_3, suggesting that our synthetic protocol produces highly dispersed Ga^{3+} centers in the zeolite.

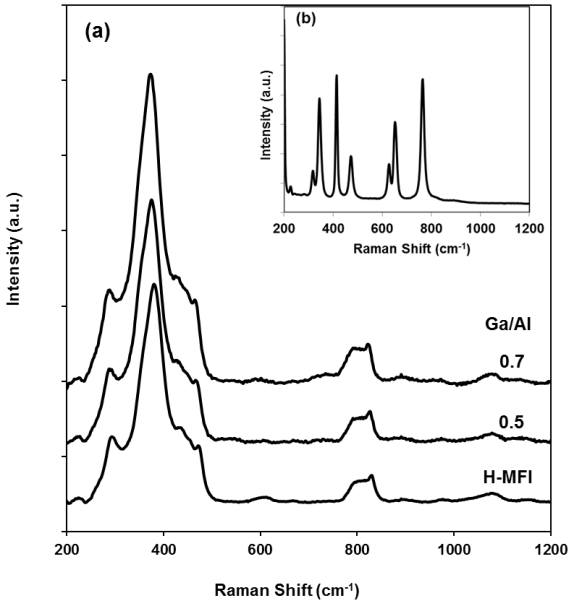

Figure 2.7-2. Raman spectra of H-MFI, Ga-MFI and β-Ga_2O3 (a) H-MFI and Ga-MFI samples were calcined in flowing synthetic air at 1023 K for 0.5 h before cooling to 323 K. Raman spectra were recorded at 323 K and normalized to intensity of Raman band at 800 cm^{-1} (b) Inset: Raman spectra of β-Ga_2O_3, recorded at ambient temperature.

2.7.3 ^{27}Al and ^{29}Si MAS NMR spectra of H-MFI and Ga/H-MFI samples.

Figure 2.7-3 shows ^{27}Al MAS NMR spectra of H-MFI and calcined samples of Ga/H-MFI that were hydrated for 24 h prior to the acquisition of the spectra. Hydration reduces the asymmetry of interaction between Al^{3+} nuclei and the magnetic field, thereby reducing line broadening caused by quadrupolar coupling.[69] All chemical shifts are reported relative to aqueous $Al(NO_3)_3$. All of the spectra presented in Figure 2.7-3 exhibit a band at 56 ppm, due to tetrahedral Al^{3+} centers, and a band at 0 ppm, due to octahedral Al^{3+} centers.[69] The ratios of octahedral to tetrahedral Al^{3+} centers for each sample, determined by integrating band areas, are shown in Table 2.7-2. For the parent H-MFI sample, the Al_{oct}/Al_{tet} ratio is approximately 0.04. A small increase in this ratio is observed upon exchange of Ga cations into H-MFI (Al_{oct}/Al_{tet} ~ 0.10 for Ga/H-MFI). This change reflects a conversion of approximately 5 % of Al_{tet} centers into Al_{oct} centers in Ga/H-MFI. Octahedral Al^{3+} centers in zeolites have been proposed to reflect extra-framework Al (EFAl) species, though this hypothesis has been disputed in the literature. Using Al K-edge EXAFS, Drake at al. have demonstrated that octahedral Al^{3+} centers in H-MFI adopt a tetrahedral symmetry upon sample dehydration.[115] It was proposed that octahedral Al centers detected by ^{27}Al MAS NMR may in fact reflect tetrahedral framework Al centers that exhibit octahedral coordination in the presence of H_2O, but revert to tetrahedral coordination upon sample dehydration.[115] On the other hand, Ong et al. conducted ^{27}Al MQMAS NMR measurements on steamed H-MFI samples and suggested that a fraction of tetrahedral Al centers detected via 1-D ^{27}Al MAS NMR may in fact, correspond to EFAl species with tetrahedral symmetry.[93] Octahedral Al^{3+} centers detected via 1-D ^{27}Al MAS NMR were then proposed to reflect Al^{3+} in neutral AlO_x.[93] In the absence of Al K-edge EXAFS and ^{27}Al MQMAS NMR data for our samples, the assignment of the peak at 0 ppm to EFAL species in our samples is equivocal.

In order to better assess the formation of EFAl centers in our samples, we measured ^{29}Si MAS NMR spectra on the parent H-MFI and the Ga/H-MFI samples. These spectra were deconvoluted via established protocols into Gaussian bands associated with Si-O tetrahedral sites having a specified coordination - Q(nSi, (4-n)Al) sites where n=1-4.[68] The integrated areas of these bands were used to compute framework Si/Al_f ratios, which reflect contributions from framework Al^{3+} atoms. Comparisons of these values with bulk Si/Al_{tot} ratios obtained from elemental analysis should in principle, yield estimates for the fraction of EFAl in the zeolite samples.

Figure 2.7-4 shows the ^{29}Si MAS NMR spectra for H-MFI and Ga/H-MFI samples. All chemical shifts were obtained with reference to Tetramethylsilane (TMS). After Gaussian band deconvolution, all spectra exhibited bands at -116 ppm, -112 ppm, -107 ppm, and a small shoulder at -100 ppm. The bands at -116 ppm and -112ppm are assigned to crystallographically inequivalent Q(4Si, 0Al) sites, while the bands at -107 ppm and -100 ppm may be assigned to Q(3Si, 1Al) and Q(2Si, 2Al) sites, respectively.[116] Si/Al_f ratios calculated from ^{29}Si MAS NMR spectra are listed in Table 2.7-2. For the parent H-MFI, a Si/Al_f ratio of 16.8 was obtained, while for the Ga/H-MFI samples, Si/Al_f ratios ranging from 17.7 to 14.5 were obtained. These Si/Al_f ratios are similar, within uncertainty to the Si/Al ratio obtained via elemental analysis (16.5± 1.0) and therefore suggest that the fraction of EFAl, if any must be ≤ 15% of the total Al centers. In agreement with these results, the NH_3/Al_{tot} value for the parent H-MFI (measured via NH_3-TPD profiles) was 0.87 ± 0.13, suggesting that ~ 13% of Al content in H-MFI is not associated with framework Al sites. Si/Al_f ratios calculated for the Ga/H-MFI samples were however, slightly lower than those predicted with the presence of 13-15% EFAl, and may reflect contributions

from Si-OH groups which exhibit bands that overlap with those for Q(3Si, 1Al) and Q(3Si, 2Al) sites. This hypothesis was confirmed by performing ^{1}H-^{29}Si CP MAS NMR spectra (not shown) that revealed a strong enhancement in signal intensity around -103 ppm, corresponding to Q(3Si, OH) sites. Still, the intensity of the infrared Si-OH band (Figure 2.4.2-1a) remains constant upon Ga^{3+} exchange up to Ga/Al ratios of 0.3. Therefore, the contribution of Si-OH groups to the ^{29}Si MAS NMR signal intensity should remain constant (up to Ga/Al ratios of 0.3). As a consequence, any additional EFAl species generated during Ga^{3+} exchange protocols should result in a systematic increase in Si/Al_f values with an increase in Ga content. Such a trend is not observed with the Si/Al_f ratios presented in Table 2.7-2. This leads us to conclude that within uncertainty (10-15%), our Ga^{3+} exchange protocols do not cause the further dealumination of the zeolite framework.

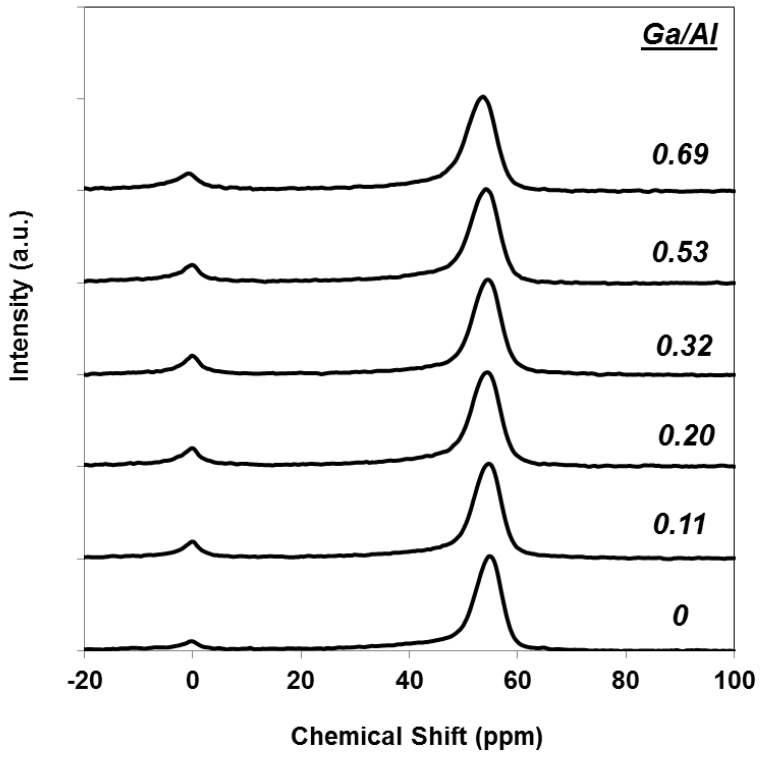

Figure 2.7-3. ^{27}Al MAS NMR spectra of H-MFI and Ga-MFI samples with Ga/Al ranging from 0.1 to 0.69 at ambient temperatures. Samples were hydrated in a dessicator containing H_2O for 24h prior to spectral measurements. All chemical shifts were referenced to $Al(NO_3)_{3\ (aq)}$ at 0ppm.

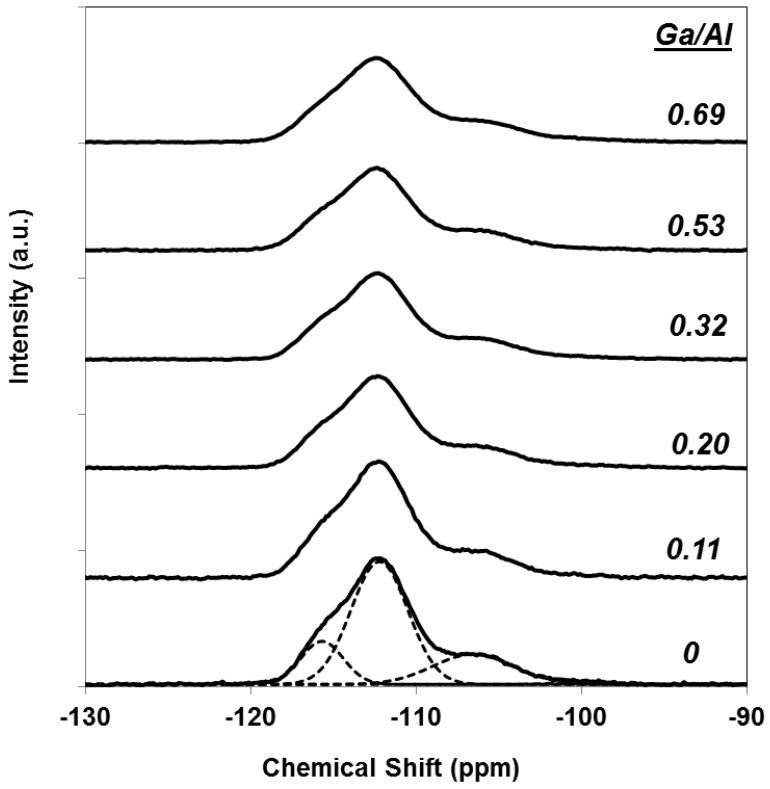

Figure 2.7-4. ^{29}Si MAS NMR spectra (solid lines) of H-MFI and Ga-MFI samples with Ga/Al ranging from 0.1 to 0.69 at ambient temperatures. Spectra were deconvoluted using Gaussian peaks (dotted lines).[68] All chemical shifts were referenced to tetramethylsilane (TMS) at 0ppm

Table 2.7-2. Ratios of octahedral to tetrahedral Al centers Al_{oct}/Al_{tet} estimated from ^{27}Al MAS NMR spectra and framework Si/Al_f ratios[d] estimated from ^{29}Si MAS NMR spectra of H-MFI[c] and Ga/H-MFI samples[c].

Sample	Al_{oct}/Al_{tet}[a]	Si/Al_f[b]
H-MFI	0.04	16.8
Ga/Al		
0.1	0.10	17.7
0.2	0.12	15.7
0.3	0.12	15.0
0.5	0.10	15.8
0.7	0.11	14.5

[a] Fraction of octahedral Al centers Al_{oct}/Al_{tet} ratios determined via integration of ^{27}Al MAS NMR spectral bands at 0 ppm (octahedral Al) and at 56 ppm (tetrahedral Al)

[b] Framework Si/Al_f ratios determined by Gaussian deconvolution and peak integration[68] of ^{29}Si MAS NMR spectra

[c] Samples were hydrated in an H_2O containing dessicator for 24 h prior to MAS NMR measurements

2.7.4 Optimized geometries of lowest Gibbs free energy configurations of Ga^{3+} structures on cation-exchange sites associated with NNN and NNNN proximate framework Al atoms, derived using QM/MM methods (see theoretical methods section 2.3.3)

For clarity, only the atoms in the QM region are shown.
Color key for atoms:

Si Al Ga O H

(1) Single cation-exchange site associated with isolated framework Al atom

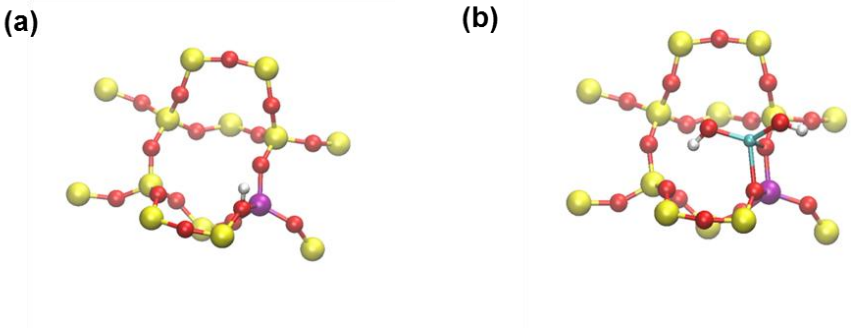

Figure 2.7-5. (a) Isolated Brønsted O-H group (b) Isolated $[Ga(OH)_2]^+$ cation

(2) Proximate cation-exchange sites associated with NNNN framework Al atoms

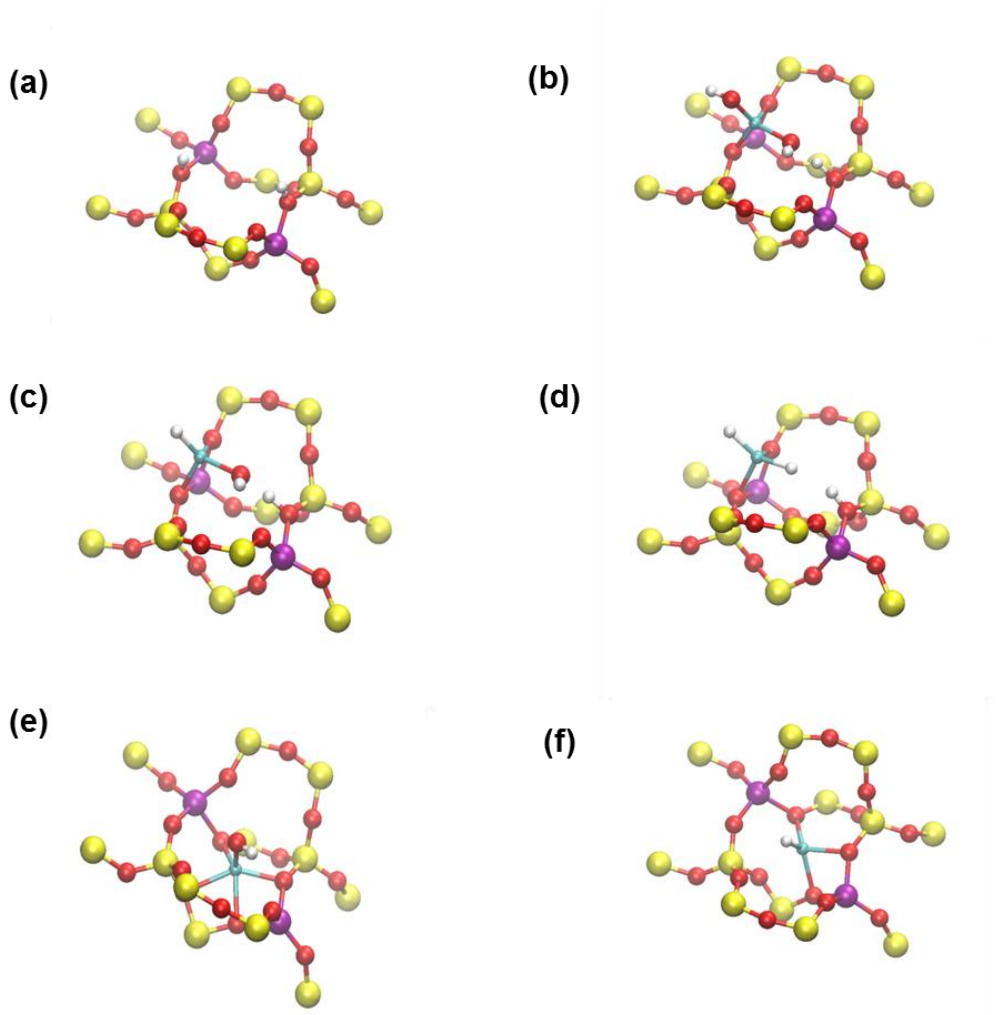

Figure 2.7-6. (a) Proximate NNNN Brønsted O-H groups (b) $[Ga(OH)_2]^+$-H^+ cation pairs (c) $[Ga(OH)H]^+$-H^+ cation pairs (d) $[GaH_2]^+$-H^+ cation pairs (e) $[Ga(OH)]^{2+}$ cation (f) $[GaH]^{2+}$ cation on proximate cation-exchange sites associated with NNNN framework Al atoms.

(3) Proximate cation-exchange sites associated with NNN framework Al atoms

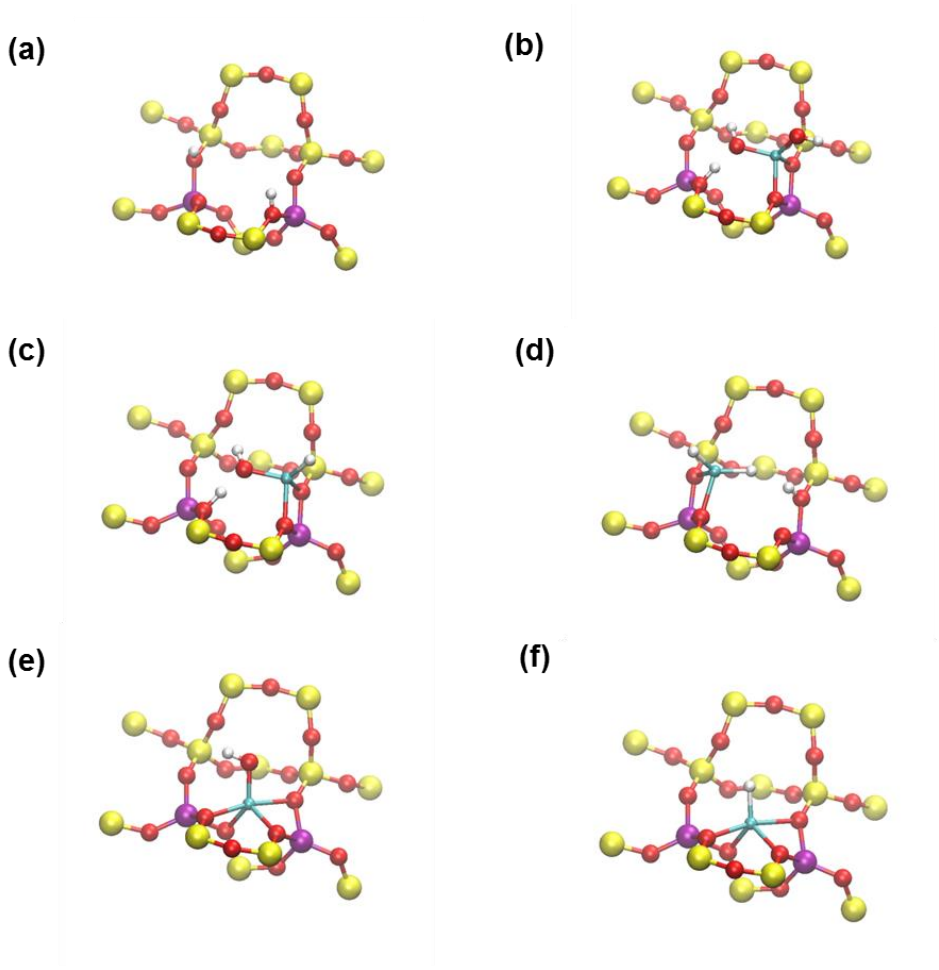

Figure 2.7-7. (a) Proximate NNN Brønsted O-H groups (b) $[Ga(OH)_2]^+$-H^+ cation pairs (c) $[Ga(OH)H]^+$-H^+ cation pairs (d) $[GaH_2]^+$-H^+ cation pairs (e) $[Ga(OH)]^{2+}$ cation (f) $[GaH]^{2+}$ cation on proximate cation-exchange sites associated with NNN framework Al atoms.

Table 2.7-3. Partial charge calculations predicted using Natural Bond Orbital (NBO) Analysis of QM/MM Structures for Ga centers associated with most stable free energy configurations of sites investigated. For Ga, [core] = $[Ar]3d^{10}$

Structure	Natural charge	Natural electronic configuration
$[Ga(OH)_2]^+$-H^+	2.00632	[core] 4s(0.43) 4p(0.57) 6p(0.01)
$[Ga(OH)]^{2+}$	1.96944	[core] 4s(0.43) 4p(0.60) 6p(0.01)
$[Ga(OH)H]^+$-H^+	1.63388	[core] 4s(0.71) 4p(0.67)
$[GaH]^{2+}$	1.58811	[core] 4s(0.74) 4p(0.68) 5p(0.01)
$[GaH_2]^+$-H^+	1.27919	[core] 4s(0.87) 4p(0.87)

The calculations in Table 2.7-3 suggest that for Ga(+3) centers in all of the structures, successive replacement of Ga-bound OH or O ligands with -H ligands results in a decrease in the natural charge and a concomitant increase in electron density at the Ga^{3+} center.

2.7.5 EXAFS in k-space and EXAFS fits using 2 Ga-O shell model and $CaGa_2O_4$ as a reference.

EXAFS spectra (k^2-weighted) of Ga/H-MFI samples and β-Ga_2O_3 were background corrected, normalized and Fourier transformed (FT) from k-space spectra (Figure 2.7-8) using the Athena and Artemis softwares.[70] The first coordination shell (1 - 2 Å) of the FT-spectra of Ga/H-MFI samples was fit (between k=2-14 $Å^{-1}$) to a model consisting of 2 Ga-O_i (i = 1,2) shells. The degeneracy (coordination number, N_i) and interatomic distance (R_i) of each shell was allowed to vary during the fit. A common energy shift parameter (E_0) and Debye-Waller factor (σ^2) were applied to both shells and were allowed to vary during the fit. The amplitude reduction factor S_0^2 was fixed at a value of 0.94. This value was obtained by fitting the first-coordination shell of the FT-EXAFS spectrum of β-Ga_2O_3. Wavenumber-dependent phase shift and amplitude functions (δ(k) and f(k), respectively) were obtained from the crystal structure of $CaGa_2O_4$, which contains Ga^{3+} in tetrahedral coordination with O atoms with a Ga-O interatomic distance of 1.86 Å.[71] EXAFS fits were performed using the Artemis software[70] using fixed k and R-space ranges, the quality of the fit was assessed on the basis of the EXAFS R-factor, which gauges the extent of mismatch between the data and the fit.[99] Fits with R-factor values less than 0.05 were considered to be satisfactory.[99]

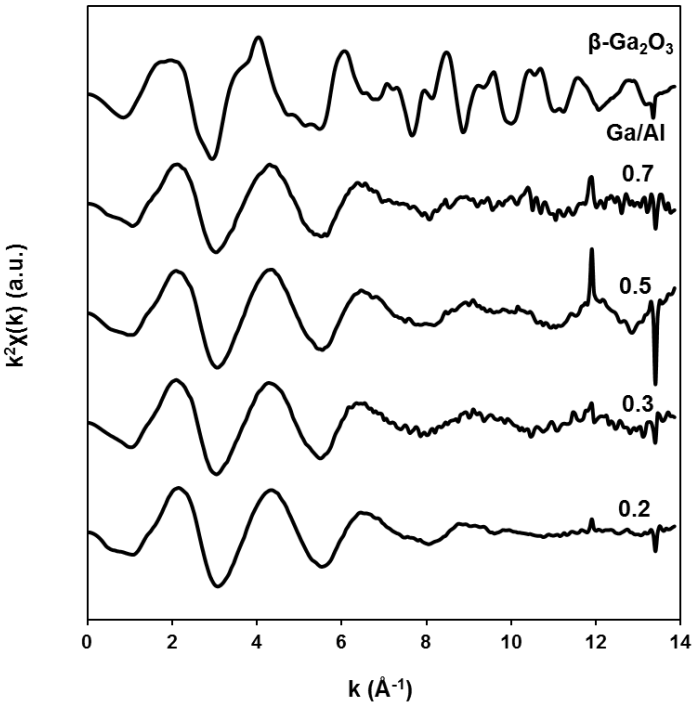

Figure 2.7-8. k^2-weighted Ga-K edge EXAFS spectra ($k^2\chi(k)$) of β-Ga_2O_3 measured at ambient temperature and of Ga/H-MFI samples (Ga/Al =0.2 - 0.7), measured at 773 K under 20% O_2/He.

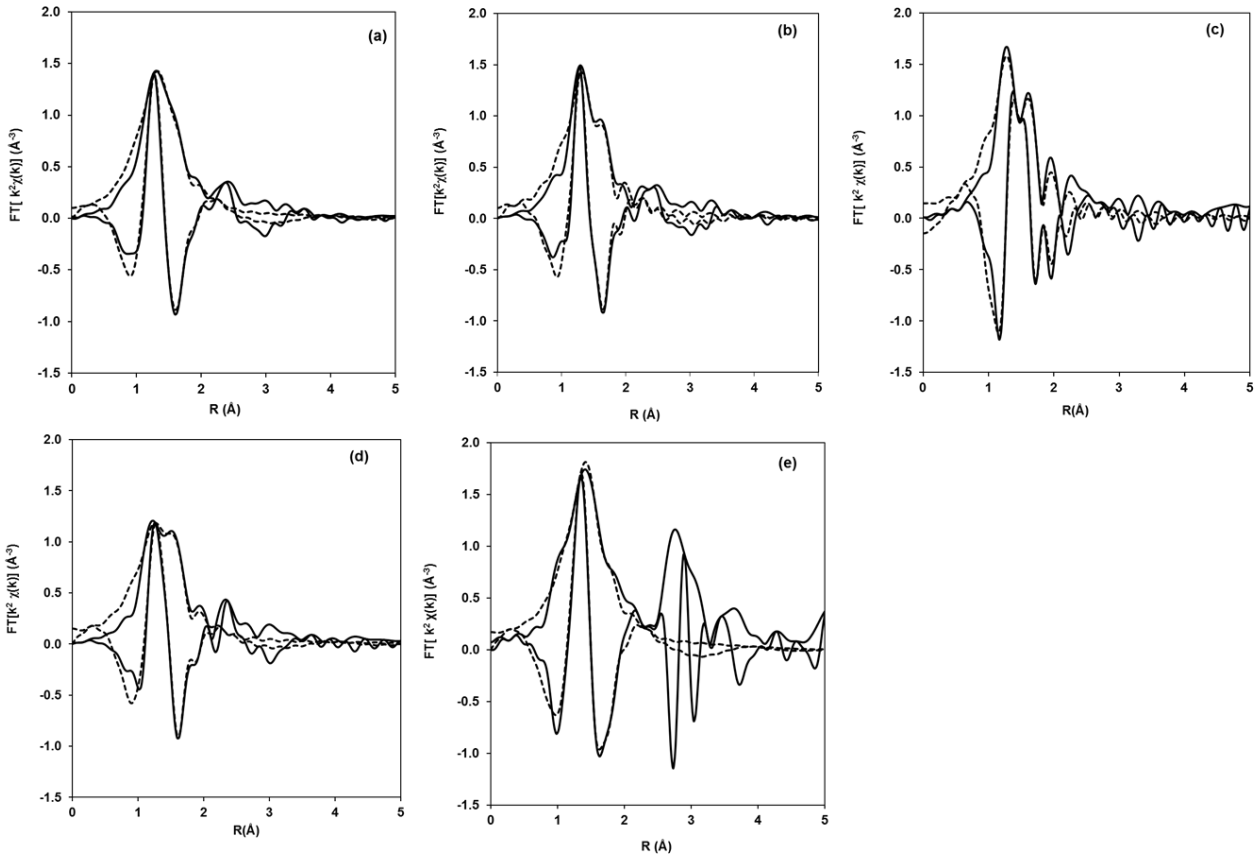

Figure 2.7-9. Magnitude and imaginary parts of Fourier-transformed k^2-weighted EXAFS spectra of Ga/H-MFI samples collected at 773K under flowing 20%O_2/He (solid lines) and first coordination shell fits (dotted lines); Fitted parameters for (a)-(e) are shown in Table 5.
(a) Ga/Al = 0.2 (b) Ga/Al =0.3 (c) Ga/Al=0.5 (d) Ga/Al=0.7 (e) β-Ga_2O

2.7.6 Simulation of EXAFS spectra and wavelet transforms using DFT-derived Ga^{3+} structures

To understand the effect of different backscattering atoms on wavelet transforms, the DFT-simulated cationic structure for the $[Ga(OH)_2]^+$ cation was used as an inputs to the FEFF9 software [117] to generate simulated χ(k) EXAFS and the latter was subjected to wavelet analysis. In addition, the experimentally measured EXAFS spectrum of β-Ga_2O_3 was also subjected to wavelet analysis. For the EXAFS simulations, the amplitude reduction factor S_0^2 was set to a value of 0.94, obtained from a fit to experimental EXAFS data for β-Ga_2O_3. A global Debye-Waller factor of 0.004Å^2 was applied to all scattering paths in order to simulate the amplitude decay of the EXAFS signal with increasing k, partially an effect of structural and thermal disorder. The resulting EXAFS spectra were then used as inputs to the HAMA software [72] in order to calculate wavelet transforms. EXAFS spectra were k^2-weighted prior to wavelet transformation in order to equally emphasize the contributions of heavier Ga^{3+} atoms in the second coordination shell, if present. A higher power k^3 weighting was also applied but wavelet transforms calculated in this manner for experimental Ga/H-MFI spectra were found to exhibit

poorer resolution owing to a higher weighting of the EXAFS signal at higher k values, at which noise is inherently present. The Morlet wavelet function was used with the κσ parameter product set to 15 for all spectra. At κσ values > 10, the R-space values of the wavelet transform asymptotically approach the R-space values of the Fourier transform.[72] Setting κσ values to 15 therefore, enables peaks observed in the Fourier transform to be directly correlated in R-space with features in the wavelet transform. The resolution of the Morlet wavelet transform, dictated by uncertainty cells, increases in R-space, but decreases in k-space for large values of κσ.[72 118] In general however, for larger R-space values, the resolution of the wavelet transform decreases in R-space, but increases in k-space.[118] At the larger R-space values (> 2Å) of interest for the second coordination shell, reasonable resolution of the wavelet features in both R and k-spaces for a κσ value of 15 is expected. The wavelet transform of β-Ga_2O_3 (experimental EXAFS spectra) and the simulated wavelet transform of the $[Ga(OH)_2]^+$ cation, are shown in Figure 2.4.2-5. Wavelet transforms for EXAFS spectra of Ga/H-MFI samples (measured at 773K under 20% O_2), are shown in Figures 2.4.2-6.

2.7.7 Thermodynamic phase diagrams computed at fixed H_2O partial pressures

1) Proximate cation-exchange sites associated with NNN framework Al atoms

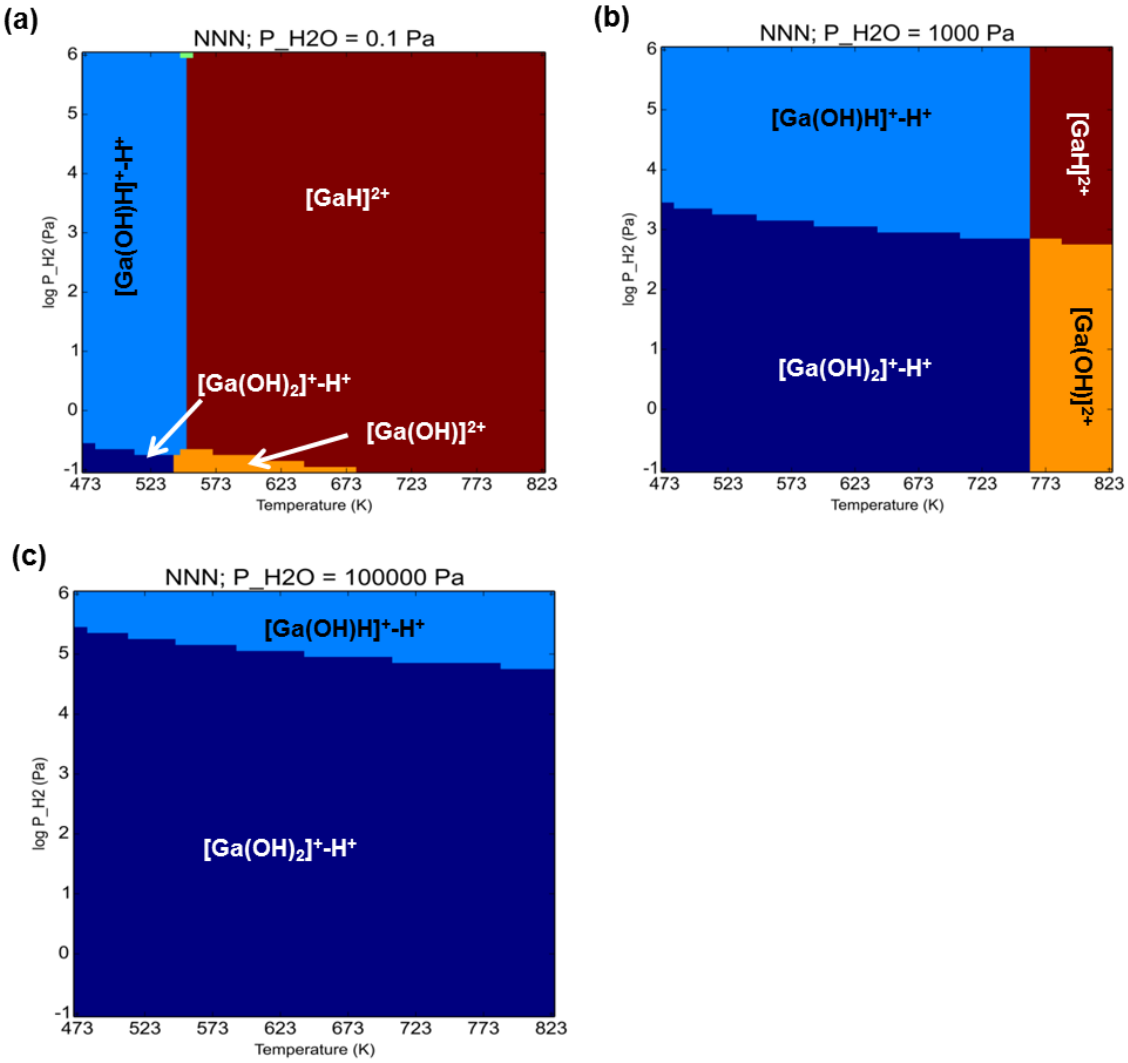

Figure 2.7-10. Phase diagrams for Ga^{3+} structures on proximate-cation sites associated with NNN framework Al atoms, as a function of temperature, H_2 and H_2O partial pressure. Regions of stability reflect minima in Gibbs free energies of formation of structures from $[Ga(OH)_2]^+$-H^+ cation pairs. H_2O partial pressure: (a) 10^{-1} Pa (b) 10^3 Pa (c) 10^5 Pa

2) Proximate cation-exchange sites associated with NNNN framework Al atoms

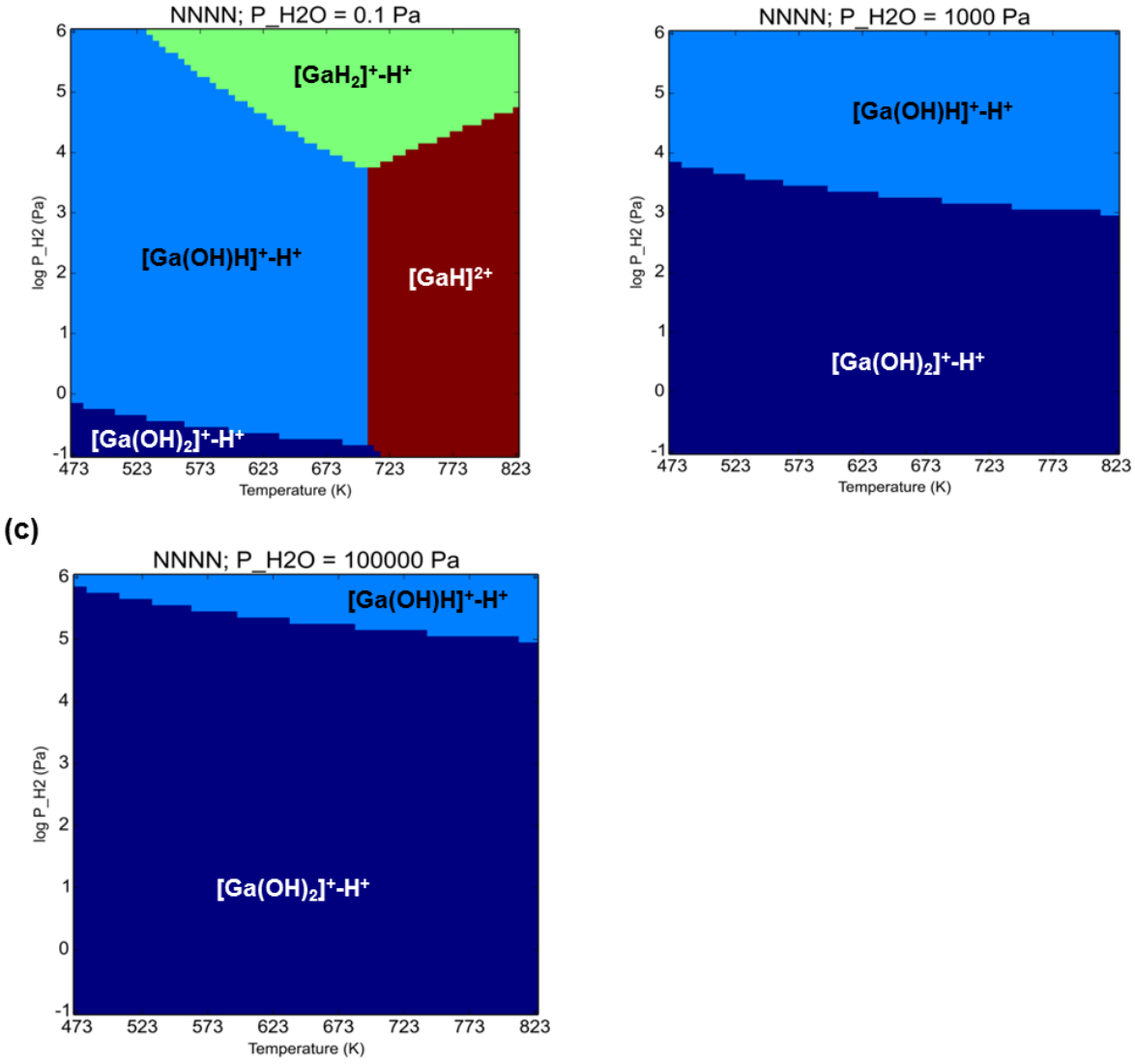

Figure 2.7-11. Phase diagrams for Ga^{3+} structures on proximate-cation sites associated with NNNN framework Al atoms, as a function of temperature, H_2 and H_2O partial pressure. Regions of stability reflect minima in Gibbs free energies of formation of structures from $[Ga(OH)_2]^+$-H^+ cation pairs. H_2O partial pressure: (a) 10^{-1} Pa (b) 10^3 Pa (c) 10^5 Pa

2.7.8 EXAFS analysis of H_2-treated Ga/H-MFI samples at 723K

Fourier analysis of EXAFS of H_2-treated Ga/H-MFI samples was performed using a procedure similar to that used to fit EXAFS of oxidized Ga/H-MFI samples, described in the methods section of the main manuscript. The $CaGa_2O_4$ reference was used to generate a 2 Ga-O shell model which was then used in the Artemis software[70] for fits to the first coordination shell of Fourier-transformed EXAFS. Fitted parameters are summarized in Table 2.7-4 and show a total Ga-O coordination of between 2 and 3. This reduction in coordination with O atoms from 4 in oxidized Ga^{3+} structures to values between 2 and 3 is consistent with a replacement of –OH and O ligands in oxidized structures with –H ligands in reduced structures upon H_2 treatment.

Table 2.7-4. Fitted coordination numbers, interatomic distances, Debye-Waller factors, energy shift parameters and R-factor values for fits to Fourier-transformed EXAFS of H_2-treated Ga/H-MFI samples at 723 K under flowing 3% H_2/He. Fits were performed using $CaGa_2O_4$ as a model structure.

Ga/Al[a]	Ga-O shell[b]	$N^c_{(i)}$	Total N	$R^d_{(i)}$ (Å)	$\sigma^{2\,e}$ (10^{-3} Å^2)	$\Delta E_0{}^f$ (eV)	R-factor (10^{-2})
0.2	$Ga\text{-}O_1$	1.1	2.5	1.74	4.0	1.7	0.5
	$Ga\text{-}O_2$	1.4		1.89			
0.3	$Ga\text{-}O_1$	0.8	1.7	1.76	1.0	3.0	1.0
	$Ga\text{-}O_2$	0.9		1.92			
0.5	$Ga\text{-}O_1$	1.0	2.3	1.72	1.0	0.8	1.0
	$Ga\text{-}O_2$	1.3		1.89			
0.7	$Ga\text{-}O_1$	1.0	2.3	1.69	0.5	-2.0	2.3
	$Ga\text{-}O_2$	1.3		1.89			

[a] EXAFS spectra, obtained after normalization and background subtraction, were k^2-weighted, a Hanning window function was applied between k = 2-14 Å^{-1} and first shell fits were performed from R = 1-2.1 Å. $S_0{}^2$ values were determined to be 0.94, by fitting experimental EXAFS spectra of β-Ga_2O_3 to Ga-O shells generated using the crystal structure of β-Ga_2O_3[103] in FEFF.

[b] Two Ga-O shells were generated in FEFF using the crystal structure of $CaGa_2O_4$, which was obtained from the literature.[71]

[c] Coordination numbers (N_i where i =1-2) for each shell were determined with a ± 0.60 uncertainty.

[d] Ga-O interatomic distances (R_i where i = 1-2) for each shell were determined with a ± 0.04Å uncertainty.

[e] Debye-Waller factors (σ^2) were held same for each shell.

[f] Energy shift parameters (E_0) were determined with a ±2 eV uncertainty.

Chapter 3

3 Mechanism and kinetics of propane dehydrogenation and cracking over Ga/H-MFI prepared via vapor-phase exchange of H-MFI with $GaCl_3$

As of the writing of this dissertation, the manuscript that this work is adapted from has been accepted for publication by the Journal of American Chemical Society (JACS) (DOI: 10.1021/jacs.8b11443*). This work was originally coauthored with Erum Mansoor, Matthieu Bondil, Martin Head-Gordon and Alexis T. Bell. These individuals have approved the inclusion of this work in this dissertation.*

3.1 Abstract

In this study, the mechanism and kinetics of C_3H_8 dehydrogenation and cracking are examined over Ga/H-MFI catalysts prepared via vapor-phase exchange of H-MFI with $GaCl_3$. The present study demonstrates that $[GaH]^{2+}$ cations are the active centers for C_3H_8 dehydrogenation and cracking, independent of the Ga/Al ratio. For identical reaction conditions, $[GaH]^{2+}$ cations in Ga/H-MFI exhibit a turnover frequency for C_3H_8 dehydrogenation that is two orders of magnitude higher and for C_3H_8 cracking that is one order of magnitude higher than the corresponding turnover frequencies over H-MFI. C_3H_8 dehydrogenation and cracking exhibit first-order kinetics with respect to C_3H_8 over H-MFI but both reactions exhibit first-order kinetics over Ga/H-MFI only at very low C_3H_8 partial pressures and zero-order kinetics at higher C_3H_8 partial pressures. H_2 inhibits both reactions over Ga/H-MFI. It is also found that the ratio of the rates of dehydrogenation to cracking over Ga/H-MFI is independent of C_3H_8 and H_2 partial pressures but weakly dependent on temperature. Measured activation enthalpies together with theoretical analysis are consistent with a mechanism in which both the dehydrogenation and cracking of C_3H_8 proceed over Ga/H-MFI via reversible, heterolytic dissociation of C_3H_8 at $[GaH]^{2+}$ sites to form $[C_3H_7\text{-}GaH]^{+}\text{-}H^{+}$ cation pairs. The rate-determining step for dehydrogenation is the β-hydride elimination of C_3H_6 and H_2 from the C_3H_7 fragment. The rate-determining step for cracking is C-C bond attack of the same propyl fragment by the proximal Brønsted acid O-H group.H_2 inhibits both dehydrogenation and cracking over Ga/H-MFI via reaction with $[GaH]^{2+}$ cations to form $[GaH_2]^{+}\text{-}H^{+}$ cation pairs.

3.2 Introduction

The increasing availability of large shale gas reserves in the US and across the world, has stimulated interest in finding routes for the catalytic conversion of the condensable components of shale gas components, principally ethane and propane, to alkenes and aromatics via dehydrogenation and dehydrocylization, respectively.[1,2,119–121] Commercially implemented processes[122] include the Oleflex and Catofin processes for dehydrogenation which utilize

alumina-supported catalysts and also the Cyclar and Aroforming Processes which use metal-modified zeolite catalysts for dehydroaromatization. Gallium-exchanged H-MFI zeolite (Ga/H-MFI) has been shown to be particularly effective for catalyzing dehydroaromatization reactions.[27,32,43,60,121,123] For example, the reaction of C_3H_8 over Ga/H-MFI produces higher selectivities to alkenes and aromatics than those observed over unmodified H-MFI.[27,124] This has led to a renewed interest in studying the structure and catalytic role of Ga species in Ga/H-MFI, as active sites for light alkane conversion.[22,33,36,62,108,125–129]

The chemical structure and catalytic function of Ga cations in Ga/H-MFI have been examined both experimentally and theoretically.[29] These studies suggest that in the oxidized or reduced state, the following types of species may exist in Ga/H-MFI: $[GaO]^+$, $[Ga_2O_2]^+$, $[Ga(OH)]^{2+}$, $[Ga(OH)_2]^+$, $[GaH_2]^+$, $[GaH]^{2+}$, Ga^+ and GaO_x clusters.[32,35,37–40,47,130–132] It should be noted that with the exception of Ga^+, the oxidation state of Ga in all of the other proposed structures is +3. Earlier studies of light alkane dehydrogenation on Ga/H-MFI have reported that oxygen-ligated species, such as monomeric $[GaO]^+$ or dimeric $[Ga_2O_2]^{2+}$ cations are more active than reduced Ga^+ cations.[37,39,40,132] However, contemporaneous studies as well as more recent ones have suggested that Ga^+ cations are the active centers for alkane dehydrogenation.[27,32,35–37,61,109] A variant of this idea has also been recently proposed, namely that Ga^+ cations in proximity to Brønsted acid O-H groups catalyze C_3H_8 dehydrogenation via oxidative addition of H^+ to Ga^+ to form a highly Lewis acidic $[GaH]^{2+}$ species in which the Ga^{3+} center has an oxidation state of +3.[22] The role of $[GaH]^{2+}$ cations as the active center for alkane dehydrogenation has also been supported by theoretical studies. These studies show that divalent $[GaH]^{2+}$ cations, located at proximate cation-exchange sites in Ga/H-MFI are more active for light alkane dehydrogenation than monovalent $[GaH_2]^+$ cations or Ga^+ cations.[22,47–49]

While a number of authors have proposed that Ga^+ cations are active for the dehydrogenation of light alkanes,[27,32,35–37,54,61,109] the presence of Ga^+ cations in H_2-reduced Ga/H-MFI has been disputed. Recent work by Getsoian et al. has called into question the interpretation of XANES evidence for Ga^+ cations.[33] These authors note that the decreases in the Ga K-edge XANES edge energy of Ga/H-MFI upon reduction, previously ascribed to formation of Ga^+,[27,32] can be ascribed, instead, to the formation of Ga-alkyl or GaH_x species, in which Ga has a formal oxidation state of +3.[33] Theoretical studies have also shown that the activation barrier for the formation of Ga^+ species in Ga/H-MFI is considerably higher than that for the formation of GaH_x species in which the Ga center has a formal oxidation state of +3.[49,50]

A further issue complicating the identification of the catalytically active species in Ga/H-MFI is the synthetic protocol typically employed for the preparation of Ga/H-MFI – incipient wetness impregnation of H-MFI with an aqueous solution of a Ga salt, most notably $Ga(NO_3)_3$.[41] Steric and electronic constraints associated with large aqueous Ga^{3+} complexes result in a slow diffusion of Ga into the MFI micropores leading to low levels of ion-exchange and the deposition of GaO_x agglomerates at the external surfaces of the zeolite crystal.[29,42] Upon contact with H_2 or alkane reactants at reaction temperatures (> 700 K), ion-exchange has been reported to occur via conversion of GaO_x into volatile Ga_2O monomers.[32] However, the resulting materials have been reported to still contain detectable concentrations of GaO_x.[42] The presence of neutral GaO_x together with ion-exchanged Ga^{3+} cations in Ga/H-MFI prepared via the conventional protocol has precluded accurate determination of the active Ga structures and their catalytic role in light alkane dehydrogenation and dehydroaromatization.

We report here a detailed study of the mechanism and kinetics of C_3H_8 dehydrogenation and cracking over Ga/H-MFI with Ga/Al ratios of 0.05 to 0.3. These catalysts were prepared by

reaction of the Brønsted acid O-H groups in H-MFI with $GaCl_3$ vapor under anhydrous conditions at elevated temperature, followed by stoichiometric removal of Ga-bound Cl by H_2 reduction, resulting in the formation of GaH_x (x = 1, 2) structures. Detailed characterization of these samples shows that for Ga/Al ratios below 0.3, and upon reduction under anhydrous conditions, all of the Ga is present as isolated $[GaH]^{2+}$ cations or as $[GaH_2]^+$-H^+ cation pairs; neutral GaO_x agglomerates are undetectable in these samples.[133] Both types of cationic species are associated with proximate cation-exchange sites associated with NNN (Next-nearest neighboring i.e separated by a –O-Si-O linkage) or NNNN (Next, next-nearest neighboring i.e separated by a –O-Si-O-Si-O linkage) pairs of framework Al atoms. Our investigations show that C_3H_8 dehydrogenation over these samples of Ga/H-MFI occurs primarily over $[GaH]^{2+}$ cations, independent of the Ga/Al ratio, at a rate (per Al_{tot} atom) that is two orders of magnitude higher than that occurring over isolated Brønsted acid O-H groups located in H-MFI, under identical reaction conditions. The rate of C_3H_8 cracking to CH_4 and C_2H_4 over Ga/H-MFI is an order of magnitude higher than that over H-MFI and also occurs over $[GaH]^{2+}$ sites. While both cracking and dehydrogenation exhibit first-order dependences on C_3H_8 partial pressure over H-MFI, the rates of both reactions exhibit a Langmuir-Hinshelwood dependence on C_3H_8 over Ga/H-MFI and are inhibited by H_2. Over H-MFI, both the dehydrogenation and cracking of C_3H_8 occur over Brønsted acid O-H groups. In the case of Ga/H-MFI, examination of alternative reaction pathways via experiment and theory suggests that both reactions occur preferentially on $[GaH]^{2+}$ sites via mechanisms involving C_3H_8 derived $[C_3H_7\text{-}GaH]^+$ intermediates. Inhibition of both reactions by H_2 is proposed to occur via the formation of $[GaH_2]^+$-H^+ cation pairs.

3.3 Experimental and theoretical methods

3.3.1 Preparation of H-MFI and Ga/H-MFI

NH_4 -MFI (Zeolyst, CBV 3024E) was converted to the H-form by heating it at 2 K min^{-1} to 773 K in dry synthetic air (Praxair, ultrazero, 100 cm^3 min^{-1}) and then holding it at this temperature for 4 h. The Si/Al_{tot} ratio of this sample is 16.5 ± 1.0, as determined by ICP-OES (Galbraith Laboratories, Knoxville, TN). Ga/H-MFI samples with varying Ga/Al ratios (0.05-0.5) were prepared via anhydrous exchange of dehydrated H-MFI with $GaCl_3$ vapor, using a protocol developed by our group. A detailed discussion of the preparation and characterization of these samples is given in Ref. 133.[133]

3.3.2 Reaction rate measurements

Reaction rates for C_3H_8 conversion over H-MFI and Ga/H-MFI were measured using a tubular quartz plug flow reactor. Catalyst samples (~5-12 mg) were placed over a quartz wool plug, fitted inside the reactor (30.5 cm in length and 0.64 cm in outer diameter). Catalyst charges less than 8 mg were diluted with SiO_2 (Silia Flash 150A). The reactor was heated by means of a ceramic cylindrical furnace. The temperature of the catalyst bed was measured by a K-type thermocouple (Omega) connected to a temperature controller (Omega), to maintain the catalyst temperature. Gases were metered into the reactor by means of mass flow controllers (MFC) (Porter), which were calibrated using a bubble flow meter. Prior to making rate measurements, samples were heated at 2 K min^{-1} from ambient temperatures to 773 K under flowing dry synthetic air (Praxair, ultrazero, 100 cm^3 min^{-1}) and held at this temperature for 1 h. This

oxidative pre-treatment was used for H-MFI and Ga/H-MFI. Reductive pre-treatment of Ga/H-MFI was carried out by purging the system with He following the oxidative treatment at 773 K and then switching the reactor feed to a gas mixture of 2.5% H_2 diluted in He (Praxair, CSG, 100 cm^3 min^{-1}). Samples were held at this temperature under H_2 for 1 h.

Following either oxidative or reductive pre-treatments, samples were exposed to flowing mixtures of C_3H_8/He prepared by diluting a 20% C_3H_8/He stream (Praxair, CSG) with He (Praxair, UHP) in order to generate C_3H_8 partial pressures ranging from 0.25-11 kPa. Experiments involving co-fed H_2 were conducted by adding H_2 to the feed flow. For this purpose, a 2.5 % H_2/He stream (Praxair, CSG) was mixed with the C_3H_8/He stream in order to obtain H_2 partial pressures ranging from 0.25-1.5 kPa. The total pressure of the system was maintained at 101.32 kPa. He, H_2 and dry synthetic air were further purified by passing these gases through purifiers (VICI) in order to remove trace amounts of H_2O or hydrocarbons. Gas flow rates were varied (100-350 cm^3 min^{-1}) in order to measure catalyst activity at different space times (defined as mol Al_{tot}*s/mol C_3H_8) for a given C_3H_8/H_2/He feed composition. A heated line connected to the outlet of the reactor was used to transfer reactants and reaction products to a gas chromatograph (GC) (Agilent 7890A). The reactor effluent present in a sample loop was injected periodically into the GC. Reactants and products were separated by a capillary column (Agilent 1909IP-Q02, 25 m X 350 μm X 10 μm) and were detected by means of a flame ionization detector (FID). FID Response factors for hydrocarbons species were obtained by diluting a pre-calibrated gas mixture containing CH_4 , C_2H_6 , C_2H_4 , C_3H_8 , C_3H_6, C_4H_{10} , C_4H_8 with He to attain different concentrations of the component hydrocarbons. The response factors for C_6H_6 and C_7H_8 were determined by directly injecting known amounts of liquid C_6H_6 and C_7H_8 into the GC injector.

The conversion of C_3H_8 over H-MFI and Ga/H-MFI was measured at differential conversions (< 9 % C_3H_8 conversion) at temperatures between 718 K and 753 K. Plots of conversion vs space time were linear for each feed composition combination and extrapolated to zero conversion at zero space time, consistent with reactor operation under a differential conversion regime. Selectivities were defined on both a C-basis and C_3H_8 basis. C_3H_8 dehydrogenation rates were determined from C_3H_6 concentrations, while C_3H_8 cracking rates were determined from the concentrations of either CH_4 or C_2H_4 cracking products. When product selectivites were extrapolated to zero space time, cracking rates derived from CH_4 concentrations were similar to those determined from C_2H_4 concentrations. The C_3H_8 partial pressures (0.25 – 11 kPa) and H_2 partial pressures (0.25-1.5 kPa) were varied in a non-systematic fashion in order to examine the effects of reactant and product pressures on measured rates. For each combination of C_3H_8/H_2 partial pressures, rates were measured at four different space times. By this means, rates could be extrapolated linearly to 0 space time. Moreover, after measurements had been made at each C_3H_8/H_2 pressure combination, rates were measured at 0.9 kPa C_3H_8/He at a space time of 9 mol Al*s /mol C_3H_8 in order to assess and correct for catalyst deactivation. Catalyst deactivation did not exceed 5% in typical experiments. Activation enthalpies and entropies were extracted by relations (equations 3.7.5-8, 3.7.5-9 and 3.7.5-10 derived in section 3.7.5) derived from transition state theory.[134] For the application of these equations, rate coefficients (per Al_{tot} atom) were normalized by the fraction of $[GaH]^{2+}$ cations per Al_{tot} atom determined via NH_3-TPD measurements (details described in section 3.7.8) [133]

3.3.3 Theoretical methods

The hybrid Quantum Mechanics/Molecular Mechanics (QM/MM)[78,73] approach used in this work takes into account the impact of long-range dispersive interactions and the polarization of the active site by the electrostatic field associated with the zeolite lattice, both of which are critical to capturing reaction energetics accurately.[135] A T437 atom cluster is used to represent the zeolite framework surrounding the active site. The QM region consists of either a T5 or a T9 cluster representing the part of the zeolite associated with the extra-framework cation (H^+ or $[Ga(H)_n]^{(3-n)+}$) and any adsorbed species. The MM region is modeled with an improved parametrization;[74] framework Si and O atoms are fixed at their crystallographic positions. The framework Al atom associated with extraframework Ga cationic species is taken to be at the T12 site. This T site is located in the channel intersections of MFI.[136] Both the activities of Brønsted acid O-H groups and Lewis acidic $[GaH]^{2+}$ cations are investigated. As shown previously, only a small difference (2.6 kcal/mol) was found in the calculated barriers for C_2H_4 methylation over H-MFI calculated for both T5 and T20 clusters,[79] which suggests that our QM/MM approach is not influenced significantly by the size of the QM region used. An illustration of the model used for the $[GaH]^{2+}$ cation in this study is shown in Figure 3.7-8 and is discussed in more detail in earlier work.[49]

Stationary and saddle point searches were conducted at the ωB97X-D/6-31G** level of theory using the default optimization procedure available in QChem.[85] The reported activation energies were computed using the ωB97X-D functional[76] with the triple-ζ, split-valence Pople basis set, with diffuse and polarization functions 6-311++G(3df,3pd). While recent developments in DFT have led to functionals with statistically improved accuracy[137,138] relative to ωB97X-D, we note that the QM/MM parameters were developed specifically for that functional. Enthalpy and entropy calculations were performed using the Quasi Rigid Rotor Harmonic Oscillator (RRHO) approximation. We have used this approach successfully in previous studies to obtain activation enthalpies and entropies for n-C_4H_{10} reactions in H-MFI, yielding good agreement with experimental results.[139] For each mechanism examined, we determined the value of $\Delta G^{\ddagger}$ from the respective free energy surface using energetic span model proposed by Kozuch and Shaik.[140–143]

3.4 Results and Discussion

3.4.1 C_3H_8 conversion over H-MFI via monomolecular dehydrogenation and cracking

For times-on-stream < 100 min, the rate of C_3H_8 dehydrogenation over H-MFI decreased monotonically, before approaching a steady-state (see Figure 3.7-1). However, the rate of C_3H_8 cracking did not change appreciably with time on stream. These trends are similar to those reported for n-C_4H_{10} dehydrogenation and cracking over H-MFI.[11] The authors of that study proposed that the high initial rate of C_3H_8 dehydrogenation is attributable to Lewis acidic, extra-framework Al (EFAl) sites that deactivate during the first 100 min of reaction. All steady–state rates were therefore measured over H-MFI, after the deactivation period (~100 min).

The steady-state product molar ratios of H_2/C_3H_6 and C_2H_4/CH_4 during C_3H_8 conversion over H-MFI were close to unity, consistent with previous studies of C_3H_8 dehydrogenation and cracking over H-MFI.[11,25,144] As seen in Figure 3.4.1-1a and 3.4.1-1b, the rates of both dehydrogenation and cracking are first-order in C_3H_8 partial pressure, also in agreement with

previous reports for monomolecular dehydrogenation and cracking catalyzed by Brønsted acid O-H groups at low alkane partial pressures.[24,145]

Apparent first-order rate coefficients were measured at different temperatures (see Figure 3.7-2) and these data were used to determine apparent activation enthalpies (ΔH_{app}) for C_3H_8 dehydrogenation and cracking. The experimentally measured apparent activation enthalpies for C_3H_8 dehydrogenation and cracking were found to be 40.6 ± 2.9 kcal/mol and 34.6 ± 3.8 kcal/mol, respectively (reported uncertainties reflect 95% confidence intervals). Both estimates are consistent with previous reported estimates of activation energies for C_3H_8 monomolecular dehydrogenation (22.7- 47.8 kcal/mol) and monomolecular cracking (35.1 -37.7 kcal/mol) over H-MFI.[25,144,146,147] We also obtained theoretical estimates of apparent activation enthalpies for these reactions occurring over isolated Brønsted acid O-H groups in H-MFI via QM/MM calculations. Apparent activation enthalpies estimated in this manner are 47.5 kcal/mol for methyl-C_3H_8 dehydrogenation, 35.3 kcal/mol for methylene-C_3H_8 dehydrogenation and 33.3 kcal/mol for C_3H_8 cracking. The activation enthalpy for methylene-C_3H_8 dehydrogenation is expected to be significantly lower than that for methyl C_3H_8- dehydrogenation, due to the higher stability of the secondary carbenium ion in the late dehydrogenation transition state of the former pathway relative to the primary carbenium formed in the late dehydrogenation transition state of the latter pathway. Consistent with this interpretation, our experimental measurements are in good agreement with theoretical predictions for methylene dehydrogenation and cracking. The transition state structures and free energy surfaces for these mechanisms are presented in Figures 3.7-13 and 3.7-14.

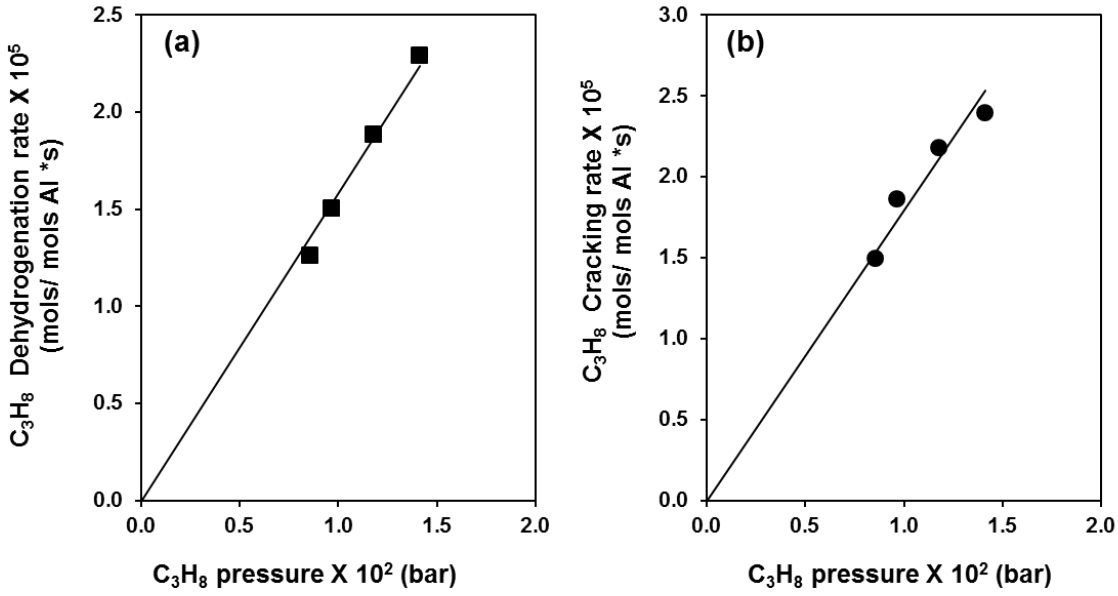

Figure 3.4.1-1. (a) Dependence of C_3H_8 dehydrogenation rates (per Al_{tot} atom) over H-MFI on C_3H_8 partial pressure at 733 K. (b) Dependence of C_3H_8 cracking rates (per Al_{tot} atom) over H-MFI at 733 K on C_3H_8 partial pressure at 733 K. Solid lines indicate regressed first-order slopes.

3.4.2 C_3H_8 conversion over oxidized and H_2-reduced Ga/H-MFI

Figure 3.4.2-1a shows the rates of C_3H_8 consumption at 733 K over Ga/H-MFI (Ga/Al = 0.2) under differential reaction conditions (C_3H_8 conversion < 9%). Following oxidative pre-treatment of Ga/H-MFI (at 773 K in flowing dry air for 1h), the rate of C_3H_8 consumption increases monotonically with time-on-stream for ~ 300 min before approaching a steady-state (red curve, Figure 3.4.2-1a). This slow induction period suggests that Ga species undergo structural transformation before reaching their steady-state structure. Also shown in Figure 3.4.2-1a, is the rate of C_3H_8 consumption as a function of time-on-stream for Ga/H-MFI (Ga/Al =0.2) reduced in 2.5% H_2/He for 1 h at 823 K prior to measurements of the reaction rate (blue curve, Figure 3.4.2-1a). In this case, no induction period is observed and the steady-state rate of C_3H_8 consumption is nearly identical to that measured for the oxidized sample.

Product selectivities (expressed as the fraction of converted carbon in each product) are shown as a function of time-on-stream in Figure 3.4.2-1b, for oxidized and H_2- reduced Ga/H-MFI. Throughout the duration of the experiment, the dominant product is C_3H_6, produced via C_3H_8 dehydrogenation. The selectivity to C_3H_6 does not change with time-on-stream or catalyst pre-treatment. The same is true for the selectivity to CH_4. For the oxidized sample, the selectivities to C_2H_4 and aromatics increase slightly as a function of time on stream, but approach the same values as that observed for the reduced sample. While C_2H_4 is formed as a primary product via cracking of C_3H_8, space time studies (see Section 3.7.3) indicate that C_2H_4 is also produced via secondary pathways at higher conversions. These experiments also show that aromatics are produced exclusively via secondary pathways which become increasingly prevalent at higher conversion. Therefore the concentrations of both C_2H_4 and aromatics are expected to increase as the rate of C_3H_8 consumption for oxidized Ga/H-MFI increases with time-on-stream. Thus, the product selectivity trends seen in Figure 3.4.2-1b suggest that similar active sites catalyze C_3H_8 dehydrogenation and cracking and that the concentration of these active sites increases with time-on-stream for oxidized Ga/H-MFI or upon pre-reduction of the catalyst in H_2.

The results presented in Figure 3.4.2-1, together with our earlier characterization work,[133] suggest that $[GaH]^{2+}$ cations and/or $[GaH_2]^{+}$-H^{+} cation pairs formed upon H_2 reduction of Ga/H-MFI are the active species for C_3H_8 dehydrogenation and cracking. We propose that during the induction period observed for oxidized Ga/H-MFI, $[Ga(OH)]^{2+}$ cations and $[Ga(OH)_2]^{+}$-H^{+} cation pairs undergo reduction to form $[GaH]^{2+}$ cations and $[GaH_2]^{+}$-H^{+} cation pairs.
As shown in Section 3.7.3, secondary reactions are prevalent even under conditions of differential conversion. We also show in Figure 3.7-4 and Section 3.7.3 that the rates of dehydrogenation and cracking over Ga/H-MFI are inhibited by H_2. To eliminate the effects of product inhibition and secondary reactions, all of the steady-state measured reaction rates reported in the balance of this study were extrapolated to zero space time (see Figure 3.7-4).

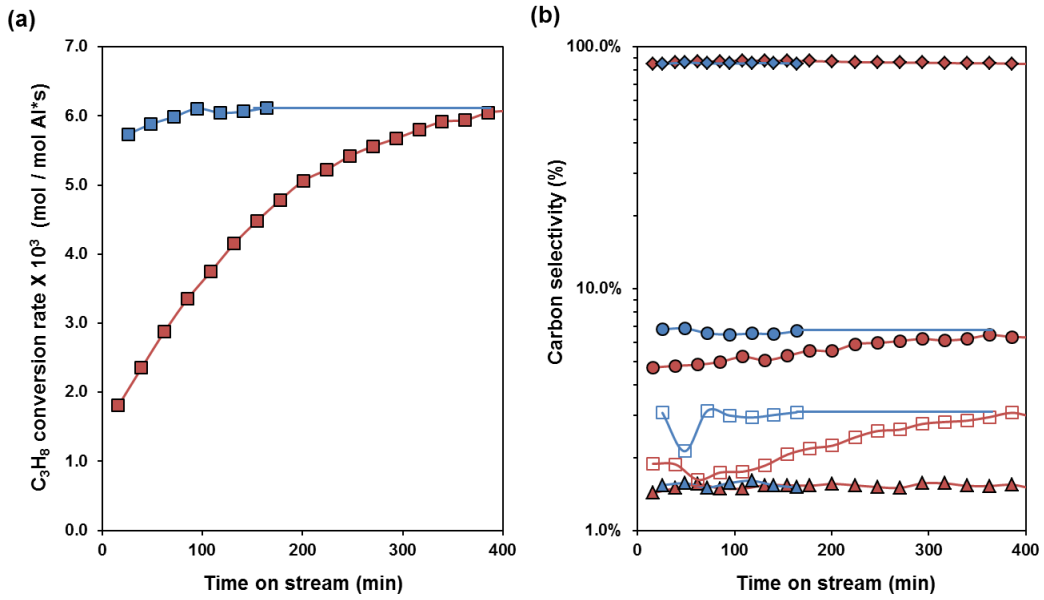

Figure 3.4.2-1. (a) C_3H_8 consumption rates (per Al_{tot} atom) and (b) Percent carbon selectivities for Ga/H-MFI (Ga/Al = 0.2) measured at 733 K with 0.9 kPa C_3H_8/He and τ = 9 (mol Al*s/mol C_3H_8) space time. Blue data points indicates Ga/H-MFI pre-treated in 2.5% H_2/He at 823 K for 1 h prior to reaction, while red data points indicates Ga/H-MFI pre-treated in synthetic dry air at 773 K for 1 h prior to reaction. In Figure 3.4.2-1b, diamonds indicate C_3H_6, circles indicate C_2H_4, open squares indicate aromatics, and triangles indicate CH_4 selectivities.

3.4.3 Effects of Ga content on the rates of C_3H_8 dehydrogenation and cracking over Ga/H-MFI

Figures 3.4.3-1a-c and 3.4.3-2a-c show C_3H_8 dehydrogenation and cracking rates, measured at 733 K and 0.9 kPa C_3H_8/He over H-MFI and Ga/H-MFI, as functions of the Ga/Al ratio. As observed in Figure 3.4.3-1a, the rate of C_3H_8 dehydrogenation (normalized per Al_{tot} atom), increases with Ga content up to a Ga/Al ratio of 0.1 but then reaches a plateau for higher values of Ga/Al ratio. At this plateau, the rate of C_3H_8 dehydrogenation is ~500 times higher than the corresponding rate over H-MFI, suggesting that the reactivity contribution of residual Brønsted acid O-H acid groups in Ga/H-MFI is negligible.

The rate of C_3H_8 dehydrogenation over Ga/H-MFI can also be normalized per Ga atom by dividing the rate per Al_{tot} by the Ga/Al_{tot} ratio. The rate of C_3H_8 dehydrogenation normalized this way, shown in Figure 3.4.3-1b, decreases monotonically as the Ga/Al ratio increases from 0.05 to 0.5, suggesting that the most active Ga species exist at the lowest Ga/Al ratios. As discussed earlier, our characterization of H_2-reduced Ga/H-MFI samples used in the present study shows that for Ga/Al $\leq$ 0.3, the dominant Ga species present are $[GaH]^{2+}$ cations and $[GaH_2]^+$-H^+ cations pairs, and that 100% of the Ga is present as $[GaH]^{2+}$ cations for Ga/Al = 0.1.[133] Moreover, the theoretical calculations supporting this work show that the formation of $[GaH]^{2+}$ cations is thermodynamically favored at NNN cation-exchange sites associated with pairs of framework Al atoms $\leq$ 5 Å apart. [133] Increasing the Ga/Al ratio results in the formation of $[GaH_2]^+$-H^+ cation pairs at NNN and NNNN cation-exchange sites associated with framework

Al-Al interatomic distances > 5 Å apart.[133] Our recent theoretical calculation have shown that $[GaH]^{2+}$ cations are more active for C_3H_8 dehydrogenation than $[GaH_2]^+$-H^+ cation pairs.[49] We also note in Figure 3.4.3-1a that the rate of dehydrogenation (per Al_{tot}) over the Ga/Al = 0.5 sample, which contains neutral GaO_x oligomeric species, in addition to cation-exchanged Ga^{3+} species, is identical to the corresponding rate (per Al_{tot}) over samples with lower Ga content. This suggests that neutral GaO_x species are much less active for C_3H_8 conversion in comparison to cation-exchanged Ga^{3+} species.

Based on the foregoing discussion, we normalized the rate of C_3H_8 dehydrogenation by the density of $[GaH]^{2+}$ cations per Al_{tot} measured for each Ga/Al ratio, measured via NH_3-TPD (see section 3.7.8 for the method by which the density of $[GaH]^{2+}$ cations was estimated).[133] Figure 3.4.3-1c shows that the rate of C_3H_8 dehydrogenation normalized this way is nearly independent of the Ga/Al ratio. It should be noted that the rate of C_3H_8 dehydrogenation per $[GaH]^{2+}$ for the Ga/Al = 0.05 sample is about 20% higher than that for the remaining samples, which may reflect small differences between the actual fraction of $[GaH]^{2+}$ cations present in the Ga/Al = 0.05 sample and our estimate. We therefore conclude that the rate of C_3H_8 dehydrogenation is approximately independent of the Ga/Al ratio. This finding supports the prediction that $[GaH]^{2+}$ cations are the most active species for C_3H_8 dehydrogenation and that $[GaH_2]^+$-H^+ cation pairs, which constitute an increasing fraction of the Ga content in Ga/H-MFI samples with Ga/Al > 0.1, do not to contribute appreciably to the measured rate.[36, 133]

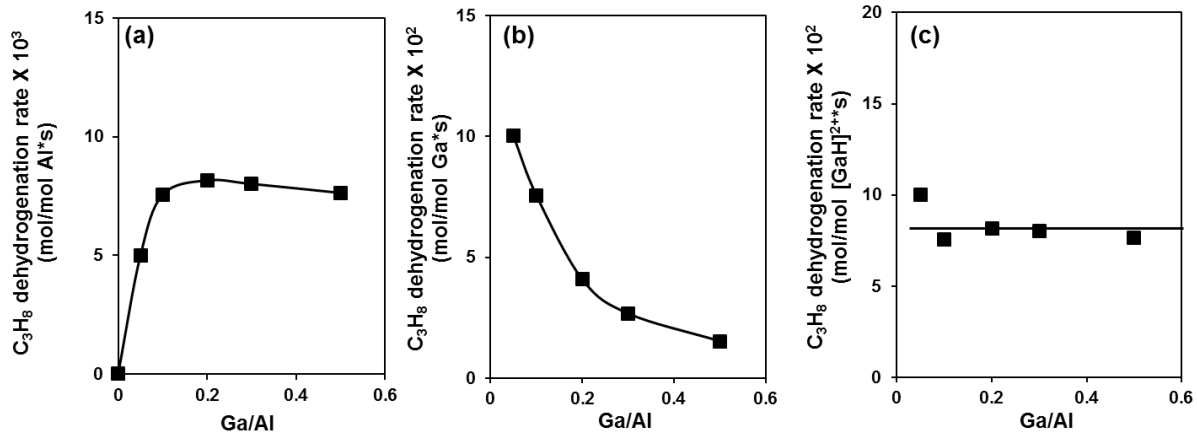

Figure 3.4.3-1. C_3H_8 dehydrogenation rates, measured at 0.9kPa C_3H_8/He and 733 K as a function of Ga/Al ratio, with rates over Ga/H-MFI extrapolated to zero space time. Conversions < 9% (a) Rates normalized per Al_{tot} atom (b) Rates normalized per Ga atom (c) Rates normalized per $[GaH]^{2+}$ estimated via NH_3-TPD.[133] Solid lines are guides for the eye.

Figures 3.4.3-2a-c show C_3H_8 cracking rates over H-MFI and Ga/H-MFI, also measured at 0.9 kPa C_3H_8 /He and 733 K. Here again, measured cracking rates over Ga/H-MFI were extrapolated to zero space time. The rate of C_3H_8 cracking normalized per Al_{tot} atom (Figure 3.4.3-2a) shows a trend similar to that of the rate of C_3H_8 dehydrogenation, increasing with Ga content up to a Ga/Al ratio of 0.1, and then reaching a plateau for higher Ga/Al ratios. At similar conditions, the maximum rate of C_3H_8 cracking over Ga/H-MFI (per Al_{tot} atom) is about 20 times higher than that over H-MFI.

It is notable that an enhancement in the rate of alkane cracking over Co, Zn and Ga-exchanged zeolites, relative to the corresponding H-forms of these zeolites, has been reported previously.[36,54,57,148,149] Alkane cracking over these metal-exchanged zeolites has been attributed to H_2-assisted alkane hydrogenolysis catalyzed by Ga sites[36,148,149] or to protolytic cracking of C-C bonds by residual Brønsted acid O-H groups,[54,61] the acid strength of which may be enhanced by proximity to exchanged metal cations.[150,151] Therefore, both of these possibilities need to be considered as possible causes for the higher rate of C_3H_8 cracking over Ga/H-MFI.

H_2-assisted hydrogenolysis of C_3H_8 would be expected to result in higher cracking rates with increasing H_2 concentration at higher space times (or C_3H_8 conversion) or upon co-feeding H_2. On the contrary, we find that the rate of C_3H_8 cracking decreases with an increase in C_3H_8 conversion and is inhibited by co-feeding H_2 (see Figure 3.7-4 and Section 3.4.2). These results suggest that hydrogenolysis does not contribute to C_3H_8 cracking over Ga/H-MFI. An alternative explanation is that the higher rate of C_3H_8 cracking over Ga/H-MFI compared to H-MFI could be attributable to an increase in the acid strength of Brønsted acid O-H groups that are proximate to metal cations (here, $[GaH_2]^+$ cations).[150,151] This phenomenon should lead to an increase in the rate of C_3H_8 cracking with an increase in the concentration of $[GaH_2]^+$-H^+ cation pairs as the Ga/Al ratio increases. However, cracking rates normalized per Al_{tot} atom do not increase with Ga content beyond a Ga/Al ratio of 0.1 (Figure 3.4.3-2a), while cracking rates normalized per Ga atom (Figure 3.4.3-2b) decrease monotonically with increasing Ga content. It is also notable, that when normalized by the estimated density of $[GaH]^{2+}$ cations per Al_{tot} (see section 3.7.8 for the method by which the density of $[GaH]^{2+}$ cations was estimated), the rate of C_3H_8 cracking is independent of the Ga/Al ratio, as can be seen in Figure 3.4.3-2c. Taken together, these data suggest that $[GaH]^{2+}$ cations rather than H_2-assisted hydrogenolysis by Ga sites or protolytic cracking by residual Brønsted acid O-H groups proximate to $[GaH_2]^+$ cations, are responsible for the observed enhancements in cracking rates over Ga/H-MFI. Further evidence in support of this conclusion is given below.

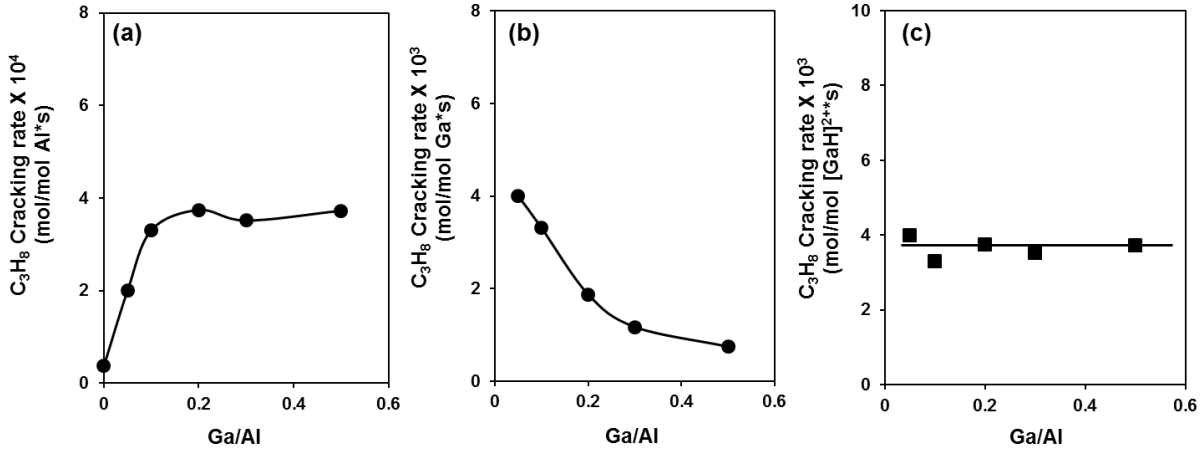

Figure 3.4.3-2. C_3H_8 cracking rates over H-MFI and Ga/H-MFI, measured at 0.9 kPa C_3H_8/He and 733 K. Rates over Ga/H-MFI were extrapolated to 0 space time. Conversions < 9% (a) Rates normalized per Al_{tot} atom (b) Rates normalized per Ga atom (c) Rates normalized per $[GaH]^{2+}$ estimated via NH_3-TPD measurements. Dotted lines are guides for the eye.

3.4.4 Effects of C_3H_8 and H_2 partial pressures on the rates of C_3H_8 dehydrogenation and cracking over Ga/H-MFI

The rates of C_3H_8 dehydrogenation and cracking (per Al_{tot} atom and extrapolated to zero space time) are shown in Figure 3.4.4-1a and b respectively as functions of C_3H_8 partial pressure and temperature. At all three temperatures (718, 733, 753 K), the rates of C_3H_8 dehydrogenation and cracking increase monotonically with C_3H_8 partial pressure at low partial pressures but become independent with respect to C_3H_8 partial pressure at higher pressures. Figure 3.4.4-1c shows the dependence of the ratio of the rate of dehydrogenation to cracking (D/C), as a function of the C_3H_8 partial pressure. For a given temperature, no discernable trend is evident in the D/C ratio as a function of C_3H_8 partial pressure, suggesting that the D/C ratio is approximately independent of the surface coverage of adsorbed C_3H_8. This observed trend suggests that both dehydrogenation and cracking proceed over similar active sites in Ga/H-MFI and via a common C_3H_8 derived reactive surface intermediate. However, the D/C ratio does exhibit a weak dependence on temperature, increasing from approximately 19.1 at 753K to approximately 24.6 at 718 K. An increase in the value of this ratio with a decrease in temperature is consistent with the activation energy for cracking being higher than that for dehydrogenation.

As shown in Figure 3.7-4, H_2 inhibits the rate of C_3H_8 dehydrogenation and cracking over Ga/H-MFI. The dependence of these rates on H_2 partial pressure at 733 K is shown in Figures 3.4.4-2a-c. While the rates of C_3H_8 dehydrogenation and cracking decrease with an increase in H_2 partial pressure, inhibition of these rates is more severe at lower partial pressures of C_3H_8 and relatively weaker at high partial pressures of C_3H_8. Apparent reaction orders of H_2 for dehydrogenation and cracking at each C_3H_8 partial pressure measured at 733 K are provided in Table 3.7-1. These effects of H_2 partial pressure are consistent with H_2 competing with C_3H_8 for adsorption on the active sites that catalyze both reactions. As shown in Figure 3.4.4-2c, the D/C ratio is independent of H_2 and C_3H_8 partial pressures, suggesting that H_2 inhibits both dehydrogenation and cracking in a similar fashion and further supports the idea that dehydrogenation and cracking occur on the same active sites.

The observed effects of C_3H_8 and H_2 partial pressures on the rates of C_3H_8 dehydrogenation and cracking are consistent with rate laws of the form given by Eqns. 3.4.4-1 and 3.4.4-2, respectively. Since the D/C ratio is nearly independent of the C_3H_8 and H_2 partial pressures, the denominator terms in Eqns. 3.4.4-1 and 3.4.4-2 are taken to be the same.

$$\frac{\text{Dehydrogenation rate}}{Al_{tot}} = \frac{\alpha_d[C_3H_8]}{1+\beta[C_3H_8]+\gamma[H_2]} \qquad (3.4.4\text{-}1)$$

$$\frac{\text{Cracking rate}}{Al_{tot}} = \frac{\alpha_c[C_3H_8]}{1+\beta[C_3H_8]+\gamma[H_2]} \qquad (3.4.4\text{-}2)$$

Here, α_d (dehydrogenation), α_c (cracking), β and γ are parameters related to the kinetics and thermodynamics of the elementary steps involved in C_3H_8 dehydrogenation and cracking. Nonlinear regression of the data shown in Figures 3.4.4-1a-c and 3.4.4-2a-c to Eqns. 3.4.4-1 and 3.4.4-2, respectively, results in a satisfactory fit, represented by the solid lines in these figures.

Values of α_d, α_c, β, and γ at 733 K are presented in Table 3.4.4-1. At very low partial pressures of C_3H_8 and in the absence of co-fed H_2, Eqns. 3.4.4-1 and 3.4.4-2 and the data in Figures 3.4.4-1 and 3.4.4-2 indicate that the rates of dehydrogenation and cracking exhibit a first-order dependence on C_3H_8 partial pressure. The parameters, α_d and α_c therefore reflect apparent first-order rate coefficients (k_{app}) for dehydrogenation and cracking with units of mol/mol Al_{tot}*s*bar. At very high partial pressures of C_3H_8 and in the absence of H_2, the rates of dehydrogenation and cracking are independent of C_3H_8 partial pressure, as seen from the data in Figure 3.4.4-1. In this case, the ratios α_d/β and α_c/β correspond to the zero-order rate coefficients (k_{int}) with units of mol/mol Al_{tot}*s. Therefore, for consistency the parameters β and γ must have units of bar^{-1} and hence correspond to the adsorption coefficients (K_{ads}) for C_3H_8 and H_2, respectively. Further interpretation of the parameters α, β, and γ is discussed below in the context of our examination of possible mechanisms for C_3H_8 dehydrogenation and cracking over Ga/H-MFI.

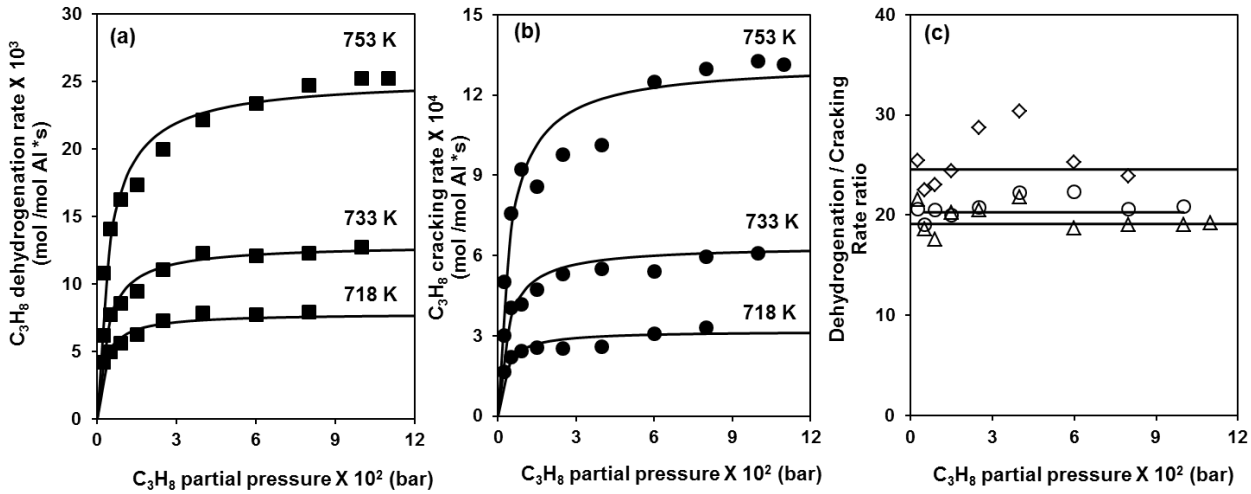

Figure 3.4.4-1. (a) Dependence of the rates of C_3H_8 dehydrogenation and (b) C_3H_8 cracking, and (c) the ratio of the rates of dehydrogenation to cracking over Ga/H-MFI (Ga/Al = 0.2) measured at 718, 733 and 753 K, on the C_3H_8 partial pressure. In Figure 3.4.4-1c, triangles, circles, and diamonds indicate the ratios of rates at 718 K, 733 K, and 753 K, respectively. All rates were extrapolated to zero space time. Solid lines show regressed fits of Eqns. 3.4.4-1 and 3.4.4-2 to the data.

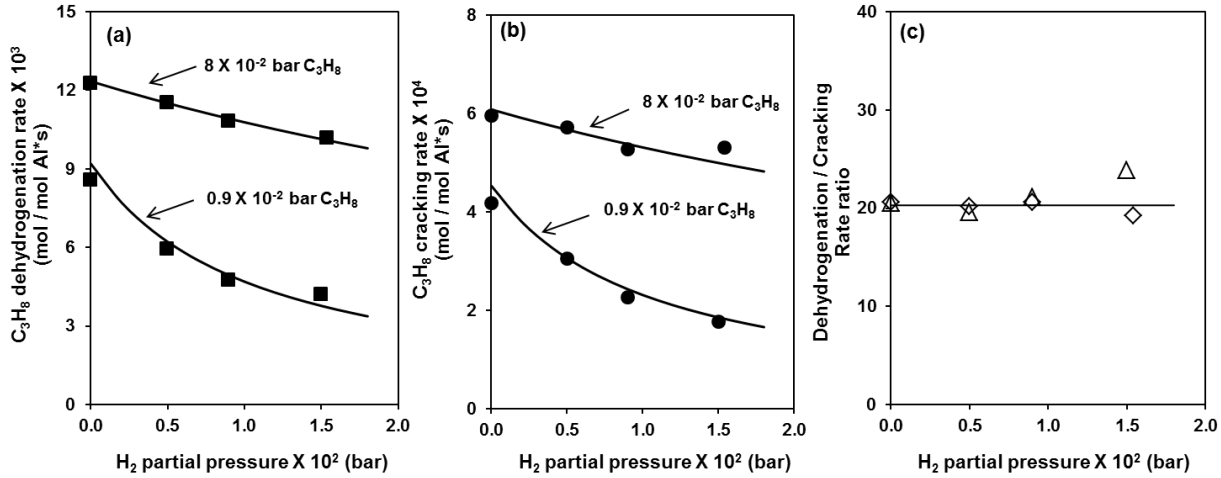

Figure 3.4.4-2. Effects of H_2 partial pressure on the rates of (a) C_3H_8 dehydrogenation and (b) C_3H_8 cracking, and (c) the ratio of the rates of dehydrogenation to cracking (D/C) measured at 733 K. All rates were extrapolated to zero space time. In Figure 3.4.4-2c, open triangles indicate the D/C ratios measured at 0.9 x 10^{-2} bar C_3H_8 and open diamonds indicate the D/C rate ratios measured at 8 x 10^{-2} bar C_3H_8. Solid lines in Figures 3.4.4-2a-c show regressed fits of data to Eqns. 3.4.4-1 and 3.4.4-2.

Table 3.4.4-1. Values of parameters obtained by non-linear least squares regression of Eqns. 3.4.4-1 and 3.4.4-2 to the rates of C_3H_8 dehydrogenation and cracking measured at 733 K, shown in Figures 3.4.4-1 and 3.4.4-2. The parameters β and γ were common to both dehydrogenation and cracking in Eqns. 3.4.4-1 and 3.4.4-2, respectively.

	α (k_{app}) (mol / mol Al_{tot} *s*bar)	β (K_{adsC3}) (bar^{-1})	γ ($K_{ads\ H2}$) (bar^{-1})	α/β(k_{int}) (mol / mol Al_{tot} *s)
Dehydrogenation	3.6	2.8 x 10^2	3.3 x 10^2	1.3 x 10^{-2}
Cracking	1.8 x 10^{-1}	2.8 x 10^2	3.3 x 10^2	6.4 x 10^{-4}

3.4.5 Mechanisms for C_3H_8 dehydrogenation and cracking over $[GaH]^{2+}$ sites

Based on the insight gained in Section 3.4.3 and 3.4.4 regarding the role of $[GaH]^{2+}$ cations in catalyzing C_3H_8 dehydrogenation, we can propose two distinct mechanisms by which C_3H_8 undergoes dehydrogenation over $[GaH]^{2+}$ sites- a) an alkyl mechanism b) a carbenium mechanism, both which we been discussed in a detailed theoretical investigation of light alkane dehydrogenation over Ga/H-MFI.[49] In addition, we propose an alkyl mechanism to describe the role of $[GaH]^{2+}$ cations in the cracking of C_3H_8. The elementary steps for the alkyl and carbenium mechanisms for C_3H_8 dehydrogenation and the alkyl mechanism for C_3H_8 cracking over $[GaH]^{2+}$ sites, are described in Schemes 3.4.5-1, 3.4.5-2 and 3.4.5-3, respectively. Detailed

Gibbs free energy and enthalpy reaction coordinate diagrams are also provided for each of the reaction mechanisms in Figures 3.7-9, 3.7-10 and 3.7-12. The elementary steps presented in Schemes 3.4.5-1-3.4.5-3 can be used to derive rate equations that describe the kinetic behavior predicted by each of the mechanisms, presented here as Equation 3.4.5-1 for alkyl mediated dehydrogenation, Equation 3.4.5-2 for carbenium mediated dehydrogenation and Equation 3.4.5-3 for alkyl mediated cracking. The assumptions and methods used to derive these equations are described in detail in Section 3.7.4.

$$\frac{\text{Dehydrogenation rate}}{[\text{GaH}]^{2+}} = \frac{k_{alk}K_{dis}K_{phys}[C_3H_8]}{1+(K_{dis}K_{phys})[C_3H_8]+K_{H2}[H_2]} \qquad (3.4.5\text{-}1)$$

$$\frac{\text{Dehydrogenation rate}}{[\text{GaH}]^{2+}} = \frac{k_{carb}K_{phys}[C_3H_8]}{1+K_{H2}[H_2]} \qquad (3.4.5\text{-}2)$$

$$\frac{\text{Cracking rate}}{[\text{GaH}]^{2+}} = \frac{k_{crack}K_{dis}K_{phys}[C_3H_8]}{1+(K_{dis}K_{phys})[C_3H_8]+K_{H2}[H_2]} \qquad (3.4.5\text{-}3)$$

In Equations 3.4.5-1 and 3.4.5-2, k_{alk} and k_{carb} are the rate coefficients for the rate-determining, β-hydride elimination step in the alkyl dehydrogenation sequence (Step 3 in Scheme 3.4.5-1) and the rate-determining carbenium C-H activation step in the carbenium dehydrogenation sequence (Step 2 in Scheme 3.4.5-2), respectively. In Equation 3.4.5-3, k_{crack} is the rate coefficient for the rate-determining C-C bond attack step in the alkyl cracking mechanism (Step 3 in Scheme 3.4.5-3). K_{dis} is the equilibrium constant for heterolytic dissociation of C_3H_8 to form $[C_3H_7\text{-GaH}]^+\text{-H}^+$ cation pairs and K_{phys} is the adsorption constant for C_3H_8 physisorption at $[\text{GaH}]^{2+}$ sites. K_{H2} is the equilibrium constant for dissociative adsorption of H_2 at $[\text{GaH}]^{2+}$ sites to form $[\text{GaH}_2]^+\text{-H}^+$ cation pairs.

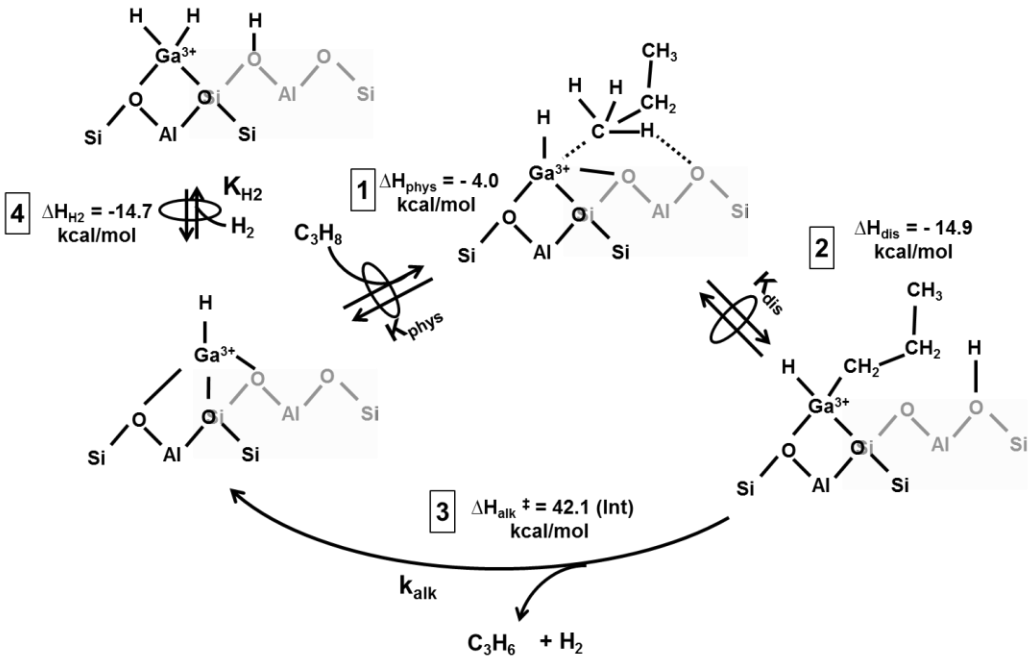

Scheme 3.4.5-1. Alkyl mechanism for activation and dehydrogenation of C_3H_8 over $[GaH]^{2+}$ sites to C_3H_6 and H_2. Enthalpies (adsorption, reaction and activation) for each step are shown here with respect to the enthalpy of the initial structure in the step. For each structure, framework atoms that are faded reflect cation-exchange sites that are behind the image plane for non-faded cation-exchange sites. Cations coordinated to the faded cation-exchange sites are also behind the image plane but have not been faded for visual purposes

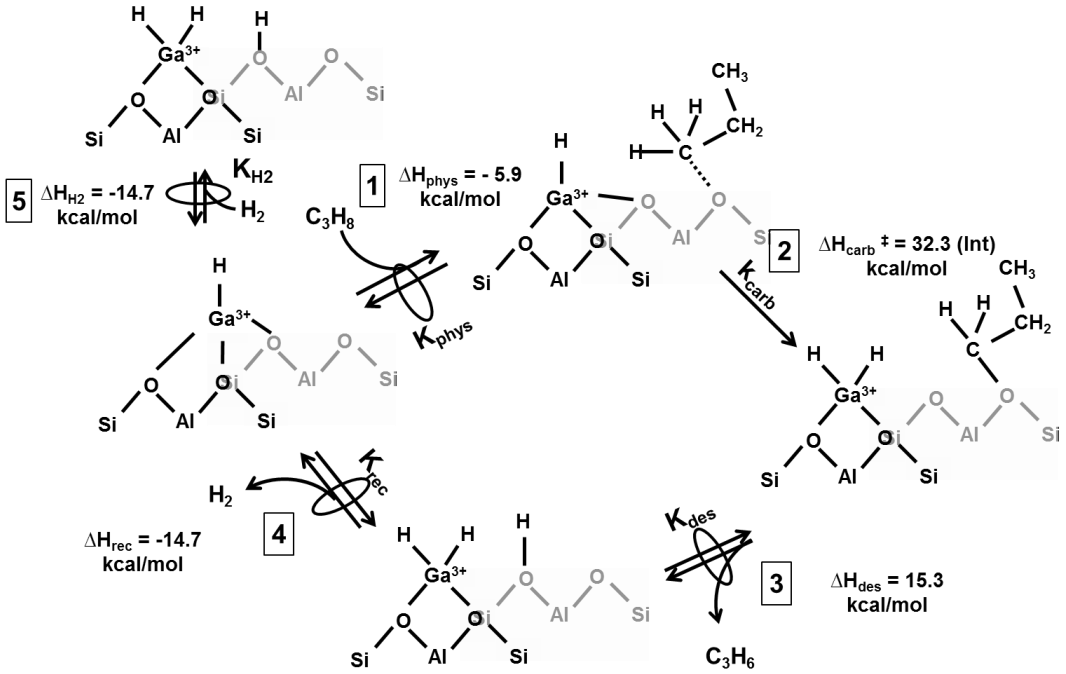

Scheme 3.4.5-2. Carbenium mechanism for the activation and conversion of C_3H_8 to C_3H_6 and H_2 over $[GaH]^{2+}$ sites. Enthalpies (adsorption, reaction and activation) for each step are shown here with respect the enthalpy of the initial structure in the step. For each structure, framework atoms that are faded reflect cation-exchange sites that are behind the image plane for non-faded cation-exchange sites. Cations coordinated to the faded cation-exchange sites are also behind the image plane but have not been faded for visual purposes

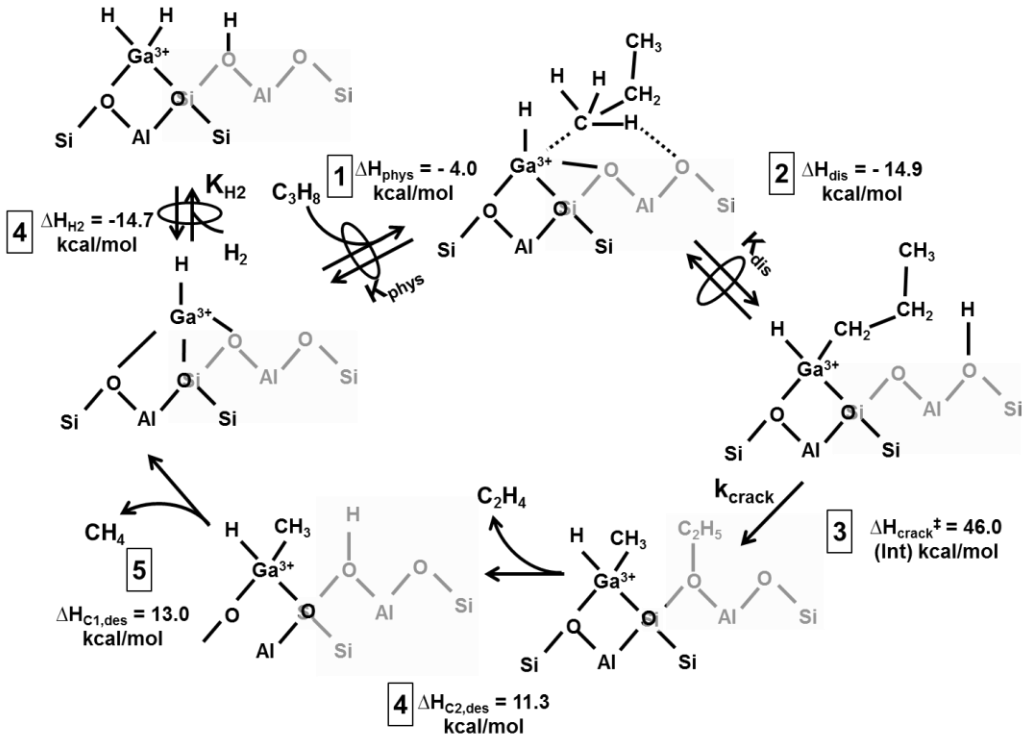

Scheme 3.4.5-3. Cracking of C_3H_8 over $[GaH]^{2+}$ sites by the alkyl mechanism. Enthalpies (adsorption, reaction and activation) for each step are shown here with respect the enthalpy of the initial structure in the step. For each structure, framework atoms that are faded reflect cation-exchange sites that are behind the image plane for non-faded cation-exchange sites. Cations coordinated to the faded cation-exchange sites are also behind the image plane but have not been faded for visual purposes

As seen in Schemes 3.4.5-1-3.4.5-3, alkyl mediated pathways for dehydrogenation and cracking over $[GaH]^{2+}$ require dissociative adsorption of C_3H_8 over $[GaH]^{2+}$ to produce $[C_3H_7\text{-}GaH]^{+}\text{-}H^{+}$ cation pairs, prior to the rate-determining step. On the other hand, the carbenium mediated dehydrogenation pathway proceeds via rate-determining C-H activation of C_3H_8 species, physisorbed at $[GaH]^{2+}$. In all three cases, inhibition of rates is predicted to occur via dissociative adsorption of H_2 at $[GaH]^{2+}$ to form $[GaH_2]^{+}\text{-}H^{+}$ cation pairs. These observations, together with an inspection of rate equations (3.4.5-1-3) show that only the alkyl-mediated mechanisms predict a first order dependence of dehydrogenation and cracking rates on C_3H_8 at low C_3H_8 partial pressures and an inhibition of these rates by C_3H_8 at high C_3H_8 partial pressures via the saturation of $[GaH]^{2+}$ sites by strongly-bound $[C_3H_7\text{-}GaH]^{+}$ species. In the carbenium mechanism, the relatively weak binding of C_3H_8 to $[GaH]^{2+}$ sites, prior to the rate-determining C-H activation step, would lead to a first-order dependence of the rate of dehydrogenation on the C_3H_8 partial pressure, in the absence of H_2, as predicted by Equation 3.4.5-2.

As seen in Figures 3.4.4-1 and 3.4.4-2, the dependence of the experimentally measured dehydrogenation and cracking rates on C_3H_8 partial pressure is only consistent with the kinetics predicted by the alkyl mediated mechanisms. Similarly, the D/C rate ratio in Figure 3.4.4-1c and Figure 3.4.4-2c is independent of C_3H_8 and H_2 partial pressures. These observations are also consistent with the conclusion that C_3H_8 dehydrogenation and cracking are catalyzed via a

common, strongly bound C_3H_8 derived surface intermediate. The alkyl mechanisms for dehydrogenation and cracking also proceed via a common C_3H_8 derived reactive intermediate i.e $[C_3H_7\text{-}GaH]^+\text{-}H^+$ cation pairs. A further assessment of the relevant mechanisms involved in C_3H_8 dehydrogenation and cracking over Ga/H-MFI can be obtained by comparing experimentally derived activation and adsorption enthalpies to their values predicted theoretically. Experimental activation and adsorption enthalpies were obtained by measuring the rates of C_3H_8 dehydrogenation and cracking at different temperatures (718-753 K) over the Ga/Al = 0.2 sample and then determining values of the apparent and intrinsic activation enthalpies for both reactions. The methods used for extracting values of these parameters from kinetic data are provided in Section 3.7.5 and plots showing the temperature dependence of rate coefficients and adsorption coefficients are provided in Figures 3.7-5, 3.7-6 and 3.7-7.

Experimental values of the activation and adsorption enthalpies for C_3H_8 dehydrogenation and cracking over Ga/H-MFI (Ga/Al =0.2) are given in Table 3.4.5-1. Also shown in this table, are the apparent and intrinsic activation and adsorption enthalpies predicted from QM/MM calculations for the alkyl and carbenium mechanisms for C_3H_8 dehydrogenation and for the alkyl mechanism for C_3H_8 cracking, in all three cases over $[GaH]^{2+}$ sites. For C_3H_8 dehydrogenation, the experimentally measured apparent activation enthalpy is 19.0 ± 6.0 kcal/mol and the intrinsic activation enthalpy is 34.6 ± 1.0 kcal/mol, whereas the adsorption enthalpy for C_3H_8 extracted from experimental data is -15.6 ± 5.0 kcal/mol. These estimates of the C_3H_8 adsorption enthalpy and the apparent and intrinsic enthalpies and are consistent with theoretical predictions for the formation of $[C_3H_7\text{-}GaH]^+\text{-}H^+$ cation pairs upon dissociative C_3H_8 adsorption at $[GaH]^{2+}$ sites (-18.9 kcal/mol) and β-hydride elimination of C_3H_6 and H_2, as predicted by the alkyl mechanism for dehydrogenation (predicted ΔH_{app} = 23.2 kcal/mol and predicted ΔH_{int} = 42.1 kcal/mol). As noted earlier, the carbenium mechanism involves the activation of an adsorbed C_3H_8 precursor that is weakly bound to the active site leading to smaller differences between the apparent and intrinsic activation enthalpies, than those measured experimentally and to a rate expression for C_3H_8 dehydrogenation that is inconsistent with that observed experimentally (compare Eqn. 3.4.4-1 with Eqns. 3.4.5-1 and 3.4.5-2).

The DFT-predicted value for the dissociative adsorption of C_3H_8 on $[GaH]^{2+}$ is more exothermic than that of dissociative adsorption of H_2, a finding which is consistent with the experimentally-measured adsorption enthalpies reported in Table 3.4.5-1; however, the value for the predicted adsorption enthalpy of H_2 at$[GaH]^{2+}$ sites is lower than that deduced from the analysis of the reaction kinetics. A part of this discrepancy may be due to the sensitivity of the predicted value to the interatomic distance between framework Al atoms involved in proximate cation-exchange sites which host $[GaH]^{2+}$ cations.[48,49] For the NNN Al atom configurations considered, the predicted enthalpy for dissociative adsorption of H_2 on $[GaH]^{2+}$ cations to form $[GaH_2]^+\text{-}H^+$ cation pairs varies between -5.5 to -15.9 kcal/mol. This range encompasses the experimental H_2 adsorption enthalpy value of -7.4 ± 3.3 kcal/mol shown in Table 3.4.5-1.

Table 3.4.5-1 also shows apparent and intrinsic activation enthalpies for C_3H_8 cracking via the alkyl mechanism over $[GaH]^{2+}$predicted from theoretical calculations. The experimentally measured apparent activation enthalpy (26.5 ± 0.3 kcal/mol) is in excellent agreement with the theoretically predicted estimate (27.1 kcal/mol). The experimentally measured intrinsic activation enthalpy, 42 ± 4.7 kcal/mol is also in good agreement with the theoretical estimate (44.9 kcal/mol).

Table 3.4.5-1. Apparent and intrinsic activation enthalpies for C_3H_8 dehydrogenation and cracking over Ga/H-MFI (Ga/Al = 0.2), extracted from Figures 3.7-5, 3.7-6 and enthalpies of dissociative adsorption for C_3H_8 and H_2 extracted from Figure 3.7-7. Also shown are theoretically predicted activation enthalpies for C_3H_8 dehydrogenation and cracking over $[GaH]^{2+}$ via alkyl and carbenium mechanisms and for the enthalpies of dissociative adsorption for C_3H_8 and H_2. Reported uncertainties reflect 95% confidence intervals.

Enthalpy (kcal/mol)	Dehydrog. Experiment[a]	Alkyl dehydrog. mechanism[b]	Carbenium dehydrog. mechanism[b]	Cracking Experiment[a]	Alkyl cracking mechanism[b]
$\Delta H^{\ddagger}_{app}$	19.0 ± 6.0	23.2	26.4	26.5 ± 0.3	27.1
$\Delta H^{\ddagger}_{int}$	34.6 ± 1.0	42.1	32.3	42.0 ± 4.7	46.0
ΔH_{ads} (C_3H_8)	-15.6 ± 5.0	-18.9	-5.9	-15.6 ± 5.0	-18.9
ΔH_{ads} (H_2)	-7.4 ± 3.3	-14.6	-14.6	-7.4 ± 3.3	-14.6

[a] From rate data measured at temperatures ranging from 718 K- 753 K for the Ga/Al =0.2 sample. Rate coefficients were obtained via non-linear regression of rate data in Figure 3.4.4-1 and 3.4.4-2 to Equation 3.4.4-1 and 3.4.4-2 and they were normalized to the fraction of $[GaH]^{2+}$ sites, estimated from NH_3-TPD measurements (see section 3.7.8).[133] Apparent and intrinsic activation enthalpies and adsorption enthalpies were obtained via linear regression of rate coefficient data to equations 3.7.5-8, 3.7.5-9 and 3.7.5-10 derived in section 3.7.5.
[b] Computed using QM/MM methods. See theoretical methods section for more details

The data presented in Table 3.4.5-1 further support the hypothesis that both dehydrogenation and cracking of C_3H_8 over Ga/H-MFI are catalyzed by $[GaH]^{2+}$ sites via a common alkyl-Ga, $[C_3H_7\text{-}GaH]^{+}$ surface intermediate. Inhibition of both rates occurs by dissociative adsorption of H_2 at $[GaH]^{2+}$ to form $[GaH_2]^{+}\text{-}H^{+}$ cation pairs. Consistent with this interpretation, the D/C ratio, shown in Figure 3.4.4-1c and Figure 3.4.4-2c, is independent of C_3H_8 and H_2 surface coverage, but weakly dependent on temperature. Therefore, the selectivity to C_3H_8 dehydrogenation versus cracking over Ga/H-MFI is not governed by the concentrations of C_3H_8, H_2 or residual Brønsted acid O-H groups in Ga/H-MFI, but rather by the difference between the free energy activation barriers for dehydrogenation and cracking over $[GaH]^{2+}$. A higher activation enthalpy for cracking than for dehydrogenation would lead to a decrease in the D/C ratio with an increase in temperature, as observed experimentally in Figure 3.4.4-1c. Indeed, Table 3.4.5-1 indicates that the difference in the measured activation enthalpies (apparent or intrinsic) between cracking and dehydrogenation over Ga/H-MFI, $\Delta\Delta H^{\ddagger}_{C/D}$ (exp) is 7.4 ± 4.8 kcal/mol. Consistent with this finding, our theoretical calculations predict a higher activation enthalpy for alkyl mediated cracking, than for alkyl mediated dehydrogenation ($\Delta\Delta H^{\ddagger}_{C/D}$ (calc) = 3.9 kcal/mol).

We turn next to a comparison of our results with those recently reported by Schreiber et al.[54] Ga/H-MFI samples (Si/Al =50) in their work were prepared using conventional incipient wetness impregnation followed by H_2 reduction. Both C_3H_8 dehydrogenation and cracking rates were shown to increase with Ga content up to a Ga/Al ratio of 0.5, with further increases in Ga content leading to lower rates of dehydrogenation and cracking. Similar to our findings, the rate

of C_3H_8 dehydrogenation was shown to exhibit a Langmuir-Hinshelwood dependence on C_3H_8 partial pressure but the dependence of the rate of dehydrogenation on H_2 partial pressure was not investigated.

Schreiber et al. have proposed that Ga^+-H^+ cation pairs are responsible for the dehydrogenation of C_3H_8 based on the observation of a peak at 10,370.2 eV in the XANES spectrum of their sample of H_2- reduced Ga/H-MFI, that they attribute to Ga^+ cations and to the observation that the rate of dehydrogenation increases with Ga content up to a Ga/Al ratio of 0.5.[54] Periodic Density Functional Theory (DFT) calculations were then employed to show how Ga^+-H^+ cation pairs residing at proximate cation-exchange sites associated with NNN pairs of framework Al atoms could catalyze C_3H_8 dehydrogenation. In this scheme, the Ga^+-H^+ cation pair is first converted into a $[GaH]^{2+}$ cation via oxidative addition and the latter species is assumed to catalyze the alkyl C−H activation of C_3H_8 to form a $[C_3H_7\text{-}GaH]^+$-H^+ cation pair. This step is then followed by a monomolecular elimination of H_2 from the $[C_3H_7\text{-}GaH]^+$-H^+ cation pair and subsequent release of C_3H_6 to regenerate Ga^+-H^+ cation pair sites. Both alkyl C-H activation and H_2 elimination steps were reported to be kinetically relevant.

We have examined several aspects of the mechanism proposed by Schreiber et al.[54] The first is the ability of $[GaH]^{2+}$ cations to undergo reductive elimination to form Ga^+-H^+ cation pairs. We find that the Gibbs free energy for this reaction is -10.4 kcal/mol and that the free energy barrier for the reductive elimination of H^+ from $[GaH]^{2+}$ to form Ga^+-H^+ cation pairs is 25.2 kcal/mol, indicating that the formation of Ga^+-H^+ cation pairs from $[GaH]^{2+}$ cations is both thermodynamically and kinetically feasible (see Figure 3.7-11). However, the free energy (77.8 kcal/mol) and enthalpy (26.3 kcal/mol) activation barriers for the C-H activation step via the mechanism reported by Scheiber et al. on the given $[GaH]^{2+}$ site, are considerably higher than the corresponding values reported in Scheme 3.4.5-1 and in Figure 3.7-10, 40.1 kcal/mol and 2.0 kcal/mol, respectively. We believe that the difference in the energetics reported here and by Scheiber et al.[54] is a consequence of how $[GaH]^{2+}$ cations are coordinated with the zeolite framework. In the latter study, $[GaH]^{2+}$ cations are bound to two framework O atoms, whereas in our work, $[GaH]^{2+}$ cations are bound to three framework O atoms (and one H ligand), thus forming the preferred tetrahedral coordination around the Ga^{3+} center.[152] The three framework O atoms in the first coordination sphere of these species withdraw more electron density from the Ga^{3+} center resulting in $[GaH]^{2+}$ cations that are more Lewis acidic and therefore more reactive towards alkane C-H activation than $[GaH]^{2+}$ cations that are bound to only two framework O atoms.

We have also investigated the free energy landscape for the dehydrogenation pathway over Ga^+-H^+ cation pairs proposed by Schreiber et al. Our calculations indicate that the rate-determining step for this sequence is the concerted elimination of C_3H_6 and H_2 from $[C_3H_7\text{-}GaH]^+$-H^+ cation pairs to reform Ga^+-H^+ cation pairs (see Figure 3.7-11). The Gibbs free energy barrier for this rate-determining transition state is about 20 kcal/mol higher than that for the rate-determining step in the alkyl sequence over $[GaH]^{2+}$ shown in Scheme 3.4.5-1 (see Figure 3.7-10), thereby rendering the former pathway less favorable. Thus, while our theoretical calculations predict that the formation of Ga^+-H^+ cation pairs from $[GaH]^{2+}$ cations is thermodynamically and kinetically feasible, these calculations also predict that the dehydrogenation of C_3H_8 via processes involving Ga^+-H^+ cation pairs would be much less favorable than those involving $[GaH]^{2+}$ cations. We also show that while Ga^+-H^+ cation pairs can activate C_3H_8 to produce $[C_3H_7\text{-}GaH]^+$-H^+ cation pairs, upon C_3H_6 formation from these species the barrier to form $[GaH]^{2+}$ cations is much lower than that to regenerate Ga^+-H^+ cation pairs

(see Figure 3.7-15). Therefore, our findings strongly suggest that $[GaH]^{2+}$ cations are the primary active sites responsible for dehydrogenation.

3.5 Conclusions

The kinetics of C_3H_8 dehydrogenation and cracking were investigated over Ga/H-MFI, prepared with Ga/Al ratios between 0.05 and 0.3, for which all of the Ga is presented as isolated cationic species. C_3H_8 conversion occurs over H-MFI via monomolecular dehydrogenation and cracking catalyzed by Brønsted O-H acid groups. C_3H_8 conversion over pre-oxidized Ga/H-MFI undergoes an induction period before reaching a steady-state activity. The induction period is significantly attenuated by pre-reducing the catalysts in H_2. Notably, the distribution of products formed via C_3H_8 dehydrogenation and cracking are virtually unchanged during the induction period and the steady-state activities of Ga/H-MFI are independent of the initial state of cationic Ga^{3+} species (oxidized or reduced). Reaction rates (expressed per Al_{tot} atom) for C_3H_8 dehydrogenation and cracking over Ga/H-MFI (Ga/Al = 0.2) are ~ 500 and ~ 20 times respectively higher than the corresponding rates over H-MFI at identical conditions. Rates of both reactions, when normalized with respect to the concentration of $[GaH]^{2+}$ cations are found to be independent of the Ga/Al ratio, suggesting that $[GaH]^{2+}$ cations are the catalytically active centers for both reactions. C_3H_8 dehydrogenation and cracking rates over Ga/H-MFI are first-order in C_3H_8 at low C_3H_8 partial pressures and are inhibited by C_3H_8 at higher C_3H_8 partial pressures. Both reactions are inhibited by the presence of H_2. Ratios of the rates of dehydrogenation to cracking (D/C) are, however, independent of the partial pressures of C_3H_8 and H_2 and only dependent upon temperature, again suggesting that both reactions involve the same active center. The observed dependences of reaction rates on the partial pressures of C_3H_8 and H_2 as well as both the apparent and intrinsic activation enthalpies are consistent with theoretical predictions based on a proposed alkyl mediated mechanism for the two reactions. The alkyl mediated mechanism for C_3H_8 dehydrogenation and cracking begins with the reversible, dissociative adsorption of C_3H_8 at $[GaH]^{2+}$ to form $[C_3H_7\text{-}GaH]^{+}\text{-}H^{+}$ cation pairs.

Dehydrogenation then proceeds via rate-determining β-hydride elimination from the C_3H_7 fragment to form C_3H_6 and H_2 in a concerted step involving a cyclic transition state. On the other hand, cracking proceeds via rate-determining C-C bond attack of the C_3H_7 fragment by the proximal Brønsted acid O-H group, resulting in the formation of $[CH_3\text{-}GaH]^{+}$ cations proximal to ethoxide species. C_2H_4 and CH_4 are then formed in subsequent steps that are not kinetically relevant. Inhibition of both dehydrogenation and cracking by H_2 occurs via dissociative adsorption of H_2 at $[GaH]^{2+}$ cations to produce $[GaH_2]^{+}\text{-}H^{+}$ cation pairs, which are much less active for C_3H_8 dehydrogenation and cracking.

3.6 Acknowledgements

This work was supported by Chevron Energy Technology Company. Computational resources were provided by UC Berkeley's Molecular Graphics and Computation Facility (supported by NIH S10OD023532). We would like to thank Christopher Ho for helpful technical discussions. M. B. acknowledges support provided to him as a visiting scholar by Prof. Liubov Kiwi-Minsker of the Ecole Polytechnique Federale de Lausanne, Lausanne, Switzerland.

3.7 Supporting Information

3.7.1 C_3H_8 dehydrogenation and cracking rates as a function of time-on-stream over H-MFI at 733 K

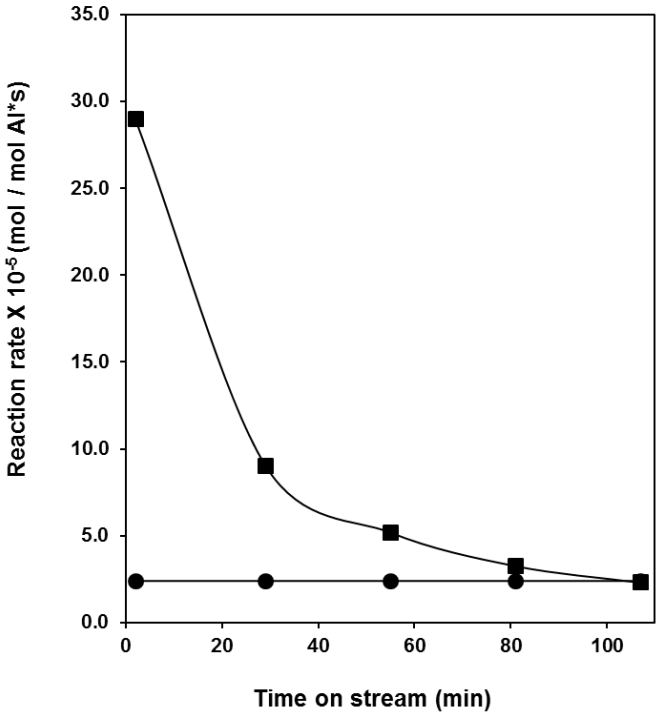

Figure 3.7-1. C_3H_8 dehydrogenation rates (filled squares) and cracking rates (filled circles) as a function of time-on-stream, measured at 1.4 kPa C_3H_8/He and τ = 10 mol Al*s/mol C_3H_8 space time and 733 K. C_3H_8 conversions were < 2 %

3.7.2 Temperature dependence of measured rate coefficients for C_3H_8 dehydrogenation and cracking over H-MFI

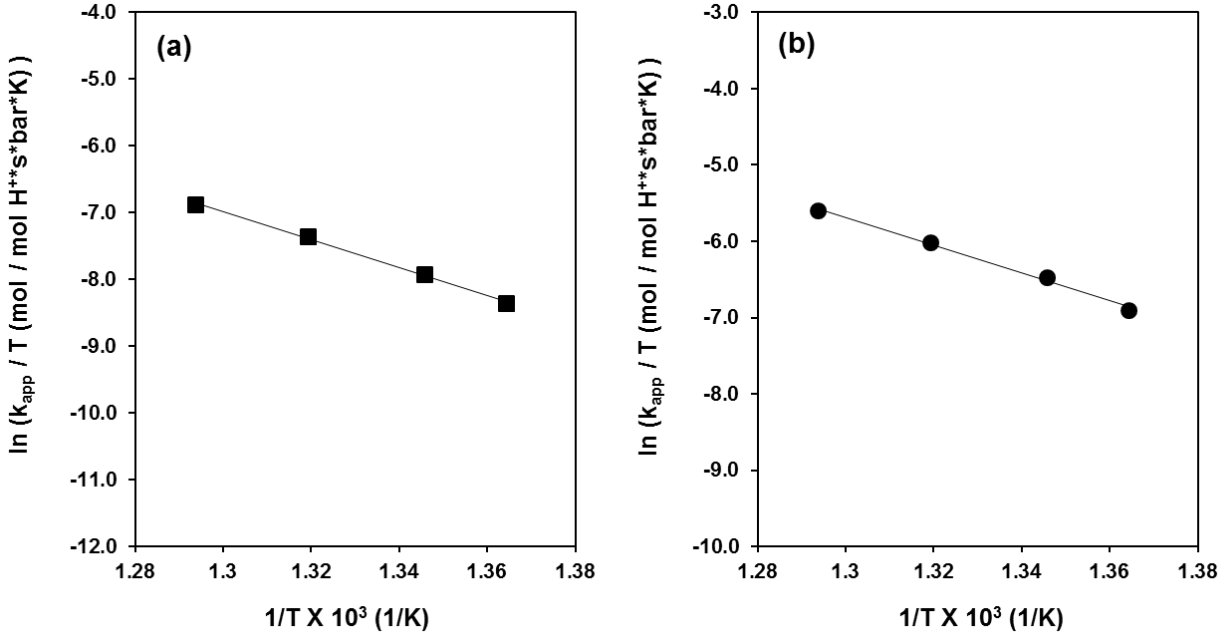

Figure 3.7-2. First-order rate coefficients (k_{app}) for (a) C_3H_8 dehydrogenation and (b) cracking as a function of temperature. Rate constants were normalized to the density of Brønsted acid O-H acid groups in H-MFI, measured via NH_3 –TPD (0.87 H^+/Al_{tot}).[133]

3.7.3 Effects of space time on steady-state product selectivities over Ga/H-MFI (Ga/Al = 0.2) during C_3H_8 conversion

Shown in Figure 3.7-3, are the steady-state product selectivities (shown as % of converted C in products) as a function of space time for the reaction of C_3H_8 over Ga/H-MFI (Ga/Al =0.2) at 733 K and 1.5kPa C_3H_8/He. Under the differential conversions employed during reactivity measurements (< 9 % C_3H_8 conversion), only C_3H_6, CH_4, C_2H_4 and aromatics (C_6H_6 and C_7H_8) were detected as reaction products in the reactor effluent. All product selectivities shown in Figure 3.7-3 were also linearly extrapolated to zero space time, as can be seen by the dotted lines in the figure. C_3H_6 is the dominant product at all space times tested (> 85% C selectivity), but the selectivity to this product decreases with increasing space time from an extrapolated C selectivity of 96 % at 0 space time. The decrease in C_3H_6 selectivity with increasing space time is attributed to secondary pathways that consume C_3H_6 to form higher molecular weight products, such as aromatics. The C selectivity to C_2H_4 is about 3% at zero space time and then increases linearly with increasing space time. By contrast the C selectivity to CH_4 is roughly independent of space time, with a value of approximately 1.5%. The ratio of the extrapolated C selectivities of C_2H_4 and CH_4 (approximately 2) is consistent with the cracking of C_3H_8 into C_2H_4 and CH_4. The increase in value of this ratio with increasing space time suggests

that additional C_2H_4 is formed by the cracking of higher molecular weight products. This could occur, for example, via β-scission of larger alkenes. The C selectivity to aromatics (C_6H_6 and C_7H_8) increased with increasing space time and at zero space time, extrapolated to a value close to zero, suggesting that these products form via secondary pathways from products of C_3H_8 dehydrogenation and cracking. This trend is consistent with previous experiments studies of C_3H_8 conversion over Ga/H-MFI.[27]

Measured selectivities of products (on a C_3H_8 basis) together with overall C_3H_8 conversion rates were used to determine the rates of C_3H_8 dehydrogenation, cracking and aromatics formation. These rates are shown as a function of space time in Figure 3.7-4a-d. The rate of C_3H_8 consumption (Figure 3.7-4a) decreases with increasing space time, possibly due to inhibition by the products of C_3H_8 conversion. To explore this possibility, reaction rates were also measured in the presence of co-fed H_2. In the presence of 1.5kPa H_2, the rates of C_3H_8 conversion (open symbols in Figure 3.7-4a) show a much weaker dependence on space time, confirming that H_2 inhibits the rates. C_3H_8 dehydrogenation rates (Figure 3.7-4b) and C_3H_8 cracking rates (Figure 3.7-4c) also decrease with increasing space time. In the presence of 1.5kPa cofed H_2, both rates show a much weaker dependence on space time. We note that while the inhibition of the rate of C_3H_8 dehydrogenation by H_2 has been reported in previously,[27,36] inhibition of the rate of C_3H_8 cracking rate by H_2 has not been reported. We note that H_2 does not inhibit Brønsted acid catalyzed monomolecular dehydrogenation and cracking on H-MFI. This observation suggests that the site requirements for both the dehydrogenation and cracking reaction over Ga/H-MFI are similar i.e., both reactions are catalyzed by Ga^{3+} sites. Both rates also exhibit a weak, but observable decrease with space time, even in the presence of 1.5kPa H_2. We speculate that this residual inhibition arises from the binding of alkene products to Ga^{3+} sites. Aromatics formation rates (Figure 3.7-4d) increased with space time, consistent with their secondary nature. The formation of aromatics was, however, strongly inhibited by H_2, suggesting that their formation also requires the participation of Ga^{3+} sites.

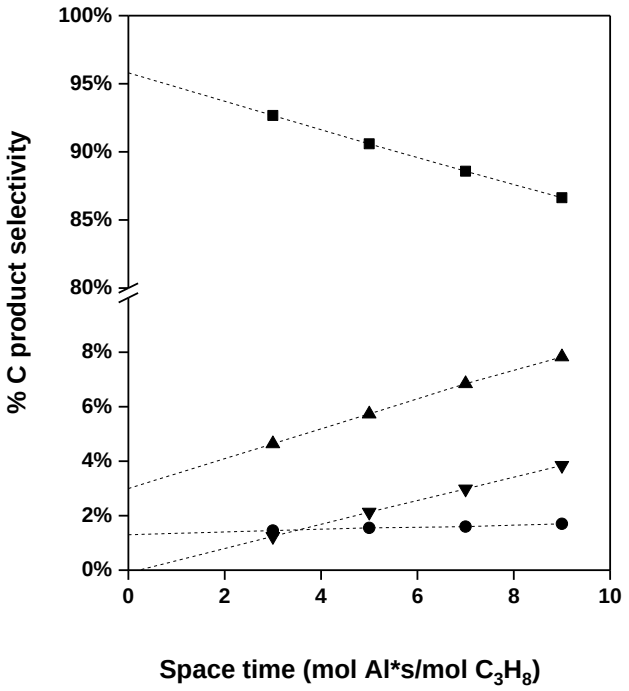

Figure 3.7-3. C product selectivities (% of C converted to products) as a function of space time, during C_3H_8 conversion over Ga/H-MFI (Ga/Al =0.2) at 1.5 kPa C_3H_8/He and 733 K. Ga/H-MFI was pre-treated in 2.5% H_2/He at 773 K, prior to reaction. C_3H_8 conversions were < 9 %. Filled squares (■) denote C_3H_6, filled triangles (▲) denote C_2H_4, filled inverted triangles (▼) denote aromatics (C_6H_6 and C_7H_8) and filled circles (●) denote CH_4. Dotted lines indicate linear extrapolations to zero space time.

Table 3.7-1. Apparent reaction orders of H_2 for C_3H_8 dehydrogenation and cracking at 0.9 kPa C_3H_8 and 8 kPa C_3H_8 measured at 733 K over Ga/Al = 0.2. Data are derived from Figure 6.

C_3H_8 partial pressure x 10^2 (bar)	Dehydrogenation[1]	Cracking[1]
0.9	-0.3	-0.5
8.0	-0.1	-0.1

[1]Apparent reaction orders were determined using the relationship Rate = $k[H_2]^X$ where k is a rate coefficient and x is the reaction order

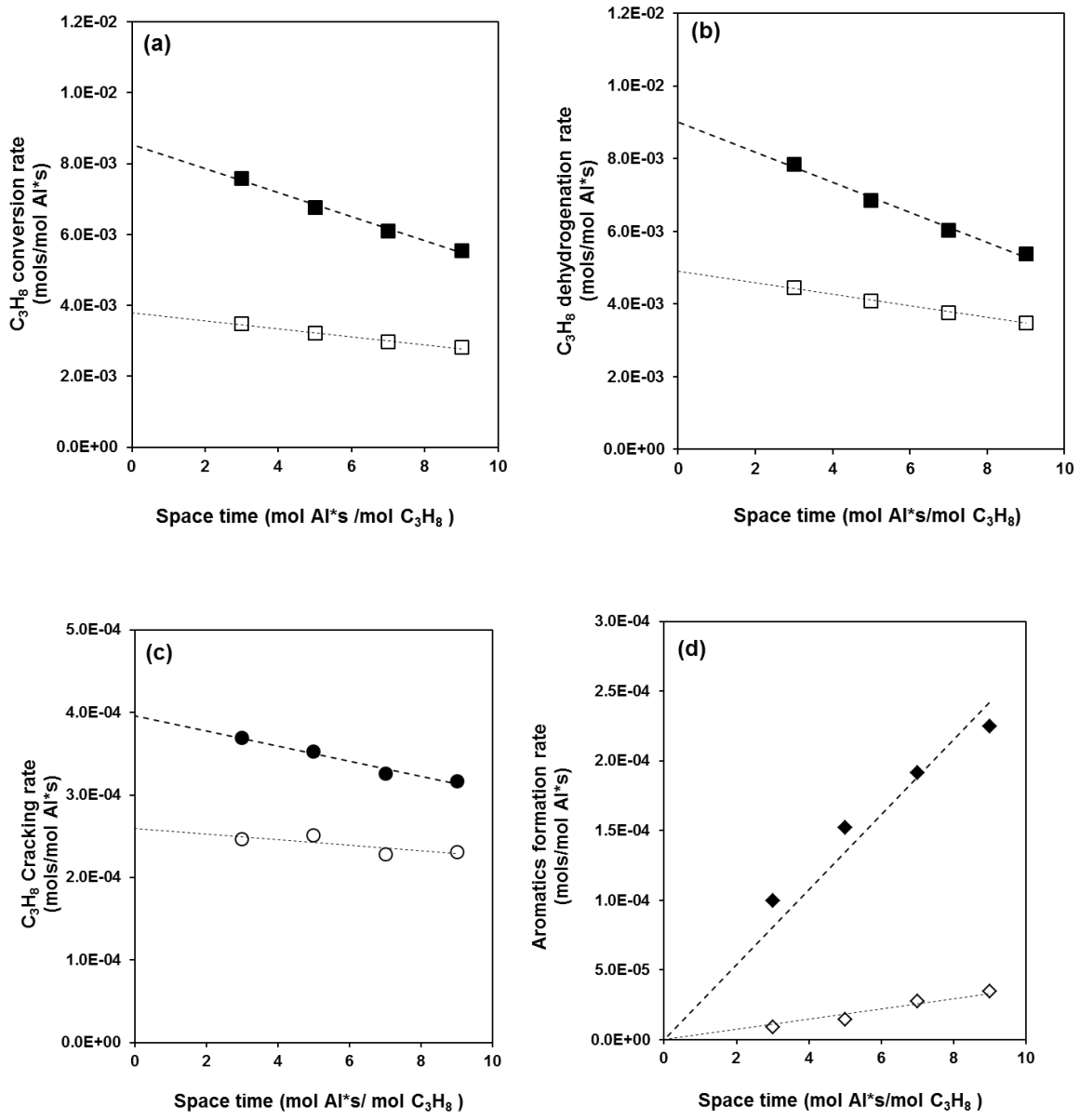

Figure 3.7-4. (a) C_3H_8 conversion rates (per Al_{tot} atom) as a function of space time. (b) C_3H_8 dehydrogenation rates (per Al_{tot} atom) as a function of space time. (c) C_3H_8 cracking rates (per Al_{tot} atom) as a function of space time. (d) Aromatics (C_6H_6 and C_7H_8) formation rates (per Al_{tot} atom) as a function of space time. In all plots, closed symbols refer to 0 kPa cofed H_2 and open symbols refer to 1.5 kPa cofed H_2. Rates were measured at 1.5 kPa C_3H_8/He at 733 K.

3.7.4 Derivation of rate equations for plausible mechanisms for dehydrogenation and cracking over Ga/H-MFI.

(a) Derivation of rate law for C_3H_8 dehydrogenation over $[GaH]^{2+}$ sites via alkyl mechanism

The elementary steps outlined in Scheme 3.4.5-1 for C_3H_8 dehydrogenation over $[GaH]^{2+}$ sites are used here to derive a rate law in terms of kinetic and thermodynamic coefficients. The steady-state hypothesis was applied to all reactive surface intermediates. On the basis of free energy and enthalpy calculations outlined in Figure 3.7-10, the physisorption of C_3H_8 onto $[GaH]^{2+}$ to form C_3H_8-$[GaH]^{2+}$ complexes (Step 1) and the dissociative adsorption of C_3H_8-$[GaH]^{2+}$ to form $[C_3H_7\text{-}GaH]^{+}\text{-}H^{+}$ cation pairs (Step 2) are predicted to have low activation barriers ($\leq$ 2 kcal/mol) and are therefore assumed to be quasi-equilibrated. This assumption leads to the derivation of equations (3.7.4-1) and (3.7.4-2) that describe the relationship between gas-phase C_3H_8 and C_3H_8 derived surface intermediates.

$$K_{phys} = \frac{[C_3H_8\text{-}[GaH]^{2+}]}{[C_3H_8][GaH]^{2+}} \qquad (3.7.4\text{-}1)$$

$$K_{dis} = \frac{[[C_3H_7\text{-}GaH]^{+}\text{-}H^{+}]}{[C_3H_8\text{-}[GaH]^{2+}]} \qquad (3.7.4\text{-}2)$$

Here, K_{phys} and K_{dis} are the thermodynamic adsorption constants for C_3H_8 physisorption at $[GaH]^{2+}$ and dissociation of C_3H_8 by $[GaH]^{2+}$ into $[C_3H_7Ga\text{-}H]^{+}\text{-}H^{+}$ cation pairs, respectively. Similarly, inhibition of reaction rates by H_2 may occur via dissociation of H_2 by $[GaH]^{2+}$ to form $[GaH_2]^{+}\text{-}H^{+}$ pairs as described by equation (3.7.4-3).

$$K_{H_2} = \frac{[[GaH_2]^{+}\text{-}H^{+}]}{[H_2][GaH]^{2+}} \qquad (3.7.4\text{-}3)$$

Here, K_{H2} is the equilibrium constant for H_2 dissociation.

As also described before, the rate-limiting step in the alkyl dehydrogenation sequence is the cyclic β-hydride elimination of C_3H_7 fragments by the Ga^{3+} center to form C_3H_6 and H_2 in a concerted step (Step 3). The overall rate of dehydrogenation (per $[GaH]^{2+}$) can be described by equation (3.7.4-4).

$$\frac{Rate,D}{[GaH]^{2+}} = k_{alk}\theta_{alk} \qquad (3.7.4\text{-}4)$$

Here, Rate, D refers to the dehydrogenation rate, k_{alk} refers to the rate coefficient for β-hydride elimination and θ_{alk} refers to the surface coverage of $[C_3H_7\text{-}GaH]^{+}\text{-}H^{+}$ cation pairs, the precursor to the rate-limiting transition state and is given by equation (3.7.4-5).

$$\theta_{alk} = \frac{[[C_3H_7\text{-}GaH]^{+}\text{-}H^{+}]}{[L]} \qquad (3.7.4\text{-}5)$$

Here, $[[C_3H_7\text{-}GaH]^+\text{-}H^+]$ refers to the surface concentration of $[C_3H_7\text{-}GaH]^+\text{-}H^+$ cation pairs and [L] refers to the total density of active sites i.e $[GaH]^{2+}$ sites. [L] can be described in terms of the various reactive surface intermediates via equation (3.7.4-6).

$$[L] = [GaH]^{2+} + [C_3H_8\text{-}[GaH]^{2+}] + [[C_3H_7\text{-}GaH]^+\text{-}H^+]+ [[GaH_2]^+\text{-}H^+] \qquad (3.7.4\text{-}6)$$

Theoretical calculations suggest that the interaction of gas-phase C_3H_8 with $[GaH]^{2+}$ is expected to be weak (~ - 6 kcal/mol adsorption enthalpy) . Therefore the second term in equation (3.7.4-6) can be neglected. This leads to a reduction in equation (3.7.4-6) to equation (3.7.4-7).

$$[L] = [GaH]^{2+} + [[C_3H_7\text{-}GaH]^+\text{-}H^+]+ [[GaH_2]^+\text{-}H^+] \qquad (3.7.4\text{-}7)$$

Solving equations (3.7.4-1) – (3.7.4-7) leads to a rate expression for C_3H_8 dehydrogenation, shown below as equation (3.7.4-8), shown in section 3.4.5 as equation 3.4.5-1.

$$\frac{\text{Rate,D}}{[GaH]^{2+}} = \frac{k_{alk}K_{dis}K_{phys}[C_3H_8]}{1+K_{dis}K_{phys}[C_3H_8]+K_{H_2}[H_2]} \qquad (3.7.4\text{-}8)$$

(b) Derivation of rate law for C_3H_8 dehydrogenation over $[GaH]^{2+}$ sites via carbenium mechanism.

The elementary steps outlined in Scheme 3.4.5-2 for C_3H_8 dehydrogenation over $[GaH]^{2+}$ sites are used here to derive a rate law in terms of kinetic and thermodynamic coefficients. The steady-state hypothesis was applied to all reactive surface intermediates. As discussed in section 3.7.4(a), we assumed the physisorption of C_3H_8 over $[GaH]^{2+}$ sites to form $[C_3H_8\text{-}[GaH]^{2+}]$ complexes (Step 1) is quasi-equilibrated. Theoretical calculations suggest that that rate-limiting step for the carbenium mechanism is the activation of the α C-H bond in C_3H_8 , resulting in a hydride transfer to the Ga^{3+} center and concomitant formation of a propyl carbenium fragment (Step 2). Accordingly, the dehydrogenation rate (per $[GaH]^{2+}$) can be expressed as equation (3.7.4-9).

$$\frac{\text{Rate,D}}{[GaH]^{2+}} = k_{carb}\theta_{phys} \qquad (3.7.4\text{-}9)$$

Here, Rate, D refers to the dehydrogenation rate, k_{carb} refers to the rate coefficient for α C-H carbenium activation and θ_{phys} refers to the surface coverage of $[C_3H_8\text{-}[GaH]^{2+}]$ complexes, the precursor to the rate-limiting transition state and is given by equation (3.7.4-10).

$$\theta_{phys} = \frac{[C_3H_8-[GaH]^{2+}]}{[L]} \qquad (3.7.4\text{-}10)$$

Here, $[C_3H_8\text{-}[GaH]^{2+}]$ refers to the surface concentration of $C_3H_8\text{-}[GaH]^{2+}$ complexes and [L] refers to the total density of active sites i.e $[GaH]^{2+}$ sites. [L] can be described in terms of the various reactive surface intermediates via equation (3.7.4-11). Inhibition by H_2 can be described via the formation of $[GaH_2]^+\text{-}H^+$ cation pairs, as shown in equation (3.7.4-3).

$$[L] = [GaH]^{2+} + [C_3H_8\text{-}[GaH]^{2+}] + [[GaH_2]^{+}\text{-}H^{+}] \quad (3.7.4\text{-}11)$$

Since the interaction of gas-phase C_3H_8 with $[GaH]^{2+}$ cations is predicted to be weak, the second term in equation (3.7.4-11) can be neglected. Together with equations (3.7.4-1), (3.7.4-9) – (3.7.4-11), a rate law for dehydrogenation via the carbenium mechanism can be derived, shown as equation (3.7.4-12) here and as equation 3.4.5-2 in section 3.4.5.

$$\frac{\text{Rate,D}}{[GaH]^{2+}} = \frac{k_{carb}K_{phys}[C_3H_8]}{1+K_{H_2}[H_2]} \quad (3.7.4\text{-}12)$$

It can be seen from equation (3.7.4-12), that in the absence of cofed H_2 at very low H_2 concentrations, equation (3.7.4-12) reduces to equation (3.7.4-13), which predicts the dehydrogenation rate to bear a first-order dependence on C_3H_8 at all C_3H_8 partial pressures.

$$\frac{\text{Rate,D}}{[GaH]^{2+}} = \frac{k_{carb}K_{phys}[C_3H_8]}{1} \quad (3.7.4\text{-}13)$$

(b) Derivation of rate law for C_3H_8 cracking over $[GaH]^{2+}$ sites via alkyl mechanism.

The elementary steps outlined in Scheme 3.4.5-3 for C_3H_8 cracking over $[GaH]^{2+}$ sites can be used to derive a rate expression containing kinetic and thermodynamic coefficients that describes the dependence of cracking rates on C_3H_8 and H_2 partial pressures. Equations (3.7.4-1), (3.7.4-2) and (3.7.4-3) also describe the surface intermediates relevant for C_3H_8 cracking, as outlined in Scheme 3.4.5-3. Theoretical calculations predict that the rate-limiting step for C_3H_8 cracking is the C-C bond attack of the anionic C_3H_7 fragment by the proximate Brønsted acid O-H group that constitutes the $[C_3H_7\text{-}GaH]^{+}\text{-}H^{+}$ cation pair (Step 3). Therefore, the rate of C_3H_8 cracking (per $[GaH]^{2+}$) can be expressed as equation (3.7.4-14).

$$\frac{\text{Rate,C}}{[GaH]^{2+}} = k_{crack}\theta_{alk} \quad (3.7.4\text{-}14)$$

Here, Rate, C refers to the C_3H_8 cracking rate, k_{crack} refers to the rate coefficient for C-C bond attack in Step 4 and θ_{alk} refers to the surface coverage of $[C_3H_7\text{-}GaH]^{+}\text{-}H^{+}$ cation pairs, the precursor to the cracking transition state. θ_{alk} can be described by equations (3.7.4-1, 2) and (3.7.4-5) – (3.7.4-7). Together, these equations lead to a rate expression for C_3H_8 cracking over $[GaH]^{2+}$ sites, in terms of C_3H_8 and H_2 partial pressures, shown as equation (3.7.4.15) here and equation 3.4.5-3 in section 3.4.5.

$$\frac{\text{Rate,C}}{[GaH]^{2+}} = \frac{k_{crack}K_{dis}K_{phys}[C_3H_8]}{1+K_{dis}K_{phys}[C_3H_8]+K_{H_2}[H_2]} \quad (3.7.4\text{-}15)$$

3.7.5 Derivations of equations relating experimentally measured rate coefficients to apparent and intrinsic activation enthalpies

Both dehydrogenation and cracking rates over Ga/H-MFI obey the behavior predicted by a Langmuir Hinshelwood kinetic model, shown in Equations 3.4.4-1 and 3.4.4-2 of the main text. At very low C_3H_8 pressures, experimentally observed dehydrogenation and cracking rates bear a first-order dependence on C_3H_8 pressure. The rate coefficient for this first order dependence (k_{app}) bears units of (mol/ mol Al*s*bar) can therefore be expressed as a product of an intrinsic, zero-order rate coefficient (k_{int}) with units of (mol/ mol Al*s) and a thermodynamic adsorption constant (K_{ads}) with units of (bar^{-1}), as shown in Equation (3.7.5-1).[134]

$$k_{app} = k_{int} * K_{ads} \qquad (3.7.5\text{-}1)$$

Here, the intrinsic rate coefficient k_{int} which purely reflects the dynamics between the transition state and the adsorbed state directly preceding it can be expressed with the aid of classical transition-state theory as Equation (3.7.5-2).[153]

$$k_{int} = \frac{\kappa k_B T}{h} \exp\left(-\frac{\Delta G_{int}}{RT}\right) \qquad (3.7.5\text{-}2)$$

Here, k_{int} is the instrinsic rate constant (s^{-1}), κ is the transmission coefficient, k_B is the Boltzmann constant, h is the Planck constant, T is temperature (K), ΔG_{int} is the intrinsic Gibbs free energy activation barrier, R is the gas constant. The thermodynamic adsorption constant K_{ads} which relates gas-phase C_3H_8 to the adsorbed state preceding the transition state can be expressed in terms of the Gibbs free energy of adsorption as Equation (3.7.5-3).[134]

$$K_{ads} = \exp\left(-\frac{\Delta G_{ads}}{RT}\right) \qquad (3.7.5\text{-}3)$$

The Gibbs free energy can be expressed in terms of enthalpy (ΔH) and entropy (ΔS), as shown in Equation (3.7.5-4)

$$\Delta G = \Delta H - T\Delta S \qquad (3.7.5\text{-}4)$$

Combining Equations (3.7.5-1) and (3.7.5-3) leads to Equation (3.7.5-5)

$$k_{app} = \frac{k_B T}{h} \exp\left(-\frac{\Delta G_{int}}{RT}\right) \exp\left(-\frac{\Delta G_{ads}}{RT}\right) \qquad (3.7.5\text{-}5)$$

Further simplification of Equation (3.7.5-5) leads to Equation (3.7.5-6)

$$k_{app} = \frac{k_B T}{h} \exp\left(-\frac{(\Delta G_{int} + \Delta G_{ads})}{RT}\right) \quad (3.7.5\text{-}6)$$

Equation (3.7.5-6) suggests that the apparent first order rate coefficient reflects the the Gibbs free energy of activation with respect to gas-phase C_3H_8 (ΔG_{app}) summarized as Equation (3.7.5-7).

$$\Delta G_{app} = \Delta G_{int} + \Delta G_{ads} \quad (3.7.5\text{-}7)$$

Combining Equation (3.7.5-4) with Equation (3.7.5-6) and (3.7.5-7), the first order rate coefficient can be expressed in terms of the apparent activation enthalpy (ΔH_{app}) and entropy (ΔS_{app}) , shown here as Equation (3.7.5-8)

$$\ln\left(\frac{k_{app}}{T}\right) = -\frac{\Delta H_{app}}{RT} + \frac{\Delta S_{app}}{R} + \ln\left(\frac{k_B}{h}\right) \quad (3.7.5\text{-}8)$$

Similarly, Equation (3.7.5-2) together with Equation (3.7.5-4) can be used to express the intrinsic rate coefficient (k_{int}) in terms of the intrinsic activation enthalpy (ΔH_{int}) and entropy (ΔS_{int}) , shown here as Equation (3.7.5-9)

$$\ln\left(\frac{k_{int}}{T}\right) = -\frac{\Delta H_{int}}{RT} + \frac{\Delta S_{int}}{R} + \ln\left(\frac{k_B}{h}\right) \quad (3.7.5\text{-}9)$$

Finally, the thermodynamic adsorption constant (K_{ads}) can be expressed in terms of the adsorption enthalpy (ΔH_{ads}) by combining Equation (3.7.5-3) and (3.7.5-4), shown here as Equation (3.7.5-10)

$$\ln(K_{ads}) = -\frac{\Delta H_{ads}}{RT} + \frac{\Delta S_{ads}}{R} \quad (3.7.5\text{-}10)$$

Plots of $\ln (k_{int}/T)$ vs $1/T$ lead to the extraction of ΔH_{app} , ΔH_{int} and ΔH_{ads} via linear regression methods. These plots are presented for dehydrogenation and cracking in Figures 3.7-5, 3.7-6 and 3.7-7.

3.7.6 Temperature dependence of dehydrogenation and cracking rate coefficients

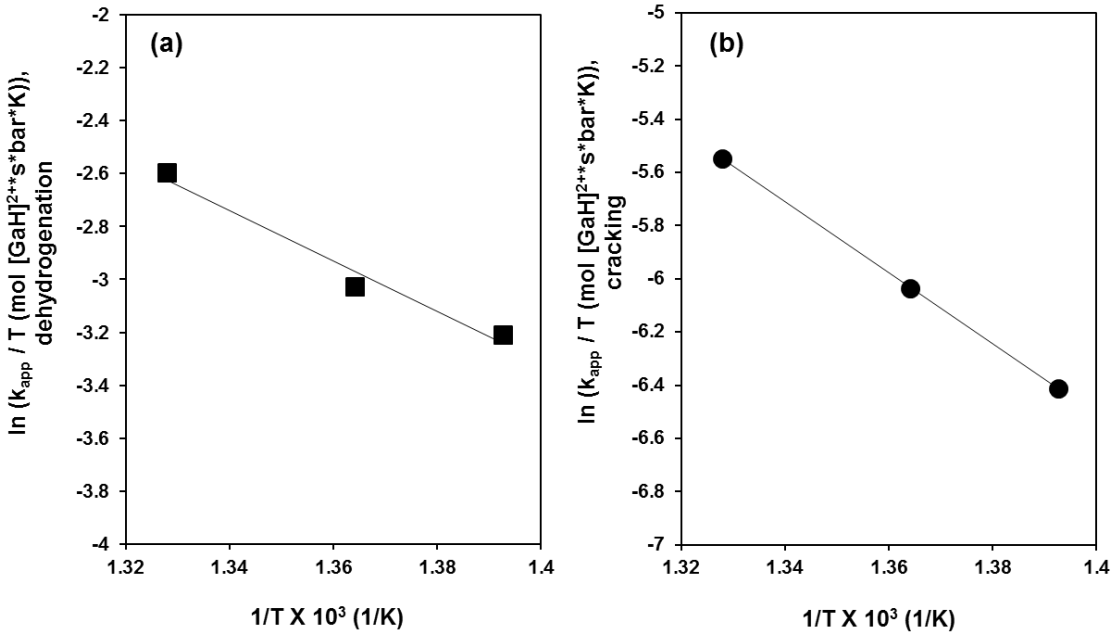

Figure 3.7-5. Plots of ln (k_{app} /T) vs 1/T for (a) C_3H_8 dehydrogenation (b) C_3H_8 cracking for the Ga/Al = 0.2 sample. Values for k_{app} (first order rate coefficients) were obtained by regression of rate data in Figures 3.4.4-1a-c and 3.4.4-2a-c to Equations 3.4.4-1 and 3.4.4-2. Rate coefficients were normalized to the fraction of $[GaH]^{2+}$ sites per Al_{tot} estimated via NH_3-TPD.[154] Solid lines reflect linear regression to Equation (3.7.5-8)

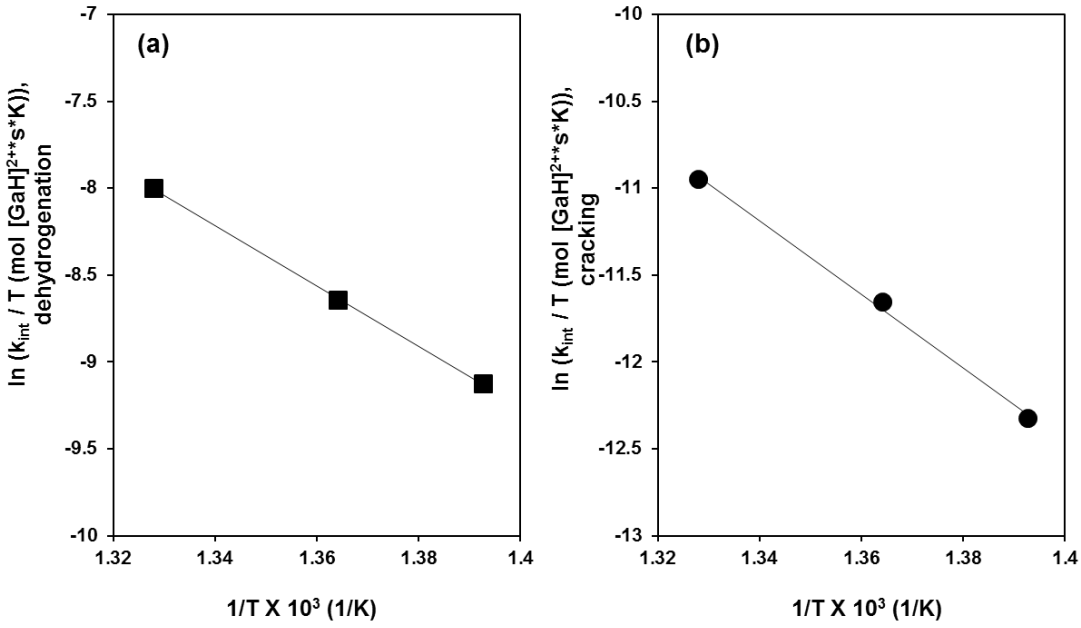

Figure 3.7-6. Plots of ln (k_{int} /T) vs 1/T for (a) C_3H_8 dehydrogenation (b) C_3H_8 cracking for the Ga/Al = 0.2 sample. Values for k_{int} (zero order rate coefficients) were obtained by regression of rate data in Figures 3.4.4-1a-c and 3.4.4-2a-c to Equations 3.4.4-1 and 3.4.4-2. Rate coefficients were normalized to the fraction of $[GaH]^{2+}$ sites per Al_{tot} estimated via NH_3-TPD.[154]Solid lines reflect linear regression to Equation (3.7.5-9).

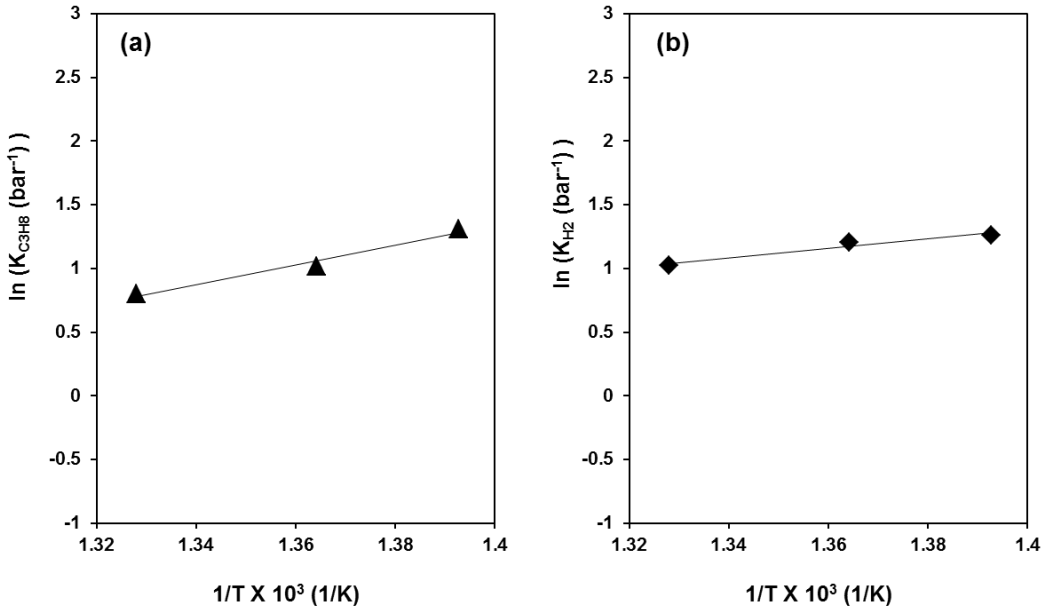

Figure 3.7-7. Plots of ln (K_{ads}) vs 1/T for (a) C_3H_8 adsorption (b) H_2 adsorption for the Ga/Al = 0.2 sample. Values for K_{ads} (adsorption constants) were obtained by regression of rate data in Figures 3.4.4-1a-c and 3.4.4-2a-c to Equations 3.4.4-1 and 3.4.4-2.Solid lines reflect linear regression to Equation (3.7.5-10).

3.7.7 Theoretical calculations

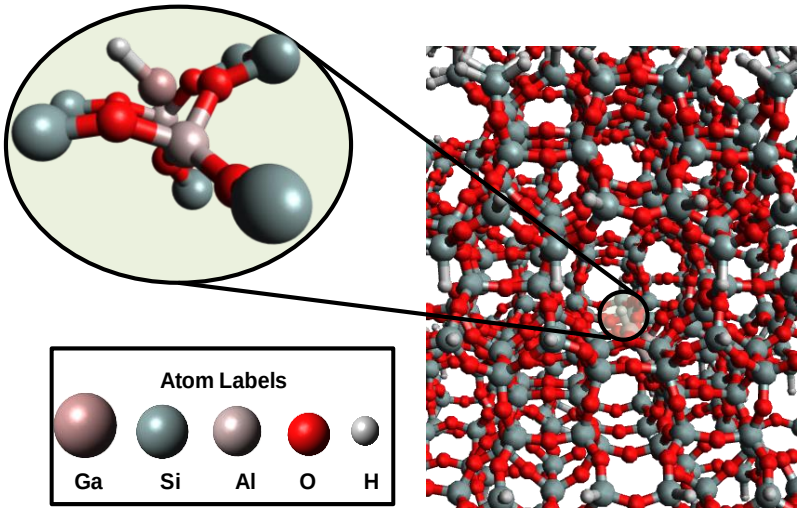

Figure 3.7-8. View along [100] axis of T437 atom MFI structure used to model $[GaH]^{2+}$ sites in Ga/H-MFI. The QM region consists of a T9 model which is electrostatically embedded in an MM region

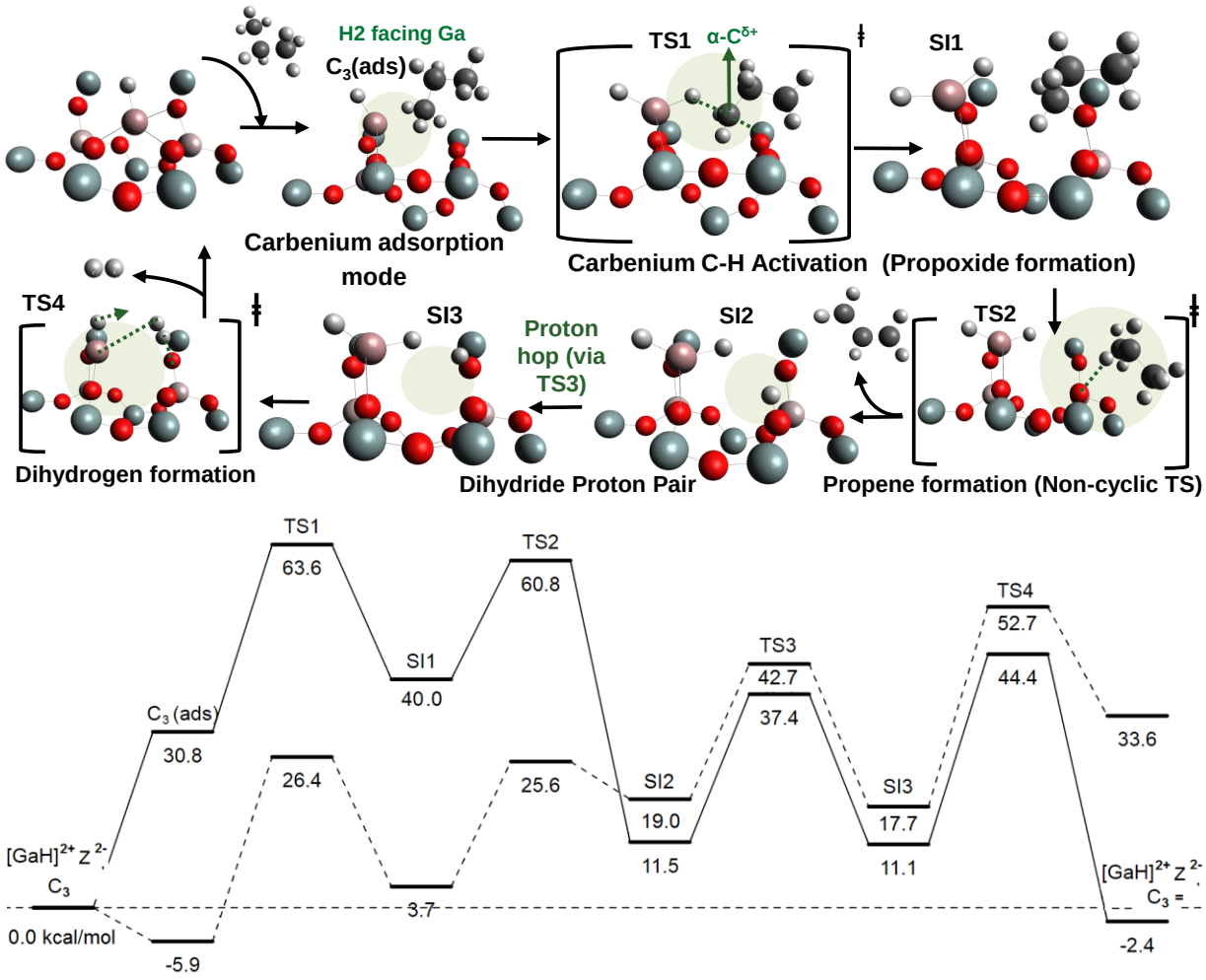

Figure 3.7-9. Free Energy (full lines) and enthalpy (dashed lines) landscapes for C_3H_8 dehydrogenation via carbenium mechanism on $[GaH]^{2+}$ sites, reported at 733 K, 10 kPa C_3H_8, 0.5 kPa C_3H_6 and 0.5 kPa H_2. Only the QM region from the QM/MM model has been displayed here to illustrate the elementary steps in this mechanism, using the key from Figure 3.7-8.

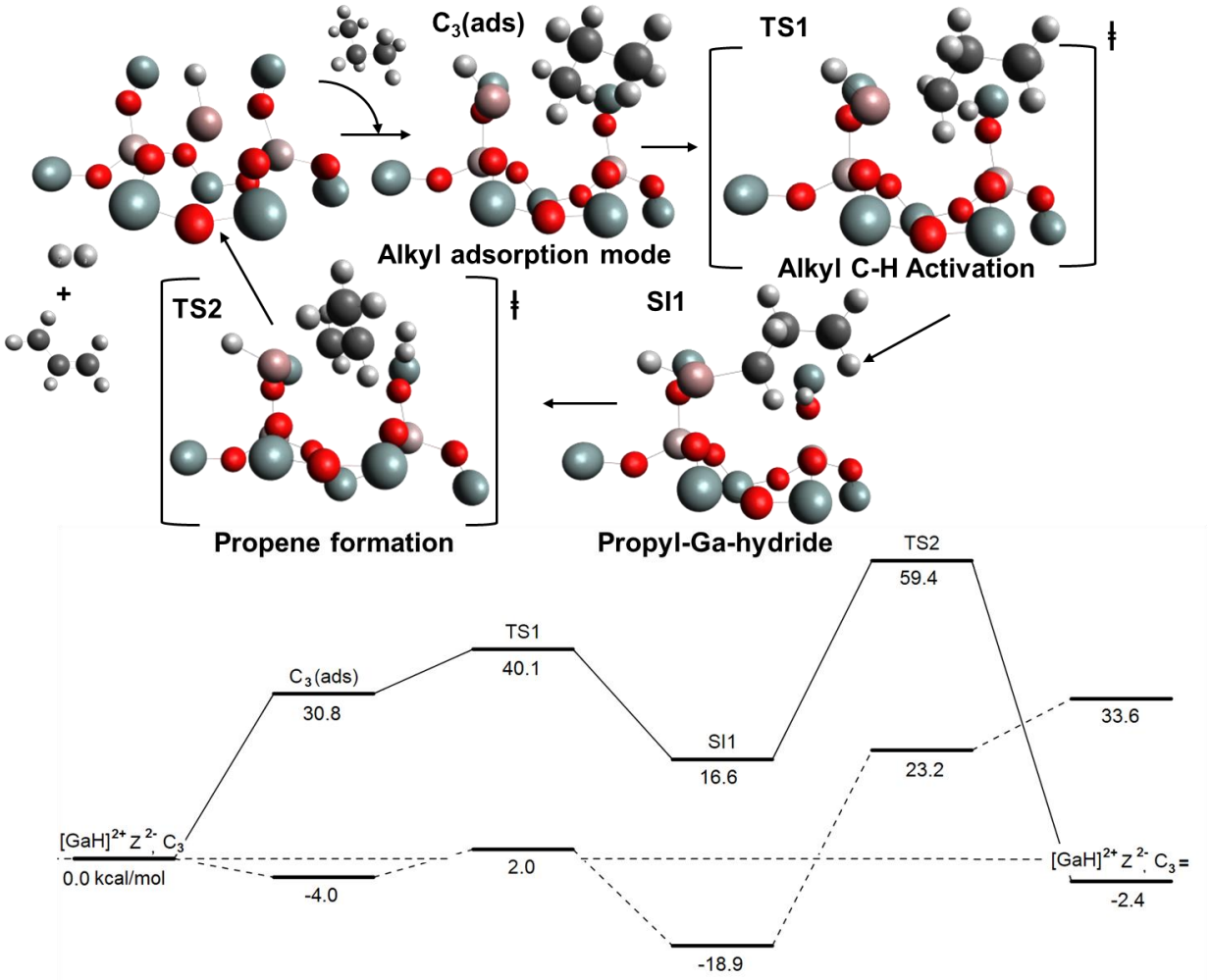

Figure 3.7-10. Free Energy (full lines) and enthalpy (dashed lines) landscapes for C_3H_8 dehydrogenation via alkyl mechanism on $[GaH]^{2+}$ sites, reported at 733 K, 10 kPa C_3H_8, 0.5 kPa C_3H_6 and 0.5 kPa H_2. Only the QM region from the QM/MM model has been displayed here to illustrate the elementary steps in this mechanism, using the key from Figure 3.7-8.

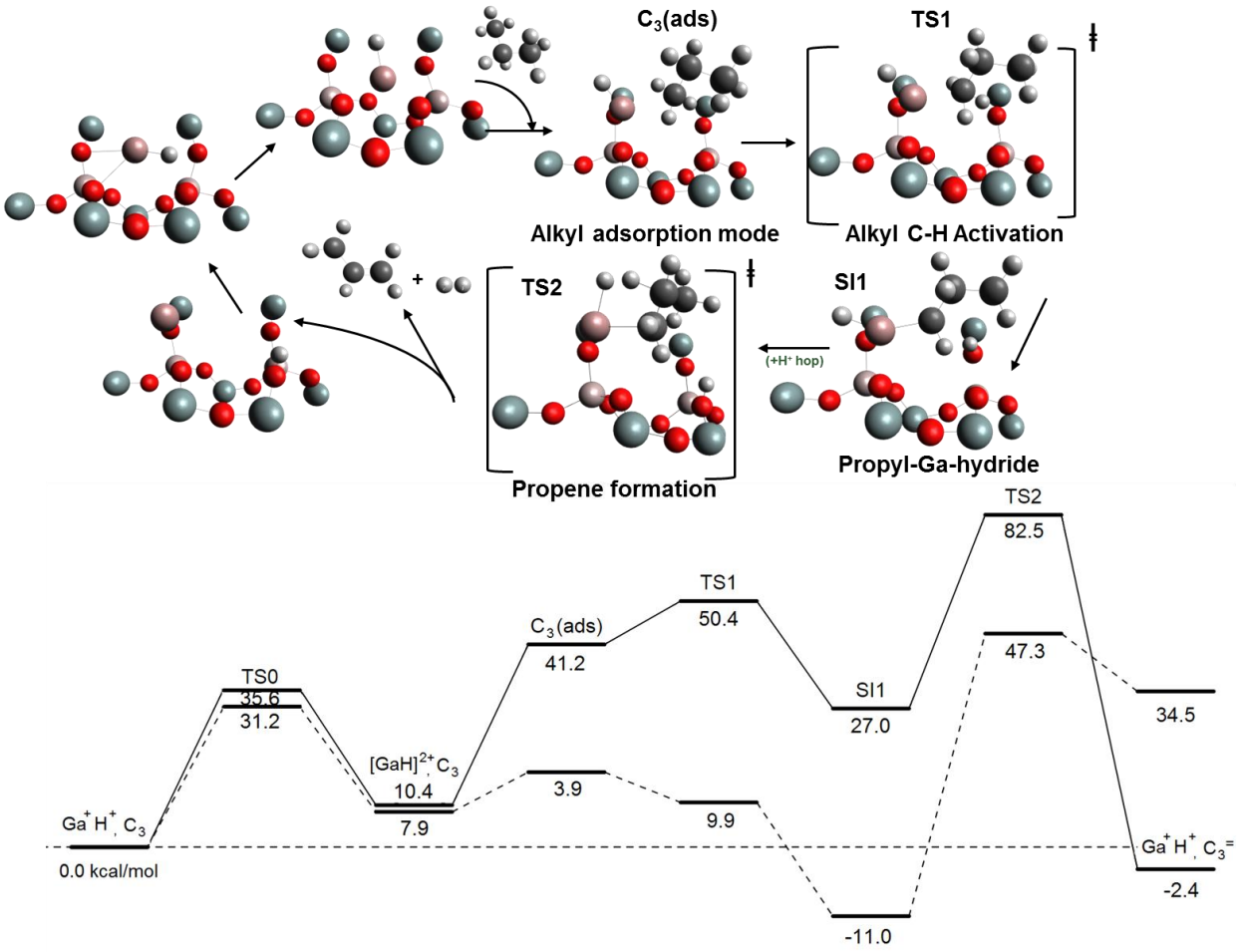

Figure 3.7-11. Free Energy (full lines) and enthalpy (dashed lines) landscapes for C_3H_8 dehydrogenation on Ga^+- H^+ sites, reported at 733 K, 10 kPa C_3H_8, 0.5 kPa C_3H_6 and 0.5 kPa H_2. Only the QM region from the QM/MM model has been displayed here to illustrate the elementary steps in this mechanism, using the key from Figure 3.7-8.

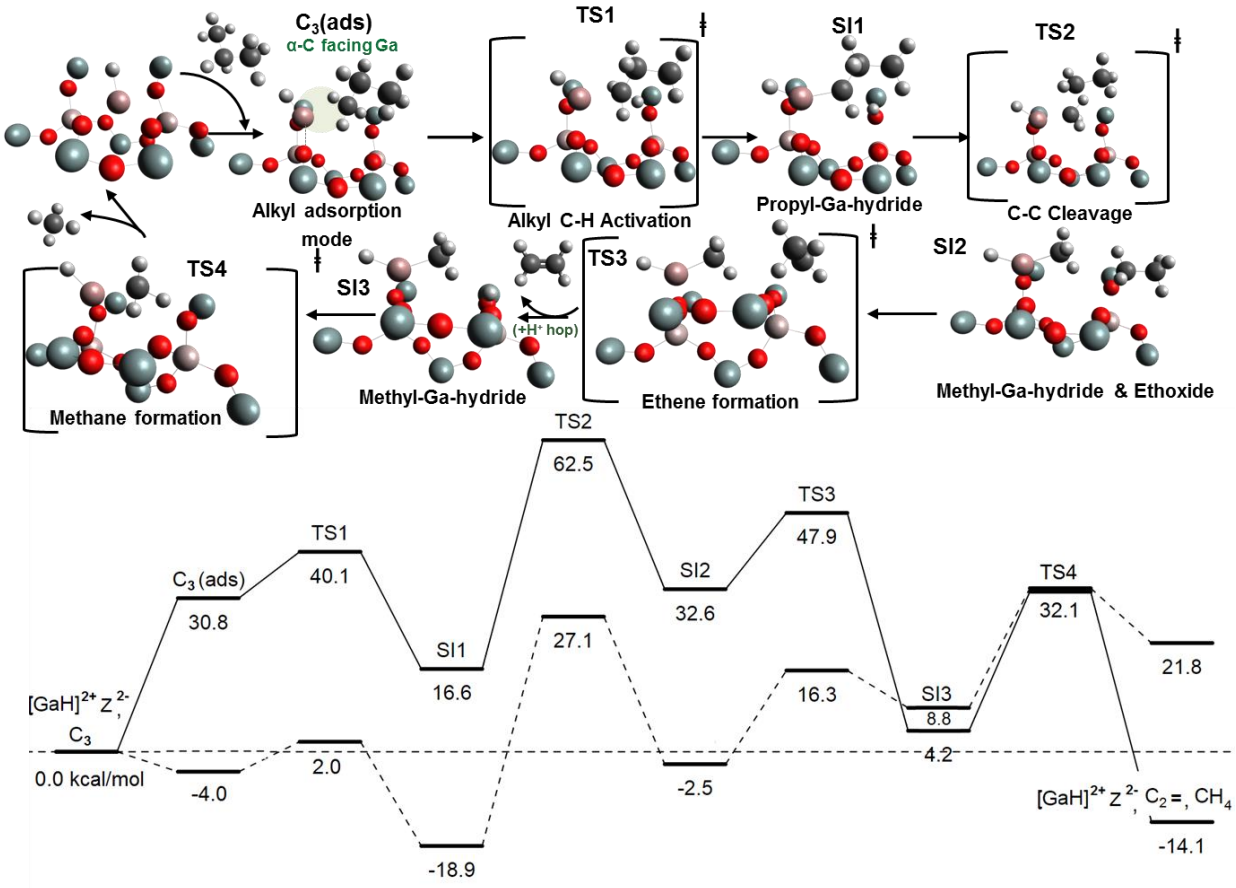

Figure 3.7-12. Free Energy (full lines) and enthalpy (dashed lines) landscapes for C_3H_8 cracking via alkyl mechanism on $[GaH]^{2+}$ sites, reported at 733 K, 10 kPa C_3H_8, 0.5 kPa C_2H_4, and 0.5 kPa CH_4. Only the QM region from the QM/MM model has been displayed here to illustrate the elementary steps in this mechanism, using the key from Figure 3.7-8.

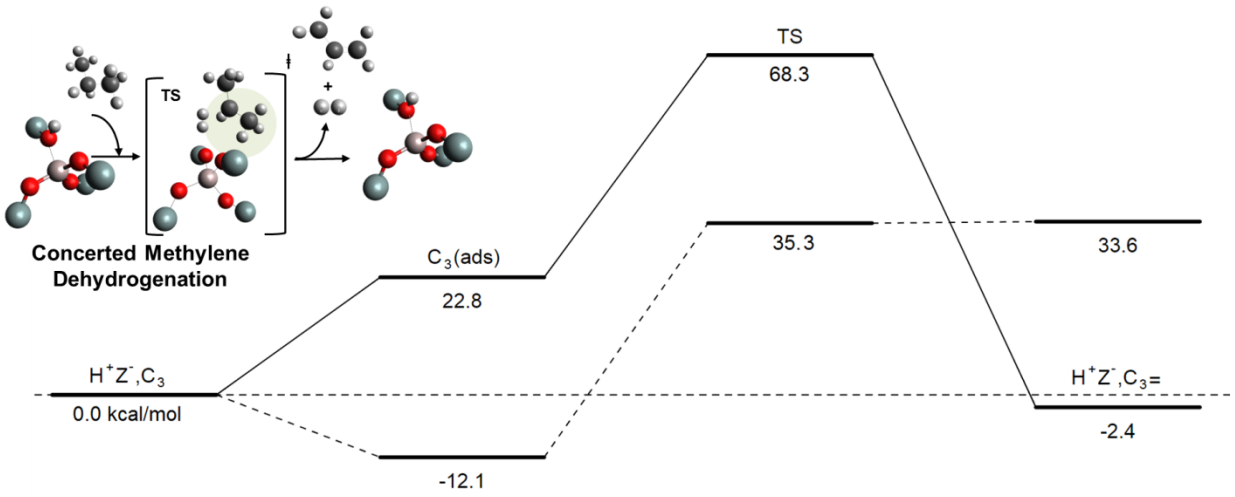

Figure 3.7-13. Free Energy (full lines) and enthalpy (dashed lines) landscapes for C_3H_8 dehydrogenation (methylene) on Brønsted acid O-H groups, reported at 733 K, 10 kPa C_3H_8, 0.5 kPa C_3H_6 and 0.5 kPa H_2. Only the QM region from the QM/MM model has been displayed here to illustrate the elementary steps in this mechanism, using the key from Figure 3.7-8.

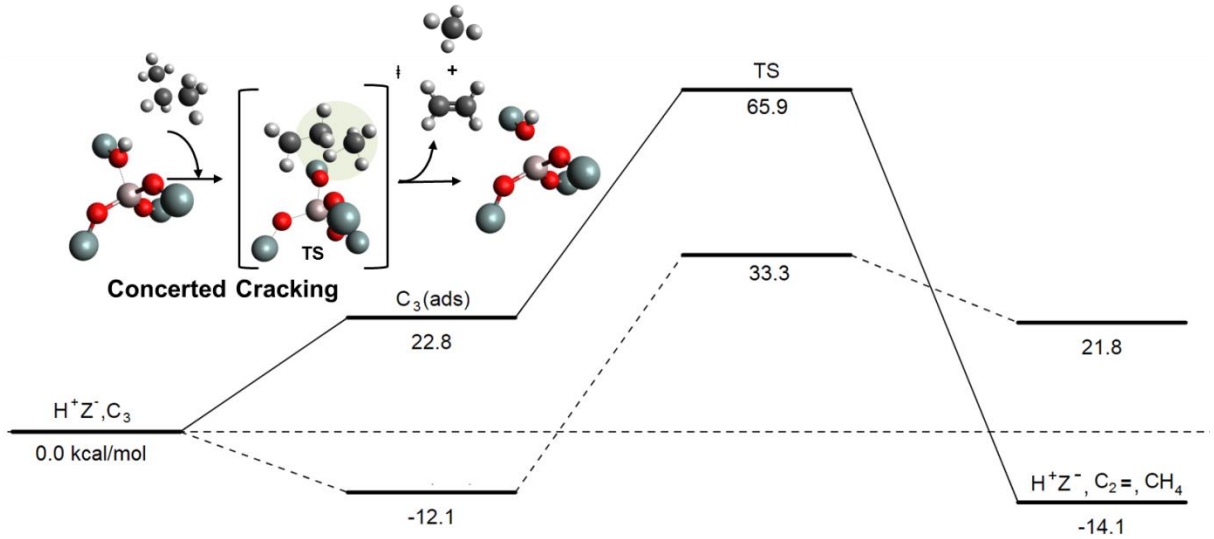

Figure 3.7-14. Free Energy (full lines) and enthalpy (dashed lines) landscapes for C_3H_8 cracking catalyzed by Brønsted acid O-H groups, reported at 733 K, 10 kPa C_3H_8, 0.5 kPa C_2H_4, and 0.5 kPa CH_4. Only the QM region from the QM/MM model has been displayed here to illustrate the elementary steps in this mechanism, using the key from Figure 3.7-8.

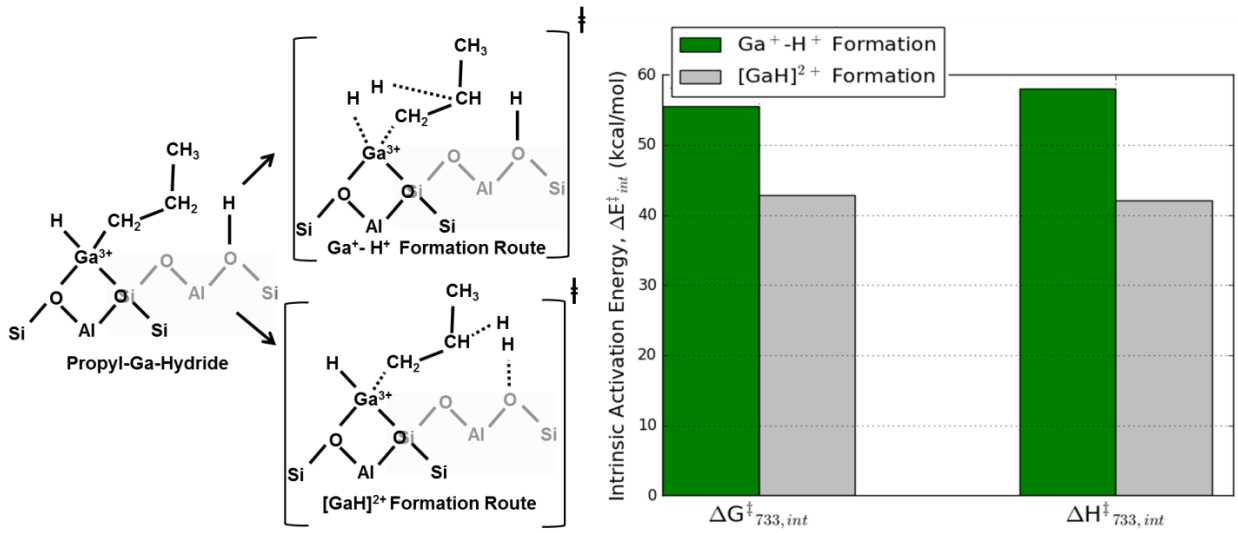

Figure 3.7-15. Free Energy and enthalpy barriers for C_3H_6 formation from C_3H_7-Ga-hydride intermediates, reported at 733 K, 10 kPa C_3H_8, 0.5 kPa C_3H_6, 0.5 kPa C_2H_4, and 0.5 kPa CH_4.

3.7.8 Estimation of exchange stoichiometries of Ga^{3+} species H_2-reduced Ga/H-MFI via NH_3-TPD and density of $[GaH]^{2+}$ cations in Ga/H-MFI samples

In a recently published study, our group developed protocols for the synthesis of well-defined and isolated Ga^{3+} cations in Ga/H-MFI via the vapor-phase exchange of dehydrated H-MFI with $GaCl_3$.[154] These materials were characterized using a number of spectroscopic and chemical probes in order to elucidate the structure of Ga^{3+} species under oxidizing and reducing conditions. These findings were also corroborated with the aid of theoretical calculations.

H_2 – temperature programmed reduction, infrared spectroscopy, Ga K-edge XANES (X-Ray Absorption Near Edge Spectroscopy) and EXAFS (Extended X-Ray Absorption Fine Structure) and theoretical calculations suggested at that at low Ga/Al ratios and under reducing anhydrous conditions, $[GaH]^{2+}$ and $[GaH_2]^{+}$-H^{+} cation pairs form in Ga/H-MFI.[154] The relative proportion of these cationic species can be determined on the basis of their exchange stoichiometry (H^{+} exchanged per Ga^{3+} atom) because $[GaH]^{2+}$ cations titrate 2 Brønsted acid O-H groups (H^{+}) per Ga^{3+} atom while $[GaH_2]^{+}$ cations titrate 1 Brønsted acid O-H group (H^{+}) per Ga^{3+} atom. The exchange stoichiometry of Ga/H-MFI samples was determined on the basis of titration of residual Brønsted acid O-H groups in Ga/H-MFI by NH_3. The quantity of NH_3 adsorbed was determined by means of NH_3 –temperature programmed desorption experiments.

These experiments were conducted over H_2-reduced Ga/H-MFI samples using protocols developed by Di Iorio et al. that enable the selective titration of residual Brønsted acid O-H groups in metal-exchanged zeolites, without concomitant titration of metal cations by NH_3.[19] The reader is referred to our characterization study of Ga/H-MFI for exact details of the experimental procedures used here to conduct NH_3-TPD experiments over Ga/H-MFI.[154] We find that NH_3-TPD spectra conducted in this fashion show only a feature at 660 K representative of NH_3 desorption from Brønsted acid O-H groups.[154] The quantity of NH_3 desorbed can be estimated by integrating the area under this feature. An assumption of a 1:1 stoichiometry between NH_3 desorbed and H^{+} leads to an estimate of the concentration of residual Brønsted acid O-H groups in the sample. This quantity together with the density of Brønsted acid O-H groups per Al_{tot} present in the parent in the H-MFI sample can be used to compute the fraction of Brønsted acid O-H groups replaced per Al_{tot} atom. When normalized by the Ga/Al ratio, the exchange stoichiometry – H^{+} exchanged per Ga^{3+} atom is obtained. The exchange stoichiometries for H_2-reduced Ga/H-MFI samples are shown in Table 3.7-2. Since $[GaH]^{2+}$ cations are expected to possess an exchange stoichiometry of 2 H^{+}_{exch} per Ga^{3+} atom, the density of $[GaH]^{2+}$ /Al can be readily estimated, as shown in Table 3.7-2. This density is similar within error (measured H^{+}_{exch}/Ga estimates have errors of ± 20%) to the expected density of $[GaH]^{2+}$ if a 100% of Ga at a Ga/Al ratio of 0.1 is $[GaH]^{2+}$ and further increases in Ga/Al ratio do not lead to the formation of any additional $[GaH]^{2+}$.

For the Ga/Al = 0.05 sample and 0.5 sample, errors in NH_3-TPD quantification were too large to accurately determine the density of $[GaH]^{2+}$ cations. On the basis of the trend observed in Table 3.7-2, where the fraction of $[GaH]^{2+}$ is maximum at a Ga/Al ratio of 0.1, it was assumed that the close distance ($\leq$ 5 Å) proximate cation-exchange sites that have been found to be required for the formation of $[GaH]^{2+}$ cations in our previous work[154] would be saturated at a Ga/Al ratio of 0.1. For Ga/Al ratios less than 0.1 therefore, it was assumed that a sufficient concentration of such cation-exchange sites would be available for Ga^{3+} siting and therefore a 100% of the Ga would be present at $[GaH]^{2+}$ cations. This analysis leads to an estimate of 0.05 $[GaH]^{2+}$ /Al_{tot} for a Ga/Al ratio of 0.05. For the Ga/Al = 0.5 sample, it was assumed any

additional Ga exceeding a Ga/Al ratio of 0.1 in this sample would not form $[GaH]^{2+}$ cations. Therefore, a value of 0.1 $[GaH]^{2+}/Al_{tot}$ was assumed for this sample.

Table 3.7-2. $H^{+}_{exch}/H^{+}_{total}$,H^{+}_{exch}/Ga and $[GaH]^{2+}/ Al_{tot}$ values measured via NH_3-TPD after H_2 treatment of Ga/H-MFI samples at 823 K.

Ga/Al	H^{+}_{exch}/H^{+}_{tot}	H^{+}_{exch}/Ga[1]	Predicted H^{+}_{exch}/G[2]	$[GaH]^{2+}/Al_{tot}$
0.1	0.2	2.2	2.0	0.1
0.2	0.3	1.5	1.5	0.1
0.3	0.4	1.2	1.3	0.1

[1] Obtained from NH_3-TPD profiles of H_2-treated Ga/H-MFI samples. NH_3/Al_{tot} values from these experiments were used together with eq (2) in order to estimate H^{+}_{exch}/H^{+}_{tot}. These values were then normalized by the Ga/Al_f ratio (obtained by dividing Ga/Al_{tot} values by the Al_f/Al_{tot} value for H-MFI, to reflect framework Al_f in order to obtain values of H^{+}_{exch}/Ga)

[2] Predicted values are based on the assumption that 100% of Ga at a Ga/Al ratio of 0.1 is present as $[GaH]^{2+}$ cations and no further $[GaH]^{2+}$ is product upon further increases in Ga content.

Chapter 4

4 The mechanism and kinetics of light alkane dehydrogenation and cracking over isolated Ga species in Ga/H-MFI

This work was originally coauthored with Alexis T. Bell who has approved the inclusion of this work in this dissertation.

4.1 Abstract

The objective of this study is to examine the mechanisms and kinetics of C_2H_6 and n-C_4H_{10} dehydrogenation and cracking over isolated Ga species in Ga/H-MFI and to compare these results to those reported previously for C_3H_8 dehydrogenation and cracking. C_2H_6 dehydrogenation is found to be catalyzed by both $[GaH]^{2+}$ and $[GaH_2]^+$ cations at similar turnover frequencies. Rate measurements over Ga/H-MFI containing predominantly $[GaH_2]^+$ cations reveal that C_2H_6 dehydrogenation rates exhibit a Langmuir-Hinshelwood dependence on C_2H_6 partial pressure at elevated temperatures (> 730 K), consistent with the involvement of chemisorbed $[C_2H_5\text{-}GaH]^+$ species. The reaction kinetics suggest that C_2H_6 dehydrogenation proceeds via heterolytic C-H cleavage of adsorbed C_2H_6 by $[GaH_2]^+$ cations to form H_2 and $[C_2H_5\text{-}GaH]^+$ species, which further decompose via β-hydride elimination to form C_2H_4. C_4H_{10} dehydrogenation and both terminal and central cracking are catalyzed exclusively by $[GaH]^{2+}$ cations. All three reactions exhibit a Langmuir-Hinshelwood dependence on C_4H_{10} partial pressure and are inhibited by H_2. Ratios of dehydrogenation to cracking (total) and terminal to central cracking are approximately independent of C_4H_{10} partial pressure consistent with the involvement of a common C_4H_{10} derived surface intermediate. The observed reaction kinetics are consistent with an alkyl mediated mechanism occurring over $[GaH]^{2+}$, analogous to that reported previously for C_3H_8 dehydrogenation and cracking over Ga/H-MFI. The mechanism proceeds via facile, heterolytic dissociation of adsorbed C_4H_{10} to form $[sec\text{-}C_4H_9\text{-}GaH]^+\text{-}H^+$ cation pairs. Dehydrogenation then proceeds via β-hydride elimination from this intermediate, while terminal and central cracking proceed via H^+ attack of the terminal and central C-C bonds of the alkyl fragment by the proximal Brønsted acid O-H group. The apparent and intrinsic activation enthalpies extracted from the measured kinetics are consistent with those determined from theoretical analysis of the mechanism.

4.2 Introduction

Gallium-exchanged MFI zeolite (Ga/H-MFI) has been identified as an effective catalyst for the conversion of light alkanes – ethane (C_2H_6), propane (C_3H_8), and n-butane (n-C_4H_{10}) – to alkenes and aromatics via dehydrogenation and dehydrocyclization.[29,123] Over the H-form of MFI (H-MFI), Brønsted acid O-H groups catalyze the dehydrogenation and cracking of light

alkanes to alkenes and lower molecular weight alkanes with similar selectivities, under conditions where monomolecular conversion pathways are prevalent.[11,25,29,139] By contrast, Ga/H-MFI exhibits higher activity than H-MFI and superior selectivities to alkenes and aromatic products compared to H-MFI under the same reaction conditions.[27] Increasing demand for light alkenes together with the low cost of C_2H_6 and C_3H_8 from the condensable fraction of natural gas and the availability of C_4H_{10} from naphtha have led to renewed interest in examining Ga/H-MFI as a catalyst for the dehydrogenation of light alkanes to alkenes, which are important feedstocks for the chemical industry.[2]

Many studies have shown that extra-framework Ga species are the active species for alkane dehydrogenation or dehydrocyclization over Ga/H-MFI.[31,155] While multiple Ga species have been identified in Ga/H-MFI, there has been little consensus regarding the structure of the Ga species and their catalytic role.[32,37,39,40,47,48,51,54,132] These studies have shown that the proportions of isolated and proximate cation-exchange sites in MFI, the interatomic distance between cation exchange sites, and conditions of catalyst pretreatment affect the structure and distribution of Ga species.[33,35,37,39,45,50,130,133,156,157] As a result, many different Ga structures have been proposed to be catalytically relevant for alkane dehydrogenation.[27,32,37,50,51,54,62] These include Ga^+, $[GaO]^+$, $[Ga_2O_2]^{2+}$, $[GaH_2]^+$, $[GaH]^{2+}$, Ga^+-H^+ cation pairs and Ga_2O_3 clusters.[27,32,36–40,47,49–51,54] Identification of which structures are catalytically active has been challenging because the conventional protocol for preparation of Ga/H-MFI, which is based on wetness impregnation of H-MFI with $Ga(NO_3)_3$ followed by calcination and H_2 reduction, produces cationic Ga species of unknown structure, as well GaO_x clusters.[29,42]

Isolated Ga^{3+} species can be produced via the preparation of Ga/H-MFI using a vapor-phase exchange procedure involving dehydrated H-MFI and $GaCl_3$.[133] Under reducing and anhydrous conditions, $[GaH]^{2+}$ cations, which are stable at proximate cation-exchange sites with framework Al-Al distances ≤ 5 Å, form at low Ga/Al ratios and are the predominant species at a Ga/Al ratio of 0.1. Increasing the Ga/Al ratio from 0.1 to 0.3, results in the titration of proximate cation-exchange sites with framework Al-Al distances > 5 Å by $[GaH_2]^+$-H^+ cation pairs.

The conversion of light alkanes to aromatics over Ga/H-MFI involves an interplay between concurrent dehydrogenation, cracking, oligomerization, hydride transfer and cyclization that may be catalyzed by both Ga species and residual Brønsted acid O-H groups.[29,46] The most energetically demanding step of this sequence is the initial dehydrogenation of the alkane to its corresponding alkene and H_2.[27] As a result, several studies have been devoted to understanding the mechanism of alkane dehydrogenation to alkenes over Ga/H-MFI.[29]

We have recently probed the mechanism and kinetics of C_3H_8 dehydrogenation and cracking over Ga/H-MFI samples prepared via vapor-phase exchange of H-MFI with $GaCl_3$.[158] We found that C_3H_8 dehydrogenation and cracking of C_3H_8 are catalyzed exclusively by $[GaH]^{2+}$ cations at low Ga/Al ratios and the specific rates (normalized per Al_{tot}) at which these reactions proceed are two orders and one order of magnitude, respectively, higher than the specific rates (normalized per Al_{tot}) for the corresponding reactions occurring over Brønsted acid O-H groups. $[GaH_2]^+$ cations, which form at Ga/Al ratios > 0.1, are inactive for both reactions. Experimental and theoretical studies suggest that both reactions proceed via facile, heterolytic activation of C-H bonds in C_3H_8 over $[GaH]^{2+}$ to form $[C_3H_7\text{-}GaH]^+$-H^+ cation pairs. The rate-limiting step for the dehydrogenation reaction is β-hydride elimination from $[C_3H_7\text{-}GaH]^+$ to form C_3H_6 and H_2, and restore $[GaH]^{2+}$, the active site. On the other hand, cracking proceeds via attack of the C-C bond in the $[C_3H_7\text{-}GaH]^+$ fragment by the proximal Brønsted acid O-H group in the $[C_3H_7$-

$GaH]^+$-H^+ cation pair. Selectivity towards either reaction pathway is governed by the difference in the intrinsic free energy barriers between the two pathways.

A number of theoretical studies have examined the mechanism for the dehydrogenation of C_2H_6 over Ga^+ , $[GaH_2]^+$, $[GaO]^+$, $[Ga_2O_2]^{2+}$, $[GaH]^{2+}$ cations in Ga-exchanged zeolites; however, these studies do not lead to a consensus regarding the relative activity of these species.[38,40,47–49,51–54] Recently, Mansoor et al. reported in a computational study that $[GaH]^{2+}$ and $[GaH_2]^+$ cations are similarly active for C_2H_6 dehydrogenation although the former structure catalyzes the reaction via an alkyl or a carbenium mechanism while the latter structure catalyzes the reaction via a three-step mechanism involving $[C_2H_5\text{-}GaH]^+$ intermediates.[49] Experimental studies of the dehydrogenation of C_2H_6 over Ga/H-MFI are scarce. Bandiera et al. have reported an activation energy of 39 kcal/mol for C_2H_6 dehydrogenation over Ga/H-MFI prepared by supporting Ga_2O_3 on H-MFI, whereas Dooley et al. have examined the effects of different catalyst pretreatments and gaseous additives on the rate of C_2H_6 dehydrogenation over Ga/H-MFI.[156,159] However, neither of these studies provided evidence for the presence isolated Ga species in Ga/H-MFI and the reaction mechanism and kinetics were not examined in detail.[159]

In contrast to C_2H_6 dehydrogenation, theoretical as well as experimental reports examining n-C_4H_{10} dehydrogenation and cracking over Ga/H-MFI are relatively few in number. Recently, Mansoor et al. have shown via theoretical analysis that $[GaH]^{2+}$ cations are more active for n-C_4H_{10} dehydrogenation than $[GaH_2]^+$ cations and that the former structure activates n-C_4H_{10} via an alkyl mechanism, similar to the one reported for C_3H_8 dehydrogenation.[49] More recently, Schreiber et al. have reported that the rate of n-C_4H_{10} dehydrogenation over Ga/H-MFI is a factor of five lower than the rate of C_3H_8 dehydrogenation, even though the measured activation energies for the two reactants are similar.[54] The effects of Ga loading, the mechanism by which C_4H_{10} dehydrogenation occurs, and whether Ga^{3+} structures also catalyze cracking of central and terminal C-C bonds in C_4H_{10} are questions that have not yet been addressed adequately.

In this study, we seek to determine the site requirements, the kinetics and the mechanisms of C_2H_6 dehydrogenation and n-C_4H_{10} dehydrogenation and cracking over Ga/H-MFI prepared via vapor phase exchange of H-MFI with $GaCl_3$. The presence of isolated and well-defined $[GaH]^{2+}$ and $[GaH_2]^+$ cations under reducing conditions in these materials enables us to derive a structure-function relationship between the chemical structure of Ga^{3+} cations and their reactivity towards alkane reactants of varying chain length under different reaction conditions. In doing so, we are able to provide insight that will enable rational catalyst design of dehydrogenation and dehydrocyclization catalysts containing Ga^{3+} moieties that are tailored to be reactive for the conversion of a given alkane reactant. This study also aims to study the ability of Ga species to activate specific C-H and C-C bonds in alkanes. Reactions of n-C_4H_{10} are well-suited for this purpose, because the activation of specific C-H bonds in C_4H_{10} via dehydrogenation leads to the formation of either 1 or 2-butene while the activation of specific C-C bonds via cracking leads to the formation of either terminal or central cracking products.

We find that the site requirements for reactions of light alkanes over Ga/H-MFI vary with the carbon chain length of alkane reactants. The dehydrogenation of C_2H_6 to C_2H_4 and H_2 is catalyzed by both $[GaH]^{2+}$ and $[GaH_2]^+$ cations with similar turnover frequencies (1.1×10^{-3} mol/mol Ga*s at 2 kPa C_2H_6 and 753 K).The reaction kinetics are consistent with the occurrence of a 4-step 'alkyl' mediated mechanism for C_2H_6 dehydrogenation over $[GaH_2]^+$ cations, a finding that is well supported by theoretical calculations. By contrast, the dehydrogenation, terminal and central cracking of n-C_4H_{10} is catalyzed exclusively by $[GaH]^{2+}$ cations in Ga/H-MFI at turnover frequencies that are 3 orders, 2 orders and 1 order of magnitude

higher than the corresponding turnover frequencies of these reactions over H-MFI under identical conditions. $[GaH_2]^+$ cations are inactive for alkane reactants with carbon chain length greater than 2 due to the considerable entropic penalties associated with the transition state for the initial C-H activation step. The reaction kinetics suggest that all three reactions of C_4H_{10} proceed over $[GaH]^{2+}$ via the formation of $[sec\text{-}C_4H_9\text{-}GaH]^+\text{-}H^+$ species with a mechanism that is analogous to the alkyl mechanism for C_3H_8 dehydrogenation and cracking over Ga/H-MFI.[158] Over $[GaH]^{2+}$ cations, dehydrogenation produces both 1-butene and 2-butene. Terminal cracking is favored over central cracking when reactions occur over $[GaH]^{2+}$ cations because the latter undergoes greater entropy losses at the rate limiting transition state.

4.3 Experimental

4.3.1 Preparation of H-MFI and Ga/H-MFI samples

NH_4-MFI (Zeolyst, CBV 3024E) was converted to its H-form by placing 1-2 g of zeolite in quartz calcination boats, which were then heated at 2 K min^{-1} from ambient temperature to 773 K, and held at this temperature for 4 h. All steps were conducted in a stream of dry air (Praxair, ultrazero) flowing at 100 cm^3 min^{-1}. The Si/Al ratio of this sample was measured to be 16.5 ± 1.0 based on ICP-OES (Galbraith Laboratories, Knoxville, TN). Ga/H-MFI samples (Ga/Al = 0.05 to 0.5) were prepared using the vapor-phase exchange of Brønsted acid O-H groups in H-MFI with $GaCl_3$ vapor. The detailed synthetic protocol used is described in Ref. [133]

4.3.2 Reaction rate measurements

Reactions of C_2H_6 and n-C_4H_{10} were investigated using a quartz flow reactor (30.5 cm in length and 0.64 cm in outer diameter). For reactions of C_2H_6, catalyst charges (typically ~ 20 mg) were placed on a quartz wool plug fitted at a pinch inside the quartz reactor. For reactions of n-C_4H_{10}, a small amount of catalyst was used (~ 4 mg) in order to attain C_4H_{10} conversions of less than 4%, and the catalyst charge was diluted with inert SiO_2 (SiliaFlash 150A, ~ 14-16 mg). The temperature of the catalyst bed was monitored by a K-type thermocouple (Omega) connected to a temperature controller (Omega). The quartz reactor was heated by means of a cylindrical ceramic furnace. The flowrate of gases fed to the reactor was measured using mass flow controllers (Porter).

Prior to measuring reaction rates, the catalyst bed was heated at 5 K min^{-1} from ambient temperatures to 773 K in a stream of flowing dry air (Praxair, ultra zero, 100 cm^3 min^{-1}) and held at this temperature for 1 h. The reactor was then purged with He (Praxair, UHP, 100 cm^3 min^{-1}) for 5 min after which the flow was switched to a stream of 2.5% H_2 /He (Praxair, CSG, 100 cm^3 min^{-1}). The catalyst bed was exposed to H_2/He for 1 h in order to convert oxidized Ga^{3+} species into catalytically active GaH_x species.[133,158]

Following reduction, the catalyst bed was exposed to mixtures of pure C_2H_6 (99.999% purity, Matheson) or n-C_4H_{10} (99.999% purity, Matheson) diluted in He to attain alkane partial pressures of 0.5 kPa – 14 kPa. Experiments involving co-fed H_2 were conducted by diluting the alkane/He feed with a stream of 2.5% H_2/He (Praxair, CSG). Reactions were conducted under a differential conversion (< 9 % product conversion). In the case of n-C_4H_{10} reactions, reactant conversions were maintained below 4 % to avoid extensive catalyst deactivation. Selectivities were defined on a C basis as well as alkane basis. C_2H_6 dehydrogenation rates were estimated on the basis of the concentration of C_2H_4 products while n-C_4H_{10} dehydrogenation rates were

estimated on the basis of the sum of the concentrations of butene isomer products (1-butene, cis, trans-2-butene, isobutene), while cracking reactions were estimated on the basis of the concentration of alkane products produced during cracking (C_2H_6 for central cracking and CH_4 for terminal cracking). Reactions rates were fitted to Langmuir-Hinshelwood models using a non-linear least squares regression. Activation enthalpies were derived from rate coefficients measured at different reaction temperatures and the application of equations derived from transition state theory.[153,158]

Measurements of reaction rates were also conducted as a function space time (defined as mol Al_{tot}*s/mol alkane) in order to assess the effects of product inhibition and secondary reactions on the rates of primary reactions. Rates were extrapolated to zero space time in order to eliminate these effects. Deactivation did not exceed 10% in a typical runs and was corrected for by periodically measuring reaction rates at a reference condition (2 kPa C_2H_6/ He, τ = 7.0 mol Al_{tot}*s/ mol C_2H_6 for C_2H_6 reactions and 0.9 kPa C_4H_{10} / He, τ = 3.5 mol Al_{tot}*s/mol C_4H_{10} for n-C_4H_{10} reactions). Products of the reactions were conveyed to a sampling loop via a heated transfer line and analyzed periodically by gas chromatography (Agilent 7890A). Reactants and products were separated by a capillary column (Agilent 1909IP-Q02, 25 m X 350 μm X 10 μm) and were detected and quantified using a Flame Ionization Detector (FID). Response factors for the FID were estimated by measuring the detector response for known concentrations of hydrocarbons.

4.4 Results and Discussion

4.4.1 Effects of Ga content on the rate of C_2H_6 dehydrogenation

The reaction of C_2H_6 over H-MFI and Ga/H-MFI leads to the formation of C_2H_4 and H_2 via dehydrogenation. Under the conditions prevalent during our measurements (conversions < 1%), C_2H_4 was the only product detected. At higher conversions and partial pressures of C_2H_6 and over Ga/H-MFI, only trace concentrations of CH_4 and C_3H_6 were detected, suggesting that these products form via secondary pathways.

Figure 4.4.1-1a shows the dependence of the rate of C_2H_6 dehydrogenation (at 2 kPa C_2H_6 and 753 K) normalized per Al_{tot} atom on the Ga/Al ratio for a range of Ga/Al ratios (Ga/Al = 0-0.5). These rates were extrapolated to zero space time in order to account for the effects of product inhibition by C_2H_4 and H_2 on C_2H_6 dehydrogenation rates measured at finite space times (see section 4.7.4). The results reveal a linear increase in the rate of C_2H_6 dehydrogenation with increasing Ga/Al ratio, suggesting that an increase in Ga content leads to an increase in the concentration of active sites with identical activity. At the highest Ga/Al ratio of 0.5, the rate of C_2H_6 dehydrogenation over Ga/H-MFI is about 11 times higher than the corresponding rate (per Al_{tot}) measured over H-MFI under similar conditions (see sections 4.7.1 and 4.7.3 for a discussion regarding the observed kinetics of C_2H_6 dehydrogenation over H-MFI) . C_2H_6 dehydrogenation rates normalized per Ga atom (after subtracting the rate contribution (per Al_{tot}) over H-MFI) , shown in Figure 4.4.1-1b are independent of the Ga/Al ratio across a broad range of Ga content, suggesting that the activity of Ga^{3+} structures across this range of Ga/Al ratios is identical.

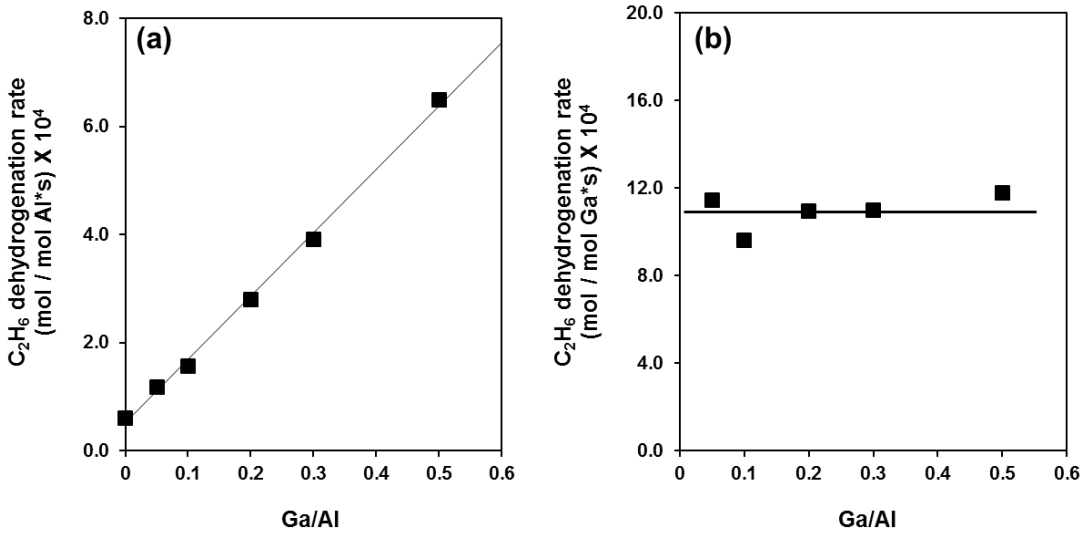

Figure 4.4.1-1. (a) Turnover frequencies for C_2H_6 dehydrogenation (normalized per Al_{tot} atom) as a function of Ga/Al ratio and (b) Turnover frequencies for C_2H_6 dehydrogenation (normalized per Ga atom) as a function of Ga/Al ratio. Rates were measured at 2 kPa C_2H_6 /He at 753 K and extrapolated to zero space time. Solid lines are guidelines for the eye. Samples were reduced in H_2 at 773 K for 1 h prior to measurement of reaction rates.

Our characterization of Ga/H-MFI has indicated that for Ga/Al ratios ≤ 0.3, Ga species are present as isolated cationic species.[133] In the H_2-reduced state, $[GaH]^{2+}$ cations are the predominant active species at a Ga/Al ratio of 0.1.[133] With an increase in the Ga/Al ratio from 0.1 to 0.3, $[GaH_2]^+$-H^+ cation pairs form in increasing concentration.[133] Both structures require the presence of proximate cation-exchange sites.[133] The monotonic increase in C_2H_6 dehydrogenation rates as a function of Ga/Al ratio, for samples with Ga/Al ratios less than 0.3 in Figure 1a suggests that $[GaH]^{2+}$ and $[GaH_2]^+$-H^+ cation pairs present in these samples are virtually identical in activity.

In the oxidized state, an increase in the Ga content of Ga/H-MFI in excess of a Ga/Al ratio of 0.3 leads to saturation of proximate cation-exchange sites and the concomitant formation of neutral GaO_x oligomers.[133] Figures 4.4.1-1a and b also show that for Ga/H-MFI samples which contain Ga in excess of the saturation stoichiometry of the proximate cation-exchange sites (i.e., for Ga/Al = 0.5), the catalyst continues to be active for C_2H_6 dehydrogenation at a rate per Ga that is similar to that for Ga sites present in Ga/H-MFI with Ga/Al < 0.3. This finding suggests that either GaO_x oligomers that are present in the Ga/Al = 0.5 sample are as active as cationic GaH_x species or that reduction in H_2 prior to reaction, transforms these neutral clusters into cationic GaH_x species. Dooley et al. has shown that GaO_x agglomerates in Ga/H-MFI catalysts are much less active for C_2H_6 dehydrogenation than cationic Ga species.[156] Therefore, it is likely GaO_x agglomerates in the Ga/Al = 0.5 sample transform into cationic GaH_x species upon pre-reduction of the catalyst samples in H_2. In agreement with this proposal, we find that the exchange stoichiometry of the Ga/Al = 0.5 sample increases from 0.55 H^+ (Brønsted acid O-H groups) exchanged per Ga atom for the catalyst in the oxidized state to 0.84 H^+ exchanged per Ga atom upon H_2-reduction (measured using NH_3-TPD). This increase in the fraction of exchanged Brønsted acid O-H groups and the resulting near-unity exchange stoichiometry

($[GaH_2]^+$ is expected to have an exchange stoichiometry of 1 H^+exchanged per Ga), is consistent with the re-dispersion of GaO_x agglomerates as $[GaH_2]^+$ cations located at residual isolated cation-exchange sites in the Ga/Al = 0.5 sample. The increase in catalytic activity with Ga/Al ratio is therefore a result of the increase in the concentration of $[GaH_2]^+$ cations with Ga content, that are identical in activity whether they are present at isolated cation-exchange sites or at cation-exchange sites that are proximate. These site requirements for C_2H_6 dehydrogenation over Ga/H-MFI vary markedly from those for C_3H_8 dehydrogenation[158] or n-C_4H_{10} dehydrogenation (see section 4.4.4 and beyond) both of which are catalyzed exclusively by $[GaH]^{2+}$ cations present in Ga/H-MFI at Ga/Al ratios below 0.3. The identical activity of $[GaH]^{2+}$ cations and $[GaH_2]^+$ cations for C_2H_6 dehydrogenation is supported by theoretical calculations reported by Mansoor et al., which predict similar apparent free energy activation barriers for C_2H_6 dehydrogenation over both structures.[49]

4.4.2 Effects of C_2H_6 partial pressure and temperature on C_2H_6 dehydrogenation over Ga/H-MFI

The effects of C_2H_6 partial pressure on C_2H_6 dehydrogenation turnover rates (normalized per Ga atom) are shown in Figure 4.4.2-1 for three different temperatures – 733 K, 753 K and 773 K. As before, rates measured at finite space times were extrapolated to zero space time in order to mitigate the effects of product inhibition on measured kinetics. At low partial pressures, dehydrogenation rates approach a first-order dependence on C_2H_6 partial pressure, while at high partial pressures these rates approach a zero-order dependence on C_2H_6 partial pressure. The Langmuir-Hinshelwood dependence of C_2H_6 dehydrogenation rates on reactant partial pressure is observed at all three temperatures in Figure 4.4.2-1 and is similar to that observed for C_3H_8 dehydrogenation and cracking over Ga/H-MFI[158]. The change in reaction order as a function of partial pressure implies the involvement of strongly-bound C_2H_6 reactive intermediates which saturate active sites at sufficiently high partial pressures, resulting in observed zero-order rate dependences. The rate data at each temperature in Figure 4.4.2-1 can be fit to a rate equation of the functional form given by Equation 4.4.2-1.

$$C_2H_6 \text{ dehydrogenation rate} = \frac{\alpha_e[C_2H_6]}{1+\beta_e[C_2H_6]} \qquad (4.4.2\text{-}1)$$

In Equation 4.4.2-1, the dehydrogenation rate has units of mols/mols Ga*s. The parameter α_e is a fitting coefficient with units of mols/ mols Ga*s*bar and β_e is a fitting coefficient with units of bar^{-1}. Both coefficients are representative of the thermodynamics and kinetics of elementary steps for the dehydrogenation of C_2H_6. As observed in Figure 4.4.2-1, at low C_2H_6 partial pressures, rates are first-order in C_2H_6 and proportional to α_e, while at very high C_2H_6 partial pressures, rates are zero-order in C_2H_6 and proportional to α_e/β_e. Therefore, the parameter α_e reflects a first order rate coefficient while the parameter ratio α_e/β_e reflects a zero-order rate coefficient. Fitted values for α_e and β_e for each temperature are given in Table 4.4.2-1. These parameters can be ascribed chemical meaning by examining plausible mechanisms for C_2H_6 dehydrogenation over Ga/H-MFI. For the Ga/Al = 0.5 sample used here, NH_3-TPD was used to estimate the concentrations of different Ga^{3+} species.[133,158] The results lead to the conclusion that only 20% of the total Ga is present as $[GaH]^{2+}$, while the remaining 80% of Ga is present as $[GaH_2]^+$. Consequently, measured rates over the Ga/Al = 0.5 sample predominantly reflect the reactivity of $[GaH_2]^+$ cations. In the next section therefore, we propose a mechanism

for C_2H_6 dehydrogenation over $[GaH_2]^+$ cations and present experimental evidence to support this mechanism.

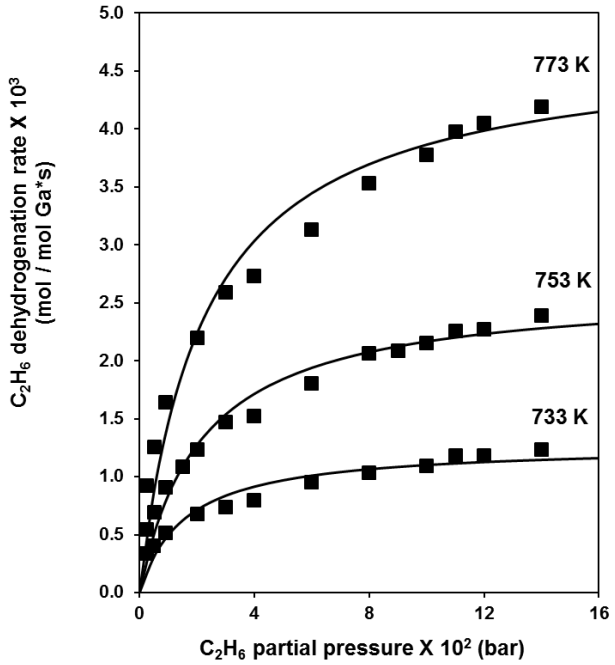

Figure 4.4.2-1. Turnover frequencies for C_2H_6 dehydrogenation (normalized per Ga atom) as a function of C_2H_6 partial pressure measured over the Ga/H-MFI (Ga/Al = 0.5) at 733 K, 753 K and 773 K. Reported rates were extrapolated to zero space time. Solid lines indicate fits of data to Equation 1 via non-linear, least squares regression**.**

Table 4.4.2-1. Fitted parameters obtained by non-linear, least squares regression of measured rates of C_2H_6 dehydrogenation, measured at 733 K, 753 K and 773 K and shown in Figure 4.4.2-1., to Eqn. 4.4.2-1

Temperature (K)	α_e (mol / mol Ga*s*bar)	β_e (bar^{-1})	α_e/β_e (mol / mol Ga*s)
733	8.1×10^{-2}	6.4×10^{1}	1.3×10^{-3}
753	1.2×10^{-1}	4.7×10^{1}	2.6×10^{-3}
773	2.1×10^{-1}	4.5×10^{1}	4.7×10^{-3}

4.4.3 Mechanistic analysis of C_2H_6 dehydrogenation over $[GaH_2]^+$ cations.

The role of $[GaH_2]^+$ cations in the dehydrogenation of C_2H_6 has been described using the 4-step alkyl mechanism in theoretical studies by Frash et al., Joshi et al., Pereira et al., and more

recently by Mansoor et al.[47,49,51,53] The steps in this mechanism are shown in Scheme 4.4.3-1. The enthalpies shown this scheme were reported recently in a computational study by Mansoor et al.[49] The first step represents the adsorption of C_2H_6 at a $[GaH_2]^+$ via weak physisorption (ΔH_{ads} = -7.2 kcal/mol). The second step involves the insertion of the Ga^{3+} center in the C-H bond of adsorbed C_2H_6 leading to C-H cleavage and the formation of $[C_2H_5\text{-}GaH_2]^+$ species while the H^+ removed during C-H cleavage migrates to a nearby framework O atom. This step is predicted to have an activation enthalpy of 27.5 kcal/mol. The third step is an almost barrier-less recombination of a Ga-bound hydride and the proximal H^+ to form H_2.The final step of the sequence involves β-hydride elimination from the alkyl fragment, resulting in the formation of surface bound C_2H_4 and $[GaH_2]^+$. This step has an activation enthalpy of 42.4 kcal/ mol. The elementary steps shown in Scheme 4.4.3-1 can be used to derive a rate law for C_2H_6 dehydrogenation over $[GaH_2]^+$ cations (see section 4.7.5 for a full derivation), shown here as Equation 4.4.3-1.

$$\frac{C_2H_6 \text{ dehydrogenation rate}}{[GaH_2]^+} = \frac{k_2K_1[C_2H_6]}{1+\frac{k_2K_1}{k_4}[C_2H_6]} \qquad (4.4.3\text{-}1)$$

In Equation 4.4.3-1, k_2 is the rate coefficient for the C-H cleavage of adsorbed C_2H_6 in Step 2, K_1 is the equilibrium adsorption constant for C_2H_6 physisorption at $[GaH_2]^+$ cations in Step 1 and k_4 is the rate coefficient for β-hydride elimination/C_2H_4 formation from $[C_2H_5\text{-}GaH]^+$ species in Step 4.

As discussed in greater detail in section 4.7.5, the second term in the denominator of Equation 4.4.3-1 (i.e k_2K_1/k_4*$[C_2H_6]$) reflects the steady-state surface concentration of $[C_2H_5\text{-}GaH]^+$ cations which are formed after Step 3 of the sequence. If the free energy of barrier for β-hydride elimination is much lower than the free energy barrier for initial C-H cleavage, i.e., $k_2K_1/k_4 << 1$, the second term in the denominator of Equation 4.4.3-1 becomes insignificant. Consequently, such a rate expression would predict dehydrogenation rates that are first-order in C_2H_6 for all C_2H_6 partial pressures and all experimental conditions and the rate-determining step would solely be step 2 of Scheme 4.4.3-1.

In order to understand if this is the case, we examined the Gibbs free energy barriers for Steps 2 and 4, predicted by the QM/MM calculations.[49] These energies were reported at 823 K and must therefore be converted to the corresponding free energies at 753 K (see section 4.7.6), a temperature that we used in our experiments. An inspection of Gibbs free energy barriers for these steps at 753 K reveals that Step 2, in which C-H cleavage of adsorbed C_2H_6 occurs, has the highest free energy activation barrier (59.4 kcal/mol with respect to gas-phase C_2H_6). Step 4 of the sequence, i.e., the β-hydride elimination/C_2H_4 formation also has a relatively high Gibbs free energy activation barrier (42.5 kcal/mol with respect to $[C_2H_5\text{-}GaH]^+$ species) but this value is lower than the free energy barrier for Step 2. It is noteworthy that the predicted intrinsic activation enthalpy for Step 4 is actually 12 kcal/mol higher than the predicted apparent activation enthalpy for Step 2 (See scheme 4.4.3-1). The opposite trend observed for the Gibbs free energy barriers of these steps has been attributed to entropic differences between their transition states.[49] Given that the Gibbs free energy barrier for Step 4 is not substantially lower than the barrier for Step 2, it is apparent that the term k_2K_1/k_4 in Equation 4.4.3-1 may become significant at sufficiently high C_2H_6 pressures. Additionally, experimentally measured dehydrogenation rates in Figure 4.4.2-1 are not purely first-order in C_2H_6 partial pressure, as expected if the second term in Equation 4.4.3-1 were to be insignificant. Instead, these rates are

first-order in C_2H_6 only at low partial pressures and approach zero-order at high partial pressures of C_2H_6. Equation 4.4.3-1 also predicts this behavior. Therefore, the functional form of Equation 4.4.3-1 is in qualitative agreement with the dependence of the rate of C_2H_6 dehydrogenation on C_2H_6 partial pressure observed in Figure 4.4.2-1.

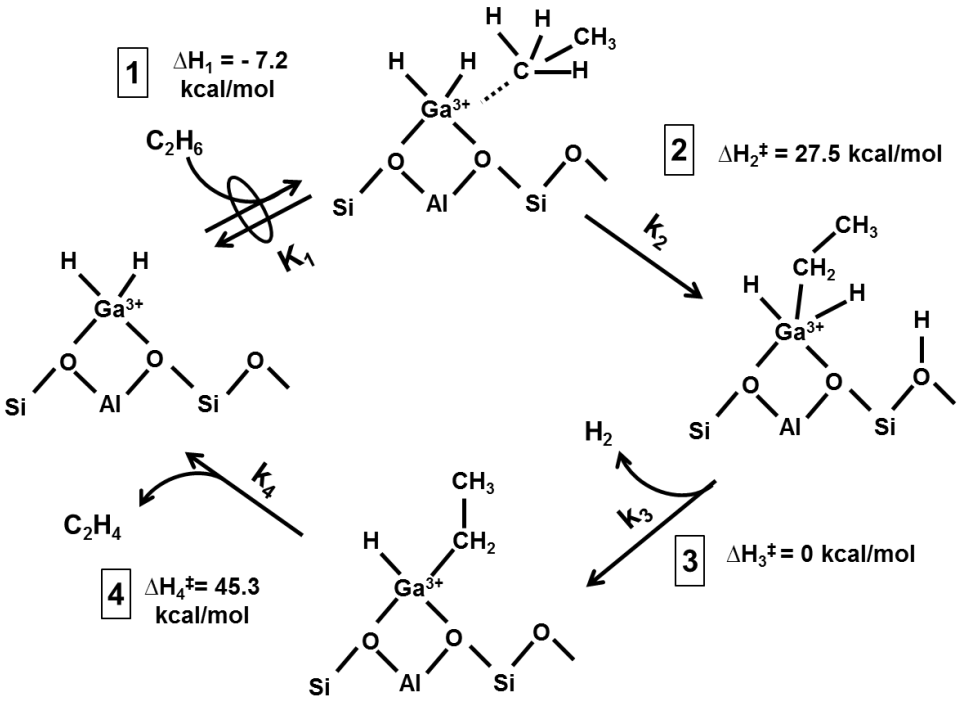

Scheme 4.4.3-1. Proposed 4-step, alkyl mechanism for C_2H_6 dehydrogenation over $[GaH_2]^+$ cations. Reported enthalpies are at 823 K and were taken from Ref.[83] Activation enthalpies are denoted with a double dagger (‡) next to ΔH.

At very low C_2H_6 partial pressures, the rate of C_2H_6 dehydrogenation is first-order in C_2H_6. A comparison of Equation 4.4.2-1 and 4.4.3-1 suggests that the first-order rate coefficient α_e in Equation 4.4.2-1 should correspond to the term k_2K_1 in Equation 4.4.3-1. Transition state theory and thermodynamic equilibrium suggest that k_2K_1 should be related to the free energy barrier for Step 2 relative to gas-phase C_2H_6. At these low partial pressures, equation 4.4.3-1 predicts that the rate of dehydrogenation is limited by Step 2. However, for very high partial pressures of C_2H_6, the rate of dehydrogenation is zero-order in C_2H_6 partial pressure. A comparison of Equation 4.4.2-1 and 4.4.3-1 suggests that in the zero-order regime, the zero order rate coefficient in Equation 4.4.2-1, α_e/β_e, should correspond to the term k_4 in Equation 4.4.3-1, which in turn is related to the free energy barrier for Step 4 relative to $[C_2H_5\text{-}GaH]^+$ species. Under these conditions, the rate of dehydrogenation will be proportional to k_4 and, therefore, limited by C_2H_4 formation via β-hydride elimination.

Activation enthalpies for C_2H_6 dehydrogenation can be extracted from fitted first and zero order rate coefficients (α_e and β_e) given in Table 4.4.2-1, using relationships derived from transition state theory.[153,158] These enthalpies, together with predictions from theory are presented in Table 4.4.3-1. Plots of the temperature dependence of rate coefficients are included

in section 4.7.7. The experimentally derived activation enthalpy from k_2K_1 (α_e) is 25.5 ± 4.7 kcal/mol. This value is in good agreement with the theoretically predicted difference between the transition state for Step 2 relative to gas-phase C_2H_6 (27. 5 kcal/mol). Similarly, the experimental activation enthalpy extracted from values of k_4 is 35.9 ± 3.5 kcal/mol, a value that is similar but slightly lower than the enthalpy difference between the transition state for Step 4 relative to $[C_2H_5\text{-}GaH]^+$ species (45.3 kcal/mol). We note that our theoretical studies examined a single $[GaH_2]^+$ configuration located at the T12 site in MFI in order to analyze reaction pathways. Variations in the location of $[GaH_2]^+$ in MFI could, therefore, alter the activity of these species and may cause small differences between experimentally measured and theoretically predicted activation enthalpies.

Table 4.4.3-1. Experimentally measured activation enthalpies for C_2H_6 dehydrogenation over Ga/H-MFI (Ga/Al = 0.5) for first- and zero-order rate coefficients. Also shown are theoretically predicted values of activation enthalpies for Steps 2 and 4 from Scheme 4.4.3-1.

Experimental		Theoretical, DFT	
Type of rate coefficient	$\Delta H^{\ddagger}$[1,2] (kcal/mol)	Step in reaction sequence	$\Delta H^{\ddagger}$ [3] (kcal/mol)
First-order (α_e , k_2K_1)	25.5 ± 4.7	2	27.5
Zero-order (α_e/β_e , k_4)	35.9 ± 3.5	4	45.3

[1]Obtained by the application of transition state theory equations to fitted rate coefficients in Table 4.4.2-1. Temperature dependence plots are included in section 4.7.7
[2] Reported errors reflect 95% confidence intervals
[3] Reported at 823 K by Mansoor et al.[49]

We conclude on the basis of the above discussion that the experimental evidence supported by theoretical calculations is reasonably consistent with the 4-step alkyl mechanism for C_2H_6 dehydrogenation over $[GaH_2]^+$. The occurrence of two different kinetic regimes for C_2H_6 dehydrogenation – one at low partial pressures of C_2H_6 and the other at very high partial pressures of C_2H_6, each with a different rate-limiting step is in stark contrast to the mechanism for C_3H_8 dehydrogenation over $[GaH]^{2+}$ cations. In the latter case, only $[GaH]^{2+}$ cations were found to be catalytically relevant, whereas $[GaH_2]^+$ cations did not contribute to the measured rates. Theoretical calculations indicate that an increase in alkane carbon chain length leads to higher activation entropies (and therefore higher free energy barriers) at the transition state associated with the first C-H cleavage over $[GaH_2]^+$.[135] This phenomenon likely leads to $[GaH_2]^+$ cations becoming unfavorable for the dehydrogenation of alkanes higher than C_2H_6.

Another interesting question regarding alkane activation over Ga/H-MFI is whether Ga^{3+} species possess the ability to selectively activate specific C-H and C-C bonds in alkanes. This question can be addressed by studying the mechanism of n-C_4H_{10} conversion over Ga/H-MFI. Depending on which C-H and C-C bonds in n-C_4H_{10} are activated, different alkene or alkane products can form via dehydrogenation and cracking reactions. Further, we would like to examine whether the site requirements for n-C_4H_{10} dehydrogenation and cracking differ from those for C_2H_6 dehydrogenation and C_3H_8 dehydrogenation and cracking. We therefore explore the mechanisms of n-C_4H_{10} conversion over Ga/H-MFI in the following sections.

4.4.4 Steady-state reactions of n-C_4H_{10} over Ga/H-MFI (Ga/Al = 0.2)

Shown in Figure 4.4.4-1a is the rate of n-C_4H_{10} consumption over Ga/H-MFI (Ga/Al = 0.2) measured at a partial pressure of 0.9 kPa C_4H_{10}/He, a space time of 3.5 mol Al*s/mol C_4H_{10}, and a temperature of 718 K. Figures 4.4.4-1b and 4.4.4-1c show the steady-state product selectivities (reported as the fraction of converted C appearing in products) as a function of time-on stream. Under the conditions employed (< 4 % conversion), C_4 species are the predominant products (~ 80% selectivity, principally butene isomers – 1-butene, trans and cis-2-butene, isobutene, and small concentrations of isobutane). C_3H_6 (~ 11 % selectivity) and C_2H_4 (~ 6 % selectivity) constitute the other major products. In addition to these species, CH_4, C_2H_6 and aromatic products are formed in low concentrations. This product distribution varies markedly from that for n-C_4H_{10} conversion over H-MFI. Over H-MFI, monomolecular dehydrogenation and cracking are catalyzed by Brønsted acid O-H groups, leading to the formation of butenes, CH_4, C_3H_6, C_2H_4, C_2H_6 with similar selectivities (see Table 4.7-2).

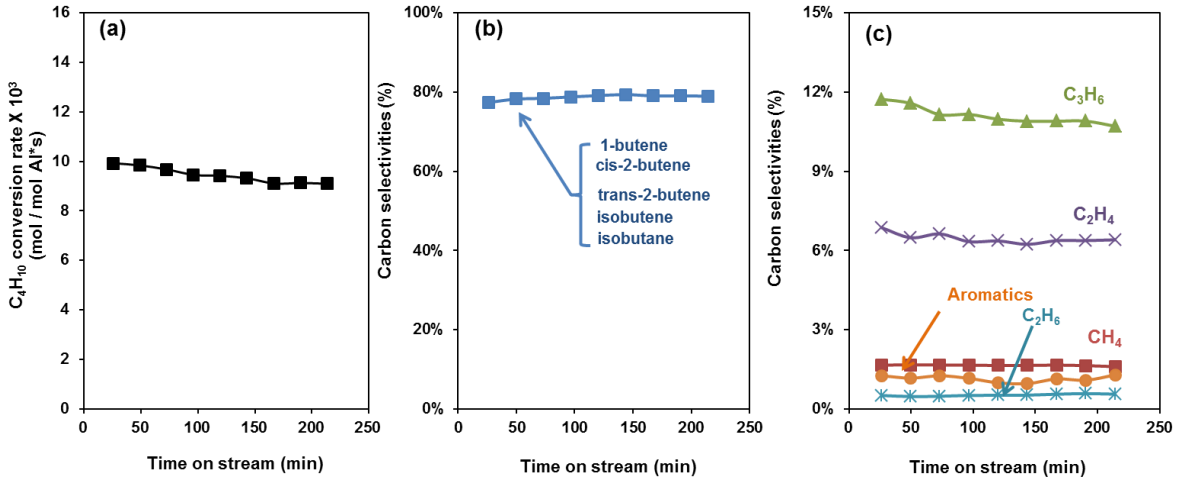

Figure 4.4.4-1. Turnover frequencies for (a) n-C_4H_{10} conversion (normalized per Al_{tot} atom) , (b) carbon selectivity to C_4 products, and (c) carbon selectivity to remaining products, measured at τ = 3.5 (mol Al*s/mol C_4H_{10}), 0.9 kPa C_4H_{10}/He and 718 K over Ga/H-MFI (Ga/Al = 0.2) for n-C_4H_{10} conversions < 4 %.

The primary reaction pathways for n-C_4H_{10} over H-MFI and Ga/H-MFI are C_4H_{10} dehydrogenation to produce butenes and H_2, central cracking of C_4H_{10} to produce C_2H_4 and C_2H_6 and terminal cracking of C_4H_{10} to produce CH_4 and C_3H_6. In the absence of secondary reactions involving any of the above products, an equimolar yield of each product pair is expected for each reaction pathway. At finite space times, measured product molar ratios of H_2/C_4H_8, C_3H_6/CH_4 and C_2H_4/C_2H_6 over Ga/H-MFI (Ga/Al = 0.2) are all greater than unity (see section 4.7.8), indicating the occurrence of secondary reactions even at the low conversions (< 4%). However, when these reatios are extrapolated to zero space time (see Figure 4.7-5), all three product molar ratios approach unity. This suggests that the rates of the three primary reactions can be extracted from rate data extrapolated to zero space time. The increase in the ratios of C_3H_6/CH_4 and

C_2H_4/C_2H_6 with increasing space time suggests that these products form via secondary pathways, such as the cracking of product butenes.[160]

During C_4H_{10} dehydrogenation, the activation of primary C-H bonds in n-C_4H_{10} leads to the formation of 1-butene while the activation of secondary C-H bonds in C_4H_{10} leads to the formation of either cis or trans 2-butene. However, it is well known that Brønsted acid O-H groups in zeolites catalyze the double-bond isomerization of linear butenes and also the skeletal isomerization of linear butenes to isobutene.[25,161] With an increase in the concentration of butenes as the space time increases, these reactions are expected to yield an equilibrated mixture of the butene isomers.[11,25] For Ga/H-MFI, space time studies (see section 4.7.9) show that 1-butene and trans-2-butene are the predominant butene products at low space times. With increasing space time, the concentrations of cis-2-butene and isobutene increase while those of 1-butene and trans-2-butene decrease. The molar ratio of trans-2-butene/1-butene is approximately constant as a function of space time, while the molar ratios of cis-2-butene/1-butene, cis-2-butene/trans-2-butene, and isobutene/1-butene increase with space time. These findings suggest that the primary dehydrogenation products over Ga/H-MFI are 1-butene and trans-2-butene.

The rates of C_4H_{10} dehydrogenation, and central and terminal cracking decrease with increasing space time for Ga/H-MFI (see section 4.7.10). This result is attributed to either consumption of primary products via secondary pathways or competitive adsorption of products at active sites resulting in inhibition. As discussed earlier, product butenes could crack to form C_3H_6 and C_2H_4 and this could result in a decrease in rate of dehydrogenation with space time. In the case of C_3H_8 dehydrogenation and cracking over Ga/H-MFI, H_2 was found to inhibit the rates of dehydrogenation and cracking over $[GaH]^{2+}$ cations by forming $[GaH_2]^{+}$- H^{+} cation pairs. In order to test the possibility of a similar inhibition for the reactions of C_4H_{10}, experiments were conducted in the presence of H_2 added to C_4H_{10}. Rates of all three reactions were lower in the presence of H_2 (see Figure 4.7-7). It was also observed that the rate of C_4H_{10} dehydrogenation decreases much more weakly with space time than in the absence of H_2 in the feed stream and that the rates of central and terminal cracking of C_4H_{10} are approximately independent of space time in the presence of H_2 (see Figure 4.7-7). These results indicate that as with C_3H_8, the dehydrogenation and cracking of C_4H_{10} over Ga/H-MFI is inhibited by H_2. In order to mitigate the effects of product inhibition and secondary reactions, all reported rates in the following sections were extrapolated to zero space time.

4.4.5 Effects of Ga/Al ratio on the rates of n-C_4H_{10} dehydrogenation and cracking.

The effects of Ga content on the rates of n-C_4H_{10} dehydrogenation, and terminal and central cracking are shown in Figures 4.4.5-1 and 4.4.5-2, respectively. The rates of dehydrogenation and both terminal and central cracking normalized per Al_{tot} atom increase with Ga content up to a Ga/Al ratio of 0.1, beyond which these rates appear to be independent of Ga content. At their maximum, n-C_4H_{10} dehydrogenation rates (normalized per Al_{tot}) over Ga/H-MFI are 180 times greater than the corresponding dehydrogenation rates over H-MFI while the rates of n-C_4H_{10} terminal cracking and n-C_4H_{10} central cracking (both normalized per Al_{tot}) are 15 and 5 times higher, respectively, than the corresponding rates over H-MFI under identical experimental conditions. This finding suggests that the reactivity contribution of residual Brønsted acid O-H groups in Ga/H-MFI is negligible for dehydrogenation and terminal cracking but is could be substantial for central cracking. While the dehydrogenation to cracking rate ratio (D/C) is close to unity over H-MFI, this ratio is approximately 10 over Ga/H-MFI. Similarly, the terminal to cracking rate ratio over H-MFI is close to unity but this ratio is approximately 3 over

Ga/H-MFI. Thus Ga/H-MFI is significantly more selective for dehydrogenation relative to cracking and more selective for terminal cracking relative to central cracking. Elucidation of these selectivity differences requires identification of the kinetically relevant Ga^{3+} species for these reaction pathways.

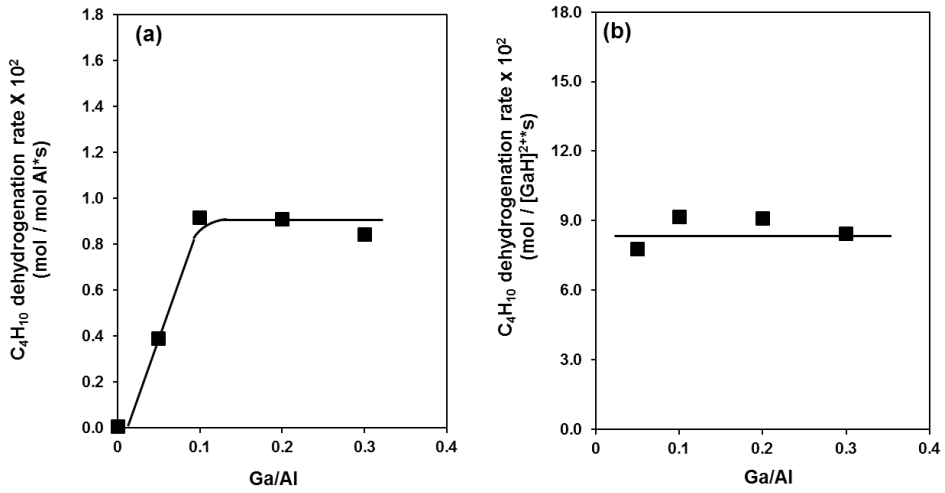

Figure 4.4.5-1. Turnover frequencies for C_4H_{10} dehydrogenation as a function of Ga/Al ratio: (a) normalized per Al_{tot} and (b) normalized per $[GaH]^{2+}$. Rates were measured at 0.9 kPa C_4H_{10} /He at 718 K and extrapolated to zero space time. $[GaH]^{2+}$ site densities were estimated by NH_3-TPD.[133] Solid lines are guides for the eye.

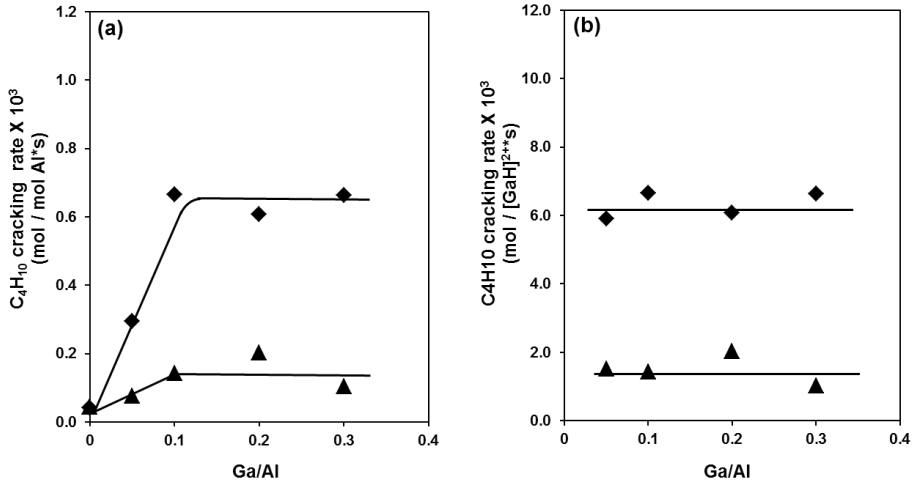

Figure 4.4.5-2. Turnover frequencies for C_4H_{10} terminal cracking (filled diamonds) and central cracking (filled triangles) as a function of Ga/Al ratio (a) normalized per Al_{tot} and (b) normalized per $[GaH]^{2+}$. Rates were measured at 0.9 kPa C_4H_{10} /He at 718 K and extrapolated to zero space time. $[GaH]^{2+}$ site densities were estimated by NH_3-TPD.[133] Solid lines are guides for the eye.

The similarity in the trends for dehydrogenation and cracking as a function of Ga/Al ratio seen in Figures 4.4.5-1a and 4.4.5-2a suggests that identical active sites catalyze all three reactions. Since the rates of all three reactions depend on Ga content only at low Ga/Al ratios, it is conceivable that $[GaH]^{2+}$ cations, which are predominant in Ga/H-MFI at low Ga/Al ratios ($Ga/Al \leq 0.1$)[133], are the active sites for n-C_4H_{10} dehydrogenation, terminal and central cracking. Shown in Figure 4.4.5-1b and 4.4.5-2b are the rates of these reactions normalized by the density of $[GaH]^{2+}$ cations estimated from NH_3-TPD.[133] It is observed that rates of all three reactions are approximately independent of the Ga/Al ratio when normalized by the concentration of $[GaH]^{2+}$ cations. Thus, $[GaH]^{2+}$ cations appear to be the sole active species for reactions of n-C_4H_{10}, analogous to the findings for C_3H_8 dehydrogenation and cracking over Ga/H-MFI.[158] $[GaH_2]^+$ cations which form in increasing concentration in Ga/H-MFI with Ga/Al ratios > 0.1, do not appear to contribute to measured rates. Consequently, turnover frequencies over Ga/H-MFI (normalized per $[GaH]^{2+}$) for dehydrogenation, terminal and central cracking are 3 orders, 2 orders and 1 order of magnitude, respectively higher than the turnover frequencies of these reactions over H-MFI (normalized per H^+). These findings are in stark contrast to the trends observed for C_2H_6 dehydrogenation, for which both $[GaH]^{2+}$ and $[GaH_2]^+$ cations are active sites. In the following section, we examine the mechanism and kinetics of C_4H_{10} dehydrogenation, terminal and central cracking over the Ga/Al = 0.2 sample.

4.4.6 Effects of n-C_4H_{10} partial pressure and temperature on the rates of n-C_4H_{10} dehydrogenation and cracking over Ga/H-MFI

The effects of C_4H_{10} partial pressure on turnover rates (per $[GaH]^{2+}$) for dehydrogenation, terminal and central cracking at 718 K are shown in Figures 4.4.6-1a-b. All three reactions exhibit a Langmuir-Hinshelwood dependence on C_4H_{10} partial pressure – rates are first order in C_4H_{10} at low partial pressures but approach a zero-order dependence on C_4H_{10} at higher partial pressures. Similar dependences of rates on C_4H_{10} partial pressure were also observed at two other reaction temperatures (see section 4.7.11). These observations are analogous to those observed for C_3H_8 dehydrogenation and cracking over Ga/H-MFI[158] for which the formation of chemisorbed alkyl-Ga intermediates upon dissociation of alkane reactants by $[GaH]^{2+}$ species was found to lead to a Langmuir-Hinshelwood dependence of rates on the alkane partial pressure.

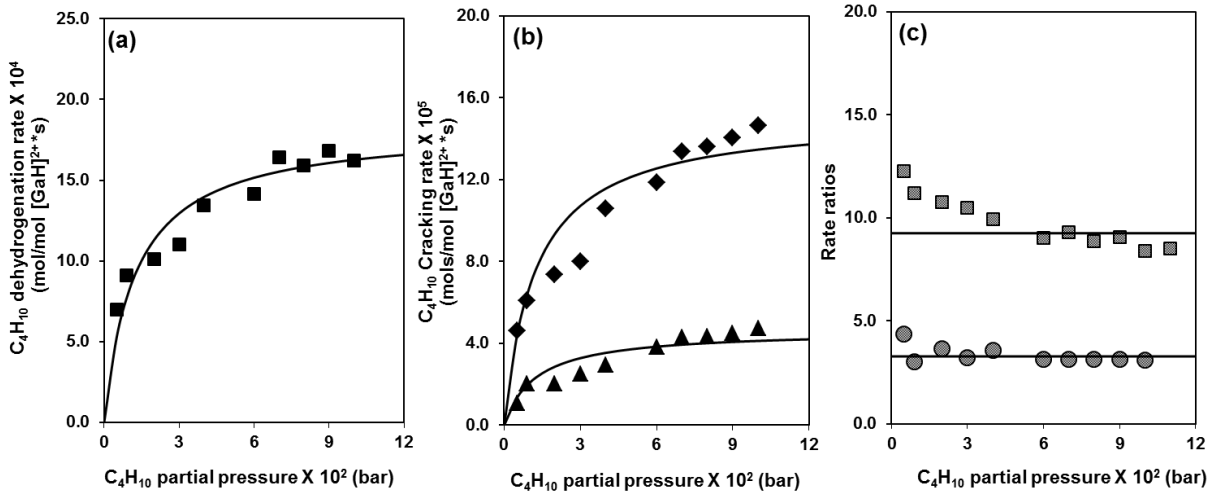

Figure 4.4.6-1. Turnover frequencies for C_4H_{10} dehydrogenation (squares, Figure 4.4.6-1a), terminal cracking (diamonds, Figure 4.4.6-1b) and central cracking (triangles, Figure 4.4.6-1b), the ratio of the turnover frequencies for dehydrogenation to cracking (shaded squares, Figure 4.4.6-1c) and terminal to central cracking (shaded circle, Figure 4.4.6-1c) as a function of C_4H_{10} partial pressure, measured at 718 K over the Ga/H-MFI (Ga/Al = 0.2). Rates were extrapolated to zero space time and are normalized per mol $[GaH]^{2+}$. Solid lines reflect fits of the data to Equations 4.4.6-1, 2 and 3 via non-linear, least squares regression.

The similar site requirements and similar effects of reactant and product partial pressure on the rate of C_4H_{10} dehydrogenation and both terminal and central cracking suggest that these reactions proceed via a common C_4H_{10}-derived intermediate. If this is the case, dehydrogenation to cracking (terminal + central) (D/C) and terminal to central cracking (C_t/C_c) rate ratios should bear the same dependence on C_4H_{10} surface coverage and should therefore be approximately independent of C_4H_{10} and H_2 partial pressures. As observed in Figure 4.4.6-1c, D/C and C_t/C_c rate ratios are only weakly dependent on C_4H_{10} partial pressure, suggesting that all three reactions likely proceed via a common C_4H_{10}-derived surface intermediate. We note that both ratios do appear to decrease slightly with increasing C_4H_{10} partial pressure but that this dependence appears to become weaker with a decrease in temperature (see section 4.7.11). We suggest that the observed effects of C_4H_{10} partial pressure on the D/C ratio and C_t/C_c ratio could arise from contributions of residual Brønsted acid O-H groups to the measured cracking rates at high C_4H_{10} partial pressures. As noted in section 4.4.5, the rate of central cracking over Ga/H-MFI (Ga/Al = 0.2) is only a factor of 5 higher than the corresponding rates over H-MFI at 0.9 kPa C_4H_{10} and 718 K. Central cracking catalyzed by Brønsted acid O-H groups has a first order dependence on C_4H_{10} partial pressure (see Figure 4.7-11) while the same reaction catalyzed by $[GaH]^{2+}$ is expected to reach a zero-order dependence on C_4H_{10} partial pressure at high C_4H_{10} partial pressure. Since the Ga/H-MFI sample used here is expected to possess 34% fewer Brønsted acid O-H groups than H-MFI (based on characterization of H_2-reduced Ga/H-MFI samples by NH_3-TPD[133]), we can correct the first-order rate coefficient (per Al_{tot} atom) for central cracking over H-MFI by a factor of 0.66. The resulting analysis shows that at 10 kPa C_4H_{10}, the rate central cracking (normalized per Al_{tot} atom) over Ga/H-MFI (Ga/Al = 0.2) will only be 1.35 times higher than the central cracking rate (normalized per Al_{tot} atom) over H-MFI.

Thus, with an increase in C_4H_{10} partial pressure, residual Brønsted acid O-H groups in Ga/H-MFI may have a non-negligible contribution toward central cracking.

An attempt was made to correct the rate of central cracking over Ga/H-MFI for contributions from protolytic central cracking reactions by subtracting the rate of central cracking over H-MFI (estimated using the measured first-order rate coefficient over H-MFI) from the rate of central cracking over Ga/H-MFI (see Figure 4.7-12). The resulting D/C ratios are found to be independent of C_4H_{10} partial pressure while C_t/C_c ratios that are nearly independent of C_4H_{10} partial pressure but show a non-systematic increase at high C_4H_{10} partial pressures (> 8 kPa C_4H_{10}). This non-systematic variation may be caused by small (15-20%) differences between the actual central cracking rate coefficient over residual Brønsted acid O-H groups in Ga/H-MFI and the measured central cracking rate coefficient over H-MFI that was used for the rate subtraction process. Previous work from our group has shown that the selectivity to central cracking relative to terminal cracking for protolytic C_4H_{10} cracking over H-MFI is sensitive to the location of Brønsted acid O-H groups in H-MFI.[11] In Ga/H-MFI, the locations of residual Brønsted acid O-H groups (in the case of the H_2-reduced Ga/Al = 0.2 sample, 66% of the total H^+ initially present in H-MFI) are unknown and inaccessible via experiments and theory. Consequently, the intrinsic reactivity of these residual Brønsted acid O-H groups for central cracking may be slightly different from that of the average of all the Brønsted acid O-H groups initially present in H-MFI. As a result, we cannot reliably use cracking rate coefficients measured over H-MFI to correct central cracking rates over Ga/H-MFI for protolytic contributions. Nonetheless, these corrections provide a qualitative explanation for the weak effects of C_4H_{10} pressure on D/C and C_t/C_c ratios in Figure 4.4.6-1c and support the conclusion that in the absence of such effects, both ratios are approximately independent of C_4H_{10} partial pressure, suggesting the prevalence of a common C_4H_{10} derived surface intermediate for all three reactions.

Additionally, even though dehydrogenation, terminal and central cracking are inhibited by H_2, the D/C ratio and C_t/C_c ratios are independent of the H_2 partial pressure (see Figure 4.7-10) consistent with the hypothesis that a common surface intermediate is involved in all three reactions, the formation of which is inhibited in the presence of H_2. As noted previously, D/C and C_t/C_c ratios measured at two lower temperatures (703 K, 688 K, see Figures 4.7-8 and 4.7-9) decrease more weakly with C_4H_{10} partial pressure than the data taken at 718 K and shown in Figure 4.4.6-1c. This is expected if $[GaH]^{2+}$-catalyzed cracking has a much lower activation energy than protolytic cracking, as was found for C_3H_8 cracking over Ga/H-MFI and H-MFI.[158] Consequently, contributions from protolytic central cracking are expected to be less significant for the rates measured at the two lower temperatures (703 K and 688 K), and, therefore, the contribution from protolytic central cracking is not expected to significantly influence our experimentally measured estimate of the activation energy for central cracking over Ga/H-MFI.

The rate data presented in Figures 4.4.6-1a and 4.4.6-1b can be fit satisfactorily to Equations 4.4.6-1-3, all three of which possess a common denominator. These empirical rate expressions contain parameters α_d, α_t, and α_c for dehydrogenation, terminal cracking and central cracking, respectively, and a parameter β common to all three equations. Inspection of Equations 4.4.6-1-3 suggests that α_d, α_t, and α_c reflect first-order rate coefficients with units of mols/mol $[GaH]^{2+}$ *s*bar for dehydrogenation, terminal, and central cracking respectively. The parameter β has units of bar^{-1}. At very high C_4H_{10} partial pressures, for which the rates of dehydrogenation, terminal and central cracking approach zero-order dependence on C_4H_{10}, the parameters α_d/β, α_t/β, α_c/β represent zero-order rate coefficients with units of mols/mol $[GaH]^{2+}$ *s.

$$C_4H_{10}\text{ dehydrogenation rate} = \frac{\alpha_d[C_4H_{10}]}{1+\beta[C_4H_{10}]} \quad (4.4.6\text{-}1)$$

$$C_4H_{10}\text{ terminal cracking rate} = \frac{\alpha_t[C_4H_{10}]}{1+\beta[C_4H_{10}]} \quad (4.4.6\text{-}2)$$

$$C_4H_{10}\text{ central cracking rate} = \frac{\alpha_c[C_4H_{10}]}{1+\beta[C_4H_{10}]} \quad (4.4.6\text{-}3)$$

4.4.7 The mechanisms of C_4H_{10} dehydrogenation and both terminal and central cracking catalyzed by $[GaH]^{2+}$ cations

The findings in sections 4.4.5 and 4.4.6 suggest that $[GaH]^{2+}$ cations catalyze C_4H_{10} dehydrogenation, terminal and central cracking via mechanisms analogous to the alkyl mechanism for C_3H_8 dehydrogenation and cracking which is mediated via a chemisorbed C_3H_8-derived surface intermediate. For n-C_4H_{10}, two types of chemisorbed alkyl-Ga species can form – 1) [n-C_4H_9-GaH]$^+$-H^+ cation pairs, in which the alkyl fragment is a linear n-C_4H_9 chain coordinated to Ga^{3+} center and 2) [sec-C_4H_9-GaH]$^+$-H^+ cation pairs, in which the alkyl fragment is a sec-C_4H_9 chain coordinated to the Ga^{3+} center. We note that β-hydride elimination, a step required to produce butene from [C_4H_9-GaH]$^+$-H^+ species, would lead to the formation of 1-butene from [n-C_4H_9-GaH]$^+$-H^+ species but both 1-butene and 2-butene from [sec-C_4H_9-GaH]$^+$ species. Our results presented in section 4.4.4 indicate that both 1-butene and trans-2-butene are primary products of C_4H_{10} dehydrogenation over Ga/H-MFI. We therefore conclude that [sec-C_4H_9-GaH]$^+$-H^+ cation pairs are the likely C_4H_{10} derived surface intermediate involved in dehydrogenation. By extension, the findings in section 4.4.6 suggest that [sec-C_4H_9-GaH]$^+$-H^+ cation pairs are also the common surface intermediate involved in C_4H_{10} terminal and central cracking.

Shown in Scheme 4.4.7-1 are the proposed elementary steps for n-C_4H_{10} dehydrogenation, terminal and central cracking over $[GaH]^{2+}$ cations. The first two steps of the sequence are common to all three reaction pathways. Step 1 involves physisorption of n-C_4H_{10} at $[GaH]^{2+}$ to form a physisorbed alkane-$[GaH]^{2+}$ complex. Step 2 involves heterolytic dissociation of secondary C-H bonds in C_4H_{10} and the concomitant formation of [sec-C_4H_9-GaH]$^+$-H^+ cation pairs. In analogy to computationally reported activation barriers for the formation of [n-C_4H_9-GaH]$^+$-H^+ from C_4H_{10},[49] both steps 1 and 2 in scheme 4.4.7-1 can be assumed to have low activation barriers and are, therefore, expected to be quasi-equilibrated. The three reaction pathways branch out from this intermediate. Dehydrogenation (Step 3d in scheme 4.4.7-1) proceeds via the rate-determining β-hydride elimination of the alkyl fragment to produce butene and H_2 in a concerted fashion. This process involves a cyclic transition state, which produces 1-butene and H_2 if the methyl C-H bonds undergo β-hydride elimination and 2-butene and H_2 if methyl C-H bonds undergo β-hydride elimination. Terminal cracking proceeds via rate-determining C-C bond attack of the terminal C-H bonds in the [sec-C_4H_9-GaH]$^+$ cation by the proximal Brønsted acid O-H group (Step 3t in scheme 4.4.7-1). This process produces [CH_3-GaH]$^+$ cations proximate to propoxide species bound to the adjacent cation-exchange site. In subsequent steps that are not expected to be kinetically relevant,[158,162] the propoxide species decomposes to form C_3H_6 and a Brønsted O-H group which subsequently recombines with the Ga-bound CH_3 fragment to form CH_4 and the $[GaH]^{2+}$ site. Central cracking proceeds via rate-determining C-C bond attack of the central C-H bond in the [sec-C_4H_9-GaH]$^+$ cation by the

proximal Brønsted acid O-H group (Step 3c in scheme 4.4.7-1) resulting in the formation of $[C_2H_5\text{-}GaH]^+$ cations proximate to ethoxide species bound to the adjacent cation-exchange site. Subsequent steps in this pathway are expected to be fast and not kinetically relevant.[158,163] These steps involve the decomposition of ethoxide species to form C_2H_4 and a Brønsted acid O-H group and the recombination of the Ga-bound C_2H_5 group with the proximal Brønsted acid O-H group to form C_2H_6.

The elementary steps shown in Scheme 4.4.7-1 can be used to derive rate expressions for each of three pathways, shown here as Equations 4.4.7-1, 4.4.7-2 and 4.4.7-3 for dehydrogenation, terminal and central cracking, respectively. A full derivation of these equations is provided in section 4.7.14.

$$\frac{C_4H_{10}\text{ dehydrogenation rate}}{[GaH]^{2+}} = \frac{k_d K_2 K_1 [C_4H_{10}]}{1+K_2 K_1 [C_4H_{10}]} \qquad (4.4.7\text{-}1)$$

$$\frac{C_4H_{10}\text{ terminal cracking rate}}{[GaH]^{2+}} = \frac{k_t K_2 K_1 [C_4H_{10}]}{1+K_2 K_1 [C_4H_{10}]} \qquad (4.4.7\text{-}2)$$

$$\frac{C_4H_{10}\text{ central cracking rate}}{[GaH]^{2+}} = \frac{k_c K_2 K_1 [C_4H_{10}]}{1+K_2 K_1 [C_4H_{10}]} \qquad (4.4.7\text{-}3)$$

In Equations 4.4.7-1, 4.4.7-2 and 4.4.7-3, k_d is the rate coefficient for β-hydride elimination from $[sec\text{-}C_4H_9\text{-}GaH]^+$ cations, a step which is predicted to be rate determining for dehydrogenation, k_t is the rate coefficient for C-C bond attack by H^+ leading to terminal cracking and k_c is the rate coefficient for C-C bond attack by H^+ leading to central cracking. The parameters K_1 and K_2 represent the equilibrium constants for n-C_4H_{10} physisorption at $[GaH]^{2+}$ and the formation of $[sec\text{-}C_4H_9\text{-}GaH]^+\text{-}H^+$ cation pairs, respectively. A comparison of Equations 4.4.7-1, 4.4.7-2, and 4.4.7-3 with Equations 4.4.6-1, 4.4.6-2 and 4.4.6-3 suggests that the first-order rate coefficients α_d ,α_t, and α_c correspond to the terms $k_dK_2K_1$, $k_tK_2K_1$ and $k_cK_2K_1$ respectively and these parameters reflect apparent Gibbs free energy activation barriers for the respective reactions (relative to gas-phase C_4H_{10}). The parameter β corresponds to the equilibrium constant product, K_2K_1, and therefore reflects the Gibbs free energy of formation of $[sec\text{-}C_4H_9\text{-}GaH]^+\text{-}H^+$ cation pairs, relative to gas-phase C_4H_{10}. Consequently, the zero-order rate constants α_d/β, α_t/β and α_c/β correspond to the terms k_d, k_t, and k_c, respectively, and these parameters therefore reflect the intrinsic Gibbs free energy barriers for the respective reactions (relative to $[sec\text{-}C_4H_9Ga\text{-}H]^+\text{-}H^+$ cation pairs).

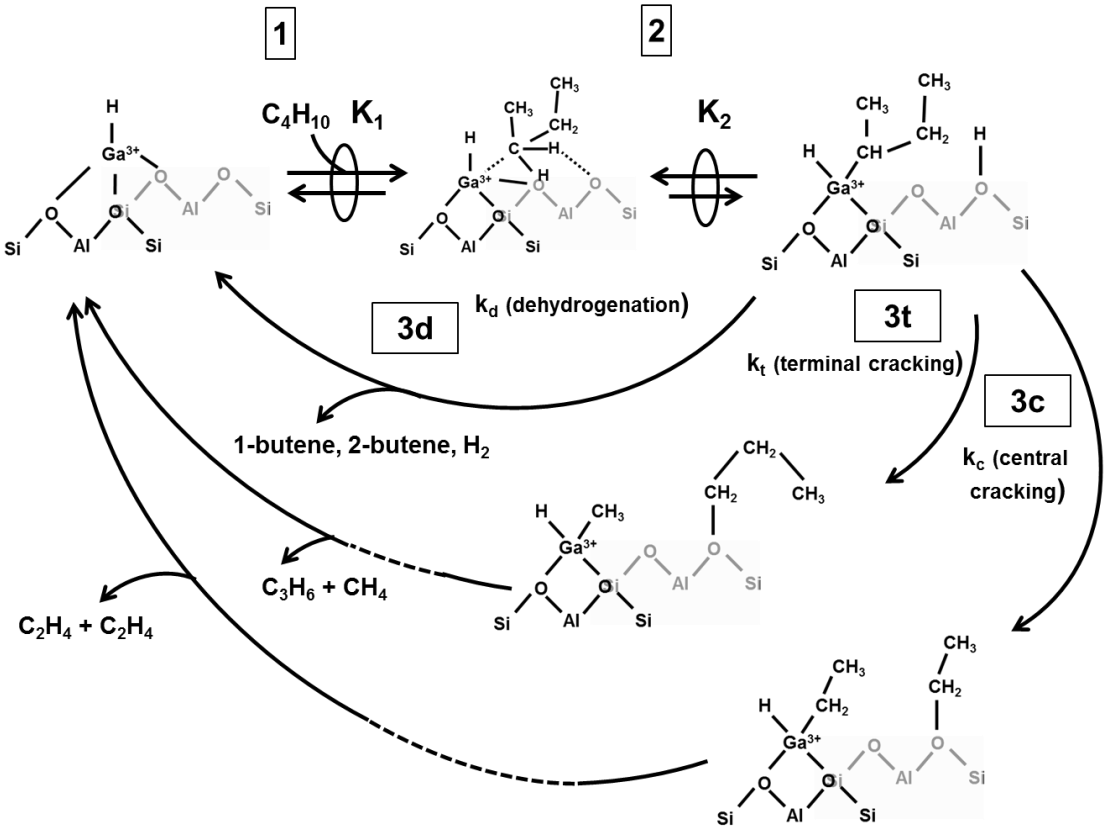

Scheme 4.4.7-1. Proposed elementary steps for n-C_4H_{10} dehydrogenation and both terminal and central cracking over $[GaH]^{2+}$ cations. Dotted lines in pathways for both terminal and central cracking indicate omission of elementary steps that are predicted to be kinetically irrelevant.

Rate coefficients obtained by fitting Equations 4.4.6-1, 4.4.6-2 and 4.4.6-3 to rates measured at different temperatures together with relationships derived from transition state theory[153,158] can be used to extract apparent and intrinsic activation enthalpies for each of the three reaction pathways over Ga/H-MFI (Ga/Al = 0.2). The temperature dependence of rate coefficients is shown in section 4.7.15. Experimentally derived apparent and intrinsic activation enthalpies for the three reactions are shown in Table 4.4.7-1. Also shown are theoretical predictions for the apparent and intrinsic activation enthalpies for C_4H_{10} dehydrogenation catalyzed via $[n\text{-}C_4H_9\text{-}GaH]^+$ species.[49] It is observed that for dehydrogenation, the experimentally derived apparent activation enthalpy (17.5 ± 4.7 kcal/mol) is in good agreement with the theoretically predicted value (19.8 kcal/mol). The intrinsic activation enthalpy for dehydrogenation (32.9 ± 2.9 kcal/mol) is, however, significantly lower than the theoretically predicted value (42.7 kcal/mol). For the theoretical results reported in Table 4.4.7-1, the intermediate preceding the dehydrogenation transition state was assumed to be a $[n\text{-}C_4H_9\text{-}GaH]^+$-$H^+$ cation pair. The intermediate found to be kinetically relevant, $[sec\text{-}C_4H_9\text{-}GaH]^+$-$H^+$ cation pairs, may have an adsorption enthalpy that is slightly different than that for $[sec\text{-}C_4H_9\text{-}GaH]^+$-$H^+$ cation pairs due to differences in the electron donating nature of the α-C in the two alkyl fragments and perhaps also due to differences in the nature and extent of Van der Waals contacts between the alkyl fragment and the zeolite framework in the two cases.

Table 4.4.7-1. Experimentally measured apparent ($\Delta H_{app}^{\ddagger}$), intrinsic ($\Delta H_{int}^{\ddagger}$) activation enthalpies, and adsorption enthalpies (ΔH_{ads}) for n-C_4H_{10} dehydrogenation and both terminal and central cracking over Ga/H-MFI (Ga/Al = 0.2). Also shown are theoretically predicted values of these quantities for dehydrogenation via [n-C_4H_9-GaH]-H^+ cation pairs.

Enthalpy (kcal/mol)	Dehydrogenation		Central cracking	
	Experiment[1]	Theory[3]	Experiment[1]	Experiment[1]
$\Delta H_{app}^{\ddagger}$ (First-order)	17.5 ± 4.7	19.8	19.9 ± 0.3	16.8 ± 0.9
$\Delta H_{int}^{\ddagger}$ (Zero-order)	32.9 ± 1.9	42.7	35.3 ± 3.0	32.1 ± 7.6
ΔH_{ads}[4]	-15.4 ± 5.1	-22.9	-	-

[1] Obtained by the application of transition state theory equations to rate coefficients obtained via fits of data in Figures 4.4.6-1,2,3 and Figures 4.7-8, 4.7-9 to Equations 4.4.6-1, 2 and 3. Temperature dependence plots are included in section 4.7.15

[2] Reported errors reflect 95% confidence intervals

[3] Reported for a temperature of 823 K by Mansoor et al.[49]

[4] Derived from denominator term β or K_1K_2 which was held common to rate expressions for all three reaction pathways

As Table 4.4.7-1 shows, the measured apparent activation enthalpy for central cracking is about 3.1 kcal/mol lower than the corresponding activation enthalpy for terminal cracking. This is unexpected, since the measured rate of terminal cracking is higher than the rate of central cracking by a factor of 3 at 718 K. In order for terminal cracking rates to be higher than central cracking rates by a factor of 3, we estimate (using transition state theory) that the Gibbs free energy activation barrier (at 718 K) for central cracking would have to be higher than the corresponding activation barrier for terminal cracking by 1.6 kcal/mol. Examination of the experimentally derived entropies of activation for the two pathways reveals that central cracking has a significantly more negative apparent entropy of activation (-0.039 ± 0.001 mol/cal*K) than the apparent entropy of activation for terminal cracking (-0.032 ± 0.001 mol/cal*K). The greater loss of entropy for the central cracking transition state relative to the terminal cracking transition state leads to a Gibbs free energy barrier for central cracking that is about 1.7 kcal/mol higher than that for terminal cracking. This analysis suggests that a more constrained transition state for central cracking relative to terminal cracking is responsible for the observed higher terminal cracking rates over Ga/H-MFI.

4.4.8 Mechanistic similarities and differences between the reactions of C_2H_6, C_3H_8, and n-C_4H_{10} over Ga/H-MFI

The findings presented in this study highlight the significant effects of alkane chain length on the activity of isolated $Ga^{3+}H_x$ species in Ga/H-MFI. First, the site requirements for dehydrogenation reactions appear to vary significantly as a function of alkane chain length. Both $[GaH]^{2+}$ cations and $[GaH_2]^+$ cations catalyze C_2H_6 dehydrogenation with similar activity. While the former species require the presence of proximate cation-exchange sites with framework Al-Al distances ≤ 5 Å apart,[133] the latter structure can form at all cation-exchange sites in MFI. This

results in the observed proportionality of C_2H_6 dehydrogenation rates (normalized per Al) with respect to Ga content. In contrast to C_2H_6, C_3H_8 and n-C_4H_{10} dehydrogenation is only catalyzed by $[GaH]^{2+}$ cations, prevalent at low Ga/Al ratios.[158] As a result, these reaction rates (normalized per Al_{tot}) are only proportional to concentration of $[GaH]^{2+}$ species in Ga/H-MFI, and $[GaH_2]^+$ cations appear to be inactive for C_3H_8 and n-C_4H_{10} dehydrogenation.

The differences in site requirements discussed above reflect differences between the mechanisms for the dehydrogenation of C_2H_6, C_3H_8 and n-C_4H_{10} over Ga/H-MFI. Over $[GaH_2]^+$ cations, which catalyze C_2H_6 dehydrogenation, there are two kinetic regimes: initial C-H cleavage of adsorbed C_2H_6 (Step 2 in scheme 4.4.3-1) appears to limit rates at low C_2H_6 partial pressures while desorption of C_2H_4 from $[C_2H_5\text{-}GaH]^+$ species (via β-hydride elimination, Step 4 in scheme 4.4.3-1) appears to limit rates at very high C_2H_6 partial pressures. The free energy barriers for these phenomena are reflected in first and zero-order C_2H_6 dehydrogenation rate coefficients, respectively. Theoretical calculations suggest that the transition state for the first kinetic regime limited by Step 2 (initial C-H cleavage) is highly constrained, leading to a significant loss of entropy.[49] These entropic losses are predicted to become more severe as the carbon chain length of the alkane increases, likely rendering $[GaH_2]^+$ cations inactive for C_3H_8 and n-C_4H_{10} dehydrogenation, as observed experimentally. On the other hand, the second kinetic regime for C_2H_6 dehydrogenation limited by Step 4 (alkene desorption) is predicted to have a much later, more product-like transition state resembling a fully formed Ga-H bond and C_2H_4 species. Consequently, this transition state is much less constrained than the one for Step 2. Unfortunately, for C_3H_8 and n-C_4H_{10}, this less constrained transition state formed over $[GaH_2]^+$ cations is inaccessible due to the high barriers associated with Step 2 predicted for these reactants.[49]

C_3H_8 and n-C_4H_{10} dehydrogenation are catalyzed by $[GaH]^{2+}$ cations. A single step, involving the formation of alkene and H_2 (via β-hydride elimination) from $[alkyl\text{-}GaH]^+\text{-}H^+$ cation pairs, appears to limit the rates of both reactions. Initial C-H activation of alkane reactants by $[GaH]^{2+}$ appears to be highly facile due to the high Lewis acidity of $[GaH]^{2+}$ cations.[49] As discussed before, the β-hydride elimination step that limits both reactions occurs via a relatively late and, therefore, less constrained transition state. In fact, entropic losses for β-hydride elimination over $[GaH]^{2+}$ may be even less than those for the same step over $[GaH_2]^+$ cations because in the former case, the abstracted hydride forms molecular H_2 while in the latter case, the abstracted hydride becomes bound to the Ga^{3+} center.

Table 4.4.8-1 shows measured first- and zero-order rate constants for C_2H_6 dehydrogenation (normalized per Ga atom) and those for C_3H_8 dehydrogenation (normalized per $[GaH]^{2+}$) at 753 K.[158] The first-order rate coefficient for C_3H_8 dehydrogenation is 453 times higher than the corresponding rate coefficient for C_2H_6 dehydrogenation, a factor that would require a difference of 9.2 kcal/mol between the free energy barriers for the two reactions. The measured apparent activation enthalpy (derived from first-order rate coefficients) for C_2H_6 dehydrogenaiton is only 6.5 kcal/mol higher than that for C_3H_8 dehydrogenation (19.0 ± 6.0 kcal/mol for C_3H_8 dehydrogenation[158] and 25.5 ± 4.7 kcal/mol for C_2H_6 dehydrogenation).[158] Thus, a greater entropic loss for C_2H_6 dehydrogenation than for C_3H_8 dehydrogenation must result in the observed difference between turnover rates for the two reactants. This conclusion is consistent with the more constrained character of the transition state for C_2H_6 dehydrogenation via Step 2 relative to the β-hydride elimination transition state for C_3H_8 dehydrogenation. We also note that the ratio of zero-order rate coefficients for C_3H_8 and C_2H_6 dehydrogenation in Table 4.4.8-1 is 97, a value much lower than the ratio of first-order rate coefficients. This

decrease may reflect the fact that in the zero-order regime, both C_2H_6 and C_3H_8 dehydrogenation are limited by similar β-hydride elimination transition states.

Table 4.4.8-1. First and zero-order rate coefficients for C_2H_6 and C_3H_8 dehydrogenation over Ga/H-MFI measured at 753 K.

	C_2H_6	C_3H_8[1]	C_3H_8 /C_2H_6
First-order coefficient (mol/mol active site *s*bar)	$1.23x10^{-1}$	$5.60x10^{1}$	$4.53x10^{2}$
Zero-order coefficient (mol/mol active site*s)	$2.61x10^{-3}$	$2.52x10^{-1}$	$9.70x10^{1}$

[1] Data obtained from Ref [158]

Comparison of C_3H_8 and C_4H_{10} dehydrogenation also provides insights. Table 4.4.8-2 lists measured first- and zero-order rate coefficients (both normalized per $[GaH]^{2+}$) for C_3H_8 and C_4H_{10} dehydrogenation and the ratio of these constants for C_3H_8 relative to C_4H_{10}. It is observed that the first order rate coefficient for C_3H_8 dehydrogenation is about a factor of two higher than that for C_4H_{10} dehydrogenation even though the zero-order rate coefficient for C_3H_8 dehydrogenation is about a factor of 0.5 lower than that for C_4H_{10} dehydrogenation. In both cases, we estimate that a difference in free energy barriers between the two reactants of about 1 kcal/mol would be sufficient to give rise to these differences in turnover frequencies. Given the similar mechanism and nature of the rate-determining transition state for the dehydrogenation of these two reactants and similar measured activation enthalpies (19.0 ± 6.0 kcal/mol for C_3H_8 dehydrogenation[158] and 17.5 ± 4.7 kcal/mol for C_4H_{10} dehydrogenation), it is reasonable to expect that free energy barriers for the two reactants would be similar. Theoretical calculations also support this conclusion.[49]

Table 4.4.8-2. First and zero-order rate coefficients for C_4H_{10} and C_3H_8 dehydrogenation over Ga/H-MFI measured at 718 K.

	C_4H_{10}	C_3H_8[1]	C_3H_8/C_4H_{10}
First-order coefficient (mol/mol $[GaH]^{2+}$ *s*bar)	1.48×10^{1}	2.89×10^{1}	1.95
Zero-order coefficient (mol/mol $[GaH]^{2+}$*s)	1.83×10^{-1}	7.81×10^{-2}	0.43

[1] Data obtained from Ref [158]

4.5 Conclusions

The kinetics and mechanisms for C_2H_6 dehydrogenation and C_4H_{10} dehydrogenation and cracking were examined over Ga/H-MFI catalysts prepared via vapor-phase exchange of dehydrated H-MFI with $GaCl_3$. Catalysts prepared via this protocol contain predominantly isolated $[GaH]^{2+}$ cations and $[GaH_2]^{+}$ cations. We find that C_2H_6 dehydrogenation is catalyzed by

both $[GaH]^{2+}$ and $[GaH_2]^+$ cations with similar turnover frequencies over the two species. C_2H_6 dehydrogenation rates over the Ga/Al = 0.5 sample, which contains $[GaH_2]^+$ cations predominantly, bears a Langmuir-Hinshelwood dependence on C_2H_6 partial pressure. These kinetics are consistent with a 4-step 'alkyl' mechanism catalyzed by $[GaH_2]^+$ cations. C_2H_6 physisorbed at $[GaH_2]^+$ cations undergoes heterolytic C-H cleavage to form $[C_2H_5\text{-}GaH]^+$ species and H_2. The final step involves β-hydride elimination from the alkyl fragment to form C_2H_4. At low partial pressures of C_2H_6, dehydrogenation rates are first-order in C_2H_6 partial pressure and are limited by the initial C-H cleavage step which produces $[C_2H_5\text{-}GaH]^+$ species. However, at high partial pressures of C_2H_6, $[GaH_2]^+$ cations become saturated with $[C_2H_5\text{-}GaH]^+$, resulting in dehydrogenation rates becoming limited by β-hydride elimination.

Reactions of n-C_4H_8 –dehydrogenation, terminal and central cracking are catalyzed by $[GaH]^{2+}$ in Ga/H-MFI with turnover frequencies that are 3 orders, 2 orders and 1 order of magnitude respectively, higher than turnover frequencies over H-MFI under identical experimental conditions. $[GaH_2]^+$ cations appear to be inactive for these reactions. Space time studies provide evidence for the formation of trans-2-butene and 1-butene as primary dehydrogenation products, CH_4 and C_3H_6 as the primary terminal cracking products and C_2H_6 and C_2H_4 as the primary central cracking products. Rates of all three reactions bear a Langmuir-Hinshelwood dependence on C_4H_{10} partial pressure. These rates are also inhibited by H_2. Ratios of dehydrogenation rates to cracking (total) rates and those of terminal to central cracking are approximately independent of C_4H_{10} partial pressure, suggesting the involvement of a common C_4H_{10}-derived surface intermediate that catalyzes all three reactions. The formation of trans-2-butene and 1-butene as primary dehydrogenation products together with the observed partial pressure dependences of the rates at which these products are formed suggests that these intermediates are $[sec\text{-}C_4H_9\text{-}GaH]^+\text{-}H^+$ cation pairs. Experimental rate data supported by theoretical calculations are consistent with the prevalence of an alkyl mechanism for C_4H_{10} dehydrogenation and cracking, analogous to previous findings for C_3H_8 dehydrogenation and cracking.

The alkyl mechanism proceeds via the facile, heterolytic dissociation of physisorbed n-C_4H_{10} at $[GaH]^{2+}$ cations to form $[sec\text{-}C_4H_9\text{-}GaH]^+\text{-}H^+$ cation pairs. Dehydrogenation proceeds via rate-determining β-hydride elimination while terminal and central cracking proceed via a rate-determining attack of terminal and central C-C bonds in the alkyl fragment by the proximate Brønsted acid O-H group. The rate of terminal cracking over Ga/H-MFI is three-fold higher than the rate of central cracking, presumably because the latter pathway encounters a more constrained transition state.

The findings of this study highlight key differences between the mechanisms for C_2-C_4 light alkane conversion over Ga/H-MFI. These mechanistic differences lead to the observed differences in site requirements and turnover rates between these alkane reactants.

4.6 Acknowledgements

This work was supported by Chevron Energy Technology Company. We would like to thank Christopher Ho and Julie Rorrer for helpful technical discussions.

4.7 Supporting Information

4.7.1 C_2H_6 dehydrogenation rates over H-MFI as a function of C_2H_6 partial pressure.

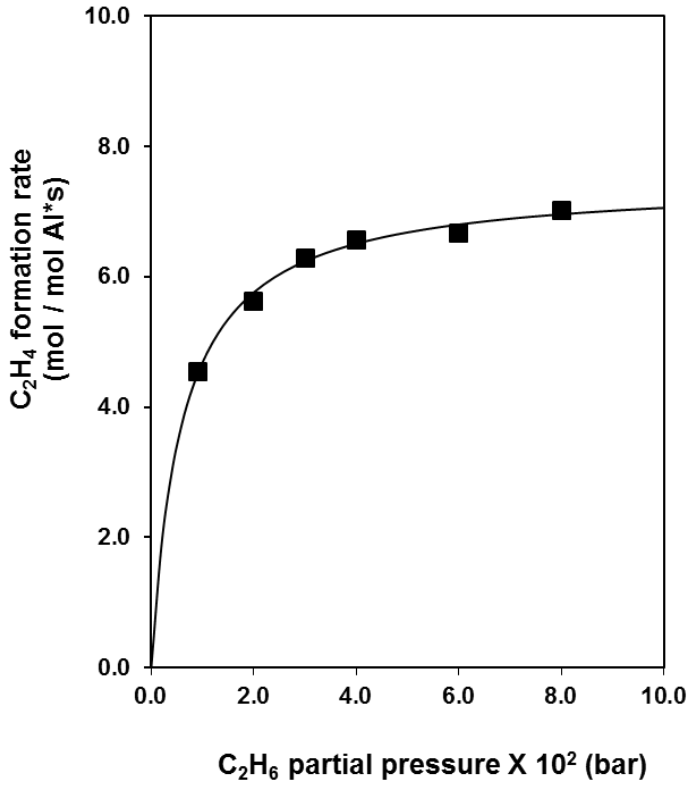

Figure 4.7-1. C_2H_6 dehydrogenation rates as a function of C_2H_6 partial pressure, measured over H-MFI at 753 K. Rates at each partial pressure were extrapolated to 0 space time. Solid lines indicate guides for the eye.

The dehydrogenation of C_2H_6 over H-MFI is catalyzed by Brønsted acid O-H groups via a monomolecular mechanism.[164–166] Steady-state C_2H_6 dehydrogenation rates over our H-MFI sample are nearly zero-order in C_2H_6 partial pressure as can seen in Figure 4.7-1. This rate dependence implies saturation of the active sites by strongly bound C_2H_6 derived intermediates, a conclusion that is inconsistent with the expected weak binding of C_2H_6 at Brønsted acid O-H active sites.[49,165] This observation suggests that active sites that are not Brønsted acidic may be responsible for the measured C_2H_6 dehydrogenation rates over our H-MFI sample. Characterization of our H-MFI sample by Na^+ exchange and NH_3-TPD has revealed that 13-15% of the total Al content in this sample is not associated with Brønsted acid O-H groups and is therefore likely present as Extra-Framework Al (EFAl) species.[11,133] These EFAl species may be catalytically active. For example, DFT studies using Al hydroxide clusters as proxies for EFAl species have revealed that such species are capable of dehydrogenating light alkanes via mechanisms involving the formation of strongly bound, chemisorbed alkyl-Al intermediates.[167] This type of mechanism would lead to a zero-order dependence of dehydrogenation rates on alkane partial pressure at sufficiently high partial pressures, as observed for C_2H_6

dehydrogenation over our H-MFI sample. Therefore, it is plausible that EFAl species are responsible for the observed C_2H_6 dehydrogenation rates over our H-MFI sample. In order to investigate this possibility further, the Brønsted acid O-H groups in our H-MFI sample were fully titrated with Na^+ cations using aqueous ion-exchange of H-MFI with $NaNO_3$ (see section 4.7.2 for ion-exchange procedure). The resulting Na-MFI was active for C_2H_6 dehydrogenation with rates that were only a factor of 1.7 lower than those measured over H-MFI (see Figure 4.7-2). The observation of catalytic activity over Na-MFI, in the absence of detectable Brønsted acid O-H groups in this material supports the hypothesis that EFAl species could contribute to measured C_2H_6 dehydrogenation rates over our H-MFI sample.

4.7.2 Procedure for preparation of Na-MFI

Na-MFI was prepared via aqueous ion-exchange of the parent H-MFI sample with 1 M $NaNO_3$ at 323 K for 6h (5 g sample per 100ml solution). This process was repeated 3 times. The sample was rinsed with 100ml H_2O in between exchanges. After the final exchange, the sample was separated from the $NaNO_3$ solution by means of vacuum filtration and washed with 100ml H_2O once again . After being dried in ambient air overnight, the sample was lightly crushed and was calcined in flowing dry air (100 cm^3 min^{-1} , Praxiar, ultrazero) by heating at 2 K min^{-1} to 773 K and holding at this temperature for 4h. An infrared spectrum of the sample (not shown) showed a near complete loss of the band at ~3600 cm^{-1} corresponding to the O-H stretch of Brønsted acid O-H groups. Thus, the Na-MFI sample had no detectable Brønsted acid O-H groups.

4.7.3 C_2H_6 dehydrogenation rates over Na-MFI and H-MFI at 2 kPa C_2H_6 and 753 K

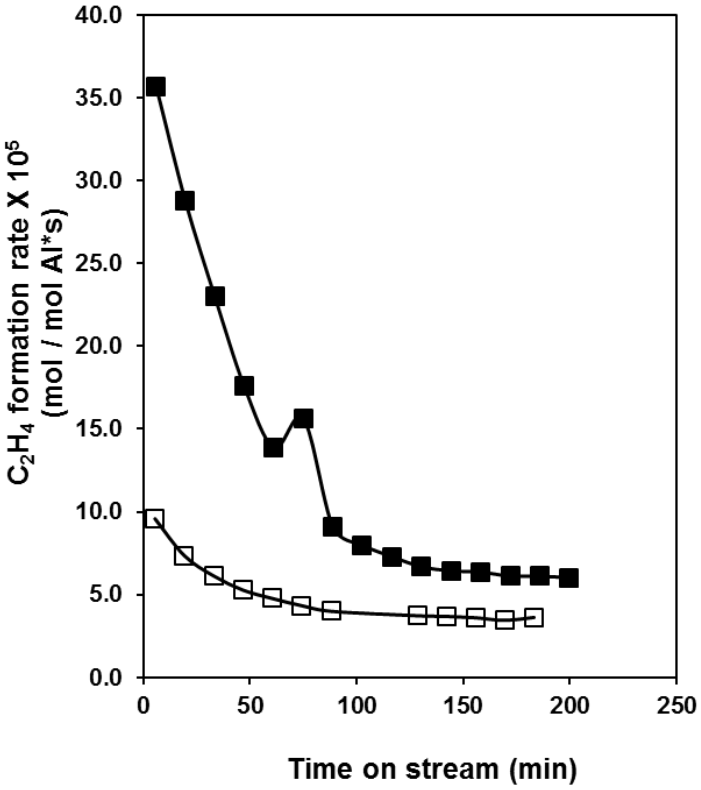

Figure 4.7-2. C_2H_6 dehydrogenation rates as a function of time-on-stream over H-MFI (filled black squares) and Na-MFI (empty black squares) measured at 2 kPa C_2H_6 , τ = 7 mol Al*s /mol C_2H_6 and 753 K. Solid lines reflect guides for the eye.

4.7.4 Effects of space time on C_2H_6 dehydrogenation over Ga/H-MFI

In this section, we examine the kinetics of C_2H_6 dehydrogenation over Ga/H-MFI. Since the highest catalytic activity was observed for a Ga/Al = 0.5, we will present data measured on this sample. Figure 4.7-3 shows the rate of C_2H_6 dehydrogenation at 2 kPa C_2H_6 /He and 753 K as a function of space time. It can be seen that the dehydrogenation rate decreases as a function of space time (dark squares, Figure 4.7-3). This suggests that either inhibition by product adsorption or conversion of C_2H_4 via secondary reactions results in a decrease in dehydrogenation rates with an increase in space time (or conversion). Since no secondary products were detected at the space times shown in Figure 4.7-3, we conclude that dehydrogenation rates are inhibited as a result of competitive adsorption by products. In order to probe the effects of product inhibition further, space time studies were also conducted in the presence of fixed partial pressures of H_2. These results are also shown in Figure 4.7-3. It is observed that the dehydrogenation rates decrease with an increase in H_2 partial pressure (shaded and empty squares in Figure 4.7-3), but only weakly. For example, at a given space time in Figure 4.7-3, the presence of 0.9 kPa H_2 only inhibits the rate by 20% or less. More significantly, even in the presence of 0.9 kPa H_2, dehydrogenation rates still decrease with space time, to an extent that is similar in the case where no H_2 is added to the system. These results suggest that inhibition by H_2 is not the sole reason for the decrease in rates with space time in Figure 4.7-3. This idea is also consistent with the nature of $[GaH_2]^+$ cations (the predominant active species in the Ga/Al = 0.5) over which H_2 cannot chemisorb to form a strongly bound inhibiting species. We suggest instead that the adsorption of C_2H_4 products at electron deficient Ga^{3+} centers causes an inhibition of rates that increases with space time. This assumption is reasonable because the physisorption of C_2H_4 at $[GaH_2]^+$ cations has been predicted to have an adsorption enthalpy of -11.5 kcal/mol, a value which is approximately 4 kcal/mol lower than the physisorption of C_2H_6 at $[GaH_2]^+$ cations (-7.2 kcal/mol).[83]

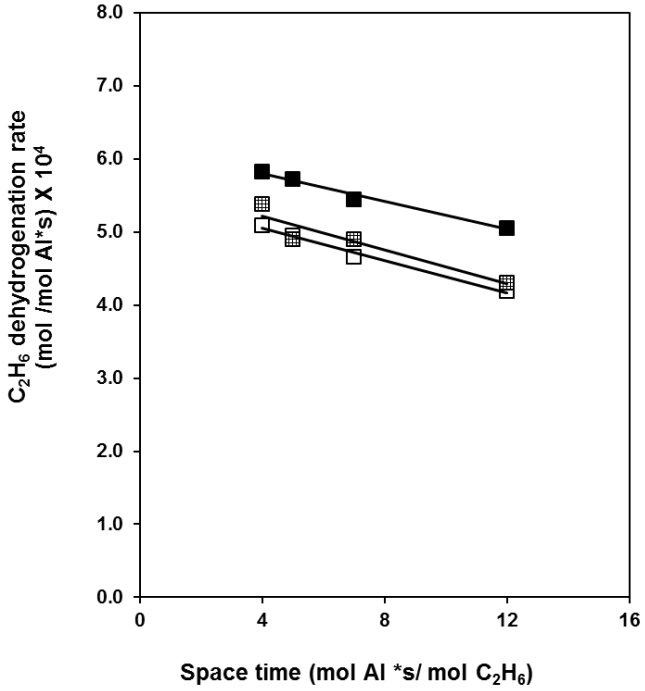

Figure 4.7-3. C_2H_6 dehydrogenation rates as a function of space time measured over the Ga/Al = 0.5 sample at 2 kPa C_2H_6 /He and at 753 K. Black squares represent rates measured in the absence of co-fed H_2 , shaded squares represent rates measured with 0.5 kPa H_2 co-fed, empty squares represent rates measured with 0.9 kPa H_2 co-fed. Solid lines reflect guidelines for the eye.

4.7.5 Derivation of rate expression for C_2H_6 dehydrogenation over $[GaH_2]^+$ cations

The elementary steps for the proposed 4-step alkyl mechanism are outlined in Scheme 4.4.3-1. A pseudo steady state hypothesis[168] was applied to all reaction intermediates. Step 1 in the sequence involves the physisorption of C_2H_6 at $[GaH_2]^+$ to form $[C_2H_6$-$[GaH_2]^+]$. The C_2H_6 is expected to be weakly bound to the $[GaH_2]^+$ cation and therefore this complex is expected to be in quasi-equilibrium with gas-phase C_2H_6, as reflected by Equation (4.7.5-1). In this equation, K_1 is the equilibrium constant for Step 1.

$$K_1 = \frac{[C_2H_6 - [GaH_2]^+]}{[C_2H_6][GaH_2]^+} \qquad (4.7.5\text{-}1)$$

The second step of the sequence involves the heterolytic cleavage of adsorbed C_2H_6 to form an alkyl Ga fragment while the abstracted H^+ coordinates to a framework O atom. This step is represented by Equation (4.7.5-2)

$$[C_2H_6 \cdots [GaH_2]^+] \xrightarrow{k_2} [C_2H_5 - GaH_2] \cdots H^+ \qquad (4.7.5\text{-}2)$$

Here, k_2 is the rate coefficient for the irreversible step 2.
The third step involves a fast and irreversible recombination of a Ga-bound hydride and adjacent H^+ to form H_2 which desorbs as gas-phase H_2 and leaves behind a $[C_2H_5$-$GaH]^+$ cation. This reaction is represented by Equation (4.7.5-3) in which k_3 is the rate coefficient for irreversible reaction.

$$[C_2H_5 - GaH_2] \cdots H^+ \xrightarrow{k_3} [C_2H_5 - GaH]^+ + H_2 \qquad (4.7.5\text{-}3)$$

The fourth step involves a β-hydride elimination within the alkyl fragment, which results in the formation of C_2H_4 and $[GaH_2]^+$ cation. This reaction is represented by equation (4.7.5-4). Here, k_4 is the rate coefficient for β-hydride elimination. C_2H_4 desorbs from $[GaH_2]^+$ in a subsequent quasi-equilibrated step.

$$[C_2H_5 - GaH]^+ \xrightarrow{k_4} [GaH_2]^+ + C_2H_4 \qquad (4.7.5\text{-}4)$$

Applying the pseudo-steady state hypothesis to intermediates $[C_2H_5$-$GaH_2]$-H^+ and $[C_2H_5$-$GaH]^+$ to yield equations (4.7.5-5) and (4.7.5-6), respectively.

$$\frac{d\left[[C_2H_5 - GaH_2] - H^+\right]}{dt} \sim 0 = k_2[C_2H_6 \cdots [GaH_2]^+] - k_3\left[[C_2H_5 - GaH_2] - H^+\right] \qquad (4.7.5\text{-}5)$$

$$\frac{d[[C_2H_5 - GaH]^+]}{dt} \sim 0 = k_3\left[[C_2H_5 - GaH_2] - H^+\right] - k_4[[C_2H_5 - GaH]^+] \qquad (4.7.5\text{-}6)$$

Finally, the turnover rate for C_2H_6 dehydrogenation can be represented by means of equation (4.7.5-7)

$$\frac{C_2H_6 \text{ dehydrogenation rate}}{[GaH_2]^+} = k_2 \frac{[C_2H_6 \cdots [GaH_2]^+]}{[L]} \qquad (4.7.5\text{-}7)$$

Here, [L] is the total number of active sites. [L] can be represented by means of the site balance which includes the concentrations of all relevant surface intermediates, as shown in Equation (4.7.5-8)

$$[\mathrm{L}] = [\mathrm{GaH_2}]^+ + [\mathrm{C_2H_6} \cdots [\mathrm{GaH_2}]^+] + [[\mathrm{C_2H_5} - \mathrm{GaH_2}] \cdots \mathrm{H}^+] + [[\mathrm{C_2H_5} - \mathrm{GaH}]^+] \quad (4.7.5\text{-}8)$$

In Equation (4.7.5-8), the second term, representing $[C_2H_6$—$[GaH_2]^+]$ species can be neglected because the concentration of this species is expected to be low due to the weak binding of C_2H_6 to $[GaH_2]^+$ cations[49] Further, the third term in Equation (4.7.5-8) representing $[C_2H_5$-$GaH_2]$—H^+ species is also expected to be insignificant because the recombination of the Ga-bound hydride with the adjacent H^+ is predicted to be almost barrier-less and therefore very fast relative to the other irreversible steps in the sequence. With two terms neglected, Equation (4.7.5-8) can be simplified to Equation (4.7.5-9).

$$[\mathrm{L}] = [\mathrm{GaH_2}]^+ + [[\mathrm{C_2H_5} - \mathrm{GaH}]^+] \quad (4.7.5\text{-}9)$$

The concentration of $[C_2H_5$-$GaH]^+$ species is obtained by simultaneously solving Equations (4.7.5-5), (4.7.5-6) and (4.7.5-1). The solution is given in terms of the concentration of C_2H_6 and $[GaH_2]^+$ by Equation (4.7.5-10).

$$[[\mathrm{C_2H_5} - \mathrm{GaH}]^+] = \frac{k_2 K_1}{k_4}[\mathrm{C_2H_6}][[\mathrm{GaH_2}]^+] \quad (4.7.5\text{-}10)$$

Equation (4.7.5-10) can be substituted into Equation (4.7.5-9) and the resulting expression can be substituted into Equation (4.7.5-7) to give a rate expression for C_2H_6 dehydrogenation in terms of C_2H_6 concentration, shown here as Equation (4.7.5-11).

$$\frac{\mathrm{C_2H_6\ dehydrogenation\ rate}}{[\mathrm{GaH_2}]^+} = \frac{k_2 K_1[\mathrm{C_2H_6}]}{1+\frac{k_2 K_1}{k_4}[\mathrm{C_2H_6}]} \quad (4.7.5\text{-}11)$$

4.7.6 Gibbs free energies for elementary steps in 4-step alkyl sequence over $[GaH_2]^+$ cations

Gibbs free energies and enthalpies for the elementary steps in Scheme 4.4.3-1 were reported by Mansoor et al. at a temperature of 823 K.[49] For sake of comparison with experiments, we estimate these free energies at 753 K, a temperature more realistic of the experimental conditions used in this study. The relationship $\Delta G = \Delta H - T\Delta S$ (G= Gibbs free energy, H= Enthalpy, S= Entropy) is used for this purpose, the results are reported in Table 4.7-1.

Table 4.7-1. Gibbs free energies for intermediates and transition states in Scheme 1 at 753 K

Nature of quantity[1]	ΔH (kcal/mol)	ΔG, 823K (kcal/mol)	ΔG, 753K (kcal/mol)
Step 1, I	-7.2	24	21.3
Step 2, TS	27.5	62.4	59.4
Step 2, I	18.8	51.8	49
Step 3, TS	18.8	55	51.9
Step 3, I	-2.9	10.7	9.5
Step 4, TS	42.4	52.9	52
Step 4, I	26.1	31.9	31.4

[1] 'I' refers to the energy (enthalpy or Gibbs free energy) of the intermediate formed at the end of the step, relative to gas-phase C_2H_6. 'TS' refers to the energy (enthalpy or Gibbs free energy) of the transition state for the step relative to gas-phase C_2H_6.

4.7.7 Temperature dependence of first and zero order rate coefficients for C_2H_6 dehydrogenation over Ga/H-MFI (Ga/Al = 0.5)

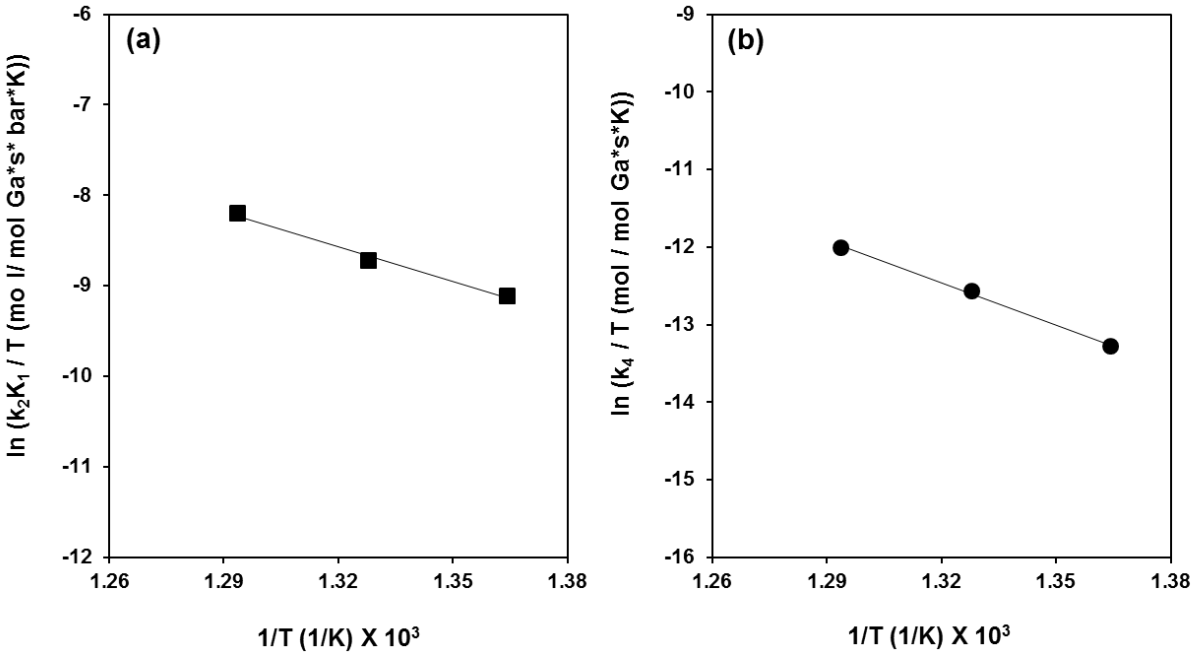

Figure 4.7-4. Temperature dependence of rate coefficients for C_2H_6 dehydrogenation over Ga/H-MFI (Ga/Al = 0.5). (a) k_2K_1 , first-order rate coefficient (b) k_4 , zero-order rate coefficient. Rate coefficients were obtained by nonlinear regression rate data in Figure 4.4.2-1 to Equation 4.4.2-1.Solid lines reflect linear regression of rate constants using equations derived from transition state theory.[153,158]

4.7.8 Effects of space time on product molar ratios during n-C_4H_{10} conversion over Ga/H-MFI (Ga/Al = 0.2) at 718 K

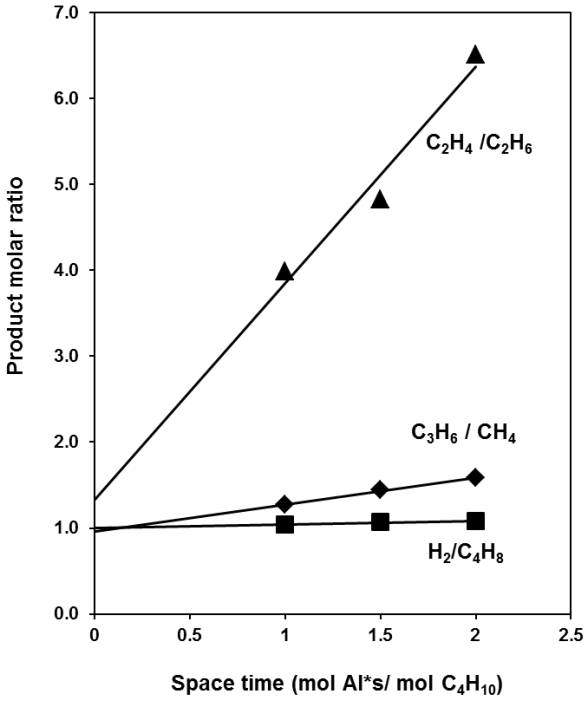

Figure 4.7-5. Product molar ratios of C_4H_8 /H_2 (filled squares), C_3H_6 /CH_4 (filled diamonds) and C_2H_4 /C_2H_6 (filled triangles) as a function of space time, measured at 2 kPa C_4H_{10} /He and 718 K over the Ga/Al = 0.2 sample. C_4H_{10} conversions < 2% Solid lines reflect linear regression of data to zero space time.

4.7.9 Effects of space time on the steady-state selectivity towards butene isomers formed during C_4H_{10} dehydrogenation

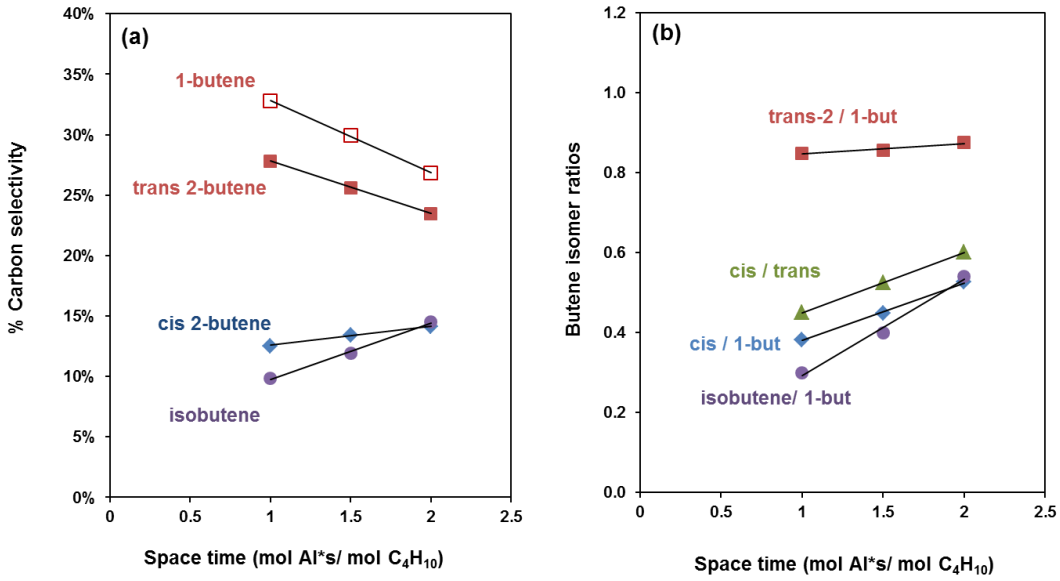

Figure 4.7-6. (a) % Carbon selectivity of butene isomers formed over Ga/H-MFI as a function of space time (b) Butene isomer ratios as a function of space time. Selectivities were measured at 2 kPa C_4H_{10} /He at 718 K over Ga/H-MFI (Ga/Al = 0.2). Solid lines reflect slopes of data.

4.7.10 Effects of space time on C_4H_{10} dehydrogenation, terminal and central cracking rates in the absence and presence of cofed H_2

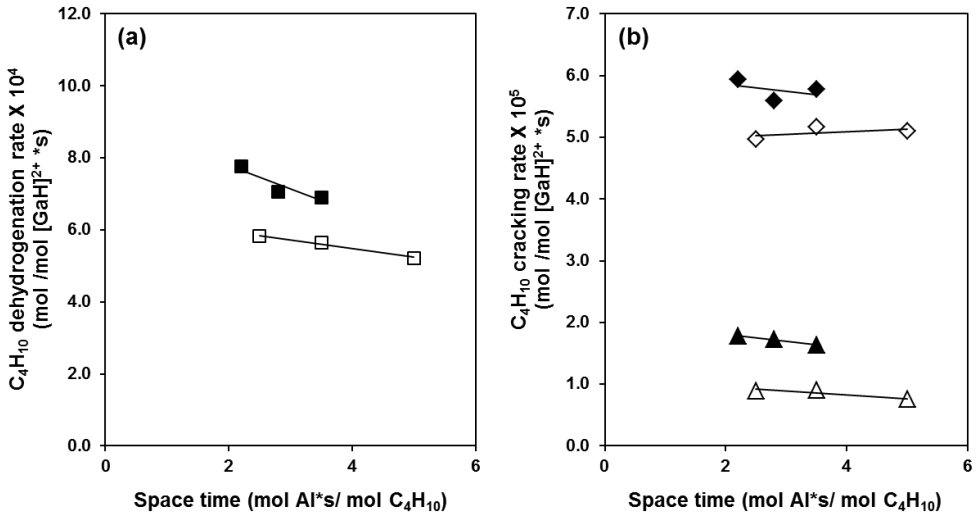

Figure 4.7-7. (a) Rates of C_4H_{10} dehydrogenation as a function of space time in the absence of cofed H_2 (filled squares) and in the presence of 0.9 kPa H_2 (empty squares). (b) C_4H_{10} terminal cracking (filled diamonds) and C_4H_{10} central cracking (filled triangles) as a function of space time in the absence of H_2 (filled diamonds and triangles respectively) and in the presence of 0.9kPa H_2 (empty diamonds and triangles respectively). Rates were measured at 2 kPa C_4H_{10}/He and 718 K over Ga/H-MFI (Ga/Al = 0.2). C_4H_{10} conversions < 2 % Solid lines reflect slopes of data points.

4.7.11 Effects of C_4H_{10} partial pressure on C_4H_{10} dehydrogenation, terminal and central cracking turnover rates (normalized per $[GaH]^{2+}$) at 703 K and 688 K

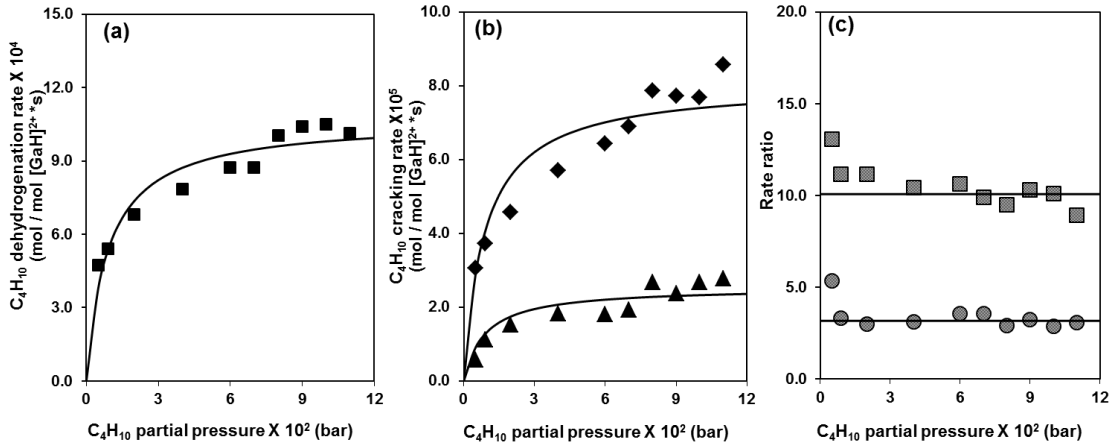

Figure 4.7-8. C_4H_{10} dehydrogenation rates (squares, Figure 4.7-8a), terminal (diamonds, Figure 4.7-8b) and central cracking turnover rates (triangles, Figure 4.7-8b), dehydrogenation to cracking rate ratio (shaded squares, Figure 4.7-8c) and terminal to central cracking rate ratio (shaded circles, Figure 4.7-8c) as a function of C_4H_{10} partial pressure, measured at 703 K over the Ga/Al = 0.2 sample. Rates were extrapolated to zero space time.

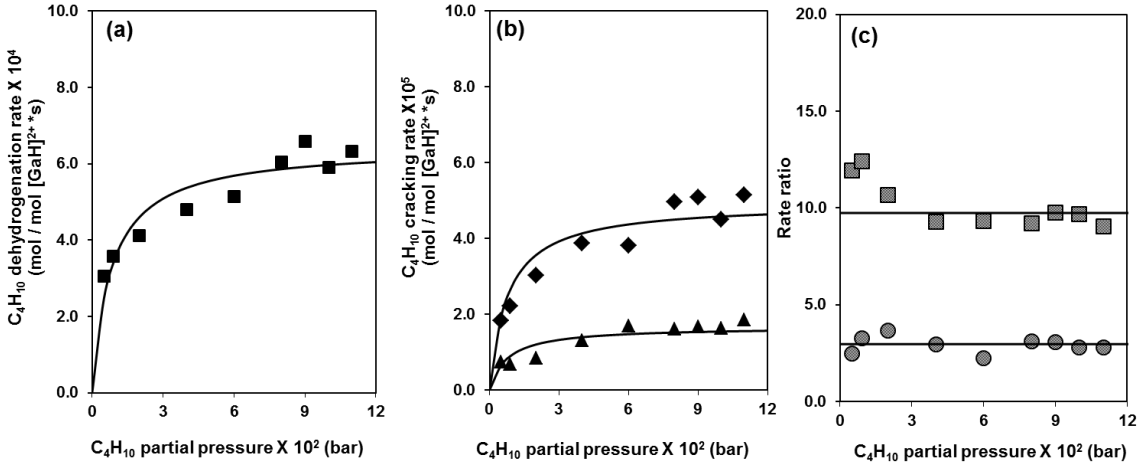

Figure 4.7-9. C_4H_{10} dehydrogenation turnover rates (squares, Figure 4.7-9a), terminal (diamonds, Figure 4.7-9b) and central cracking turnover rates (triangles, Figure 4.7-9b), dehydrogenation to cracking rate ratio (shaded squares, Figure 4.7-9c) and terminal to central cracking rate ratio (shaded circle, Figure 4.7-9c) as a function of C_4H_{10} partial pressure, measured at 688 K over the Ga/Al = 0.2 sample. Rates were extrapolated to zero space time.

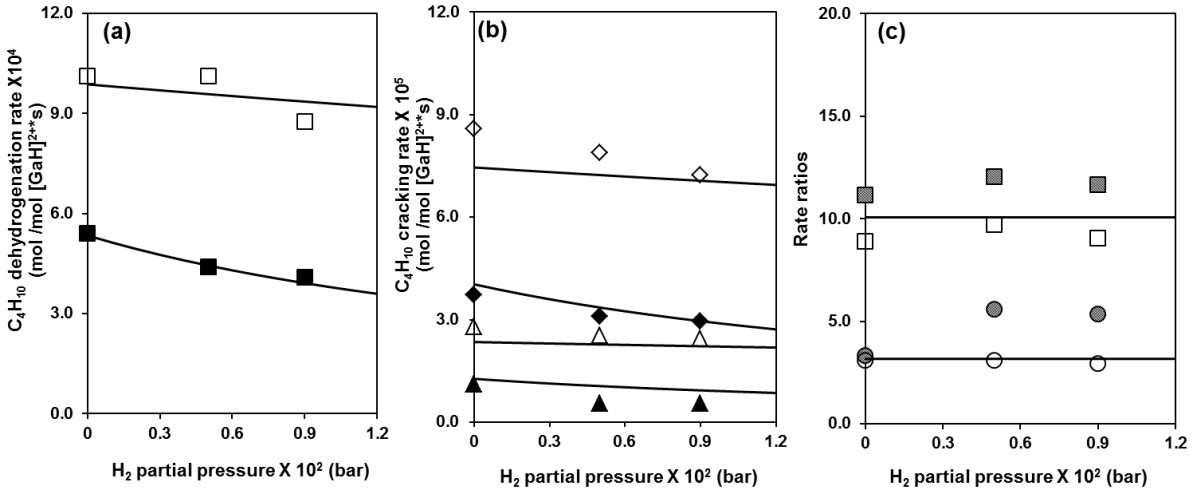

Figure 4.7-10. C_4H_{10} dehydrogenation turnover rates (squares, Figure 4.7-10a), terminal and central cracking turnover rates (diamonds and triangles respectively, Figure 4.7-10b), dehydrogenation to cracking rate ratio (squares, Figure 4.7-10c) and terminal to central cracking rate ratio (circles, Figure 4.7-10c) as a function of H_2 partial pressure, measured at 703 K over the Ga/Al = 0.2 sample. Dark and shaded symbols reflect data collected at 0.9 kPa C_4H_{10}/He while open symbols reflect data collected at 11 kPa C_4H_{10}/He. Rates were extrapolated to zero space time. Solid lines reflect regression to Equation S23, S24 and S25.

4.7.12 Effects of C_4H_{10} partial pressure on C_4H_{10} dehydrogenation, terminal and central cracking turnover rates over H-MFI at 718 K

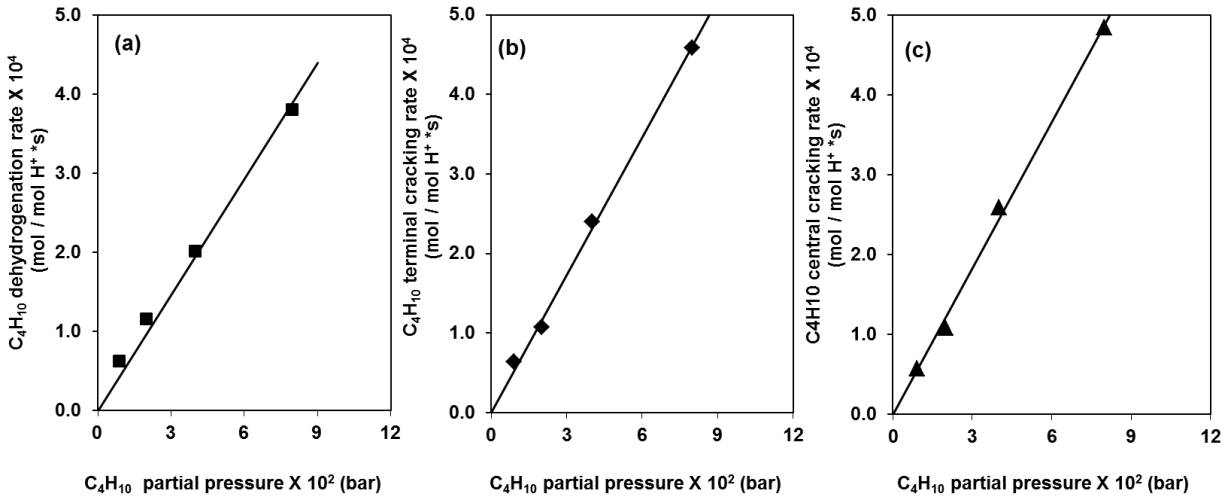

Figure 4.7-11. C_4H_{10} turnover rates (normalized per H^+) as a function of C_4H_{10} partial pressure over H-MFI at 718 K. (a) Dehydrogenation (b) Terminal cracking (c) Central cracking. Reported rates were extrapolated to 0 space time. Solid lines reflect linear regression of rate data.

Table 4.7-2. Steady-state product selectivities (on a % C basis) during n-C_4H_{10} conversion over H-MFI at 0.9 kPa C_4H_{10}, τ = 48 mol Al*s/mol C_4H_{10} and 718 K. C_4H_{10} conversions < 1%

Product	CH_4	C_2H_4	C_2H_6	C_3H_6	Butenes
Selectivity (%)	7.8	18.3	17.1	27.0	27.7

4.7.13 Effects of C_4H_{10} partial pressure on dehydrogenation /cracking and terminal/central cracking rate ratios after correcting for contributions from Brønsted acid catalyzed reactions in Ga/H-MFI

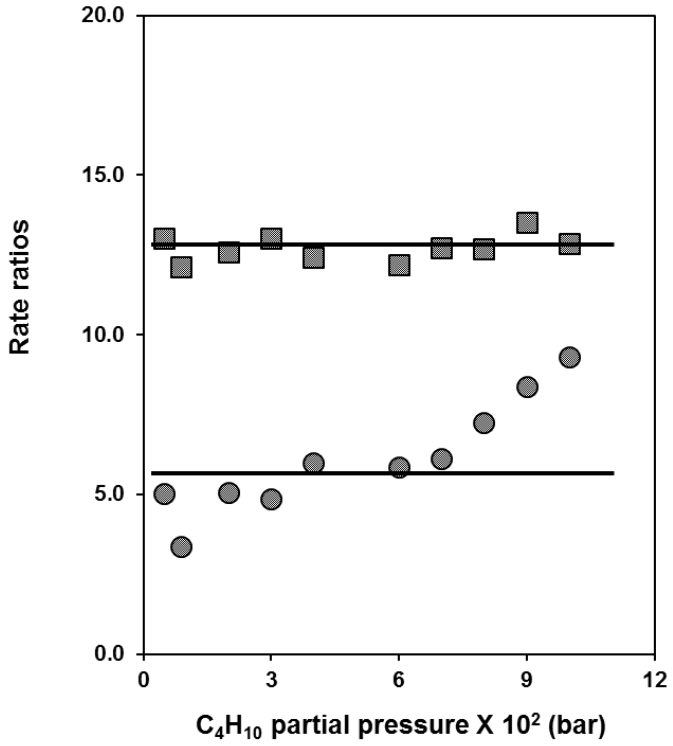

Figure 4.7-12. Dehydrogenation to cracking rate ratios (D/C) (shaded squares) and terminal to central cracking rate ratios (C_t/C_c) (shaded circles) over Ga/H-MFI (Ga/Al = 0.2) after correction of terminal and central cracking rates for contributions from protolytic cracking catalyzed by Brønsted acid O-H groups. The solid lines reflect guides for the eye.

4.7.14 Derivation of rate expressions for C_4H_{10} dehydrogenation, terminal and central cracking over $[GaH]^{2+}$ sites.

The elementary steps for proposed 'alkyl' mediated mechanisms for C_4H_{10} dehydrogenation, terminal and central cracking over $[GaH]^{2+}$ sites are shown in Scheme 4.4.7-1. The pseudo steady-state hypothesis[168] was applied to all reactive surface intermediates. The first two steps of the mechanisms are common for all three reaction pathways. Step 1 involves the physisorption of C_4H_{10} at $[GaH]^{2+}$ cations to form $[C_4H_{10}$—$[GaH]^{2+}]$ complexes. Step 2 involves the fast, heterolytic dissociation of adsorbed C_4H_{10} by $[GaH]^{2+}$ to form sec-$[C_4H_9$-$GaH]^+$-H^+ cation pairs. Steps 1 and 2 are expected to have low activation barriers, analogous to C_3H_8 conversion over Ga/H-MFI[158] and these steps are therefore assumed to be quasi-equilibrated. Both steps are represented by Equations (4.7.14-1) and (4.7.14-2), respectively.

$$K_{phys} = \frac{[C_4H_{10}-[GaH]^{2+}]}{[C_4H_{10}][GaH]^{2+}} \qquad (4.7.14\text{-}1)$$

$$K_{dis} = \frac{[[C_4H_9-GaH]^+-H^+]}{[C_4H_{10}-[GaH]^{2+}]} \qquad (4.7.14\text{-}2)$$

Here, K_{phys} is the equilibrium constant for n-C_4H_{10} physisorption at $[GaH]^{2+}$ cations, while K_{dis} is the equilibrium constant for heterolytic dissociation of adsorbed C_4H_{10} by $[GaH]^{2+}$ cations. The surface concentration of $[C_4H_9$-$GaH]^+$-H^+ cation pairs can be expressed in terms of the concentrations of gas-phase C_4H_{10} ($[C_4H_{10}]$) and $[GaH]^{2+}$ cations by combining Equations (4.7.14-1) and (4.7.14-2), shown here as Equation (4.7.14-3).

$$[[C_4H_9 - GaH]^+ - H^+] = K_{dis}K_{phys}[C_4H_{10}][[GaH]^{2+}] \qquad (4.7.14\text{-}3)$$

The three reaction pathways bifurcate after Step 2. Dehydrogenation proceeds via irreversible, rate-determining β-hydride elimination in the alkyl fragment, resulting in the formation of C_4H_8 and H_2 in a concerted fashion. The dehydrogenation rate (per $[GaH]^{2+}$) can therefore be represented by Equation (4.7.14-4). Here, k_d is the rate coefficient for β-hydride elimination and [L] is the total concentration of active sites.

$$\frac{C_4H_{10}\text{ dehydrogenation rate}}{[GaH]^{2+}} = k_d \frac{[[C_4H_9-GaH]^+-H^+]}{[L]} \qquad (4.7.14\text{-}4)$$

Terminal cracking proceeds via rate-determining H^+ attack of a terminal C-C bond in $[C_4H_9$-$GaH]^+$-H^+ cation pairs (Step 3t in Scheme 4.4.7-1), resulting in the formation of $[CH_3$-$GaH]^+$-propoxide pairs. CH_4 and C_3H_6 form in subsequent steps that are kinetically irrelevant. The terminal cracking rate can be represented by Equation (4.7.14-5). Here, k_t is the rate coefficient for H^+ bond attack of the terminal C-C bond and [L] is the total concentration of active sites.

$$\frac{C_4H_{10}\text{ terminal cracking rate}}{[GaH]^{2+}} = k_t \frac{[[C_4H_9-GaH]^+-H^+]}{[L]} \qquad (4.7.14\text{-}5)$$

Central cracking proceeds via rate-determining H^+ attack of the central C-C bond in $[C_4H_9\text{-}GaH]^+\text{-}H^+$ cation pairs (Step 3c in Scheme 4.4.7-1), resulting in the formation of $[C_2H_5\text{-}GaH]^+$-ethoxide pairs. C_2H_6 and C_2H_4 form in subsequent steps that are kinetically irrelevant. The central cracking rate can be represented by Equation (4.7.14-6). Here, k_c is the rate coefficient for H^+ bond attack of the central C-C bond and [L] is the total concentration of active sites.

$$\frac{C_4H_{10}\text{ central cracking rate}}{[GaH]^{2+}} = k_c \frac{[[C_4H_9-GaH]^+-H^+]}{[L]} \qquad (4.7.14\text{-}6)$$

The concentration of active sites [L] can be represented by means of the site balance. The site balance contains the concentrations of all relevant surface intermediates. Since all the steps succeeding Step 3d, 3t and 3c are expected to be fast, the surface intermediates formed after these steps are not likely to be present in significant concentrations. Then, the site balance takes the form of Equation (4.7.14-7).

$$[L] = [GaH]^{2+} + [C_4H_{10} - [GaH]^{2+}] + [[C_4H_9 - GaH]^+ - H^+] \qquad (4.7.14\text{-}7)$$

In Equation (4.7.14-7), the second term representing $C_4H_{10}\text{-}[GaH]^{2+}$ species is expected to be insignificant due to the predicted weak binding of C_4H_{10} to $[GaH]^{2+}$ in the physisorbed state. Therefore, Equation (4.7.14-7) simplifies to:

$$[L] = [GaH]^{2+} + [[C_4H_9 - GaH]^+ - H^+] \qquad (4.7.14\text{-}8)$$

Equation (4.7.14-8), together with Equation (4.7.14-3) and Equations 4.7.14-4-6 can be solved to obtain the rate expressions for C_4H_{10} dehydrogenation, terminal and central cracking shown in section 4.4.7 as Equations 4.4.7-1, 2 and 3.

4.7.15 Temperature dependence of first and zero order rate coefficients for C_4H_{10} dehydrogenation, terminal and central cracking over Ga/H-MFI (Ga/Al = 0.2)

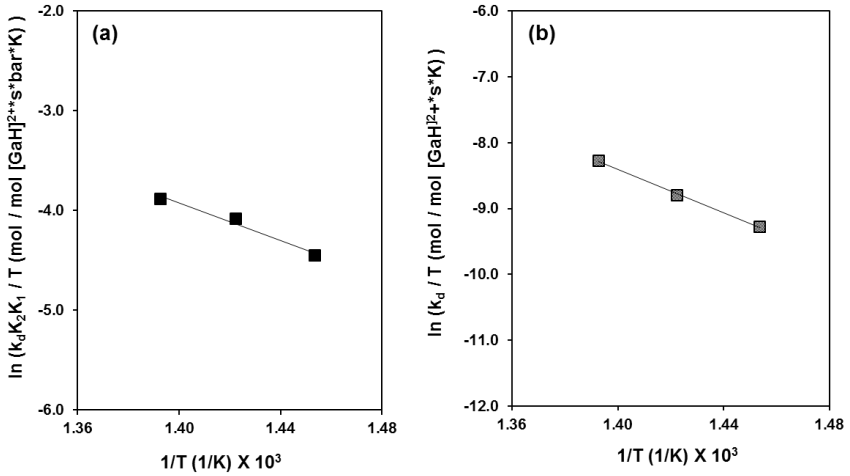

Figure 4.7-13. (a) First-order C_4H_{10} dehydrogenation rate constants- $k_dK_2K_1$ as a function of temperature (b) Zero-order C_4H_{10} dehydrogenation rate constants- k_d as a function of temperature. Rate constants were obtained by nonlinear least squares regression of rate data in Figure 4.4.6-1a to Equation 4.4.6-1. Solid lines in figure denote linear regression fits to equations derived from transition state theory.[153,158]

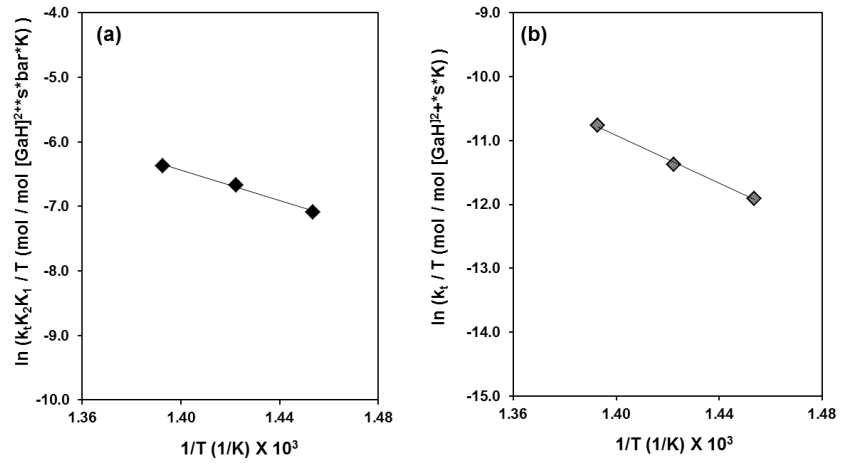

Figure 4.7-14. (a) First-order C_4H_{10} terminal cracking rate constants- $k_tK_2K_1$ as a function of temperature (b) Zero-order C_4H_{10} terminal cracking rate constants- k_t as a function of temperature. Rate constants were obtained by nonlinear least squares regression of rate data in Figure 4.4.6-1b to Equation 4.4.6-2. Solid lines in figure denote linear regression fits to equations derived from transition state theory.[153,158]

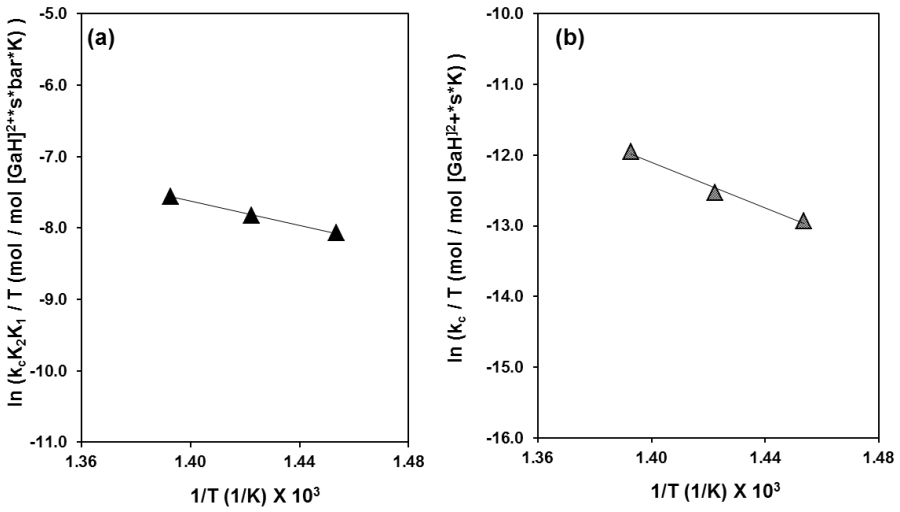

Figure 4.7-15. (a) First-order C_4H_{10} central cracking rate constants- $k_cK_2K_1$ as a function of temperature (b) Zero-order C_4H_{10} central cracking rate constants- k_c as a function of temperature. Rate constants were obtained by nonlinear least squares regression of rate data in Figure 4.4.6-1b to Equation 4.4.6-3. Solid lines in figure denote linear regression fits to equations derived from transition state theory.[153,158]

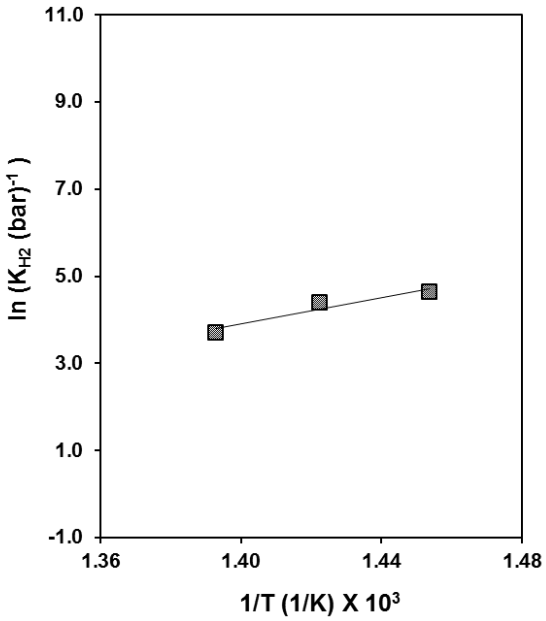

Figure 4.7-16. Dependence of H_2 adsorption constants as a function of temperature. Adsorption constants were derived by regressing rate data to Equation (4.7.16-1,2,3). Solid lines in figure denote linear regression fits to equations derived from transition state theory.[153,158]

4.7.16 Modification of Equations 4.4.6-1,2 and 3 to obtain adsorption constant for H_2 inhibition

As discussed in the main text, H_2 appears to inhibit dehydrogenation, terminal and cracking reactions. As seen in Figure 4.7-10, dehydrogenation to cracking (D/C) and terminal to central cracking (C_t/C_c) rate ratios are approximately independent of H_2 partial pressure. This finding suggests that all three reactions are inhibited by a common surface intermediate. In the case of C_3H_8 dehydrogenation and cracking, it was found that H_2 inhibits both reactions by dissociating at $[GaH]^{2+}$ cations to form $[GaH_2]^+$ -H^+ cations.[158] The $[GaH_2]^+$ cations in these species are not catalytically active for C_3H_8 dehydrogenation and cracking.[158] In analogy to these findings, the data in the present study suggests that a similar inhibition mechanism may be involved during C_4H_{10} dehydrogenation and cracking. In order to test this possibility, Equations 4.4.6-1, 2 and 3 may be modified as Equations (4.7.16-1), (4.7.16-2) and (4.7.16-3) to include a denominator term to reflect inhibition by H_2. The adsorption constant (K_{H2}) for H_2 in these equations is the parameter γ with units of $(bar)^{-1}$

$$C_4H_{10}\text{ dehydrogenation rate} = \frac{\alpha_d[C_4H_{10}]}{1+\beta[C_4H_{10}]+\gamma[C_4H_{10}]} \qquad (4.7.16\text{-}1)$$

$$C_4H_{10}\text{ terminal cracking rate} = \frac{\alpha_t[C_4H_{10}]}{1+\beta[C_4H_{10}]+\gamma[C_4H_{10}]} \qquad (4.7.16\text{-}2)$$

$$C_4H_{10}\text{ central cracking rate} = \frac{\alpha_c[C_4H_{10}]}{1+\beta[C_4H_{10}]+\gamma[C_4H_{10}]} \qquad (4.7.16\text{-}3)$$

The temperature dependence of K_{H2} is shown in Figure 4.7-16. The adsorption enthalpy for H_2 extracted from this data with the aid of thermodynamic relationships[158] is - 30.1 ± 17.3 kcal/mol. This highly exothermic value is consistent (within the error margins shown) to DFT predictions for the dissociative adsorption of H_2 at $[GaH]^{2+}$ to form $[GaH_2]^+$-H^+ cation pairs (-14.7 kcal/mol). We therefore conclude that C_4H_{10} dehydrogenation, terminal and central cracking over $[GaH]^{2+}$ are inhibited by H_2 via the formation of $[GaH_2]^+$-H^+ cation pairs. As shown in the main text, $[GaH_2]^+$ cations in these species are inactive for C_4H_{10} dehydrogenation, terminal and central cracking.

Chapter 5

5 Conclusions

The mechanisms of light alkane dehydrogenation over Ga/H-MFI catalysts were studied by synthesizing and characterizing well-defined Ga species in Ga/H-MFI and by combining experimental kinetic rate measurements with theoretical calculations. In chapter 2, Ga/H-MFI catalysts with a range of Ga/Al ratios (0.1-0.7) were synthesized via anhydrous vapor-phase exchange of Brønsted acid O-H groups in H-MFI with $GaCl_3$. This procedure led to the grafting of $[GaCl_2]^+$ cations at cation-exchange sites in H-MFI. Ga-bound Cl ligands were stoichiometrically removed by treating $[GaCl_2]^+$/H-MFI materials in H_2 at 823 K. This procedure led to the formation of $[GaH_2]^+$ cations and HCl. Upon oxidation of these materials in O_2 , oxidized cationic Ga^{3+} species formed and crystalline domains of β-Ga_2O_3 were undetectable by Raman spectroscopy in any of the samples. Exchange stoichiometry measurements using infrared spectroscopy and NH_3-TPD together with theoretical calculations suggested that for Ga/Al ratios ≤ 0.3, $[Ga(OH)_2]^+$-H^+ cation pairs are the predominant cationic Ga species in Ga/H-MFI. A small concentration of divalent $[Ga(OH)]^{2+}$ cations is also present at low Ga/Al ratios (Ga/Al ≤ 0.1). Both structures require the presence of proximate cation-exchange sites that are associated with pairs of framework Al atoms that are either NNN (Next-nearest neighbors) or NNNN (Next, next-nearest neighbors). Ga K-edge XANES and EXAFS and wavelet analyses of samples with Ga/Al ratios ≤ 0.3 are consistent with the predominant presence of isolated $[Ga(OH)_2]^+$-H^+ cation pairs in Ga/H-MFI. At low Ga/Al ratios (~ 0.1), chemical and spectroscopic probes together with theoretical calculations suggest that $[Ga(OH)]^{2+}$ cations form at proximate cation-exchange sites with framework Al-Al distances that are ≤ 5 Å apart while $[Ga(OH)_2]^+$-H^+ cation pairs are more stable at proximate cation-exchange sites with framework Al-Al distances that are > 5 Å apart. The concentration of $[Ga(OH)_2]^+$-H^+ cation pairs increases with an increase in Ga content until the all available proximate cation-exchange sites are saturated with Ga species at a Ga/Al ratio of 0.3. Further increases in Ga content lead to the formation neutral GaO_x oligomers-Ga-O-Ga linkages in these structures are detectable by wavelet analysis of EXAFS spectra.

Upon exposure of oxidized Ga/H-MFI samples to H_2 at elevated temperatures (> 700 K), H_2-TPR, NH_3-TPD, infrared spectroscopy, Ga K-edge XANES and EXAFS suggest that $[Ga(OH)]^{2+}$ cations and $[Ga(OH)_2]^+$-H^+ cation pairs convert into $[GaH]^{2+}$ cations, $[Ga(OH)H]^+$-H^+ cation pairs and $[GaH_2]^+$-H^+ cation pairs. Under sufficiently anhydrous reducing conditions (≤ 10^{-1} Pa H_2O), $[Ga(OH)H]^+$ -H^+ cation pairs further reduce to $[GaH_2]^+$-H^+ cation pairs. Ga-H vibrational stretches in $[GaH]^{2+}$ cations and $[GaH_2]^+$ cations are detectable via infrared spectroscopy of H_2-treated Ga/H-MFI. Ga K-edge XANES suggests that at temperatures > 713 K, 4-coordinate $[GaH_2]^+$ cations transform into 3-coordinate $[GaH_2]^+$ cations, with one framework Ga-O_f bond. Theoretically computed thermodynamic phase diagrams suggest that Ga^{3+} speciation is highly sensitive to framework Al-Al distances between proximate cation-exchange sites, H_2 and H_2O partial pressures and temperature. The fraction of $[GaH]^{2+}$ cations can be quantified by H_2-TPR and NH_3-TPD measurements. These data together with thermodynamic phase diagrams suggest that under anhydrous reducing conditions and for Ga/Al ratios ≤ 0.3, $[GaH]^{2+}$ cations are more stable on proximate cation-exchange sites with framework

Al-Al distances that are ≤ 5 Å apart and predominantly form at low Ga/Al ratios (≤ 0.1). $[GaH_2]^+$-H^+ cation pairs are more stable on proximate cation-exchange sites with framework Al-Al distances that are > 5 Å apart and appear to form in increasing concentration in Ga/H-MFI between Ga/Al ratios of 0.1 and 0.3.

In chapter 3, the kinetics and mechanism of propane (C_3H_8) dehydrogenation were examined over Ga/H-MFI catalysts (Ga/Al = 0.05- 0.5) prepared using the protocols described in chapter 2. Upon exposure of oxidized Ga/H-MFI catalysts to C_3H_8 reactants at temperatures > 700 K, an induction period was observed during which the C_3H_8 conversion rates increased with time-on-stream before reaching steady-state. If catalysts were pre-exposed to H_2 prior to reaction, the induction period was nearly eliminated and similar steady-state rates were achieved suggesting that GaH_x species that form upon pretreatment of Ga/H-MFI catalysts in H_2 are the catalytically relevant species for C_3H_8 conversion. Steady-state C_3H_8 dehydrogenation and cracking rates (normalized per Al_{tot} atom) increased with Ga content up to a Ga/Al ratio of 0.1 Increases in Ga content beyond this value did not lead to further increases in both reaction rates. At their maximum, C_3H_8 dehydrogenation rates and cracking rates (normalized per Al_{tot}) were found to be 2 orders and 1 order of magnitude higher than the corresponding reaction rates over H-MFI under identical conditions suggesting that the reactivity of residual Brønsted acid O-H groups in Ga/H-MFI is negligible relative to the reactivity of Ga species. Dehydrogenation and cracking rates normalized per $[GaH]^{2+}$ site ($[GaH]^{2+}$ site densities were estimated by measuring the concentration of residual Brønsted acid O-H groups in Ga/H-MFI using NH_3-TPD), were found to be independent of the Ga/Al ratio suggesting that $[GaH]^{2+}$ cations catalyze both reactions while $[GaH_2]^+$ cations are inactive for C_3H_8 conversion.

Dehydrogenation and cracking rates exhibited a Langmuir-Hinshelwood dependence on C_3H_8 partial pressure suggesting the involvement of strongly-bound C_3H_8 derived surface intermediates. Rates for both reactions were inhibited by H_2. Dehydrogenation to cracking rate ratios were found to be independent of C_3H_8 and H_2 partial pressures, suggesting that both reactions are mediated by a common C_3H_8 derived reactive surface intermediate and are inhibited by a common surface intermediate. Experimentally measured activation enthalpies together with theoretical predictions were consistent with an alkyl mediated mechanism for both C_3H_8 dehydrogenation and cracking. Both reactions were found to proceed via the heterolytic dissociation of physisorbed C_3H_8 by $[GaH]^{2+}$ to form $[C_3H_7\text{-}GaH]^+$-H^+ cation pairs. Dehydrogenation then to proceeds via rate-determining β-hydride elimination from the $[C_3H_7\text{-}GaH]^+$ species to form C_3H_6 and H_2 in a concerted fashion. Cracking proceeds via the rate-determining attack of the C-C bond in $[C_3H_7\text{-}GaH]^+$ species by the proximal Brønsted acid O-H group to form $[CH_3\text{-}GaH]^+$ species and an ethoxide species at the proximate cation-exchange site. In steps that are kinetically irrelevant, ethoxide species decompose to form C_2H_4 and a Brønsted acid O-H group. This O-H group then recombines with the Ga-bound CH_3 group to form CH_4 thereby restoring the $[GaH]^{2+}$ site. Thus, the selectivity of Ga/H-MFI towards dehydrogenation vs. cracking was found to depend only on the difference between the intrinsic activation barriers of the dehydrogenation and cracking transition states. This finding was consistent with the observation that the dehydrogenation to cracking rate ratio is independent of C_3H_8 and H_2 partial pressures but weakly dependent on temperature. Both dehydrogenation and cracking were similarly inhibited by H_2 due to the dissociative adsorption of H_2 at $[GaH]^{2+}$ to form $[GaH_2]^+$-H^+ cation pairs which are much less active for C_3H_8 conversion.

In chapter 4, we examined the site requirements, kinetics and mechanisms for ethane (C_2H_6) and n-butane (n-C_4H_{10}) dehydrogenation and cracking over Ga/H-MFI catalysts prepared

using the protocols described in chapter 2. We found that the site requirements for alkane dehydrogenation and cracking reactions depend on the carbon chain length of the alkane. C_2H_6 dehydrogenation is catalyzed by both $[GaH]^{2+}$ and $[GaH_2]^+$ cations with similar turnover frequencies (1.1 x 10^{-3} mol/mol Ga*s at 753 K). C_2H_6 dehydrogenation rates catalyzed by $[GaH_2]^+$ exhibited a Langmuir-Hinshelwood dependence on C_2H_6 partial pressure, consisting with the involvement of chemisorbed $[C_2H_5\text{-}GaH]^+$ intermediates. Kinetic rate data together with theoretical calculations were consistent with the occurrence of an alkyl mechanism by which $[GaH_2]^+$ cations catalyze the dehydrogenation of C_2H_6. Dehydrogenation proceeds via the C-H activation of adsorbed C_2H_6 by $[GaH_2]^+$ to form $[C_2H_5\text{-}GaH]^+$ species and H_2. The final step of the sequence involves β-hydride elimination from $[C_2H_5\text{-}GaH]^+$ species to form C_2H_4 and $[GaH_2]^+$. We also found that dehydrogenation rates exhibit first-order kinetics and are limited by initial C-H activation at low C_2H_6 pressures while these rates exhibit zero-order kinetics and are limited by β-hydride elimination from $[C_2H_5\text{-}GaH]^+$ at high C_2H_6 partial pressures. The site requirements and mechanism for C_2H_6 dehydrogenation over Ga/H-MFI were thus found to differ significantly from those for C_3H_8 dehydrogenation and cracking.

The dehydrogenation, terminal and central cracking of n-C_4H_{10} was found to be catalyzed exclusively by $[GaH]^{2+}$ sites in Ga/H-MFI with turnover frequencies that were 3 orders, 2 orders and 1 order of magnitude higher than the turnover frequencies of these reactions over H-MFI under identical reaction conditions. $[GaH_2]^+$ cations were found to be inactive for these reactions. All three reactions pathways for C_4H_{10} conversion exhibited a Langmuir-Hinshelwood type dependence on C_4H_{10} partial pressure and were inhibited by H_2. Ratios of dehydrogenation to cracking (D/C) and of terminal to central cracking (C_t/C_c) were found to be approximately independent of C_4H_{10} and H_2 partial pressures. Thus, analogous to C_3H_8 dehydrogenation and cracking catalyzed by $[GaH]^{2+}$, dehydrogenation, terminal and central cracking of n-C_4H_{10} was found to be mediated by a common C_4H_{10} derived surface intermediate. Measured activation enthalpies together with theoretical predictions suggested that C_4H_{10} is activated by $[GaH]^{2+}$ to form $[sec\text{-}C_4H_9\text{-}GaH]^+\text{-}H^+$ cation pairs. Dehydrogenation then proceeds via β-hydride elimination from the alkyl fragment to form 1-butene and 2-butene. Terminal and central cracking proceed via an attack of terminal and central C-C bonds in the alkyl fragment by the proximal Brønsted acid O-H group, resulting in the formation of terminal cracking products (CH_4 and C_3H_6) and central cracking products (C_2H_6 and C_2H_4). Turnover rates for terminal cracking over Ga/H-MFI were found to be a factor of 3 higher than turnover rates for central cracking because the latter pathway encounters a more constrained transition state than the former pathway. While both $[GaH]^{2+}$ and $[GaH_2]^+$ cations are catalytically active for C_2H_6 dehydrogenation, only $[GaH]^{2+}$ cations are catalytically active for C_3H_8 and n-C_4H_{10} dehydrogenation and cracking. These differences in site requirements likely reflect the significantly higher entropic penalties associated with the activation of light alkanes by $[GaH_2]^+$ than their activation and conversion by $[GaH]^{2+}$ cations.

6 Bibliography

(1) Siirola, Jeffrey, J. The Impact of Shale Gas in the Chemical Industry. *AIChe J.* **2014**, *60*, 810–819.

(2) Sattler, J. J. H. B.; Ruiz-Martinez, J.; Santillan-Jimenez, E.; Weckhuysen, B. M. Catalytic Dehydrogenation of Light Alkanes on Metals and Metal Oxides. *Chem. Rev.* **2014**, *114*, 10613–10653.

(3) Leitch, D. C.; Lam, Y. C.; Labinger, J. A.; Bercaw, J. E. Upgrading Light Hydrocarbons via Tandem Catalysis: A Dual Homogeneous Ta/Ir System for Alkane/Alkene Coupling. *J. Am. Chem. Soc.* **2013**, *135*, 10302–10305.

(4) Labinger, J. A.; Leitch, D. C.; Bercaw, J. E.; Deimund, M. A.; Davis, M. E. Upgrading Light Hydrocarbons: A Tandem Catalytic System for Alkane/Alkene Coupling. *Top. Catal.* **2015**, *58*, 494–501.

(5) Corma, A. Transformation of Hydrocarbons on Zeolite Catalysts. *Catal. Letters* **1993**, *22*, 33–52.

(6) Corma, a. Inorganic Solid Acids and Their Use in Acid-Catalyzed Hydrocarbon Reactions. *Chem. Rev.* **1995**, *95*, 559–614.

(7) Corma, A. State of the Art and Future Challenges of Zeolites as Catalysts. *J. Catal.* **2003**, *216*, 298–312.

(8) Fricke, R.; Kosslick, H.; Lischke, G.; Richter, M. Incorporation of Gallium into Zeolites: Syntheses, Properties and Catalytic Application. *Chem. Rev.* **2000**, *100*, 2303–2405.

(9) Bhan, A.; Iglesia, E. A Link between Reactivity and Local Structure in Acid Catalysis on Zeolites. *Acc. Chem. Res.* **2008**, *41*, 559–567.

(10) Gounder, R.; Iglesia, E. Catalytic Consequences of Spatial Constraints and Acid Site Location for Monomolecular Alkane Activation on Zeolites. *J. Am. Chem. Soc.* **2009**, *131*, 1958–1971.

(11) Janda, A.; Bell, A. T. Effects of Si/Al Ratio on the Distribution of Framework Al and on the Rates of Alkane Monomolecular Cracking and Dehydrogenation in H-MFI. *J. Am. Chem. Soc.* **2013**, *135*, 19193–19207.

(12) Janda, A.; Vlaisavljevich, B.; Lin, L. C.; Smit, B.; Bell, A. T. Effects of Zeolite Structural Confinement on Adsorption Thermodynamics and Reaction Kinetics for Monomolecular Cracking and Dehydrogenation of N-Butane. *J. Am. Chem. Soc.* **2016**, *138*, 4739–4756.

(13) Van der Mynsbrugge, J.; Janda, A.; Mallikarjun Sharada, S.; Lin, L.-C.; Van Speybroeck, V.; Head-Gordon, M.; Bell, A. T. Theoretical Analysis of the Influence of Pore Geometry on Monomolecular Cracking and Dehydrogenation of N-Butane in Brønsted-Acid Zeolites. *ACS Catal.* **2017**, *7*, 2685–2697.

(14) Dedecek, J.; Kaucky, D.; Wichterlova, B. Co 2 + Ion Siting in Pentasil-Containing Zeolites , Part 3 . Co 2 + Ion Sites and Their Occupation in ZSM-5 : A VIS Diffuse Reflectance Spectroscopy Study. *Microporous Mesoporous Mater.* **2000**, *36*, 483–494.

(15) Dedecek, J.; Balgova, V.; Pashkova, V.; Klein, P.; Wichterlova, B. Synthesis of ZSM‐5 Zeolites with Defined Distribution of Al Atoms in the Framework and Multinuclear MAS NMR Analysis of the Control of Al Distribution. *Chem. Mater.* **2012**, *24*, 3231–3239.

(16) Bernauer, M.; Tabor, E.; Pashkova, V.; Kaucký, D.; Sobalík, Z.; Wichterlová, B.; Dedecek, J. Proton Proximity – New Key Parameter Controlling Adsorption, Desorption and Activity in Propene Oligomerization over H-ZSM-5 Zeolites. *J. Catal.* **2016**, *344*, 157–172.

(17) Paolucci, C.; Parekh, A. A.; Khurana, I.; Di Iorio, J. R.; Li, H.; Albarracin Caballero, J. D.; Shih, A. J.; Anggara, T.; Delgass, W. N.; Miller, J. T.; Ribeiro, F. H.; Gounder, R.; Schneider, W. F. Catalysis in a Cage: Condition-Dependent Speciation and Dynamics of Exchanged Cu Cations in SSZ-13 Zeolites. *J. Am. Chem. Soc.* **2016**, *138*, 6028–6048.

(18) Da Costa, P.; Moden, B.; Meitzner, G. D.; Lee, D. K.; Iglesia, E. Spectroscopic and Chemical Characterization of Active and Inactive Cu Species in NO Decomposition Catalysts Based on Cu-ZSM5. *Phys. Chem. Chem. Phys.* **2002**, *4*, 4590–4601.

(19) Di Iorio, J. R.; Bates, S. A.; Verma, A. A.; Delgass, W. N.; Ribeiro, F. H.; Miller, J. T.; Gounder, R. The Dynamic Nature of Brønsted Acid Sites in Cu-Zeolites During NO_x Selective Catalytic Reduction: Quantification by Gas-Phase Ammonia Titration. *Top. Catal.* **2015**, *58*, 424–434.

(20) Battiston, A. A.; Bitter, J. H.; De Groot, F. M. F.; Overweg, A. R.; Stephan, O.; Van Bokhoven, J. A.; Kooyman, P. J.; Van Der Spek, C.; Vank??, G.; Koningsberger, D. C. Evolution of Fe Species during the Synthesis of Over-Exchanged Fe/ZSM5 Obtained by Chemical Vapor Deposition of FeCl3. *J. Catal.* **2003**, *213*, 251–271.

(21) Lacheen, H. S.; Iglesia, E. Synthesis, Structure, and Catalytic Reactivity of Isolated V^{5+} -Oxo Species Prepared by Sublimation of $VOCl_3$ onto H-ZSM5. *J. Phys. Chem. B* **2006**, *110*, 5462–5472.

(22) Schreiber, M. W.; Plaisance, C. P.; Baumgärtl, M.; Reuter, K.; Jentys, A.; Bermejo-Deval, R.; Lercher, J. A. Lewis-Brønsted Acid Pairs in Ga/H-ZSM-5 to Catalyze Dehydrogenation of Light Alkanes. *J. Am. Chem. Soc.* **2018**, *140*, 4849–4859.

(23) Krannila, H.; Haag, W. O.; Gates, B. C. Monomolecular and Bimolecular Mechanisms of Paraffin Cracking: N-Butane Cracking Catalyzed by HZSM-5. *J. Catal.* **1992**, *135*, 115–124.

(24) Kotrel, S.; Knözinger, H.; Gates, B. C. The Haag-Dessau Mechanism of Protolytic Cracking of Alkanes. *Microporous Mesoporous Mater.* **2000**, *35–36*, 11–20.

(25) Gounder, R.; Iglesia, E. Catalytic Consequences of Spatial Constraints and Acid Site Location for Monomolecular Alkane Activation on Zeolites. *J. Am. Chem. Soc.* **2009**, *131*, 1958–1971.

(26) Ono, Y. Transformation of Lower Alkanes into Aromatic Hydrocarbons over ZSM-5 Zeolites. *Catal. Rev.* **1992**, *34*, 179–226.

(27) Biscardi, J. A.; Iglesia, E. Structure and Function of Metal Cations in Light Alkane Reactions Catalyzed by Modified H-ZSM5. *Catal. Today* **1996**, *31*, 207–231.

(28) Sendoda, Y.; Ono, Y. Transformation of Propane into Aromatic over ZSM-5 Zeolites. *J. Catal.* **1986**, *101*, 12–18.

(29) Bhan, A.; Nicholas Delgass, W. Propane Aromatization over HZSM-5 and Ga/HZSM-5 Catalysts. *Catal. Rev.* **2008**, *50*, 19–151.

(30) Gabrienko, A. A.; Arzumanov, S. S.; Toktarev, A. V; Freude, D.; Haase, J.; Stepanov, A. G. Hydrogen H/D Exchange and Activation of C 1 – n- C 4 Alkanes on Ga-Modified Zeolite BEA Studied with 1 H Magic Angle Spinning Nuclear Magnetic Resonance in Situ. *J. Phys. Chem. C* **2011**, *115*, 13877–13886.

(31) Giannetto, G.; Montes, A.; Gnep, N. S.; Florentino, A.; Cartraud, P.; Guisnet, M. Conversion of Light Alkanes into Aromatic Hydrocarbons.VII. Aromatization of Propane on Gallosilicates: Effect of Calcination in Dry Air. *Journal of Catalysis*. 1994, pp 86–95.

(32) Meitzner, G. D.; Iglesia, E.; Baumgartner, J. E.; Huang, E. S. The Chemical State of Gallium in Working Alkane Dehydrocyclodimerization Catalysts. In Situ Gallium K-Edge

X-Ray Absorption Spectroscopy. *J. Catal.* **1993**, *140*, 209–225.
(33) Getsoian, A. "Bean"; Das, U.; Camacho-Bunquin, J.; Zhang, G.; Gallagher, J. R.; Hu, B.; Cheah, S.; Schaidle, J. A.; Ruddy, D. A.; Hensley, J. E.; Krause, T. R.; Curtiss, L. A.; Miller, J. T.; Hock, A. S. Organometallic Model Complexes Elucidate the Active Gallium Species in Alkane Dehydrogenation Catalysts Based on Ligand Effects in Ga K-Edge XANES. *Catal. Sci. Technol.* **2016**, *101*, 12–18.
(34) Kazansky, V. B.; Subbotina, I. R.; van Santen, R. A.; Hensen, E. J. M. DRIFTS Study of the Chemical State of Modifying Gallium Ions in Reduced Ga/ZSM-5 Prepared by Impregnation. I. Observation of Gallium Hydrides and Application of CO Adsorption as Molecular Probe for Reduced Gallium Ions. *J. Catal.* **2004**, *227*, 263–269.
(35) Kazansky, V. B.; Subbotina, I. R.; Van Santen, R. A.; Hensen, E. J. M. DRIFTS Study of the Nature and Chemical Reactivity of Gallium Ions in Ga/ZSM-5: II. Oxidation of Reduced Ga Species in ZSM-5 by Nitrous Oxide or Water. *J. Catal.* **2005**, *233*, 351–358.
(36) Rodrigues, V. D. O.; Faro Júnior, A. C. On Catalyst Activation and Reaction Mechanisms in Propane Aromatization on Ga/HZSM5 Catalysts. *Appl. Catal. A Gen.* **2012**, *435–436*, 68–77.
(37) Rane, N.; Overweg, A. R.; Kazansky, V. B.; van Santen, R. A.; Hensen, E. J. M. Characterization and Reactivity of Ga^+ and GaO^+ Cations in Zeolite ZSM-5. *J. Catal.* **2006**, *239*, 478–485.
(38) Pidko, E. A.; Kazansky, V. B.; Hensen, E. J. M.; van Santen, R. A. A Comprehensive Density Functional Theory Study of Ethane Dehydrogenation over Reduced Extra-Framework Gallium Species in ZSM-5 Zeolite. *J. Catal.* **2006**, *240*, 73–84.
(39) Hensen, E. J. M.; Pidko, E. A.; Rane, N.; Van Santen, R. A. Water-Promoted Hydrocarbon Activation Catalyzed by Binuclear Gallium Sites in ZSM-5 Zeolite. *Angew. Chemie - Int. Ed.* **2007**, *46*, 7273–7276.
(40) Pidko, E. a.; Hensen, E. J. M.; van Santen, R. a. Self-Organization of Extraframework Cations in Zeolites. *Proc. R. Soc. A Math. Phys. Eng. Sci.* **2012**, *468*, 2070–2086.
(41) Meriaudeau, P.; Naccache, C. H-ZSM-5 Supported Ga_2O_3 Dehydrocyclisation Catalysts Infrared Spectroscopic Evidence of Gallium Oxide Surface Mobility. *Appl. Catal.* **1991**, *73*, 13–18.
(42) Joly, J. F.; Ajot, H.; Merlen, E.; Raatz, F.; Alario, F. Parameters Affecting the Dispersion of the Gallium Phase of Gallium H-MFI Aromatization Catalysts. *Appl. Catal. A, Gen.* **1991**, *79*, 249–263.
(43) Price, G. L.; Kanazirev, V. Ga_2O_3/HZSM-5 Propane Aromatization Catalysts: Formation of Active Centers via Solid-State Reaction. *J. Catal.* **1990**, *126*, 267–278.
(44) García-Sánchez, M.; Magusin, P. C. M. M.; Hensen, E. J. M.; Thüne, P. C.; Rozanska, X.; Van Santen, R. A. Characterization of Ga/HZSM-5 and Ga/HMOR Synthesized by Chemical Vapor Deposition of Trimethylgallium. *J. Catal.* **2003**, *219*, 352–361.
(45) Hensen, E. J. M.; García-Sánchez, M.; Rane, N.; Magusin, P. C. M. M.; Liu, P. H.; Chao, K. J.; Van Santen, R. A. In Situ Ga K Edge XANES Study of the Activation of Ga/ZSM-5 Prepared by Chemical Vapor Deposition of Trimethylgallium. *Catal. Letters* **2005**, *101*, 79–85.
(46) Krishnamurthy, G.; Bhan, A.; Delgass, W. N. Identity and Chemical Function of Gallium Species Inferred from Microkinetic Modeling Studies of Propane Aromatization over Ga/HZSM-5 Catalysts. *J. Catal.* **2010**, *271*, 370–385.
(47) Joshi, Y. V.; Thomson, K. T. The Roles of Gallium Hydride and Brønsted Acidity in

Light Alkane Dehydrogenation Mechanisms Using Ga-Exchanged HZSM-5 Catalysts: A DFT Pathway Analysis. *Catal. Today* **2005**, *105*, 106–121.
(48) Joshi, Y. V.; Thomson, K. T. High Ethane Dehydrogenation Activity of $[GaH]^{2+}$ Al Pair Sites in Ga/H-[Al]ZSM-5: A DFT Thermochemical Analysis of the Catalytic Sites under Reaction Conditions. *J. Catal.* **2007**, *246*, 249–265.
(49) Mansoor, E.; Head-Gordon, M.; Bell, A. T. Computational Modeling of the Nature and Role of Ga Species for Light Alkane Dehydrogenation Catalyzed by Ga/H-MFI. *ACS Catal.* **2018**, *8*, 6146–6162.
(50) Gonzales, N. O.; Chakraborty, A. K.; Bell, A. T. A Density Functional Theory Study of Hydrogen Recombination and Hydrogen-Deuterium Exchange on Ga / H-ZSM-5. *Top. Catal.* **1999**, *9*, 207–213.
(51) Frash, M. V.; van Santen, R. A. Activation of Small Alkanes in Ga-Exchanged Zeolites: A Quantum Chemical Study of Ethane Dehydrogenation. *J. Phys. Chem. A* **2000**, *104*, 2468–2475.
(52) Pereira, M. S.; Da Silva, A. M.; Nascimento, M. A. C. Effect of the Zeolite Cavity on the Mechanism of Dehydrogenation of Light Alkanes over Gallium-Containing Zeolites. *J. Phys. Chem. C* **2011**, *115*, 10104–10113.
(53) Pereira, M. S.; Nascimento, M. A. C. Theoretical Study on the Dehydrogenation Reaction of Alkanes Catalyzed by Zeolites Containing Nonframework Gallium Species. *J. Phys. Chem. B* **2006**, *110*, 3231–3238.
(54) Schreiber, M. W.; Plaisance, C. P.; Baumgärtl, M.; Reuter, K.; Jentys, A.; Bermejo-Deval, R.; Lercher, J. A. Lewis-Brønsted Acid Pairs in Ga/H-ZSM-5 to Catalyze Dehydrogenation of Light Alkanes. *J. Am. Chem. Soc.* **2018**, *140*, 4849–4859.
(55) Gnep, N. S.; Doyemet, J. Y.; Seco, A. M.; Ribeiro, F. R.; Guisnet, M. Conversion of Light Alkanes into Aromatic Hydrocarbons: 1-Dehydrocyclodimerization of Propane on PtHZSM-5 Catalysts. *Appl. Catal.* **1987**, *35*, 93–108.
(56) Biscardi, J. A.; Meitzner, G. D.; Iglesia, E. Structure and Density of Active Zn Species in Zn/H-ZSM5 Propane Aromatization Catalysts. *J. Catal.* **1998**, *179*, 192–202.
(57) Li, W.; Yu, S. Y.; Meitzner, G. D.; Iglesia, E. Structure and Properties of Cobalt-Exchanged H-ZSM5 Catalysts for Dehydrogenation and Dehydrocyclization of Alkanes. *J. Phys. Chem. B* **2001**, *105*, 1176–1184.
(58) Seddon, D. Paraffin Oligomerisation to Aromatics. *Catal. Today* **1990**, *6*, 351–372.
(59) Chen, N. Y.; Yan, T. Y. M2 Forming-A Process for Aromatization of Light Hydrocarbons. *Ind. Eng. Chem. Process Des. Dev.* **1985**, *25*, 151–155.
(60) Anderson, R.F.; Johnson, J.A.; Mowry, J. R. Cyclar: One Step Processing of LPG to Aromatics and Hydrogen. In *Inst. Chem. Eng., Spring National Meeting, Houston, Texas*; 1985.
(61) Rane, N.; Kersbulck, M.; van Santen, R. A.; Hensen, E. J. M. Cracking of N-Heptane over Brønsted Acid Sites and Lewis Acid Ga Sites in ZSM-5 Zeolite. *Microporous Mesoporous Mater.* **2008**, *110*, 279–291.
(62) De O. Rodrigues, V.; Eon, J. G.; Faro, A. C. Correlations between Dispersion, Acidity, Reducibility, and Propane Aromatization Activity of Gallium Species Supported on HZSM5 Zeolites. *J. Phys. Chem. C* **2010**, *114*, 4557–4567.
(63) Kwak, B.; Sachtler, W. Effect of Ga/Proton Balance in Ga/HZSM-5 Catalysts on C_3 Conversion to Aromatics. *J. Catal.* **1994**, *145*, 456–463.
(64) Nowak, I.; Quartararo, J.; Derouane, E. G.; Védrine, J. C. Effect of Reducing and

Oxidizing Pre-Treatments on the State of Gallium in Ga/H-ZSM-5 Propane Aromatisation Catalysts. *Appl. Catal. A Gen.* **2003**, *251*, 107–120.
(65) Abdul Hamid, S. B.; Derouane, E.; Mériaudeau, P.; Naccache, C. Effect of Reductive and Oxidative Atmospheres on the Propane Aromatisation Activity and Selectivity of Ga/H-ZSM-5 Catalysts. *Catal. Today* **1996**, *31*, 327–334.
(66) Yoder, L. Adaptation of the Mohr Volumetric Method to General Determinations of Chlorine. *Ind. Eng. Chem.* **1919**, *11*, 1919.
(67) Signorile, M.; Bonino, F.; Damin, A.; Bordiga, S. UV-Raman Fingerprint of Brønsted Sites in MFI Zeolites: A Useful Marker in Dealumination Detection. *J. Phys. Chem. C* **2016**, *120*, 18088–18092.
(68) Engelhardt, G.; Lohse, U.; Lippmaa, E.; Tarmak, M.; Magi, M. ^{29}Si-NMR-Untersuchungen Zur Verteilung Der Silicium Und Aluminiumatome Im Alumosilicatgitter von Zeolithen Mit Faujasit-Struktur.R. *Zeitschrift für Anorg. und Allg. Chemie* **1981**, *482*, 49–64.
(69) Kentgens, A. P. M.; Scholle, J.; Veeman, W. S. Effect of Hydration on the Local Symmetry around Aluminum in ZSM-5 Zeolites Studied by Aluminum-27 Nuclear Magnetic Resonance. *J. Phys. Chem.* **1983**, *87*, 4357–4360.
(70) Ravel, B.; Newville, M. ATHENA , ARTEMIS , HEPHAESTUS : Data Analysis for X-Ray Absorption Spectroscopy Using IFEFFIT. *J. Synchrotron Radiat.* **2005**, *12*, 537–541.
(71) Deiseroth, V. H. J.; Muller-buschbaum, H. K. Uber Erdalkalimetalloxogallate. 111 Untersuchung Des Aufbaus von $CaGa_2O_4$. *Zeitschrift für Anorg. und Allg. Chemie* **1973**, *396*, 157–164.
(72) Funke, H.; Scheinost, A. C.; Chukalina, M. Wavelet Analysis of Extended X-Ray Absorption Fine Structure Data. *Phys. Rev. B* **2005**, *71*, 094110.
(73) Zimmerman, P. M.; Head-Gordon, M.; Bell, A. T. Selection and Validation of Charge and Lennard-Jones Parameters for QM/MM Simulations of Hydrocarbon Interactions with Zeolites. *J. Chem. Theory Comput.* **2011**, *7*, 1695–1703.
(74) Li, Y.-P.; Gomes, J.; Mallikarjun Sharada, S.; Bell, A. T.; Head-Gordon, M. Improved Force-Field Parameters for QM/MM Simulations of the Energies of Adsorption for Molecules in Zeolites and a Free Rotor Correction to the Rigid Rotor Harmonic Oscillator Model for Adsorption Enthalpies. *J. Phys. Chem. C* **2015**, *119*, 1840–1850.
(75) Chai, J.-D.; Head-Gordon, M. Systematic Optimization of Long-Range Corrected Hybrid Density Functionals. *J. Chem. Phys.* **2008**, *128*, 84106.
(76) Chai, J.-D.; Head-Gordon, M. Long-Range Corrected Hybrid Density Functionals with Damped Atom–atom Dispersion Corrections. *Phys. Chem. Chem. Phys.* **2008**, *10*, 6615.
(77) Swisher, J. A.; Hansen, N.; Maesen, T.; Keil, F. J.; Smit, B.; Bell, A. T. Theoretical Simulation of N-Alkane Cracking on Zeolites. *J. Phys. Chem. C* **2010**, *114*, 10229–10239.
(78) Mallikarjun Sharada, S.; Zimmerman, P. M.; Bell, A. T.; Head-Gordon, M. Insights into the Kinetics of Cracking and Dehydrogenation Reactions of Light Alkanes in H-MFI. *J. Phys. Chem. C* **2013**, *117*, 12600–12611.
(79) Gomes, J.; Zimmerman, P. M.; Head-Gordon, M.; Bell, A. T. Accurate Prediction of Hydrocarbon Interactions with Zeolites Utilizing Improved Exchange-Correlation Functionals and QM/MM Methods: Benchmark Calculations of Adsorption Enthalpies and Application to Ethene Methylation by Methanol. *J. Phys. Chem. C* **2012**, *116*, 15406–15414.
(80) Van Speybroeck, V.; Van der Mynsbrugge, J.; Vandichel, M.; Hemelsoet, K.; Lesthaeghe,

D.; Ghysels, A.; Marin, G. B.; Waroquier, M. First Principle Kinetic Studies of Zeolite-Catalyzed Methylation Reactions. *J. Am.Chem.Soc* **2011**, *133*, 888–899.

(81) Van der Mynsbrugge, J.; Hemelsoet, K.; Vandichel, M.; Waroquier, M.; Van Speybroeck, V. Efficient Approach for the Computational Study of Alcohol and Nitrile Adsorption in H-ZSM-5. *J. Phys. Chem. C* **2012**, *116*, 5499–5508.

(82) Van der Mynsbrugge, J.; Visur, M.; Olsbye, U.; Beato, P.; Bjørgen, M.; Van Speybroeck, V.; Svelle, S. Methylation of Benzene by Methanol: Single-Site Kinetics over H-ZSM-5 and H-Beta Zeolite Catalysts. *J. Catal.* **2012**, *292*, 201–212.

(83) Mansoor, Erum.; Head-Gordon, Martin; Bell, A. T. Theoretical Study of the Nature and Role of Ga Species in Zeolite-Catalyzed Light Alkane Dehydrogenation Reactions. *Submitted* **2018**, 1–47.

(84) Verstraelen, T.; Van Speybroeck, V.; Waroquier, M. ZEOBUILDER: A GUI Toolkit for the Construction of Complex Molecular Structures on the Nanoscale with Building Blocks. *J. Chem. Inf. Model.* **2008**, *48*, 1530–1541.

(85) Shao, Y.; Gan, Z.; Epifanovsky, E.; Gilbert, A. T. B.; Wormit, M.; Kussmann, J.; Lange, A. W.; Behn, A.; Deng, J.; Feng, X.; Ghosh, D.; Goldey, M.; Horn, P. R.; Jacobson, L. D.; Kaliman, I.; Khaliullin, R. Z.; Kuś, T.; Landau, A.; Liu, J.; Proynov, E. I.; Rhee, Y. M.; Richard, R. M.; Rohrdanz, M. A.; Steele, R. P.; Sundstrom, E. J.; Woodcock, H. L.; Zimmerman, P. M.; Zuev, D.; Albrecht, B.; Alguire, E.; Austin, B.; Beran, G. J. O.; Bernard, Y. A.; Berquist, E.; Brandhorst, K.; Bravaya, K. B.; Brown, S. T.; Casanova, D.; Chang, C.-M.; Chen, Y.; Chien, S. H.; Closser, K. D.; Crittenden, D. L.; Diedenhofen, M.; DiStasio, R. A.; Do, H.; Dutoi, A. D.; Edgar, R. G.; Fatehi, S.; Fusti-Molnar, L.; Ghysels, A.; Golubeva-Zadorozhnaya, A.; Gomes, J.; Hanson-Heine, M. W. D.; Harbach, P. H. P.; Hauser, A. W.; Hohenstein, E. G.; Holden, Z. C.; Jagau, T.-C.; Ji, H.; Kaduk, B.; Khistyaev, K.; Kim, J.; Kim, J.; King, R. A.; Klunzinger, P.; Kosenkov, D.; Kowalczyk, T.; Krauter, C. M.; Lao, K. U.; Laurent, A. D.; Lawler, K. V; Levchenko, S. V; Lin, C. Y.; Liu, F.; Livshits, E.; Lochan, R. C.; Luenser, A.; Manohar, P.; Manzer, S. F.; Mao, S.-P.; Mardirossian, N.; Marenich, A. V; Maurer, S. A.; Mayhall, N. J.; Neuscamman, E.; Oana, C. M.; Olivares-Amaya, R.; O'Neill, D. P.; Parkhill, J. A.; Perrine, T. M.; Peverati, R.; Prociuk, A.; Rehn, D. R.; Rosta, E.; Russ, N. J.; Sharada, S. M.; Sharma, S.; Small, D. W.; Sodt, A.; Stein, T.; Stück, D.; Su, Y.-C.; Thom, A. J. W.; Tsuchimochi, T.; Vanovschi, V.; Vogt, L.; Vydrov, O.; Wang, T.; Watson, M. A.; Wenzel, J.; White, A.; Williams, C. F.; Yang, J.; Yeganeh, S.; Yost, S. R.; You, Z.-Q.; Zhang, I. Y.; Zhang, X.; Zhao, Y.; Brooks, B. R.; Chan, G. K. L.; Chipman, D. M.; Cramer, C. J.; Goddard, W. A.; Gordon, M. S.; Hehre, W. J.; Klamt, A.; Schaefer, H. F.; Schmidt, M. W.; Sherrill, C. D.; Truhlar, D. G.; Warshel, A.; Xu, X.; Aspuru-Guzik, A.; Baer, R.; Bell, A. T.; Besley, N. A.; Chai, J.-D.; Dreuw, A.; Dunietz, B. D.; Furlani, T. R.; Gwaltney, S. R.; Hsu, C.-P.; Jung, Y.; Kong, J.; Lambrecht, D. S.; Liang, W.; Ochsenfeld, C.; Rassolov, V. A.; Slipchenko, L. V; Subotnik, J. E.; Van Voorhis, T.; Herbert, J. M.; Krylov, A. I.; Gill, P. M. W.; Head-Gordon, M. Advances in Molecular Quantum Chemistry Contained in the Q-Chem 4 Program Package. *Mol. Phys.* **2015**, *113*, 184–215.

(86) Grimme, S. Supramolecular Binding Thermodynamics by Dispersion-Corrected Density Functional Theory. *Chemistry* **2012**, *18*, 9955–9964.

(87) Brunetti, B.; Piacente, V.; Scardala, P.; Roma, S.; Dipartimento, C. N. R.; La, R.; Moro, P. A. Vapor Pressures of Gallium Trifluoride , Trichloride , and Triiodide and Their Standard Sublimation Enthalpies. *J. Chem. Eng. Data* **2010**, *55*, 98–102.

(88) Nogai, S.; Schmidbaur, H. Dichlorogallane $(HGaCl_2)_2$: Its Molecular Structure and Synthetic Potential. *Inorg. Chem.* **2002**, *41*, 4770–4774.
(89) Collins, S. E.; Baltanás, M. A.; Bonivardi, A. L. Hydrogen Chemisorption on Gallium Oxide Polymorphs. *Langmuir* **2005**, *21*, 962–970.
(90) Vecchietti, J.; Baltanás, M. A.; Gervais, C.; Collins, S. E.; Blanco, G.; Matz, O.; Calatayud, M.; Bonivardi, A. Insights on Hydride Formation over Cerium-Gallium Mixed Oxides: A Mechanistic Study for Efficient H_2 Dissociation. *J. Catal.* **2017**, *345*, 258–269.
(91) Jacobs, P. A.; Von Ballmoos, R. Framework Hydroxyl Groups of H-ZSM-5 Zeolites. *J. Phys. Chem.* **1982**, *86*, 3050–3052.
(92) Woolery, G. L.; Alemany, L. B.; Dessau, R. M.; Chester, A. W. Spectroscopic Evidence for the Presence of Internal Silanols in Highly Siliceous ZSM-5. *Zeolites* **1986**, *6*, 14–16.
(93) Ong, L. H.; Dömök, M.; Olindo, R.; Van Veen, A. C.; Lercher, J. A. Dealumination of HZSM-5 via Steam-Treatment. *Microporous Mesoporous Mater.* **2012**, *164*, 9–20.
(94) Klinowski, J.; Thomas, J. M.; Anderson, M. W.; Fyfe, C. A.; Gobbi, G. C. Dealumination of Mordenite Using Silicon Tetrachloride Vapour. *Zeolites* **1983**, *3*, 5–7.
(95) Pokrovski, G. S.; Schott, J.; Hazemann, J.; Farges, F.; Pokrovsky, Oleg, S. An X-Ray Absorption Fine Structure and Nuclear Magnetic Resonance Spectroscopy Study of Gallium–silica Complexes in Aqueous Solution. *Geoch Cosmochim. Acta* **2002**, *66*, 4203–4322.
(96) Zheng, B.; Hua, W.; Yue, Y.; Gao, Z. Dehydrogenation of Propane to Propene over Different Polymorphs of Gallium Oxide. *J. Catal.* **2005**, *232*, 143–151.
(97) Dymock, K.; Palenik, G. J. Tris(Acetylacetonato)Gallium(III). *Acta Cryst.* **1974**, *B30*, 1364–1366.
(98) Teo, B. K. *EXAFS: Basic Principles and Data Analysis (Inorganic Chemistry Concepts)*, 9th ed.; Springer US, 1986.
(99) Calvin, S. *XAFS for Everyone*, 1st ed.; CRC Press: Boca Raton, 2013.
(100) Eisenberger, P.; Brown, G. S. The Study of Disordered Systems by EXAFS: Limitations. *Solid State Commun.* **1979**, *29*, 481–484.
(101) Clausen, B. S.; Nørskov, J. K. Asymmetric Pair Distribution Functions in Catalysts. *Top. Catal.* **2000**, *10*, 221–230.
(102) Bus, E.; Miller, J. T.; Kropf, a J.; Prins, R.; van Bokhoven, J. a. Analysis of in Situ EXAFS Data of Supported Metal Catalysts Using the Third and Fourth Cumulant. *Phys. Chem. Chem. Phys.* **2006**, *8*, 3248–3258.
(103) Åhman, J.; Svensson, G.; Albertsson, J. A Reinvestigation of β-Gallium Oxide. *Acta Crystallogr. Sect. C Cryst. Struct. Commun.* **1996**, *52*, 1336–1338.
(104) Munoz, M.; Argoul, P.; Farges, F. Continuous Cauchy Wavelet Transform Analyses of EXAFS Spectra: A Qualitative Approach. *Am. Mineral.* **2003**, *88*, 694–700.
(105) Muñoz, M.; Farges, F.; Argoul, P. Continuous Cauchy Wavelet Transform of XAFS Spectra. *Phys. Scr.* **2005**, No. T115, 221–222.
(106) Funke, H.; Chukalina, M.; Voegelin, A.; Scheinost, A. C. Improving Resolution in k and r Space: A FEFF-Based Wavelet for EXAFS Data Analysis. *AIP Conf. Proc.* **2007**, *882*, 72–74.
(107) Fleischman, S. D.; Scott, S. L. Evidence for the Pairwise Disposition of Grafting Sites on Highly Dehydroxylated Silicas via Their Reactions with $Ga(CH_3)_3$. *J. Am. Chem. Soc.* **2011**, *133*, 4847–4855.
(108) Searles, K.; Siddiqi, G. G.; Safonova, O. V.; Coperet, C. Silica-Supported Isolated

Gallium Sites as Highly Active, Selective and Stable Propane Dehydrogenation Catalysts. *Chem. Sci.* **2017**, *8*, 2661–2666.
(109) Faro, A. C.; Rodrigues, V. D. O.; Eon, J. G. In Situ X-Ray Absorption Study of the Genesis and Nature of the Reduced Gallium Species in Ga/HZSM5 Catalysts. *J. Phys. Chem. C* **2011**, *115*, 4749–4756.
(110) Zhang, Y.; Drake, I. J.; Bell, A. T. Characterization of Cu-ZSM-5 Prepared by Solid-State Ion Exchange of H-ZSM-5 with CuCl. *Chem. Mater.* **2006**, *18*, 2347–2356.
(111) Camacho-Bunquin, J.; Aich, P.; Ferrandon, M.; Getsoian, A. "Bean"; Das, U.; Dogan, F.; Curtiss, L. A.; Miller, J. T.; Marshall, C. L.; Hock, A. S.; Stair, P. C. Single-Site Zinc on Silica Catalysts for Propylene Hydrogenation and Propane Dehydrogenation: Synthesis and Reactivity Evaluation Using an Integrated Atomic Layer Deposition-Catalysis Instrument. *J. Catal.* **2017**, *345*, 170–182.
(112) Lengeler, B. Lattice Site Location of Hydrogen by Use of Extended X-Ray Absorption Fine Structure. *Phys. Rev. Lett.* **1984**, *53*, 74–77.
(113) Kwak, B. S.; Sachtler, W. M. H. Characterization and Testing of Ga/H-ZSM-5 Prepared by Sublimation of $GaCl_3$ into HZSM-5. *J. Catal.* **1993**, *141*, 729–732.
(114) Rao, R.; Rao, A. M.; Xu, B.; Dong, J.; Sharma, S.; Sunkara, M. K. Blueshifted Raman Scattering and Its Correlation with the [110] Growth Direction in Gallium Oxide Nanowires. *J. Appl. Phys.* **2005**, *98*, 1–5.
(115) Drake, I. J.; Zhang, Y.; Gilles, M. K.; Teris Liu, C. N.; Nachimuthu, P.; Perera, R. C. C.; Wakita, H.; Bell, A. T. An in Situ Al K-Edge XAS Investigation of the Local Environment of H^+- And Cu^+-Exchanged USY and ZSM-5 Zeolites. *J. Phys. Chem. B* **2006**, *110*, 11665–11676.
(116) Brunner, E.; Ernst, H.; Freude, D.; Fröhlich, T.; Hunger, M.; Pfeifer, H. Magic-Angle-Spinning NMR Studies of Acid Sites in Zeolite H-ZSM-5. *J. Catal.* **1991**, *127*, 34–41.
(117) Rehr, J. J.; Kas, J. J.; Vila, F. D.; Micah, P.; Jorissen, K. Parameter-Free Calculations of X-Ray Spectra with FEFF9. *Phys. Chem. Chem. Phys.* **2010**, *12*, 5503–5513.
(118) Penfold, T. J.; Tavernelli, I.; Milne, C. J.; Reinhard, M.; Nahhas, A. El; Abela, R.; Rothlisberger, U.; Chergui, M. A Wavelet Analysis for the X-Ray Absorption Spectra of Molecules. *J. Chem. Phys.* **2013**, *138*, 0141041–0141047.
(119) Al-Douri, A.; Sengupta, D.; El-Halwagi, M. M. Shale Gas Monetization – A Review of Downstream Processing to Chemicals and Fuels. *J. Nat. Gas Sci. Eng.* **2017**, *45*, 436–455.
(120) Sousa-Aguiar, E. F.; Noronha, F. B.; Faro, A. The Main Catalytic Challenges in GTL (Gas-to-Liquids) Processes. *Catal. Sci. Technol.* **2011**, *1*, 698–713.
(121) Guisnet, M.; Gnep, N. S.; Alario, F. Aromatization of Short Chain Alkanes on Zeolite Catalysts. *Appl. Catal. A, Gen.* **1992**, *89*, 1–30.
(122) Al-Zahrani, S. M. Catalytic Conversion of LPG to High-Value Aromatics: The Current State of the Art and Future Predictions. *Dev. Chem. Eng. Miner. Process.* **2008**, *6*, 101–120.
(123) Guisnet, M.; Gnep, N. S. Aromatization of Propane over GaHMFI Catalysts. Reaction Scheme, Nature of the Dehydrogenating Species and Mode of Coke Formation. *Catal. Today* **1996**, *31*, 275–292.
(124) Hensen, E. J. M.; Pidko, E. A.; Rane, N.; van Santen, R. A. *Modification of Brønsted Acidity of Zeolites by Ga^+, GaO^+ and AlO^+: Comparison for Alkane Activation*; Elsevier B.V., 2007; Vol. 170.
(125) Faro, C.; Oliveira, V. De. Pulse Reaction Studies of Gallium Modified H-ZSM5 Catalysts

with Propane. **2008**, 1155–1158.
(126) Taha, Z. A.; Deguns, E. W.; Chattopadhyay, S.; Scott, S. L. Formation of Digallium Sites in the Reaction of Trimethylgallium with Silica. *Organometallics* **2006**, *25*, 1891–1899.
(127) Szeto, K. C.; Gallo, A.; Hernández-Morejudo, S.; Olsbye, U.; De Mallmann, A.; Lefebvre, F.; Gauvin, R. M.; Delevoye, L.; Scott, S. L.; Taoufik, M. Selective Grafting of $Ga(i\text{-}Bu)_3$ on the Silanols of Mesoporous H-ZSM-5 by Surface Organometallic Chemistry. *J. Phys. Chem. C* **2015**, *119*, 26611–26619.
(128) Cybulskis, V. J.; Pradhan, S. U.; Lovón-Quintana, J. J.; Hock, A. S.; Hu, B.; Zhang, G.; Delgass, W. N.; Ribeiro, F. H.; Miller, J. T. The Nature of the Isolated Gallium Active Center for Propane Dehydrogenation on Ga/SiO_2. *Catal. Letters* **2017**, *147*, 1252–1262.
(129) Kim, W. G.; So, J.; Choi, S. W.; Liu, Y.; Dixit, R. S.; Sievers, C.; Sholl, D. S.; Nair, S.; Jones, C. W. Hierarchical Ga-MFI Catalysts for Propane Dehydrogenation. *Chem. Mater.* **2017**, *29*, 7213–7222.
(130) Dooley, K. M.; Chang, C.; Price, G. L. Effects of Pretreatments on State of Gallium and Aromatization Activity of Gallium/ZSM-5 Catalysts. *Appl. Catal. A, Gen.* **1992**, *84*, 17–30.
(131) Dooley, K. M.; Price, G. L.; Kanazirev, V. I.; Hart, V. I. Gallium-Loaded Zeolites for Light Paraffin Aromatization: Evidence for Exchanged Gallium Cation Active Centers. *Catal. Today* **1996**, *31*, 305–315.
(132) Price, G. L.; Kanazirev, V.; Dooley, K. M.; Hart, V. I. On the Mechanism of Propane Dehydrocyclization over Cation-Containing, Proton-Poor MFI Zeolite. *J. Catal.* **1998**, *173*, 17–27.
(133) Phadke, N.; Van Der Mynsbrugge, J.; Mansoor, E.; Getsoian, A.; Head-Gordon, M.; Bell, A. T. Characterization of Isolated Ga^{3+} Cations in Ga/H-MFI Prepared by Vapor-Phase Exchange of H-MFI with $GaCl_3$. *ACS Catal.* **2018**, *8*, 6106–6126.
(134) Vannice, Albert, M. *Kinetics of Catalytic Reactions*; Springer US: New York, 2005.
(135) Mansoor, E.; Van der Mynsbrugge, J.; Head-Gordon, M.; Bell, A. T. Impact of Long-Range Electrostatic and Dispersive Interactions on Theoretical Predictions of Adsorption and Catalysis in Zeolites. *Catal. Today* **2018**, 1–55.
(136) Olson, D. H.; Khosrovani, N.; Peters, A. W.; Toby, B. H. Crystal Structure of Dehydrated CsZSM-5 (5.8Al): Evidence for Nonrandom Aluminum Distribution. *J. Phys. Chem. B* **2000**, *104*, 4844–4848.
(137) Mardirossian, N.; Head-Gordon, M. Thirty Years of Density Functional Theory in Computational Chemistry: An Overview and Extensive Assessment of 200 Density Functionals. *Mol. Phys.* **2017**, *115*, 2315–2372.
(138) Goerigk, L.; Hansen, A.; Bauer, C. A.; Ehrlich, S.; Najibi, A.; Grimme, S. A Look at the Density Functional Theory Zoo with the Advanced GMTKN55 Database for General Main Group Thermochemistry, Kinetics and Noncovalent Interactions. *Phys. Chem. Chem. Phys.* **2017**, *19*, 32184–32215.
(139) Janda, A.; Vlaisavljevich, B.; Lin, L. C.; Mallikarjun Sharada, S.; Smit, B.; Head-Gordon, M.; Bell, A. T. Adsorption Thermodynamics and Intrinsic Activation Parameters for Monomolecular Cracking of N-Alkanes on Brønsted Acid Sites in Zeolites. *J. Phys. Chem. C* **2015**, *119*, 10427–10438.
(140) Kozuch, S. A Refinement of Everyday Thinking: The Energetic Span Model for Kinetic Assessment of Catalytic Cycles. *Wiley Interdiscip. Rev. Comput. Mol. Sci.* **2012**, *2*, 795–815.

(141) Kozuch, S.; Shaik, S. How to Conceptualize Catalytic Cycles? The Energetic Span Model. *Acc. Chem. Res.* **2011**, *44*, 101–110.
(142) Kozuch, S.; Martin, J. M. L. " Turning Over " Definitions in Catalytic Cycles. *ACS Catal.* **2012**, *2*, 2787–2794.
(143) Kozuch, S.; Shaik, S. A Combined Kinetic-Quantum Mechanical Model for Assessment of Catalytic Cycles: Application to Cross-Coupling and Heck Reactions. *J. Am. Chem. Soc.* **2006**, *128*, 3355–3365.
(144) Narbeshuber, T. F.; Vinek, H.; Lercher, J. A. Monomolecular Conversion of Light Alkanes over H-ZSM-5. *J. Catal.* **1995**, *157*, 388–395.
(145) Haag, W. O.; Dessau, R. M.; Lago, R. M. Kinetics and Mechanism of Paraffin Cracking with Zeolite Catalysts. *Stud. Surf. Sci. Catal.* **1991**, *60*, 255–265.
(146) Narbeshuber, T. F.; Brait, A.; Seshan, K.; Lercher, J. A. Dehydrogenation of Light Alkanes over Zeolites. *J. Catal.* **1997**, *172*, 127–136.
(147) Xu, B.; Sievers, C.; Hong, S. B.; Prins, R.; van Bokhoven, J. A. Catalytic Activity of Brønsted Acid Sites in Zeolites: Intrinsic Activity, Rate-Limiting Step, and Influence of the Local Structure of the Acid Sites. *J. Catal.* **2006**, *244*, 163–168.
(148) Kolyagin, Y. G.; Ordomsky, V. V.; Khimyak, Y. Z.; Rebrov, A. I.; Fajula, F.; Ivanova, I. I. Initial Stages of Propane Activation over Zn/MFI Catalyst Studied by in Situ NMR and IR Spectroscopic Techniques. *J. Catal.* **2006**, *238*, 122–133.
(149) Gabrienko, A. A.; Arzumanov, S. S.; Freude, D.; Stepanov, A. G. Propane Aromatization on Zn-Modified Zeolite BEA Studied by Solid-State NMR in Situ. *J. Phys. Chem. C* **2010**, *114*, 12681–12688.
(150) Gonzales, N. O.; Chakraborty, A. K.; Bell, A. T. A Density Functional Study of the Effects of Metal Cations on the Bronsted Acidity of H-ZSM-5. *Catal. Letters* **1998**, *50*, 135–139.
(151) Vayssilov, G. N.; Rösch, N. Influence of Alkali and Alkaline Earth Cations on the Brønsted Acidity of Zeolites. *J. Phys. Chem. B* **2001**, *105*, 4277–4284.
(152) Wilkinson, G.; Gillard, R. D.; McCleverty, J. A. *Comprehensive Coordination Chemistry : The Synthesis, Reactions, Properties & Applications of Coordination Compounds*; Pergamon Press, 1987.
(153) Rooney, J. J. Eyring Transition-State Theory and Kinetics in Catalysis. *J. Mol. Catal. A Chem.* **1995**, *96*, L1–L3.
(154) Phadke, N.; Van der Mynsbrugge, J.; Mansoor, E.; Getsoian, A.; Head-gordon, M.; Bell, A. T. Characterization of Isolated Ga^{3+} Cations in Ga / H-MFI Prepared by Vapor-Phase Exchange of H-MFI Zeolite with $GaCl_3$. *ACS Catal.* **2018**, *8*, 6106–6126.
(155) Montes, A.; Giannetto, G. A New Way to Obtain Acid or Bifunctional Catalysts V. Considerations on Bifunctionality of the Propane Aromatization Reaction over [Ga, Al]-ZSM-5 Catalysts. *Appl. Catal. A Gen.* **2000**, *197*, 31–39.
(156) Dooley, K. M.; Guidry, T. F.; Price, G. L. Control of Intrazeolitic Gallium Cation Content and Its Effects on C2dehydrogenation in Ga-MFI Catalysts. *Journal of Catalysis*. 1995, pp 66–75.
(157) El-Malki, E.-M.; van Santen, R. a.; Sachtler, W. M. H. Introduction of Zn, Ga, and Fe into HZSM-5 Cavities by Sublimation: Identification of Acid Sites. *J. Phys. Chem. B* **1999**, *103*, 4611–4622.
(158) Phadke, N. M.; Mansoor, E.; Bondil, M.; Head-Gordon, M.; Bell, A. T. Mechanism and Kinetics of Propane Dehydrogenation and Cracking over Ga/H-MFI Prepared via Vapor-

Phase Exchange of H-MFI with $GaCl_3$. *Submitted* **2018**.
(159) Bandiera, J.; Taârit, Y. Ben. Ethane Conversion: Kinetic Evidence for the Competition of Consecutive Steps for the Same Active Centre. *Appl. Catal. A Gen.* **1997**, *152*, 43–51.
(160) Sazama, P.; Dedecek, J.; Gabova, V.; Wichterlova, B.; Spoto, G.; Bordiga, S. Effect of Aluminium Distribution in the Framework of ZSM-5 on Hydrocarbon Transformation . Cracking of 1-Butene. *J. Catal.* **2008**, *254*, 180–189.
(161) Boronat, M.; Corma, A. Are Carbenium and Carbonium Ions Reaction Intermediates in Zeolite-Catalyzed Reactions? *Appl. Catal. A Gen.* **2008**, *336*, 2–10.
(162) Sarazen, M. L.; Doskocil, E.; Iglesia, E. Effects of Void Environment and Acid Strength on Alkene Oligomerization Selectivity. *ACS Catal.* **2016**, *6*, 7059–7070.
(163) Sarazen, M. L.; Doskocil, E.; Iglesia, E. Catalysis on Solid Acids: Mechanism and Catalyst Descriptors in Oligomerization Reactions of Light Alkenes. *J. Catal.* **2016**, *344*, 553–570.
(164) Guisnet, M.; Gnep, N. S.; Aittaleb, D.; Doyemet, J. Y. Conversion of Light Alkanes into Aromatic Hydrocarbons, VI. Aromatization of C2- C4 Alkanes on H-ZSM5-Reaction Mechanisms. *Appl. Catal. A, Gen.* **1992**, *87*, 255–270.
(165) Blaszkowski, S. R.; Nascimento, M. A. C.; Van Santen, R. A. Activation of C-H and C-C Bonds by an Acidic Zeolite: A Density Functional Study. *J. Phys. Chem.* **1996**, *100*, 3463–3472.
(166) Lukyanov, D. B.; Beckett, S. J.; Vazhnova, T. Toward Better Understanding of the Catalytic Action of Acidic Zeolites: Investigation in Methane and Ethane Activation and Transformation. *ACS Catal.* **2012**, *2*, 2596–2601.
(167) Fărcaşiu, D.; Lukinskas, P. Mechanism and Reactivity of Alkane C-H Bond Dissociation on Coordinatively Unsaturated Aluminum Ions, Determined by Theoretical Calculations. *J. Phys. Chem. A* **2002**, *106*, 1619–1626.
(168) Djéga-Mariadassou, G.; Boudart, M. Classical Kinetics of Catalytic Reactions. *J. Catal.* **2003**, *216*, 89–97.